PEOPLE'S DEMOCRATIC REPUBLIC OF ALGERIA

Ministry of Higher Education and Scientific Research

Amar Telidji University - Laghouat

Faculty of TECHNOLOGY

DOCTORAL THESIS IN SCIENCES

Specialty: Electrical Engineering

Presented by:

BEN LEKHDIM Ahmed

Theme

Elaboration, Characterizations and Modeling of Photovoltaic Structures Based on III-V Materials

THE JURY MEMBERS :

Mr. LIDJICI Hamza	**Professor**	**University of Laghouat**	**Jury President**
Mr. CHEKNANE Ali	**Professor**	**University of Laghouat**	**Thesis Supervisor**
Mr. ZOUKEL Abdelhalim	**MCA**	**University of Laghouat**	**Examiner**
Mr. MANSOUR Omar	**MCA**	**University of Djelfa**	**Examiner**
Mrs. KHODJA Khadîdja	**Research Master A**	**Renewable Energy Research Unit of Ghardaia**	**Examiner**

2018/2019

في هذه الاطروحة ، قدمنا دراسة لنمذجة وتطوير الخلايا الشمسية التي سيكون لها قيمة كبيرة للمطورين و صناعة الخلايا الكهروضوئية. نظرًا لأن جميع الأبحاث تقريبًا حول الخلايا الشمسية المتقدمة تجرى حاليًا من خلال تجارب باهظة الثمن و معقدة، فمن المتوقع أن تساعد طريقة المحاكاة المقترحة في تقليل هذه التكلفة وتبسيط عملية التصميم والسماح للمصمم بالتركيز على النتيجة النهائية.

الموضوع الرئيسي في بحث الدكتوراه هذا هو وصف منهجية و نتائج المحاكاة للخلية شمسية ثلاثية الوصلات المتوافقة شبكيا InGaP / GaAs / Ge ، بما في ذلك تطوير تكنولوجيا التراص للخلايا الفرعية و ترابطها ؛ و كذا فهم و توقع أداء الخلايا الشمسية متعددة الوصلات المتجانسة من خلال المحاكاة العددية للخصائص الضوئية والكهربائية للخلية.

حققت الخلايا الشمسية متعددة الوصلات التي تعتمد على المواد III-V أعلى مستويات الكفاءة بالنسبة لأي تكنولوجيا كهروضوئية حالية. العمل المقدم في هذه الاطروحة يتعلق بدراسة ونمذجة بنيات كهروضوئية بناءً على المواد III-V . في هذه الاطروحة ، جهودنا الناجحة في نمذجة وتحسين كفاءة الخلايا الشمسية InGaP / GaAs / Ge متعددة الوصلات المتجانسة تكللت بتحقيق كفاءة عالية ، من أجل فهم وتوقع أداء الخلايا الشمسية متعددة الوصلات المتجانسة ، تم محاكاة الخلايا الشمسية المكدسة ميكانيكيا أولاً.

تم الحصول على أداء عالي للخلايا الشمسية أحادية الوصلة الفردية من نوع III-V ، مع أفضل كفاءة بنسبة 18.55٪ لـ InGaP ، و 29.39٪ لـ GaAs و 7.11٪ لـ Ge على التوالي. بعد محاكاة الخلايا الفردية، تم تكديسها ميكانيكيا ثم بطريقة متجانسة للخلايا GaAs / Ge مزدوجة الوصلة و InGaP / GaAs / Ge ثلاثية الوصلات.تم الحصول على كفاءة 33.28 ٪ للخلية الشمسية GaAs / Ge المزدوجة الوصلة، في حين أن 35.54 ٪ للخلية الشمسية InGaP / GaAs / Ge ثلاثية الوصلات تحت طيف إضاءة AM1.5G للتطبيقات الأرضية قد تتحقق بأقل جهد و تكلفة.

يوفر Silvaco برنامجًا للنمذجة يسمى ATLAS تم تصميمه خصيصًا لتصميم أجهزة أشباه الموصلات . Silvaco ATLAS هو البرنامج المستخدم في هذه الاطروحة لمحاكاة أداء الخلايا الشمسية. تم استخدام ATLAS لنمذجة الخلايا الشمسية متعددة الوصلات III-V التي يتم إنتاجها حاليًا للتحقق من صحة النموذج.

يهدف هذا العمل إلى تكملة وتعهد المشاريع التجريبية مع أساس نظري قوي. ويتم ذلك عن طريق الحسابات العددية على أساس نموذج مفصل و قاعدة فزيائية لمحاكاة الجهاز. تشير نتائج المحاكاة المشجعة لدينا إلى مستقبل متفائل لدمج تكنولوجيا الخلايا الشمسية III-V وستكون مفيدة في مستقبل تصميم و توقع أداء الخلايا الشمسية III-V متعددة الوصلات.

الكلمات المفتاحية: الخلية الشمسية أحادية الوصلة ، الخلايا الشمسية III-V متعددة الوصلات ، InGaP، GaAs، Ge، الكفاءة ، النمذجة ، المحاكاة ، Silvaco ATLAS.

Abstract

In this thesis, we presented a study for modeling and developing solar cells. It is believed that it will be of great value to the developers and photovoltaic industry. Since almost all research on advanced solar cells is currently conducted via expensive and complex experimentation, the proposed simulation method is expected to help reduce that cost, simplify the design process, and allow the designer to focus on the final result.

The main topic of this Ph.D. research is to describe the simulation methodology and simulation results of a lattice-matched InGaP/GaAs/Ge triple-junction solar cell, including the development of monolithically stacking technology of the sub-cells and their interconnections; understanding and predicting the performance of the Monolithically Multi-Junction (MMJ) solar cells through numerical simulation of the optical, electrical characteristics of the cell.

Multi-junction solar cells based on III-V materials have achieved the highest efficiencies of any present photovoltaic technology. The work presented in this thesis concerns of study and modeling of photovoltaic structures based on III-V Materials. In this thesis, our successful effort in modeling and optimization of higher efficiency InGaP/GaAs/Ge monolithically triple-junction solar cell is investigated, in order to understand and predict the performance of the MMJ solar cells, Mechanically Stacked Multi-Junction (MSMJ) solar cell was simulated first.

Very high performance III-V single-junction solar cells have been demonstrated, with the best efficiencies of 18.55% for InGaP, 29.39% for GaAs and 7.11% for Ge respectively under 1-sun (AM1.5G spectrum) illumination used for terrestrial applications. After the demonstration of individual sub-cells, mechanically and monolithically stacked for GaAs/Ge dual-junction cells and InGaP/GaAs/Ge triple junction cells are demonstrated as well. The efficiency of 33.28% for GaAs/Ge dual-junction solar cell, while 35.54% for InGaP/GaAs/Ge triple-junction solar cell under AM1.5G spectrum to illumination are realized with minimal effort and cost.

Silvaco provides a modeling program called ATLAS that is specifically designed to model semiconductor devices. Silvaco ATLAS is the software used in this thesis to simulate the performance of solar cells. ATLAS was used to model III-V multi-junction solar cells that are currently being produced to verify the validity of the model.

This work aims to supplement and ground the experimental undertakings with a strong theoretical basis. This is accomplished by numerical calculations based on the detailed model and by physics based device simulation. Our simulation results suggest an optimistic future for integrating III-V solar cell technology and will be useful for future design and prediction of multi-junction III-V solar cell performance.

Keywords: Single-junction solar cell, Multi-junction III-V solar cell, InGaP, GaAs, Ge, Efficiency, Modeling, simulation, Silvaco ATLAS.

Dans cette thèse, nous avons présenté une étude de modélisation et de développement de cellules solaires. On pense qu'il sera d'une grande valeur pour les développeurs et l'industrie photovoltaïque. Étant donné que presque toutes les recherches sur les cellules solaires avancées sont actuellement menées au moyen d'expérimentations coûteuses et complexes, la méthode de simulation proposée devrait permettre de réduire ce coût, de simplifier le processus de conception et de permettre au concepteur de se concentrer sur le résultat final.

Le sujet principale de cette thèse de doctorat sont de décrire la méthodologie et les résultats de simulation d'une cellule solaire triple jonction à base InGaP/GaAs/Ge en accord de maille, comprennent le développement de la technologie d'empilement monolithique des sous-cellules et de leurs interconnexions; comprendre et prédire les performances des cellules solaires multi-jonctions monolithique par la simulation numérique des caractéristiques optiques et électriques de la cellule.

Les cellules solaires multi-jonctions basées sur des matériaux III-V ont obtenu les rendements les plus élevés de toutes les technologies photovoltaïques actuelles. Les travaux présentés dans cette thèse concernent l'étude et la modélisation de structures photovoltaïques à base de matériaux III-V. Dans cette thèse, notre effort couronné de succès dans la modélisation et l'optimisation de cellules solaires monolithiques triple-jonctions à base InGaP/GaAs/Ge est étudié, afin de comprendre et de prédire les performances des cellules solaires multi-jonctions empilement monolithiques, la cellule solaire multi-jonctions empilées mécaniquement a été simulée en premier.

Des cellules solaires mono-jonction à base III-V de très haute performance ont été démontrées, avec des rendements optimaux de 18,55% pour InGaP, 29,39% pour GaAs et 7,11% pour Ge respectivement sous 1-soleil (AM1,5G) utilisées pour des applications terrestres. Après la démonstration de sous-cellules individuelles, les empilements mécanique et monolithique des cellules à double-jonctions GaAs/Ge et des cellules à triple-jonctions InGaP/GaAs/Ge sont également démontrés. L'efficacité de 33,28% pour la cellule solaire à double-jonctions GaAs/Ge, tandis que 35,54% pour la cellule solaire à triple-jonction InGaP/GaAs/Ge sous spectre AM1.5G à l'éclairage sont réalisées avec un minimum d'effort et de coût.

Silvaco fournit un programme de modélisation appelé ATLAS spécialement conçu pour modéliser des dispositifs à semi-conducteur. Silvaco ATLAS est le logiciel utilisé dans cette thèse pour simuler les performances des cellules solaires. ATLAS a été utilisé pour modéliser des cellules solaires multi-jonctions III-V qui sont actuellement produites pour vérifier la validité du modèle.

Ce travail vise à compléter et à fonder les entreprises expérimentales d'une base théorique solide. Ceci est accompli par des calculs numériques basés sur le modèle détaillé et par une simulation de dispositif basée sur la physique. Nos résultats de simulation suggèrent un avenir optimiste pour l'intégration de la technologie des cellules solaires à base III-V et seront utiles pour la conception et la prévision futures des performances des cellules solaires multi-jonction III-V.

Mots-clés: Cellule solaire mono-jonction, Cellule solaire multi-jonction à base III-V, InGaP, GaAs, Ge, Efficacité, Modélisation, simulation, Silvaco ATLAS.

Acknowledgments

This doctoral work has been a very interesting and rewarding journey, thanks to the contributions of various individuals, who have been indispensable in bringing this research to light.

First of all, academically I would like to deeply thank my supervisor Prof. Ali Cheknane, for giving me the opportunity to work under his guidance over the years throughout my Ph.D. study, he's been extremely supportive and I'm grateful to him for his continued encouragement and faith in my ideas. I learned to be an independent researcher with self-initiating and problem-solving skills thank him for his corrections and his careful proofreading of this thesis text. Is an honor for me to work under his supervision. His passion and successful career path set an unprecedented role model for many young students to learn and admire. I am also thankful for the freedom you have given me to test my own ideas and satisfy my curiosity.

I also wish to thank all my jury members, Prof. Hamza Lidjici, Dr. Abdelhalim Zoukel, Dr. Omar Mansour and Dr. Khodja Khadidja for their useful and valuable comments, criticisms and suggestions on this Ph.D. thesis. Thank you to my examiners for taking the time to thoroughness in reviewing my work. Furthermore, I want to thank Mr. Abdelwaheb Hamdi, for his continued encouragement, who has been very kind to me and greatly helped me in many academic and administrative matters.

This thesis is based on the Silvaco Atlas simulator; I must also thank my contacts to Silvaco for their valuable suggestions about the software that helped me recently, for his expertise with Silvaco ATLAS and his help to troubleshooting the program.

I thank my parents as well since they have always been my "home supervisors" ever since I started my education, for their unconditional love, who brought me up with a love for science and encouraged me to pursue my dreams during all these years. Their loving care and hopes for me have become the greatest source of my motivation.

Finally, I would like to thank my family members and my friends for their support through all of my trials and tribulations. Their support is what gives me the strength to continue. It would have been very difficult to complete this thesis without her full support and encouragement during my studies.

Ahmed BEN LEKHDIM,
2019

This list shows symbols and abbreviations of physical parameters frequently used in the thesis

Symbols

a_0	Crystal lattice constant
D_n	Electron diffusion coefficient
D_p	Hole diffusion coefficient
E	Energy
E_C	Conduction band energy
E_F	Fermi energy
E_{Fn}	Quasi-Fermi energy for electrons
E_{Fp}	Quasi-Fermi energy for holes
E_i	Intrinsic energy level
E_g	Band gap energy
E_v	Valence band energy
E_t	Trap energy
f	Fermi distribution function for electrons
G	Generation rate
G_n	Electron generation
G_p	Hole generation
h	Planck's constant
$\hbar$	Reduced Planck's constant. $\hbar = h/2\pi$
I	Illumination intensity
J_0	Generalized saturation current density
J_{drif}	Drift current
J_{diff}	diffusion current
J_n	Electron current density
J_p	Hole current density
$J_{n,diff}$	Diffusion current for electrons
$J_{n,drift}$	Drift current for electrons
$J_{p,diff}$	Diffusion current for holes
$J_{p,drift}$	Drift current for holes
k	Wave vector
k_B	Boltzmann constant
m_0	Free electron mass
m_c	Electron effective mass
m_n	Effective mass of an electron
m_p	Effective mass of a hole
$m^*_{e,h}$	electron/hole effective mass (e denotes electron, h denotes hole)
n	Electron concentration
n_0	Equilibrium electron concentration

n_i	Intrinsic carrier concentration
N_A	Effective density of states in the conduction band
N_A^+	Concentration of ionized acceptors
Nc	Acceptor atom concentration
N_D	Donor atom concentration
N_D^+	Concentration of ionized donors
Nv	Effective density of states in the valence band
p	Hole concentration
p_0	Equilibrium hole concentration
p	Momentum
q	Elementary charge
R_{Auger}	Auger recombination rate
R_{SRH}	Shockley–Read–Hall recombination rate
R_{surf}	Surface recombination rate
$R_{Radiati}$	Radiative recombination rate
Sn	Surface recombination velocity of electrons
Sp	Surface recombination velocity of holes
t	Time
T	Temperature
V	Voltage
V_{OC}	Open-Circuit Voltage
Vm	Maximum power Voltage
V_{bi}	Built-in voltage
v	Carrier velocity
ρ	Resistivity
α_o	Optical absorption coefficient
ε_0	Vacuum electrical permittivity
λ	Optical wavelength
μ	Electron or hole mobility
μ_n	Electron mobility
μ_p	hole mobility
τ_n	Electron recombination lifetime
τ_p	Hole recombination lifetime
σ	Conductivity
η	Efficiency
μ_n	Electron mobility
μ_p	Hole mobility

Abbreviations

1D	One-dimensional
2D	Two-dimensional
3D	Three- dimensional
3 J	Triple-junctions
AlGaAs	Aluminum gallium arsenide
APSS	Simulation software by Crosslight Software, Inc.
AM	Air-mass
AM0	Air Mass zero spectrum
AM1.5	Air Mass 1.5 spectrum
AM1.5G	Reference global solar spectral irradiance for an air mass of 1.5
AR	Anti-Reflection
BSF	Back Surface Field
CPV	Concentrator photovoltaic
EHP	Electron-hole-pair
EQE	External quantum efficiency
FF	Fill-Factor
FSF	Front-S urface-Field
Ge	Germanium
GaAs	Gallium arsenide
J_{SC}	Short circuit current density
Isc	Short circuit current
InGaP	Indium Gallium phosphide
I-V	Current vs voltage
IMM	Inverted metamorphic
LM	Lattice-matched
MJ	Multi-junction
MJSC	Multi-Junction Solar Cells
MM	Metamorphic
MOCVD	Metal organic chemical vapor deposition
MOVPE	Metal organic vapor phase
MSSC	Mechanically Stacked Solar Cells
Pmax	Maximum power
PV	Photovoltaic
QD	Quantum Dot
QW	Quantum well
QE	Quantum efficiency
Rs	Series resistance
Rsh	Shunt resistance
SC	Solar Cell
SRH	Shockley-Read-Hall
SR	Spectral response
TCAD	Technology Computer-Aided Design
TJ	Tunnel junctions
Voc	Open circuit voltage

Contents

Contents

Chapter 3
Simulating Single Junction Solar Cells Using Silvaco TCAD

List of Figures

Chapter 1
Solar Cell Physics and Modeling

Chapter 2
High-efficiency Multi-junction Solar Cells

Chapter 3
Simulating Single Junction Solar Cells Using Silvaco TCAD

Chapter 4
Simulating Multi-Junction Solar Cells Using Silvaco TCAD

List of Tables

Chapter 1
Solar Cell Physics and modeling

Chapter 2
High-efficiency Multi-junction Solar Cells

Chapter 3
Simulating Single Junction Solar Cells Using Silvaco TCAD

Chapter 4
Simulating Multi-Junction Solar Cells Using Silvaco TCAD

General Introduction

General Introduction

Modern life requires ever greater amount of energy usage. Energy is needed to power all sorts of electrical machinery that make our life so much easier as well as all kinds of electronics, be it for work or pleasure. Energy is needed everywhere, even in extremely remote places such as outer space. Thus, it is necessary to replace existing sources, which are mostly fossil fuels, with alternative ones which are friendlier to the environment. In addition, fossil fuels are not abundant in nature and their finite amount requires the development of renewable energy sources. Renewable energy such as solar energy, wind and water power, geothermal and biomass energy, may hold the key to solving the energy puzzle as they are abundant and do not produce any CO_2. One of the most important renewable energy sources is the electromagnetic energy from the sun. Devices which are able to convert the sun energy (electromagnetic waves) into electrical energy are generally called photovoltaic devices (PV), solar cells (SC) or photovoltaic cells (PVCs). Solar cells convert the energy of the sunlight to electricity. It is an optical to electrical energy conversion. In principle, they make use of the photovoltaic (PV) effect, i.e., the generation of a potential difference between two electrodes under illumination. It was first observed by A. E. Becquerel (Becquerel, 1839). The requirements of a PV device are high efficiency, low cost, environment resistance (durability) and easy fabrication method. Concerning photovoltaic devices, we can find different types, where the energy process conversion is different for each of them.

This thesis presents a simulation work developing high-efficiency photovoltaics through mechanically and monolithically stacked integration of solar cells with lattice matched constants. This thesis is structured in two main parts, accompanied by this general introduction and the final conclusions and future works. Part I is the theoretical background, comprising chapters 1 and 2, is devoted to the theoretical Physics, modeling and design of the single-junction and High-efficiency multi-junction solar cells. Part II, comprising chapters 3 and 4, is devoted to the simulation results of the single junction and multi-junction solar cells using Silvaco ATLAS TCAD and discussions.

In Chapter 1, the mathematical models and the physical principles underlying the operation of solar cells are the subject of this chapter. To accurately analyze an arbitrary semiconductor structure which is intended as a self-contained device under various operating conditions, a mathematical model has to be given. The equations which form this mathematical model are commonly called the basic semiconductor equations. Modeling is obviously a necessity for analysis and simulation. With a model, one can analyze some phenomena, provided that effects one wants to extract are built in the model, possibly in a very complex manner. This chapter reviews the physical mechanisms that affect the carrier transport in optoelectronic devices, including *pn*-junctions. With this chapter, we begin on solar radiation with a short introduction about the Sun and solar spectra, a short overview of detailed numerical modeling of solar cells. Solar cell modeling is fundamental to a detailed understanding of the device operation, and a comprehensive model requires detailed knowledge of the material parameters. A brief overview of the semiconductor properties relevant to solar cell operation is given in this chapter, including the semiconductor band structure and carrier statistics, transport and optical properties, then generation and recombination of electron-hole pairs Processes. Next, the electrostatic properties of the *pn*-junction diode are reviewed, which are required to understand the operation of solar cells, followed by a description of the design and working principle and characteristics of the

solar cell. This is used to define the basic solar cell figures of merit, namely, the open-circuit voltage, V_{OC}; the short-circuit current, I_{SC}; the fill factor, *FF*; the conversion efficiency, η, the solar cell spectral response, parasitic resistive effects. Finally, Losses mechanisms in solar cell and solutions are introduced.

Chapter 2: the first part is briefly reviews the history of solar cells. We also review recent progress with laboratory cells; the efficiency records solar cells are included. In addition, describe special features of III-V multi-junction (MJ) solar cells in comparison to conventional single-junction solar cells. In the second part, we describe the principle, design, and configurations, cell interconnection technologies of III–V multi-junction solar cells. In addition, we describes some of the different approaches and designs for III–V solar cells and make some predictions about the future of MJ cells in the last part in order to provide a foundation to facilitate the discussion of results in terms of the long-term goal of this work: multi-junction solar cells are able to achieve significantly higher efficiencies than single junctions due to better spectral utilization.

In Chapter 3, two-dimensional numerical simulations are performed by commercial software Silvaco ATLAS TCAD, to model different single junction solar cell types, with optimization results. Armed with a foundation in fundamental semiconductor properties from chapter 1, the features and characteristics of semiconductor *p-n* junctions are investigated by using the SILVACO Atlas software. From this point, the important characteristics short circuit current density (Jsc), open circuit voltage (Voc), maximum power (Pmax), Fill factor (FF), efficiency η and also the frequency response, photogeneration rate of single junction solar cells will be discussed. The effects of window and back surface field BSF layers on the important characteristics, which determine the performance of a solar cell, will be discussed. A comparison of solar cell performance is also given for various materials such as gallium indium phosphide (InGaP), gallium arsenide (GaAs) and germanium (Ge). In order to validation of the models, a comparison between simulated and reported performances in the literature is also included. Optimization of single junction solar cell is the basis for multi-junction solar cell optimization and therefore is introduced first, which will be discussed in detail in chapter 4.

Chapter 4 has been dedicated to the methodology introduced in chapter 1, chapter 2 and the results of chapter 3 to provide a complete simulation of a multi-junction solar cell. After successfully modeling the single-junction InGaP, GaAs and Ge solar cells in chapter 3, to its inclusion in the dual-junction and triple-junction solar cells structure, the primary goal of this chapter is to describe the multi-junction optimization of solar cell and simulation results of a lattice matched mechanically and monolithically InGaP/GaAs dual-junction and InGaP/GaAs/Ge triple-junction stacked solar cell. We design and optimize mechanically and monolithically III-V solar cells by using a commercial software Silvaco ATLAS simulator to obtain the important device characteristics short circuit density (Jsc), open circuit voltage (Voc), maximum power (Pmax), Fill factor (FF), efficiency η. For the optimized cell structure, the frequency response and the photogeneration rate distributions are also investigated, with promising results. As validation of the models, a comparison between simulated and reported performances in the literature is also included.

Finally, the most important conclusions of the research carried out in this thesis are summarized, and the recommendations of the future works intended for the development of more advanced versions of multi-junction solar cells are outlined.

Chapter 1

Solar Cell Physics and Modeling

Chapter 1

Solar Cell Physics and Modeling

Introduction

Solar cells convert the energy of the sunlight to electricity. It is an optical to electrical energy conversion. In principle, they make use of the photovoltaic (PV) effect, i.e., the generation of a potential difference between two electrodes under illumination. It was first observed by A. E. Becquerel (Becquerel, 1839). The physical principles underlying the operation of solar cells are the subject of this chapter. To accurately analyze an arbitrary semiconductor structure which is intended as a self-contained device under various operating conditions, a mathematical model has to be given. The equations which form this mathematical model are commonly called the basic semiconductor equations. Modeling is obviously a necessity for analysis and simulation. With a model, one can analyze some phenomena, provided that the effects one wants to extract are built in the model, possibly in a very complex manner.

Electrical current flow in semiconductors is mainly dominated by drift and diffusion of electrons and holes. This chapter reviews the physical mechanisms that affect the carrier transport in optoelectronic devices, including *pn*-junctions. With this chapter we begin on solar radiation with a short introduction about the Sun and solar spectra, a short overview of detailed numerical modeling of solar cells. Solar cell modeling is fundamental to a detailed understanding of the device operation, and a comprehensive model requires a detailed knowledge of the material parameters. A brief overview of the semiconductor properties relevant to solar cell operation is given in this chapter, including the semiconductor band structure and carrier statistics, transport and optical properties, then generation and recombination of electron-hole pairs Processes. Next, the electrostatic properties of the *pn*-junction diode are reviewed, which are required to understand the operation of solar cells, followed by a description of the design and working principle and characteristics of the solar cell. This is used to define the basic solar cell figures of merit, namely, the open-circuit voltage, V_{OC}; the short-circuit current, I_{SC}; the fill factor, *FF*; the conversion efficiency, η, the solar cell spectral response, parasitic resistive effects. Finally, Losses mechanisms in solar cell and solutions are introduced.

I Solar Radiation

The Sun is the central star of our solar system. It consists mainly of hydrogen and helium. Some basic facts are [1, 2]:

- Mean distance from the Earth: 149 600 000 km (the astronomic unit, AU)
- Diameter: 1 392 000 km (109 x that of the Earth)
- Volume: 1 300 000 x that of the Earth
- Mass: 1.993 x 10^{27} kg (332 000 times that of the Earth)
- Density (at its center): >10^5 kg m^{-3} (over 100 times that of water)
- Pressure (at its center): over 1 billion atmospheres
- Temperature (at its center): about 15 000 000 K
- Temperature (at the surface): 6 000 K
- Energy radiation: 3.8 x 10^{26} W
- The Earth receives: 1.7 x10^{18} W

The mass of the Sun is so large that it contributes to 99.68% of the total mass of the solar system. In the center of the Sun the pressure-temperature conditions are such that nuclear fusion can take place. In the major nuclear reaction, the proton-proton reaction, via a number of steps four protons react into [1, 2],

- a helium core (two protons and two neutrons),
- 2 positrons (the anti-particles of electrons),
- 2 neutrinos,
- Electromagnetic radiation.

The core of the sun is so dense that radiation cannot travel freely but is continuously absorbed and re-emitted, such that it takes the radiation between 10 000 and 170 000 years to travel to the solar surface. The surface of the Sun is called the photosphere. It has a temperature of about 6000 K. It behaves quite perfectly as a blackbody and is the source of the solar radiation that hits the Earth. The total power density of the solar radiation at the mean Earth-sun distance on a plane perpendicular to the direction of the Sun, outside the Earth's atmosphere, is referred to as the solar constant. Its value is approximately 1361 W/m^2 [1, 2].

I.1 Solar Spectrum

All electromagnetic radiation, including sunlight, is composed of particles called photons, which carry specific amounts of energy determined by the spectral properties of their source. Photons also exhibit a wavelike character with the wavelength, λ, being related to the photon energy, E_λ, by

$$E_\lambda = \frac{hc}{\lambda} \tag{1.1}$$

where λ is the wavelength (in m), h is Planck's constant (6.626 10^{-34} J.s) and c is the speed of light in vacuum (2.998 10^8 m/s).

Only photons with sufficient energy to create an electron–hole pair in a semiconductor material, that is, those with energy greater than the semiconductor band gap (E_g), will contribute to the energy conversion process. Thus, the spectral nature of sunlight is an important consideration in the design of efficient solar cells [3]. Therefore, it is important to know the spectral distribution of solar radiation, i.e. the number of photons of particular energy as a function of the wavelength λ. Two quantities are used to describe the solar radiation spectrum, namely the spectral irradiance $I_{e\lambda}$ and the spectral photon flux $\Phi_{ph}(\lambda)$.

The surface temperature of the Sun is about 6000 K. If it would be a perfect black body, it would emit a spectrum. The blackbody spectrum is illustrated in Figure 1.1. The spectrum outside the atmosphere of the Earth is already very different. It is called the AM0 spectrum because no (or "zero") atmosphere is traversed. AM0 also is shown in Figure 1.1. The irradiance at AM0 is I_e(AM0) = 1361 W.m^{-2} [3].

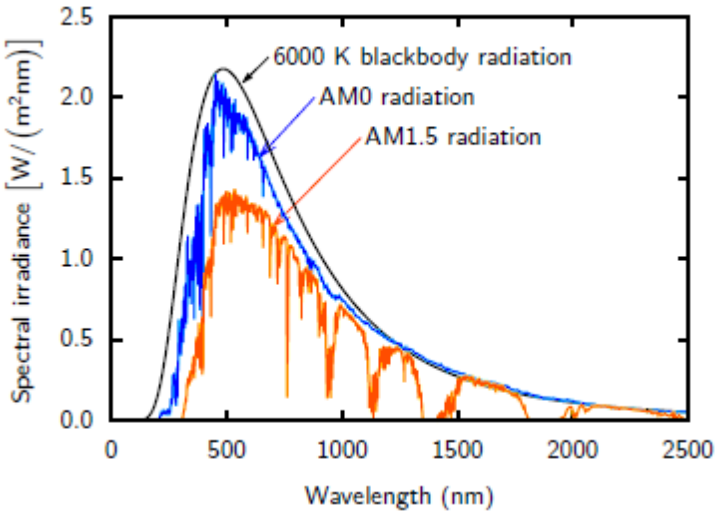

Figure 1.1: Different solar spectra: the blackbody spectrum of a blackbody at 6000 K, the extraterrestrial AM0 spectrum and the AM1.5 global spectrum [3].

When solar radiation passes through the atmosphere of the Earth, it is attenuated. The most important parameter that determines the solar irradiance under clear sky conditions is the distance that the sunlight has to travel through the atmosphere. This distance is the shortest when the Sun is at the zenith, i.e. directly overhead. The ratio of an actual path length of the sunlight to this minimal distance is known as the optical air mass. When the Sun is at its zenith the optical air mass is unity and the spectrum is called the air mass 1 (AM1) spectrum. The Air Mass is a measure of how absorption in the atmosphere affects the spectral content and intensity of the solar radiation reaching the Earth's surface. When the Sun is at an angle θ with the zenith the Air Mass number is given by [3]:

$$AM = \frac{1}{cos\theta} \tag{1.2}$$

Depending on the position on the Earth and the position of the Sun in the sky, terrestrial solar radiation varies both in intensity and the spectral distribution. The attenuation of solar radiation is due to scattering and absorption by air molecules, dust particles and/or aerosols in the atmosphere. Especially, steam (H_2O), oxygen (O_2) and carbon dioxide (CO_2) cause absorption. Since this absorption is wavelength-selective, it results in gaps in the spectral distribution of solar radiation as apparent in Figure 1.1. Ozone absorbs radiation with wavelengths below 300 nm. Depletion of ozone from the atmosphere allows more ultraviolet radiation to reach the Earth, with consequent harmful effects upon biological systems. CO_2 molecules contribute to the absorption of solar radiation at wavelengths above 1 μm. By changing the CO_2 content in the atmosphere the absorption in the infrared, which has consequences for our climate [3].

Solar cells and photovoltaic modules are produced by many different companies and laboratories. Further, many different solar cell technologies are investigated and sold. It is therefore of utmost importance to define a reference solar spectrum that allows a comparison of all the different solar cells and PV modules. The industrial standard is the AM1.5 spectrum, which corresponds to an angle of 48.2°. While the "real" AM1.5 spectrum corresponds to a total irradiance of 827 $W.m^{-2}$, the industrial standard corresponds to $I_e(AM1.5) = 1000\ W.m^{-2}$ and is close to the maximum received at the surface of the Earth.

II Physical Models for Solar Cell Simulation

Semiconductor device models can be classified into two categories: physical device models and equivalent circuit models. Physical device models account for the physics of device operation, and equivalent circuit models are based on electrical circuit analogies representing electrical behavior. The latter approach is generally limited in its applicability because of the frequency dependence and the non-linear behavior of most devices with respect to signal level. The advantage of this technique is that it is easy to implement. In contrast, physical device models can provide greater insight into the detailed operation of semiconductor devices but usually require lengthy analysis. The analysis requirements for physical models are typically satisfied using numerical techniques implemented on computers. With the advent of fast and powerful computing resources, this makes physical modeling techniques a very attractive proposition for the physicist.

Physical device models are solved using either bulk carrier transport equations, solutions to the Boltzmann transport equation, or quantum transport concepts. Historically, bulk transport solutions have satisfied most device models, while Boltzmann and quantum transport solutions have provided strong insight into the detailed device physics. However, the trend toward very small geometry devices, operating in the hot electron range, means that non-equilibrium transport conditions must be accounted for. The understanding of physical boundary conditions and device-circuit interaction is steadily improving, allowing more intricate models to be developed.

During the technology development in the past years, solar cells with higher performance are more and more desirable. Theoretical simulations of cell devices can not only help to optimize the device performance but also save time and cost. In the early years of solar cell research, people already developed various theoretical models, such as the detailed balance models developed by Shockley and

Queisser, to predict solar cell efficiency limits. Years of research in the physics of the devices was based semiconductors have led to the realization of a mathematical model. This model is able to operate in virtually any semiconductor-based device.

Semiconductor device simulators can model the electrical, optical and thermal properties of devices. These tools allow the user to work on band structure engineering, quantum confinement and other optimizations that would be difficult to accomplish using experimental results alone. Most device simulators are based on 2D/3D finite element analysis of electrical, thermal and optical properties of compound and silicon semiconductor devices. Once the device parameters are defined, a set of nonlinear equations for each layer in the structure need to be solved, with the boundary conditions for each interface. These equations include Poisson Equation, current continuity equations and carrier transport equations (drift-diffusion equations).

Numerous software tools that use the material parameters and physical models for the numerical simulation solar cell operation have been developed over the years, The most widespread one-dimensional numerical simulators are PC1D, ADEPT, AMPS, and AFORS-HET, all of them being free software. For two-and three-dimensional calculations, commercial semiconductor device simulation software packages include Synopsys SENTAURUS, Crosslight APSYS, COMSOL Multiphysics, and Silvaco ATLAS is the software to be used in this simulation thesis. An introduction to Silvaco's ATLAS software and general simulation methodology will be presented in Appendix I.

II.1 Silvaco ATLAS Simulation Software

Simulation methodology is based on the fundamental physical equations. The choice of physical models is important to improve the accuracy of the numerical simulation results. Silvaco ATLAS is a physics-based simulator which was specifically designed for the purpose of modeling the semiconductor devices. For this, the software SILVACO puts at our disposal a wide variety of physiques. In this work, the commercial software package Silvaco is used to design and optimize the various solar cell structures. Silvaco is one of the TCAD (technology computer-aided design) tools, which use 2D/3D finite element analysis to model various semiconductor devices [4]. These TCAD tools can usually model both semiconductor device fabrication and device operation by using various physical models. Although simulations using Silvaco usually takes longer to complete, these simulations use real material parameters and considers both radiative and non-radiative recombination. Therefore, the efficiency predictions from Silvaco are closer to experimental ones. Moreover, solar cell structure designs, including layer thickness and doping, can be optimized by using Silvaco simulations. The knowledge learned from this optimization process is important to the understanding of limiting factors of solar cell performance, such as carrier mobility, photon absorption coefficients, and recombination coefficients. Furthermore, the modeling accuracy often depends on the choice of physical models and associated material parameters.

III Fundamental Properties of Semiconductors

An understanding of the operation of semiconductor solar cells requires familiarity with some basic concepts of solid-state physics. This section is provided to the essential concepts needed to examine the physics of solar cells. This discussion will give us a basic understanding of how solar cells based on semiconductor materials work.

III.1 Categories of Materials

All materials are made up of atoms. These atoms contribute to the electrical properties of a material, including its ability to conduct electrical current. In terms of their electrical properties, materials can be classified into three groups: conductors, semiconductors, and insulators. The conductivity of a semiconductor is generally sensitive to temperature, illumination, magnetic field, and minute amounts of impurity atoms. This sensitivity in conductivity makes the semiconductor one of the most important materials for electronic applications.

III.2 Semiconductor Materials

Semiconductors are a group of materials having conductivities between those of metals and insulators. Semiconductor materials are the basic materials which are used in photovoltaic (PV) devices. A semiconductor material has a conductivity σ (in S/cm) that is used to distinguish conducting materials from insulating materials. This conductivity is particularly sensitive to temperature, light, and impurities in the material. Therefore, the conductivity and therefore also the resistivity, ρ (in Ω cm) can be tuned to the desired values by changing the amount of impurities, called donor and acceptor dopants [5].

Two general classifications of semiconductors are the elemental semiconductor materials, found in group IV of the periodic table, and the compound semiconductor materials, most of which are formed from special combinations of group III and group V elements. The elemental materials, those that are composed of single species of atoms, Examples of elemental materials are germanium (Ge) and silicon (Si), also called Group IV materials because they can be found in column IV of the Periodic Table of Elements, the two-element, or *binary*, compounds such as gallium arsenide or gallium phosphide are formed by combining one group III and one group V element. Gallium arsenide (GaAs), which is a III‑V compound because it is a combination of gallium from column III and arsenic from column V in the Periodic Table of Elements, is one of the more common of the compound semiconductors. Its good optical properties make it useful in optical devices. We can also form a three-element, or *ternary*, compound semiconductor. An example is $Al_xGa_{1-x}As$, in which the subscript x indicates the fraction of the lower atomic number element component. More complex semiconductors can also be formed that provide flexibility when choosing material properties. Compound materials can also be made from a combination of column II and column VI elements, for instance, cadmium telluride (CdTe), which is then called a II‑VI compound made from cadmium and tellurium [5].

Solar cells can be fabricated from a number of semiconductor materials, most commonly silicon (Si) – crystalline, polycrystalline, and amorphous. Solar cells are also fabricated from GaAs, GaInP, $Cu(InGa)Se_2$, and CdTe, to name but a few. Solar cell materials are chosen largely on the basis of how well their absorption characteristics match the solar spectrum and their cost of fabrication. In Table 1.1, a section of the Periodic Table of Elements is shown, with relevance to a large share of the established semiconductors which are used for photovoltaic devices as presented in this work.

Table 1.1**:** Part of the Periodic table of elements related to semiconductors used in photovoltaic devices

Column III	Column IV	Column V
B	C	N
Al	Si	P
Ga	Ge	As
In	Sn	Sb

III.3 Energy Bands in Semiconductors

At zero Kelvin, electrons in a semiconductor are all bound to their atoms in their lowest energy states; they stay in what is called the valence band. The valence shell of an atom represents a band of energy levels and that the valence electrons are confined to that band. When an electron acquires enough additional energy, it can leave the valence shell, become a *free electron,* and exist in what is known as the *conduction band*. This is the amount of energy that a valence electron must have in order to jump from the top of the valence band Ev to the bottom of the conduction band Ec where it is free to move to other empty states under the forces of an electric field or diffusion. Once in the conduction band, the electron is free to move throughout the material and is not tied to any given atom. The discreet amount of energy to move an electron from the valence band to the conduction band must, therefore, be higher than (E_C-E_V) [5]. The difference in energy between the edges of valence band Ev and the conduction band Ec is called an *energy gap* or *bandgap* E_g,

$$E_g = E_C - E_V \tag{1.3}$$

The energy gap (or band gap) Eg is an important material parameter and its structure as a function of the wave vector are key characteristics of the semiconductor material and of fundamental importance to the operation of the solar cell. The bandgap energy depends among other things on the composition of the material and the temperature. For semiconductor materials used in photovoltaic devices, *Eg* is in the range of ~1.1 eV for silicon up to values of ~2.5 eV for III-V compounds [5].

When an electron leaves the valence band, a 'void' remains in the crystal, which is called a hole. This hole is in principle a deficient electron, for which reason it can be considered an electron with a positive charge. The creation of what are called electron-hole pairs in pure semiconductor materials – also called intrinsic semiconductors – happens at temperatures above zero Kelvin. This process is called thermal excitation. The density of electrons and holes in intrinsic semiconductors is mainly determined by thermal excitation and therefore by temperature. The density of electrons and holes is equal and is called the intrinsic carrier concentration n_i (in cm^{-3}).

Besides energy band diagrams, other schemes such as energy-momentum diagrams are used to explain the optical-electrical functioning of semiconductor materials. In principle, an energy-momentum diagram represents the energy of charge carriers – electrons or holes – *E*, in relation to their momentum, *p*, using Equation (1.4) for electrons [5],

$$E = \frac{p^2}{2m_n^*} \tag{1.4}$$

where m_n^* (in g) is the effective mass of an electron and a similar equation for holes where m_n^* is replaced by m_p^* the effective mass of a hole. The effective mass depends on the semiconductor material and therefore also on the crystalline structure.

Equation (1.4) can also be represented by the energy-momentum diagram shown in Figure 1.2. A simplified energy band structure is illustrated in Figure 1.2. The allowed electron energies are plotted against the crystal momentum, $p = \hbar k$, where $\hbar$ is the reduced Planck constant and k is the wave vector. Only the energy bands of immediate interest are shown – energy bands below the valence band are presumed to be fully occupied by electrons and those above the conduction band are presumed to be empty. Electrons (*) fill the states from bottom to top and the states near the top of the valence band are empty (o) due to some electrons being thermally excited into the conduction band. These empty states can conveniently be regarded as positively charged carriers of current called *holes* with a positive effective mass [3].

When the minimum of the conduction band occurs at the same value of the crystal momentum, as the maximum of the valence band, as it does in Figure 1.2, the semiconductor is a direct bandgap semiconductor. When they do not align, the semiconductor is said to be an indirect bandgap semiconductor [3]. This is especially important when the absorption of light by a semiconductor is considered later in this chapter.

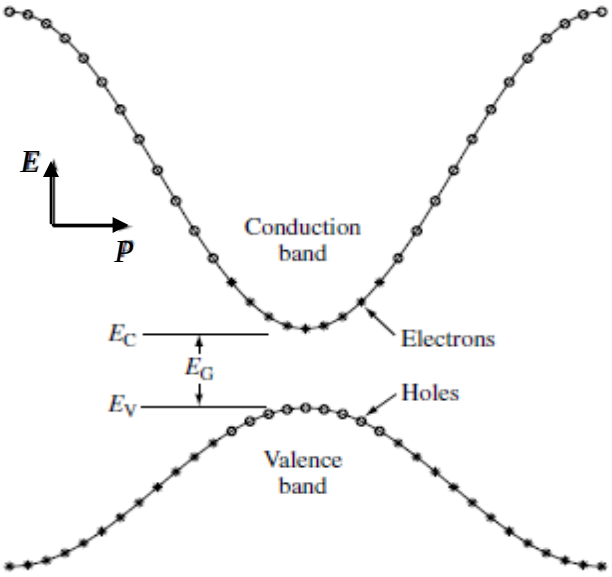

Figure 1.2: A simplified energy band diagram at T >0 K for a direct band gap (E_G) semiconductor [3].

III.4 Conduction-Band and Valence-Band Densities of State

In order to determine the carrier concentration one has to know the function of the density of allowed energy states of electrons and the occupation function of the allowed energy states. The density of energy states function, $g(E)$, describes the number of allowed states per unit volume and energy. The occupation function is the well known Fermi-Dirac distribution function, $f(E)$, which describes the ratio of states filled with an electron to total allowed states at given energy E.

The dynamics of the electron motion in a semiconductor has been approximated by a negatively charged particle with *effective mass* m_n^* in the conduction band and by a positively charged particle with *effective mass* m_p^* in the valence band; it is possible to calculate the density of states in each band.
The density of energy states at an energy E in the conduction band E_C is given by [3],

$$g_C(E) = \frac{m_n^* \sqrt{2m_n^*(E-E_C)}}{\pi^2 \hbar^3}\ cm^{-3}\ eV^{-1} \tag{1.5}$$

The density of energy states at an energy E in the valence band E_V is given by [3],

$$g_V(E) = \frac{m_p^* \sqrt{2m_p^*(E_V-E)}}{\pi^2 \hbar^3}\ cm^{-3}\ eV^{-1} \tag{1.6}$$

III.5 Equilibrium Carrier Concentrations

Any operation of a semiconductor device depends on the concentration of carriers that transport charge inside the semiconductor and hence cause electrical currents. In order to determine and to understand device operation, it is important to know the precise concentration of these charge carriers. In this section, the concentrations of charge carriers inside a semiconductor are derived assuming the semiconductor is under equilibrium. The term equilibrium is used to describe the unperturbed state of a system, to which no external voltage, magnetic field, illumination, mechanical stress, or other perturbing forces are applied. In the equilibrium state, the observable parameters of a semiconductor do not change with time.

When the semiconductor is in thermal equilibrium (i.e. at a constant temperature with no external injection or generation of carriers), the probability of finding an electron at an energy *E* is given by the Fermi distribution function given by [3],

$$f(E) = \frac{1}{1+e^{(E-E_F)/KT}} \tag{1.7}$$

where k is Boltzmann's constant (k = 1.38 x 10^{-23} J/K), *T* is the Kelvin temperature, and E_F is the so-called Fermi energy. kT is the thermal energy, at 300 K it is 0.0258 eV.

The Fermi energy is the electrochemical potential of the electrons in a material and in this way it represents the averaged energy of electrons in the material. As seen in Figure 1.3, the Fermi function is a strong function of temperature. At absolute zero, it is a step function and all the states below E_F are filled with electrons and all those above E_F are completely empty. As the temperature increases, thermal excitation will leave some states below E_F empty, and the corresponding number of states above E_F will be filled with the excited electrons [3].

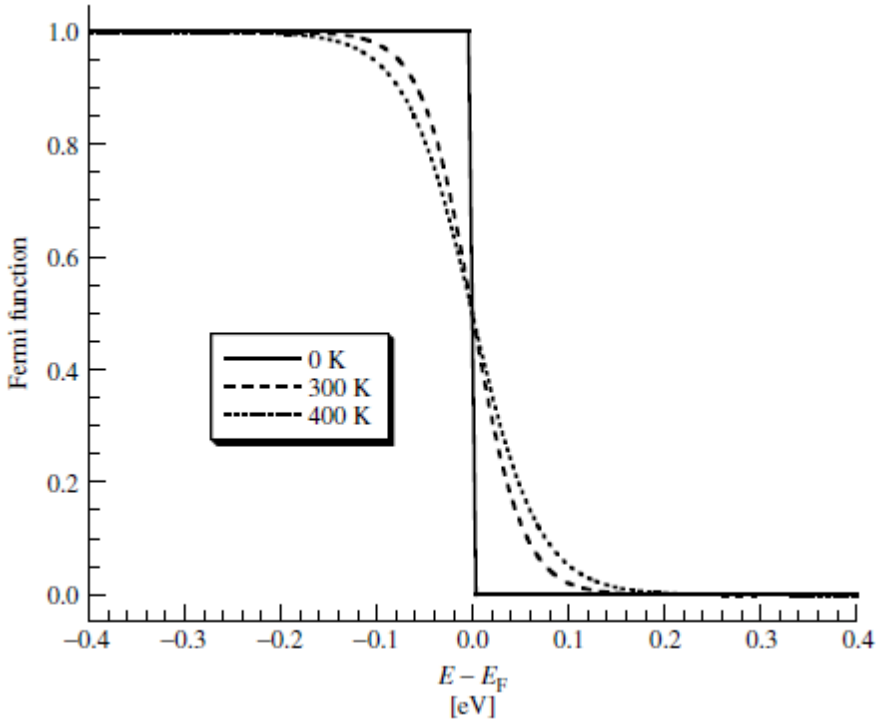

Figure 1.3: The Fermi function at various temperatures [3].

The carriers that contribute to charge transport are electrons in the conduction band and holes in the valence band. The total concentration of electrons in the conduction band and the total concentration of holes in the valence band is obtained by multiplying density of states function with the distribution function and integrating across the whole energy band [3],

$$n = \int_{E_C}^{+\infty} g_C(E)\, f(E) dE \qquad (1.8a)$$

$$p = \int_{-\infty}^{E_V} g_v(E)\, [1 - f(E)] dE \qquad (1.8b)$$

Substituting the density of states and the Fermi-Dirac distribution function into Eq. (1.8) the resulting expressions for n and p are obtained after solving the equations. The thermal-equilibrium electron concentration n_0 in the conduction band can be written as [3],

$$n_0 = N_C \exp\left(\frac{E_F - E_C}{KT}\right) \; for\; E_C - E_F \geq 3KT \qquad (1.9a)$$

The thermal-equilibrium holes concentration p_0 in the valance band can be written as,

$$p_0 = N_V \exp\left(\frac{E_V - E_F}{KT}\right) \; for\; E_F - E_V \geq 3KT \qquad (1.9b)$$

where N_C and N_V are the effective densities of the conduction band states and the valence band states, respectively.

For an intrinsic semiconductor, where no dopants present, the concentration of electrons in the conduction band is equal to the concentration of holes in the valence band. We may denote n_i and p_i as the electron and hole concentrations, respectively, in the intrinsic semiconductor. These parameters are usually referred to as the intrinsic electron concentration and intrinsic hole concentration. However, $n_i = p_i$, so normally we simply use the parameter n_i as the intrinsic carrier concentration, which refers to either the intrinsic electron or hole concentration. The Fermi energy level for the intrinsic semiconductor is called the intrinsic Fermi energy, or $E_F = E_{Fi}$.

If we apply Equations (1.9a) and (1.9b) to the intrinsic semiconductor, the intrinsic carrier concentration given as [3],

$$np = n_i^2 = N_C N_V \exp\left(\frac{E_V - E_C}{KT}\right) \tag{1.10}$$

$$n_i = \sqrt{N_C N_V}\, exp\left(\frac{-E_g}{2KT}\right) \tag{1.11}$$

where E_g is the energy bandgap, k is the Boltzmann constant, N_C and N_V are the effective density of states for conduction and valence bands, respectively are given by [3],

$$N_C = 2\left(\frac{2\pi m_n^* KT}{h^2}\right)^{3/2} \tag{1.12a}$$

$$N_V = 2\left(\frac{2\pi m_p^* KT}{h^2}\right)^{3/2} \tag{1.12b}$$

where m_n^* and m_p^* are electron and hole effective mass, respectively.

The Fermi energy in an intrinsic semiconductor, $E_i = E_F$, is given by [4],

$$E_i = E_F = \frac{E_V + E_C}{2} + \frac{KT}{2}\ln\left(\frac{N_V}{N_C}\right) \tag{1.13}$$

which is typically very close to the middle of the band gap.

III.6 Carrier Concentration in Non-Equilibrium

When a semiconductor is illuminated, additional electrons and holes are generated in the material by the absorption of photons. The photo-generated carriers interact with the semiconductor lattice. The extra energy that the electron-hole pairs receive from the photons with energies larger than the band gap of the semiconductor is released into the lattice in form of heat. After this so-called *thermalization* process, which is very fast, the carrier concentrations achieve a steady-state. In this non-equilibrium state the electron and hole concentrations are different than those in the equilibrium state. In non-equilibrium states, two Fermi distributions are used to describe the electron and hole concentrations. One Fermi distribution with the *quasi-Fermi energy for electrons*, E_{Fn}, describes the occupation of states in the conduction band with electrons. Another Fermi distribution with the *quasi- Fermi energy for holes*, E_{Fp}, describes the occupation of states in the valence band with electrons and therefore determines also the concentration of holes.

The density of electrons and holes under non-equilibrium conditions is described by [4],

$$n = N_C \exp\left(\frac{E_{Fn} - E_C}{KT}\right) \quad (1.14a)$$

$$p = N_V \exp\left(\frac{E_V - E_{Fp}}{KT}\right) \quad (1.14b)$$

where N_C and N_V are the effective density of states of the conduction and valence band, respectively. The effective density of state can be expressed as [4],

$$N_C = 2\left(\frac{2\pi m_n^* KT_L}{h^2}\right)^{3/2} \quad (1.15a)$$

$$N_V = 2\left(\frac{2\pi m_p^* KT_L}{h^2}\right)^{3/2} \quad (1.15b)$$

where m_n^* and m_p^* are electron and hole effective mass, respectively. T_L is the lattice temperature, k is the Boltzmann constant.

The np product can be redefined under non-equilibrium conditions as,

$$np = n_i^2 \exp\left(\frac{E_{Fn} - E_{Fp}}{KT}\right) \quad (1.16)$$

where $np \neq n_i^2$, the difference of E_{Fn} in the n-type region and E_{Fp} in the p-type region correspond to the external voltage V, so that

$$E_{Fn} - E_{Fp} = qV \quad (1.17)$$

III.7 Poisson-Drift-Diffusion Model

The Poisson-drift-diffusion model is based on three first-order differential equations: the carrier continuity equations for electrons and holes and the Poisson's law. Fundamentally, device operation is described in a set of two coupled, partial differential equations: the Poisson equation and the equation of continuity. Continuity and Poisson equations are very important for semiconductor physics devices. These equations are solved iteratively by ATLAS to obtain a modeled solution of device operation.

The first one is the Poisson's equation. In a region where space charge exists (for example, in the junction), the Poisson equation is needed to link the electrostatic potential Φ with the charge density ρ and is given as [4],

$$\nabla(\varepsilon\nabla\Phi) = -q(p - n + N_D^+ - N_A^-) \quad (1.18)$$

where ε is the static dielectric constant of the semiconductor, Φ is the electrostatic potential, q is the absolute value of electron charge, p is the hole density, n is the electron density, N_D^+ is the ionized donor doping concentration, N_A^- is the ionized acceptor doping concentration.

The second one is the continuity equation. The continuity equation describes a basic concept, namely that a change in carrier density over time is due to the difference between the incoming and outgoing flux of carriers plus the generation and minus the recombination. The continuity equation based on the drift-diffusion DD model for electrons and holes given as [4],

$$\frac{\partial n}{\partial t} = G_n - R_n + \frac{1}{q} \nabla . J_n \quad (1.19.a)$$

$$\frac{\partial p}{\partial t} = G_p - R_p + \frac{1}{q} \nabla . J_p \quad (1.19.b)$$

where J_n, G_n, R_n are electron current density, generation rate, and recombination rate, respectively. J_p, G_p, R_p are hole current density, generation rate, and recombination rate, respectively. The continuity equation describes the particle conservation law.

As a result of consideration of particle current, a Net rate of particle flow = Particle flow rate due to current − Particle loss rate due to recombination + Particle gain due to generation.

III.8 Carrier Transport Phenomena

In order to analyze the basic pn junction diode in the later section, we must have some understanding of the mechanisms that govern carrier transport in a semiconductor. Importantly, we must understand carrier transport under the non-equilibrium conditions that prevail in a solar cell, for example, light illumination and voltage bias. In contrast to the equilibrium conditions, under operational conditions a net electrical current flows through a semiconductor device. The electrical currents are generated in a semiconductor due to the transport of charge by electrons and holes. The two basic transport mechanisms in a semiconductor are drift and diffusion. In this section we consider two basic transport mechanisms in a semiconductor crystal: drift, the movement of charge due to electric fields, and diffusion, the flow of charge due to density gradients, the two main mechanisms that give rise to current flow, Then we will tie the current flows together with the recombination and generation mechanisms using the continuity equations.

III.8.1 Drift

Drift is charged-particle motion in response to an electric field. In an electric field, the force acts on the charged particles in a semiconductor, which accelerates the positively charged holes in the direction of the electric field and the negatively charged electrons in the direction opposite to the electric field. The net drift of charge gives rise to a *drift current.* The resulting motion of electrons and holes can be described by average drift velocities v_{dn} and v_{dp} for electrons and holes, respectively. In the case of low electric fields, the average drift velocities are directly proportional to the electric field as expressed by [5],

$$v_{dn} = -\mu_n E \quad (1.20.a)$$

$$v_{dp} = \mu_p E \quad (1.20.b)$$

where μ_n *is the* electron mobility, μ_p *is the* hole mobility and E is the electric field.

The mobility is an important parameter of the semiconductor for carrier transport because it describes how well a particle will move due to an electric field. The unit of mobility is usually expressed in terms of $cm^2V^{-1}s^{-1}$. It is a central parameter that characterizes electron and hole transport due to drift.

Although the electrons move in the opposite direction to the electric field, because the charge of an electron is negative the resulting electron drift current is in the same direction as the electric field [5].
The electron and hole drift-current densities are then given as [5],

$$J_{n,drift} = -qnv_{dn} = qn\mu_n E \tag{1.21a}$$

$$J_{p,drift} = qpv_{dp} = qp\mu_p E \tag{1.21b}$$

Combining Eqs. (1.21a) and (1.21b) leads to the total drift current density J_{drift}(A/cm^2),

$$J_{drift} = q(n\mu_n + p\mu_p)E \tag{1.22}$$

III.8.2 Diffusion

There is a second mechanism, in addition to drift, that can induce a current in a semiconductor. Semiconductor devices fall into two broad categories: majority carrier devices and minority carrier devices. In the majority carrier devices, current flow is dominated by electric field driven current. In minority carrier devices, the current flow is dominated by the diffusion effects. Diffusion is a process whereby particles flow from a region of high concentration toward a region of low concentration. Currents resulting from diffusion are proportional to the gradient in particle concentration. For electrons and holes, they are given by [5],

$$J_{n,diff} = qD_n\nabla n \tag{1.23a}$$

$$J_{p,diff} = -qD_p\nabla p \tag{1.23b}$$

where D_n and D_p are called the *electron and hole diffusion coefficients*, respectively.

Combining Eqs. (1.23a) and (1.23b) leads to the total diffusion current,

$$J_{diff} = q(D_n\nabla n - D_p\nabla p) \tag{1.24}$$

The diffusion coefficients of electrons and holes are linked with the mobilities of the corresponding charge carriers by the Einstein relationship that is given by [5],

$$\frac{D_n}{\mu_n} = \frac{D_p}{\mu_p} = \frac{KT}{q} \tag{1.25}$$

Combining Eqs. (1.21a) and (1.23a) leads to the total electrons current,

$$J_n = J_{n,drift} + J_{n,diff} = qn\mu_n E + qD_n\nabla n \tag{1.26}$$

Combining Eqs. (1.21b) and (1.23b) leads to the total holes current,

$$J_p = J_{p,drift} + J_{p,diff} = qp\mu_p E - qD_p\nabla p \tag{1.27}$$

The total current in a semiconductor is equal to the sum of the drift and the diffusion currents. Combining Eqs. (1.22) and (1.24) leads to the total free carrier current:

$$J = J_n + J_p = q(n\mu_n + p\mu_p)E + q(D_n\nabla n - D_p\nabla p) \quad (1.28)$$

For numerical solar cell simulation a coupled set of differential equations, which are the basic equations of semiconductor device physics, have to be solved by an iterative procedure. This set consists of the Poisson Equation, which describes the relationship between the electrostatic potential Φ and the charge distribution, the continuity equations for electrons and holes, which conserve the quantity charge carrier, and the current density equations in the drift-diffusion approach.

III.9 Generation and Recombination of Electron-Hole Pairs Processes

The most important function of a solar cell is the generation of photocurrent and photovoltage. In order to do this, the solar cell must first absorb light from the sun and generate charge carriers. In this section, we discuss carrier generation and recombination, which we can define as follows: *generation* is the process whereby electrons and holes are created. However, *recombination* is the opposite of a generation corresponds to the mechanisms leading to the loss of electron-hole pairs, with the excess energy is emitted as photons or phonons as well the process of absorption of light by a semiconductor.

In thermal equilibrium the relationship $np = n_i^2$ is valid. Assume that a semiconductor is illuminated by a light pulse, which leads to excitations of electrons from the valence band to the conduction band and consequently to the creation of holes in the valence band. This illumination will disturb the semiconductor from the state of thermal equilibrium. In the valence band, an excess concentration of holes $p>p_0$ is present, where p_0 denotes the equilibrium concentration. Similarly, in the conduction band the electron concentration is larger than the equilibrium concentration, $n>n_0$, which means that excess carriers are present, so that, $np > n_i^2$, we have a *nonequilibrium situation*. After the pulse stops, the excess electrons will recombine with holes, until the equilibrium state is reached again.

Depending on the properties of the semiconductor different types of recombination can and will occur. The recombination rate strongly determines the performance of the solar cells. On the one hand, it will reduce the current that can be collected and hence utilized from the solar cell. However, the photo-generation rate often is several magnitudes higher than the recombination rate, such that the effect of recombination on the solar cell current is negligible. Recombination phenomena can be classified as direct and indirect processes. Direct recombination, also called *band-to-band recombination*, usually dominates in direct-bandgap semiconductors, such as gallium arsenide GaAs, whereas indirect recombination via bandgap recombination centers dominates in indirect-bandgap semiconductors, such as silicon Si. The current produced by solar cells is generated by optical transitions across the band gap. Before we can actually start with the treatment of the different generation and recombination mechanisms, we mention that we have to distinguish between direct and indirect semiconductors. Figure 1.4 shows the energy-momentum space of the electrons, which also is called the electronic dispersion diagram of (a) a direct bandgap semiconductor and (b) an indirect bandgap semiconductor [3].

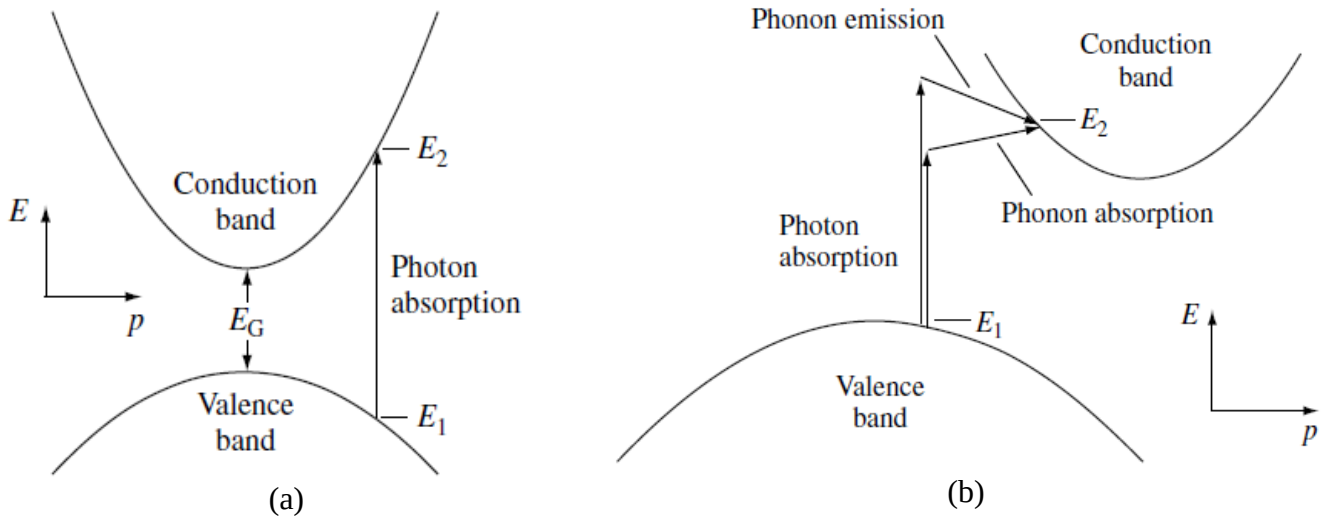

Figure 1.4: (a) Photon absorption in a direct band gap semiconductor; (b) Photon absorption in an indirect band gap semiconductor [3].

On the vertical axis, the energy state (E) in the electronic bands is plotted. On the horizontal axis, the momentum (P) of the charge carrier is shown. This momentum is also called the crystal momentum; it is also related to the wave vector k of the electron. It is important to realize that the position of the valence and conduction band may differ in different directions of the lattice coordination. For a direct bandgap material the highest point of the valence band is vertically aligned with the lowest point of the conduction band, as shown in Figure 1.4 (a). This means that exciting an electron from the valence to the conduction band requires only the energy provided by a photon without any additional momentum transfer. In contrast, for an indirect bandgap material, the highest point of the valence band is not aligned with the lowest point of the conduction band, as shown in Figure 1.4 (b). Therefore, exciting an electron from the valence to conduction band requires energy provided by a photon and momentum, this transition requires the assistance of a phonon (quantum of lattice vibration). Therefore, the excitation of an electron induced by photon absorption is more likely to happen for direct band gap materials than for indirect bandgap materials and hence the absorption coefficient for direct band gap materials is significantly higher than for indirect band gap materials. The same principle makes the reverse process of radiative recombination more likely to happen in a direct bandgap material. In an indirect band gap material, additional momentum is required to make the electron and hole recombine [3].

III.9.1 Generation of Electron Hole Pairs in Semiconductors

Generation is a process that increases the density of either free electrons, holes or both. This process requires some minimum generation energy, which in most cases except for impurities, is equal to the bandgap energy *Eg*. The four basic processes that lead to free carrier generation include impact ionization, thermal generation, photogeneration (also called optical generation), and impurity-mediated generation. The processes are explained briefly below [5]:

1. *Impact ionization*: Carriers (electrons or holes) with sufficient kinetic energy can promote a valence electron into the conduction band, basically knocking a bound electron away from the host atom. This process requires significant kinetic energy, for example, under a high electric field, and is typically not encountered in a standard solar cell in forward bias.

2. *Thermal generation*: Occurs due to high energy lattice vibrations, called phonons, interacting with the host atoms. At higher temperatures or for low bandgap materials, thermal vibration can be great enough to free an electron from the host atom and create free carriers.

3. *Photogeneration*: The most important process for solar cells is a photogeneration (generation from photons). In this case, the input photon energy must be greater than the bandgap energy in order to create an Electron-Hole Pair (EHP).
4. *Impurity-mediated generation*: Localized trap states in the bandgap can generate single free carriers by interaction with photons or phonons.

As well, due to the principle of microscopic reversibility, each of these generation processes discussed above must have an equivalent recombination process. In equilibrium, there is a continuous process of generation and recombination of carriers, while under non-equilibrium conditions; one process may dominate in order to attempt to restore equilibrium conditions. It should be noted that thermal generation occurs in all semiconductors and will depend strongly on the bandgap and temperature. At any nonzero temperature, electron-hole pairs are constantly being generated *and* lost (by recombination).

III.9.1.1 Absorption and Photogeneration

The most important optoelectronic interaction in semiconductors as far as devices are concerned is the band-to-band transition. Generation and recombination processes that happen from bandgap to bandgap are also called direct generation and recombination. They are much more likely to happen in direct bandgap materials, as there no change in momentum is required for an electron that is excited into the conduction band. These processes most usually are radiative, which means that a photon is absorbed when an electron-hole pair is created, and a photon is emitted if electron-hole pairs recombine directly.

When light penetrates into a material it will be (partially) absorbed as it propagates through the material. If the photon energy is higher than the bandgap energy of the semiconductor, it is sufficient to break bonds and to excite a valence electron into the conduction band and leaving a hole behind in the valance band. The absorption profile in the material depends on the absorption coefficient of the material, which is wavelength dependent.

The photogeneration is the most important optical process in solar cells. The rate of photogenerated carriers G (EHP/cm^{3}s) must be known when working with solar cells under illumination. In order to calculate G, first we need to understand how the intensity or flux of photons varies with depth and energy within a bulk semiconductor material.

III.9.1.1.1 Light Absorption

The creation of electron-hole pairs via the absorption of sunlight is fundamental to the operation of solar cells. Absorption results in the creation of an electron-hole pair since a free electron is excited to the conduction band leaving a free hole in the valence band. Therefore we will use this section to discuss how absorption of light in a medium can be described mathematically. Since the refractive index is given by,

$$\tilde{n} = n + ik \tag{1.29}$$

where n denotes the real part and the k is the imaginary part of the refractive index.

As light propagates through a material, a loss in the optical intensity will usually be incurred. The absorption profile in the material depends on the absorption coefficient of the material, which is wavelength dependent. The most frequent approach to calculate the absorption profile of photons in semiconductor devices is by using Lambert-Beer's law that in Eq. (1.30), the attenuation of the intensity of the electromagnetic field is given by,

$$I(x) = I_0 \exp(-\alpha x) \tag{1.30}$$

where x is the depth, I_0 is the optical intensity, α is the absorption coefficient is related to the other properties via,

$$\alpha = \frac{4\pi k}{\lambda} \tag{1.31}$$

where λ is the wavelength (in m), k is the extinction coefficient; it is the imaginary part of the complex index of refraction.

The energy of a photon is $E = hv$ where h is Plank's constant and v is the frequency. We can also relate the wavelength and energy by

$$\lambda = \frac{c}{v} = \frac{hc}{hv} = \frac{hc}{E} = \frac{1.24}{E}\mu m \tag{1.32}$$

where E is the photon energy in eV and c is the speed of light.

Figure 1.5 shows α(E) for various semiconductors based. As we expect, both GaAs and $InGaP_2$ have very steep absorption edges and maintain a relatively high value beyond the bandgap. However, indirect semiconductors such as Si show a slower, more graduate increase in absorption beyond the bandgap, eventually reaching higher values of absorption coefficient due to direct transitions [5].

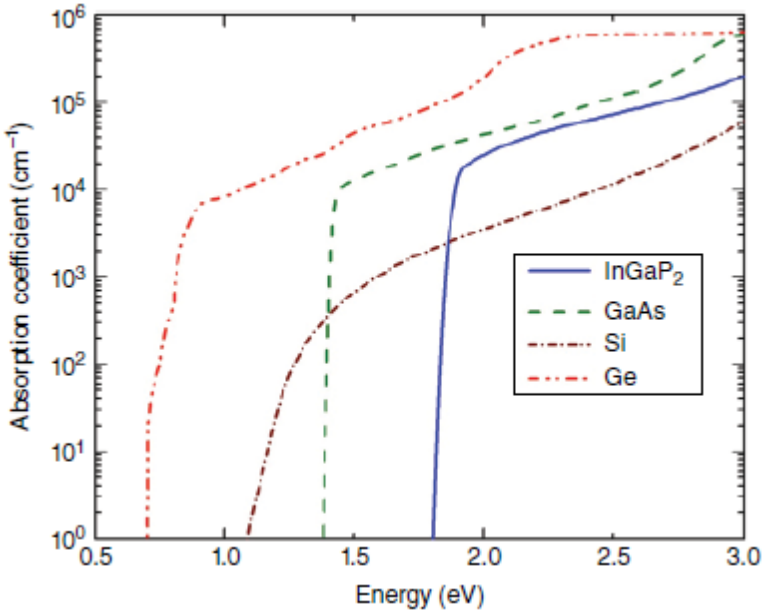

Figure 1.5: Plot of the absorption coefficient for a number of direct (GaAs, $InGaP_2$) and indirect (Ge, Si) semiconductors [5]

III.9.1.1.2 Photogeneration rate

When photons with sufficient energy impinge onto a semiconductor, those photons may excite valence electrons up to the conduction band thus photogenerating an electron-hole pair. This is the basis on which a solar cell operates upon. The photogeneration rate G is modeled in ATLAS as [4],

$$G = \eta_0 \frac{p\lambda}{hc} \alpha e^{-\alpha y} \qquad (1.33)$$

where η_0 is the internal quantum efficiency of an absorbed photon, λ is the optical wavelength, α is the absorption coefficient, y is the relative distance for the ray in question, and P is a coefficient that tracks the cumulative effects of transmission, reflection, and loss throughout the device, α the absorption coefficient, sometimes called the attenuation coefficient.

The model for photogeneration is solved by ATLAS at every node located in a semiconductor material; it is automatically invoked whenever a light source is included. The value determined at each node for (1.33) then becomes an input for the carrier continuity equations.

III.9.2 Recombination Process

When a semiconductor is taken out of thermal equilibrium, for example by illumination, the concentrations of electrons (*n*) and holes (*p*) tend to relax back toward their equilibrium values through a process called *recombination* in which an electron falls from the conduction band to the valence band, thereby eliminating a valence-band hole [3]. Recombination processes can be classified in a number of ways. Most texts distinguish between bulk and surface recombination, and between band-to-band recombination as opposed to transitions with the participation of defect levels within the band gap.

Recombination processes can also be classified according to the medium that absorbs the energy of the recombining electron-hole pair: radiative recombination (associated with photon emission) or the two principal nonradiative mechanisms by Auger and multi-phonon transitions, where the recombination energy is absorbed by a free charge carrier or by lattice vibrations, respectively. An opposite process to Auger recombination (in which an electron-hole pair is generated rather than consumed) is called impact ionization [6].

In a solar cell, recombination acts to restore the non-equilibrium light generated EHP population to its thermal equilibrium value. There are four different paths to recombination mechanisms for carriers important to the operation of solar cells: recombination through traps (defects) in the forbidden gap, radiative (band-to-band) recombination, Auger recombination, and Surface recombination-that will be discussed in this section [3]. The three types of recombination in a bulk semiconductor summarized schematically in Figure 1.6 which are [5]:

- Radiative recombination, resulting in the emission of a photon. This is often called band-to- band recombination or direct recombination.
- Auger recombination resulting when kinetic energy is imparted to a third carrier. This is also a non-radiative process.
- Non-radiative recombination resulting in phonon emission. This is often called trap-assisted recombination or Schockley-Read-Hall (SRH).

Each of these processes is illustrated in Figure 1.6 and will be discussed in depth below. From the above types of recombination, radiative and Auger are a basic property of the semiconductor materials being used, while non-radiative depends on the quality of the material through the density of non-radiative traps.

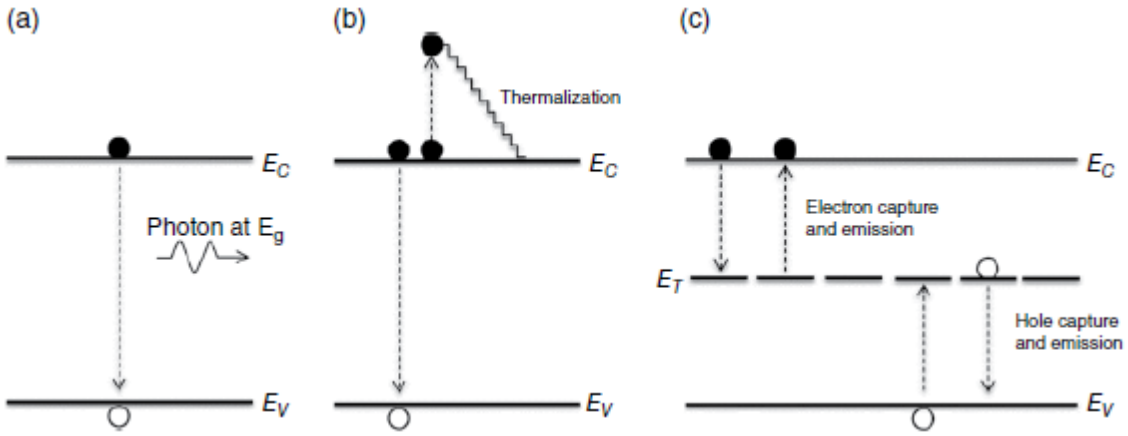

Figure 1.6: The three basic types of recombination processes: (a) radiative band-to-band; (b) nonradiative Auger; and (c) non-radiative recombination centers (traps) [5]

III.9.2.1 Radiative Recombination

When a photon is emitted, the process is called radiative recombination; otherwise, it is called non-radiative recombination. Radiative recombination is important recombination mechanism for direct bandgap solar cells. In this process, as shown in Figure 1.6 (a), an electron in the conduction band directly recombines with a hole in the valence band and releases a photon with energy equal to the bandgap and is strongest in direct-gap semiconductors. A simple expression for band-to-band radiative recombination for a non-degenerate semiconductor under non-equilibrium conditions is given as [5],

$$R_{Radiative} = B(np - n_i^2) \tag{1.34}$$

where B (cm^3/s) is the radiative recombination coefficient.

The first term in the expression corresponds to the non-equilibrium electron-hole population (from illumination or external bias), while the second term contains the intrinsic thermal carrier population ($n_i^2 = n_0 p_0$). The above rate describes the change in radiative recombination from its equilibrium value, which will be useful when considering solar cell operation through the continuity equations discussed in the previous section. The radiative recombination coefficient, B, depends on a material's bandgap as well as the strength of the absorption coefficient [5]. This process is invoked in ATLAS in the MODELS statement by calling OPTR and by defining COPT in the MATERIALS statement.

III.9.2.2 Auger Recombination

Auger recombination is a non-radiative process where the energy of the photogenerated carrier is dissipated not by photon emission, but rather by increasing the kinetic energy of another free carrier. For example, the collision of two electrons can result in recombination of one of the electrons with a hole and the resulting energy is given up to increase the kinetic energy of the second electron. This kinetic energy is then very quickly dissipated through the process of thermalization, where the electron emits multiple phonons and returns to energy near the band edge. This is shown graphically in Figure 1.6 (b). For Auger recombination, accounting for the background thermal Auger processes, the net change in recombination rate under non-equilibrium conditions is [5],

$$R_{Auger} = B_{Auger,p}(n^2 p - n_0^2 p_0) \tag{1.35}$$

for two electrons, where $B_{Auger,p}$ (cm^6/s) is the hole Auger recombination coefficient, and

$$R_{Auger} = B_{Auger,n}(p^2 n - p_0^2 n_0) \tag{1.36}$$

for two holes, where $B_{Auger,n}$ (cm^6/s) is the electron Auger recombination coefficient.
The expression for the Auger recombination rate R_{Auger} is modeled in ATLAS as [4],

$$R_{Auger} = AUGN(pn^2 - nn_i^2) + AUGP(np^2 - pn_i^2) \tag{1.37}$$

where and are the electron and hole Auger recombination coefficients, respectively.

To take into account the temperature dependence of AUGN AUGP Auger recombination coefficients, the Klaassen's model is used and given as [4],

$$AUGN(T_L) = AUGN_{300}\left(\frac{T_L}{300}\right)^{1.18} \quad (1.38)$$

$$AUGP(T_L) = AUGP_{300}\left(\frac{T_L}{300}\right)^{0.72} \quad (1.39)$$

where $AUGN_{300}$ and $AUGP_{300}$ are the electron and hole Auger recombination coefficients at 300 K, respectively. T_L is the lattice temperature.

III.9.2.3 Non-Radiative (Shockley-Read-Hall) Recombination

In the Shockley-Read-Hall (SRH) recombination process, which is illustrated in Figure 1.6 (c), the recombination of electrons and holes does not occur directly from bandgap to bandgap. It is facilitated by an impurity atom or lattice defects and usually dominates the recombination is solar cells. Traps located near the middle of the bandgap are sometimes called recombination centers; these recombination centers introduce allowed energy levels (E_T) within the forbidden gap, so-called trap states. For example, an empty acceptor-like recombination center can capture an electron followed by a hole capture from the valance band. As shown in Figure 1.6 (c), we have illustrated a trap at energy E_t(eV) with density N_t (cm^3). The traps in this example are acceptor ‑ like and thus are neutral when empty and negative when full. The process is typically non-radiative and the excess energy is dissipated into the lattice in form of heat. The net rate of the Shockley_Read_Hall recombination is given by [5],

$$R_{SRH} = \frac{np - n_i^2}{\tau_{p0}\left[n + n_i exp\left(\frac{E_t - E_i}{KT}\right)\right] + \tau_{n0}\left[p + n_i exp\left(\frac{E_i - E_t}{KT}\right)\right]} \quad (1.40)$$

where τ_{p0} and τ_{n0} are hole and electron lifetimes, which can be defined by the user. E_i is the intrinsic Fermi level. E_t is the defect energy level and is usually set to E_i corresponding to the most efficient recombination center.

This form of the Shockley-Read-Hall model is utilized by ATLAS by calling SRH in the MODELS statement. The carrier lifetimes may be regarded as empirical parameters and are set in the MATERIALS statement by the TAUN0 and TAUP0 parameters for electrons and holes, respectively.

III.9.2.4 Surface Recombination

In addition to recombination within the bulk of the semiconductor, electrons or holes may recombine at interfaces. The rate of surface recombination may be even greater than within the bulk. The standard method for modeling the effects of surface recombination is then given by an expression very similar to R_{SRH} [4],

$$R_{surf} = \frac{np - n_i^2}{\tau_p^{eff}\left[n + n_i exp\left(\frac{E_t - E_i}{KT_L}\right)\right] + \tau_n^{eff}\left[p + n_i exp\left(\frac{E_i - E_t}{KT_L}\right)\right]} \quad (1.41)$$

For the effective lifetimes which are modeled by ATLAS for electrons and holes, respectively, as [4],

$$\frac{1}{\tau_n^{eff}} = \frac{1}{\tau_n} + \frac{d_m}{A_m} S_n \tag{1.42a}$$

$$\frac{1}{\tau_p^{eff}} = \frac{1}{\tau_p} + \frac{d_m}{A_m} S_p \tag{1.42b}$$

where τ_n^{eff} and τ_p^{eff} are the bulk Shockley-Read-Hall lifetimes and d_m and A_m are the length and area, respectively, of the surface corresponding to node m, S_n and S_p are the surface recombination velocities for electrons and holes, respectively [4],

$$S_n = \sigma_n \nu_{th} N_{st}^{'} \tag{1.43}$$

$$S_p = \sigma_p \nu_{th} N_{st}^{'} \tag{1.44}$$

where $N_{st}^{'}$ is surface state density, σ_n an σ_p are the capture cross-sections for electrons and holes, respectively and ν_{th} is the thermal velocity.

To achieve optimal operation, surface recombination is reduced by a passivating or window layer that prevents minority carriers from reaching the surface [6]. Surface passivation using high- quality hetero-epitaxial growth is able to significantly reduce the surface recombination velocity [5].

III.10 Luminous Module

The operation of a solar cell is heavily dependent on the light that impinges onto it as well as the subsequent propagation of electromagnetic radiation throughout the device. How much light is able to transmit through each layer of the device and the propensity for that light to be absorbed and induce carrier photogeneration all play important roles in a solar cell's ultimate performance.

The Luminous module supplements the ATLAS framework by including ray tracing and photoabsorption algorithms [4]. After inputting any variant of a monochromatic or spectral light source, Luminous determines the intensity of the optical field throughout the device and determines photogeneration rates for use in the carrier continuity equations. Luminous is invoked by specifying a light source in the BEAM statement. This light source is monochromatic; its wavelength is determined by setting a value to the LAMBDA parameter of the SOLVE statement. The light source can be made spectral in the BEAM statement by including a data file specified by the POWER.FILE parameter. In this work, the AM1.5 solar spectrum utilized to obtain device I-V characteristics. A spectrally varying monochromatic source is used to obtain a short-circuit current and spectral response.

III.11 Band-to-Band Tunneling

The tunnel diodes that allow for the flow of carriers between sub-cell s in multi-junction solar cells operate via band-to-band tunneling across a degenerately doped p++/n++ junction. In the tunnel junctions, the presence of sufficiently large electric fields or sufficiently thin potential barriers, band to band tunneling may occur. This effect is modeled in ATLAS as an additive generation term to the carrier continuity equations as [4],

$$G = AE^{\gamma} e^{-B/E} \quad (1.45)$$

where E is the magnitude of the local electric field and A, B, and γ are adjustable fitting parameters. For direct-gap semiconductors, A, B, and γ are usually given as 9.6615×10^{18} V^{-1}-s^{-1}-cm^{-2}, 30 MV/cm, and 2, respectively. For indirect-gap semiconductors, these parameters are usually given as 4×10^{14} V^{-1}-s^{-1}-cm^{-2}, 19 MV/cm, and 2.5, respectively [4].

It should be noted that in ATLAS this model is invoked in the MODELS statement by specifying BBT.STD for direct-gap transitions and BBT.KL for indirect-gap transitions.

III.12 Material Parameters

To accurately simulate a semiconductor device, the correct fundamental material parameters must be provided for use in the models previously discussed. ATLAS contains a vast library of the most recently accepted values of many of these parameters.

III.13 Numerical Method

The above equations are sometimes strongly coupled and a numerical scheme is needed to solve them self consistently. This includes: i) meshing, ii) discretization, and iii) iterative scheme. Silvaco produces numerical solutions to the above equations by firstly defining a mesh of points within the device structure. Then the equations are discretized and the values of unknowns on the meshing points are calculated iteratively. In the limit of small separations between meshing points, the calculation results should approximately recover the original continuous situation. The specification of meshes involves a trade-off between calculation accuracy and speed. In practice, more meshing points are usually attributed to areas where physical quantities change rapidly and less points to areas where physical quantities change slowly to achieve both faster convergence and better accuracy [4].

After meshing and discretization are defined in the device, iteration techniques are usually used to solve the equations since they are usually coupled together. Among all the iteration approaches, Gummel, Newton and Block methods are adopted in Silvaco [4]. The default in Silvaco is Newton's method, which is a coupled procedure that solves the equations simultaneously. One round of Newton iteration typically involves one matrix inversion and takes longer to complete. But usually, the convergence is faster if the initial guess is close to the final solution.

III.14 p-n junction

p-n junctions are of great importance both in modern electronic applications and in understanding other semiconductor devices. The p-n junction theory serves as the foundation of the physics of semiconductor devices. The pn junction is the heart of many solar cells (e.g. Si, GaAs and other inorganic devices).

Almost all solar cells contain junctions between (different) materials of different doping. Since these junctions are crucial to the operation of the solar cell, we will discuss their physics in this section. A p-n junction fabricated in the same semiconductor material such as c-Si is an example of a p-n *homojunction*. There are also other types of junctions: A p-n junction that is formed by two chemically

different semiconductors is called a p-n *heterojunction*. In a *p-i-n junctions*, the region of the internal electric field is extended by inserting an intrinsic, i, layer between the p-type and the n-type layers. The i-layer behaves like a capacitor and it stretches the electric field formed by the p-n junction across itself. Another type of the junction is a junction between a metal and a semiconductor, a so-called *MS junction*. The Schottky barrier formed at the metal-semiconductor interface is a typical example of the MS junction.

III.14.1 Formation of a Space-Charge Region in the *P-N* Junction

Majority carriers in p-type semiconductors are holes and electrons are the minority carriers Inversely, in n-type semiconductors electrons are referred to as the majority carriers and holes are referred to as minority carriers, when a p-type and an n-type semiconductor are brought together, a very large difference in electron concentration between n- and p-type regions causes a diffusion current of electrons from the n-type material across the junction into the p-type material will likely recombine with a hole, creating negative ions. The term *junction* denotes the interface between the n- and p-type regions. Similarly, the difference in hole concentration causes a diffusion current of holes from the p- to the n-type material and recombine with electrons there to produce positive ions, when almost all electrons and holes recombine around the junction creating a negative zone on the p-side and a positive zone on the n-side. Due to this diffusion process, the region close to the junction becomes almost completely depleted of mobile charge carriers. The gradual depletion of the charge carriers gives rise to a space charge created by the charge of the ionized donor and acceptor atoms that is not compensated by the mobile charges any more. This region of the space charge is called the *space-charge region* or *depleted region* where the mobile carrier densities are zero and is schematically illustrated in Figure 1.7. Regions outside the depletion region, in which the charge neutrality is conserved, are denoted as the quasi-neutral regions [5].

The space charge around the junction results in the formation of an internal electric field which forces the charge carriers to move in the opposite direction than the concentration gradient. The diffusion currents continue to flow until the forces acting on the charge carriers, namely the concentration gradient and the internal electrical field, compensate each other. The driving force for the charge transport does not exist anymore and no net current flows through the p-n junction.

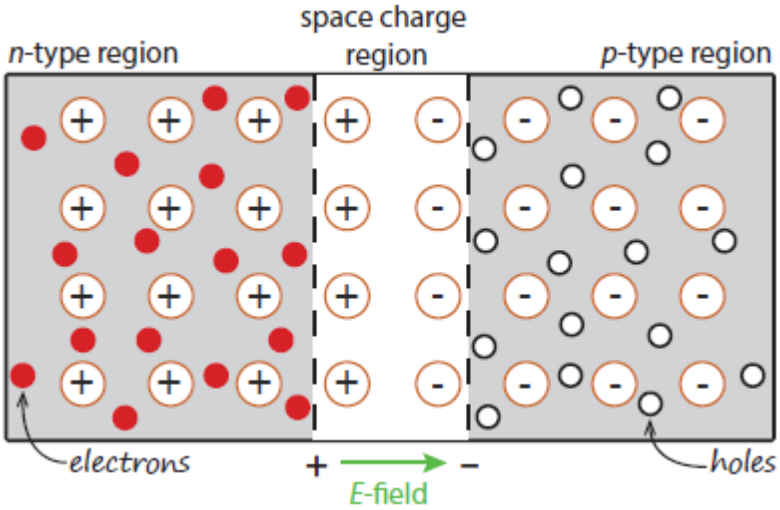

Figure 1.7: Formation of a space-charge region of pn junction [7].

The two aforementioned zones create a potential barrier that counteracts the diffusion of the electrons from the n-side to the p-side. This potential barrier, the so called *built-in voltage* qV_{bi}, is obtained using the band model and the requirement that the Fermi levels line up in thermal equilibrium. This principle is illustrated in Figure 1.8.

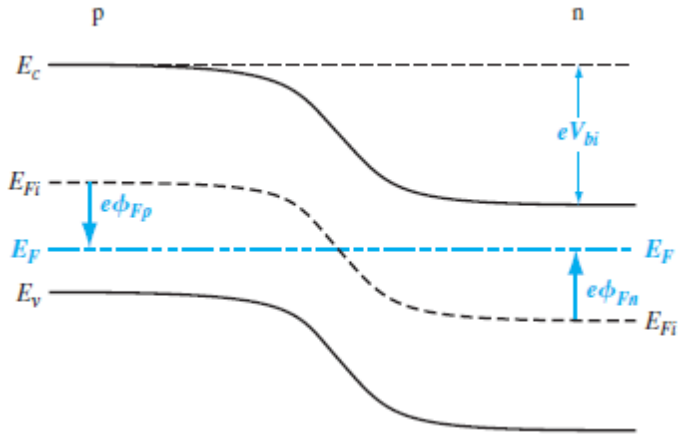

Figure 1.8: Energy-band diagram of a p-n junction in thermal equilibrium [5].

We find that p–n junctions are often used as diodes, namely, as circuit elements that allow current flow only in one direction and not in the reverse. This property can be explained by the terms forward and reverse applied polarization, where the term polarization refers to the voltage applied to the p–n junction.

IV Layers Structure of Single Junction Solar Cells

To derive the equations for the photocurrent and the recombination currents of a solar cell it is necessary to know its semiconductor layer structure. In this case, we are interested in the typical layer structure of a single junction solar cell made from III-V semiconductors, III-V compound semiconductors have been the materials of choice to implement high-efficiency MJSCs. Practical solar cell structures contain additional features that serve the purpose of reducing losses that are inherent in real devices. Figure 1.9 is the basic structure of a conventional n-on-p single junction III-V solar-cell, the typical layer structure consists of four layers, namely, 1) window; 2) emitter; 3) base; and 4) BSF (Back Surface Field). In essence, we have a core p-n junction formed by the emitter and base whose top side is passivated by the window and its rear side by the BSF.

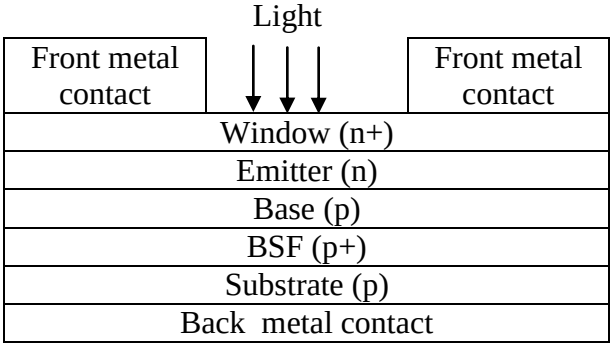

Figure 1.9: The basic structure of a conventional single-junction III-V solar-cell

IV.1 Metal Contacts

The metal contacts are formed at the front and back sides of the device, A metal grid or also called *finger* form is usually used at the front contact, the front metal contact is required to be an ohmic contact to minimize shadowing and prevent recombination and in addition, it must cover the minimum device area possible in order to allow incident light passing through and be absorbed by the solar cell. Theoretically, increasing the density of the metal grids will enhance the collection efficiency of photocurrent and decreasing the series resistance, but the too large density of metal grids will increase the shadow loss and decrease the conversion efficiency, thus the pattern design of top contact is an important issue of solar-cells. The bottom contact would cover the entire bottom surface of the cell to prevent recombination and, the gold back platting act as a reflective surface to force the light back into the solar cell.

IV.2 Window layer

The front layer is called the *window* layer. The front surface, due to the high number of trap states present in the band gap, is a significant source of recombination losses for minority carriers. A practical way of reducing the front surface recombination is with the addition of a high band gap material on the front surface. The high band gap material reflects the minority carriers back. The n^+ window layer is designed to have a large valence band-offset to reflect the holes. The window is heterostructure, which is designed to reduce the recombination at the interfaces by passivation. The conditions to design an effective window layer for an n-on-p cell the materials should have [8]: 1) Lattice constant close to the material used for the sub-cell layer, 2) Bandgap Eg much higher than that of emitter, 4) High electron concentration ($n \geq 10^{18}/cm^3$) and 5) Material quality good to produce low interface-recombination velocity. In addition, the window layer should be largely transparent to the light that would be absorbed by the underlying p-n junction.

IV.3 Emitter and Base layers

The emitter and base layers are the simple p-n junctions as discussed earlier. The layer that is illuminated first is the emitter layer and is usually more heavily doped and thinner than the base layer. Most of the light absorption in a solar cell happens in the thicker and lightly doped base layer. Lower doping ensures higher minority carrier lifetime and higher diffusion coefficients, which in turn improves the carrier diffusion length. Furthermore, lower doping in the base increases the depletion region in the base, which can aid in carrier collection due to the electric field. However, too low doping may increase the dark current, which may significantly degrade the device performance [8].

IV.4 Back Surface Field (BSF) layer

Minority carriers will be lost in a similar fashion at the rear of the n-type region. The substrate, typically around 300μm, is far longer than the diffusion length of the minority carriers. Thus any minority carriers entering the substrate will unquestionably be lost by recombination. This can be avoided by inserting a heavily doped region n-type region, which will create a small electric field in the base region. This field will reflect the minority carriers, P^+ BSF layer is designed to have a large conduction band-offset to reflect the electrons back to the depleted region, thereby increasing the short circuit voltage of the solar cell. Another way of achieving this is by inserting a layer of larger band gap semiconductor similar to the window layer called the *back surface field* or BSF layer. The requirements of a good back-surface field layer are similar to the window layers. They should have the following characteristics [8]: 1) Lattice

constant close to the next sub-cell layer material, 2) Bandgap Eg higher than that of the next sub-cell layer, 3) Relatively high hole concentration (of the order of p = 10^{18}/cm^3), 4) High transparency to photons.

IV .5 Tunnel-junction Interconnects

Tunnel junctions act like diodes in reverse polarity to the original configuration in the stack of sub-cell s and are used to make better optical, electrical and mechanical matching between the sub-cell layers. The tunnel-junction interconnects between sub-cell layers is to provide a low resistance connection between the *p*-type back surface field (BSF) layer of a sub-cell and the *n*-type window layer of the sub-cell beneath it. In absence of tunnel-junctions, this *p*-*n* junction has a polarity of forward turn-on voltage that is opposite to that of the top or bottom sub-cell s. If tunnel junction is not present in the design, the *p*-*n* junction could produce a photo-voltage that could roughly negate the photo-voltage generate by the top sub-cell in case of illumination. Tunnel-junction is made up of a *p*++*n*++ junction where *p*++ and *n*++ represents degenerately doped material. The space-charge region for a *p*++*n*++ junction should be very narrow ~ 10 nm. In case of small forward bias and any reverse bias, the normal thermal characteristic of a *p*++*n*++ junction is shorted by tunneling through the narrow space-charge region and the tunnel-junction behave like a resistor [9].

V The Working Principle of a Solar Cell

The working principle of solar cells is based on the photovoltaic effect, i.e. the generation of a potential difference at the junction of two different semiconductor materials in response to electromagnetic radiation. In a single-junction solar cell, incident photons with energies higher than the band-gap energy of the cell typically get absorbed, while the photons with energies lower than the band-gap typically pass through the cell unabsorbed. When a photon is absorbed, it excites an electron from the valence band to the conduction band, creating an electron-hole pair. These generated carriers diffuse through the quasi-neutral region until they reach the p-n junction where the drift mechanism begins to dominate the carrier transport due to the built-in electric field and sweeps away the carriers across the depletion region to become majority carriers.

Electrons generated in the p-side travel towards the n-side and holes generated in the n-side travel towards the p-side. This redistribution of carriers sets up a potential difference, Voc which is created due to the splitting of the thermal equilibrium Ferm-level (E_F) into minority electron quasi-Fermi level E_{Fn}, and minority hole quasi-Fermi level E_{Fp}. This difference gives rise to the open-circuit voltage, Voc ≈ (E_{Fn}-E_{Fp})/q. This separation in the quasi-Fermi level is represented in the band-diagram shown in Figure 1.10. The electrons generated move towards the top cathode and the holes moves towards the bottom anode.

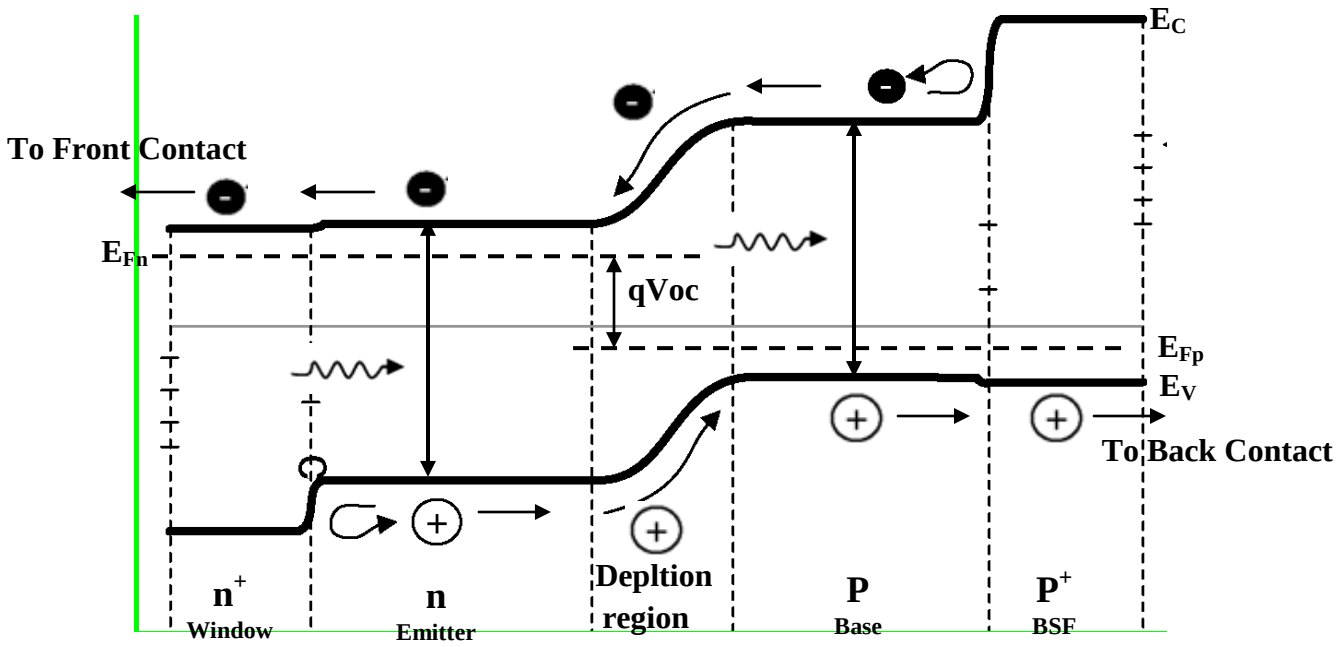

Figure 1.10: Schematic of the mechanism inside the band diagram of an illuminated solar cell [8]

The band diagram of the structure shown in Figure 1.10 gives a more precise description of the mechanism inside a solar-cell and to helps clarify understand how the window and BSF layers work:

Generally, the incident photons will excite electron-hole pairs in three different regions, the p-type base region, the depletion (space-charge) region, and the n-type emitter region. We will discuss the behaviors of the electron-hole pairs that generated in these three regions separately.

Firstly, in the p-type base region, when electron-hole pairs have been generated, the majority carriers, holes, will diffuse toward the back contact and then been collected. While the minority carriers, electrons, will diffuse toward the depletion region due to the concentration gradient produced by the photo-generated excess carriers. Once the electrons arrive at the depletion region, they will be swept to the n-type emitter region by the internal electric-field and go on to diffuse toward the front contact then been collected. But as can be seen in Figure 1.10, the minority carriers, electrons, will also have the probability to diffuse toward the back contact and been recombined. Therefore, we usually employ a BSF layer to reflect the minority carriers and make them back to the correct diffusion direction because the interface between the normally doped p-region and the highly doped p+-region BSF acts like an n-p junction. Here, this junction acts as a large barrier (i.e. discontinuity) that prevents minority electrons in the p-region from diffusing to the back contact, so that reflects minority carriers (electrons) towards the junction. On the other hand, in the majority carrier (holes) band no discontinuity should be present so as not to hinder the transport of majority carriers.

Next, the electron-hole pairs generated in the depletion region will be separated to opposite direction by the internal electric field in the depletion region, the electrons will reach the n-type emitter region, diffuse toward the front contact and been collected by the electrode. While the holes will reach the p-type base region, diffuse toward the back contact and been collected by the electrode.

Finally, in the n-type emitter region, the situation is similar to the base region. The majority carriers, electrons, will diffuse toward the front contact and then been collected. The minority carriers, holes, will diffuse toward the depletion region, drift to the p-type base region, then diffuse toward the back contact and been collected. Just like the BSF, we usually utilize a window layer to minimize the unwanted recombination of minority carriers because analogously, the interface between the normally doped n-region and the highly doped n+-region window acts like an n-p junction. Here, this junction acts as a large barrier that prevents minority holes in the n-region from diffusing to the back surface, so that reflects minority carriers (holes) towards the junction. On the other hand, in the majority carrier (electrons) band no discontinuity should be present so as not to hinder the transport of majority carriers.

The charge carriers are extracted from the solar cells with electrical contacts so that they can perform work in an external circuit. The electrons passed through the external circuit, they will recombine with holes at a metal-absorber interface. The chemical energy of the electron-hole pairs is finally converted to electric energy.

VI Solar Cell Parameters and Equivalent Circuit

When a load is connected between the electrodes of the illuminated p-n junction, only a fraction of the photogenerated current will flow through the external circuit. The net current of the illuminated p-n junction of a solar-cell can be expressed by the form [3],

$$I = I_{SC} - I_{S1}\left(e^{qV/KT} - 1\right) - I_{S2}\left(e^{qV/2KT} - 1\right) \tag{1.46}$$

where, I_{SC} is the short-circuit current represents the photo-generated current, I_{S1} is the dark saturation current due to recombination in the quasi-neutral n- and p-type regions, I_{S2} is the dark saturation current due to recombination in the depletion region, q is the elementary charge, V is voltage, k is the Boltzmann constant, T is the absolute temperature, the numerals 1 and 2 at the denominators of the last two exponential terms are defined as ideality factors.
The last two terms of Eq. (1.46) can be combined, thus deducing [3],

$$I = I_{SC} - I_S\left(e^{qV/nKT} - 1\right) \tag{1.47}$$

where I_S is the dark saturation current, n is the ideality factor, and the value of n equals 1 or 2.

VI.1 External Solar Cell Parameters

The main parameters that are used to characterize the performance of solar cells are the peak power Pmax, the short-circuit current Isc, the open-circuit voltage Voc, and the fill factor FF. These parameters are determined from the illuminated I-V characteristic as illustrated in Figure 1.11. The conversion efficiency η can be determined from these parameters.

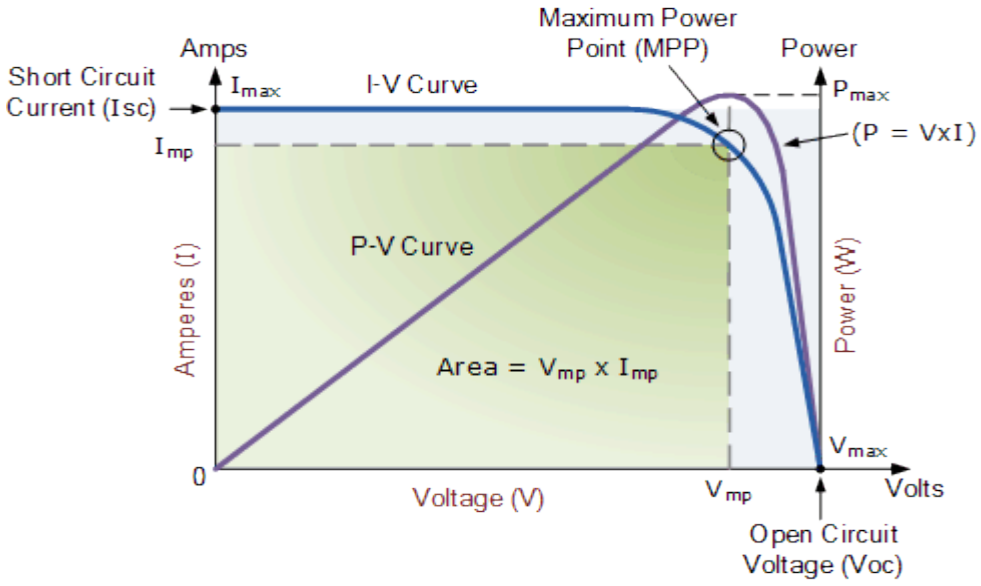

Figure 1.11: I-V and P-V Characteristic Curve for a Solar Cell [10].

VI.1.1 Short-Circuit Current

The short-circuit current Isc represents the photo-generated current, it is the maximum current provided by the solar cell that flows through the external circuit when the electrodes of the solar cell are short-circuited (a short circuit condition), this value is much higher than I_{mp} which relates to the normal operating circuit current. The short-circuit current of a solar cell depends on the photon flux density incident on the solar cell, which is determined by the spectrum of the incident light. The maximum current that the solar cell can deliver strongly depends on the optical properties of the solar cell, such as absorption in the absorber layer and reflection. The short-circuit current, I_{SC}, is the current when the voltage is zero see Figure 1.11. At small applied voltages, the diode current is negligible and the current is just the short-circuit current, I_{SC}, as can be seen when V is set to zero in equation(1.47). When the applied voltage is high enough so that the diode current (recombination current) becomes significant, the solar cell current drops quickly.

VI.1.2 Open-Circuit Voltage

The open-circuit voltage is the voltage at which no current flows through the external circuit see Figure 1.11. It is the maximum voltage that a solar cell can deliver when it is not connected to any load (an open circuit condition), this value is much higher than V_{mp} which is fixed by the load. Voc corresponds to the forward bias voltage, at which the dark current compensates the photocurrent. Voc depends on the photo-generated current density and can be calculated from Eq. (1.46) assuming that the net current is zero (for simplicity, here we make an assumption that the dark current due to recombination in the depletion region (n = 2) can be neglected [3],

$$V_{OC} = \frac{KT}{q} ln \frac{I_{SC}+I_{S1}}{I_{S1}} \approx \frac{KT}{q} ln \frac{I_{SC}}{I_{S1}} \tag{1.48}$$

where $I_{SC} >> I_{S1}$.

VI.1.3 Maximum Power

Of particular interest is the point on the I-V curve where the power produced is at a maximum. This is referred to as the maximum power point with V = Vmp and I = Imp. As seen in Figure 1.11, this point defines a rectangle whose area, given by Pmax = Vmp Imp, is the largest rectangle for any point on the I-V curve.

VI.1.4 Fill Factor

The fill factor, FF, represents the *squareness* of the I-V curve and is defined as the rectangle area ratio between (Im Vm) and (I_{SC} V_{OC}), the fill factor is the ratio between the maximum power (Pmax = JmpVmp) generated by a solar cell and the product of Voc with Jsc (see Figure 1.11), this fill factor value is always less than one and gives an idea of the quality of the array and the closer the fill factor is to 1 (unity) , and is defined as [3],

$$FF = \frac{P_{max}}{I_{SC}\ V_{OC}} = \frac{I_{mp}\ V_{mp}}{I_{SC}\ V_{OC}} \tag{1.49}$$

VI.1.5 Conversion Efficiency

The power conversion efficiency, η, is the most important figure-of-merit for assessing a solar-cell. The conversion efficiency is calculated as the ratio between the maximal generated power and the incident power. The performance metrics of V_{OC}, J_{SC}, and fill factor combine to give the cell's efficiency and is defined as [3],

$$\eta = \frac{P_{max}}{P_{in}} = \frac{I_{mp}\ V_{mp}}{P_{in}} = \frac{I_{SC}\ V_{OC}\ FF}{P_{in}} \tag{1.50}$$

where P_{in} is the incident power, is determined by the properties of the light spectrum incident upon the solar cell. The irradiance value P_{in} of 1000 W/m^2 for the AM1.5 spectrum has become a standard for measuring the conversion efficiency of solar cells,

VI.2 Spectral Response

The spectral response SR(λ) or called The quantum efficiency QE(λ) of a solar cell permits an examination of how photons of different wavelengths (energy) contribute to the short-circuit current. The spectral response is defined as the short-circuit current, I_{SC}(λ), resulting from a single wavelength of light normalized by the maximum possible current. The quantum efficiency QE(λ) is classified to external quantum efficiency, EQE(λ), and internal quantum efficiency, IQE(λ). The external spectral response is defined as [3],

$$SR_{ext}(\lambda) = EQE(\lambda) = \frac{I_{SC}(\lambda)}{qA\Phi(\lambda)} \tag{1.51}$$

where q is the elementary charge, A is the area of solar-cell, and Φ(λ) is the incident photon flux (number of photons incident per unit area per second per wavelength),

The EQE percentage is a measure of the spectral response of a solar cell and can give information regarding the performance of each individual sub-cell within a multi-junction cell design. Important factors that are revealed by the EQE can be used to improve and further optimize solar cell design.

VI.3 Solar Cell Equivalent Circuit

From a circuit perspective, Figure 1.12 is a simple equivalent circuit model of a solar cell. The short-circuit current I_{SC} is regard as an ideal current-source (I_{SC}). The dark saturation currents can be represented by two diodes which are in parallel with the ideal current-source but have opposed the direction of current flow. Diode 1 with an ideality factor of 1 and represents the recombination current in the quasi-neutral regions, and diode 2 with an ideality factor of 2 and represents the recombination current in the depletion region.

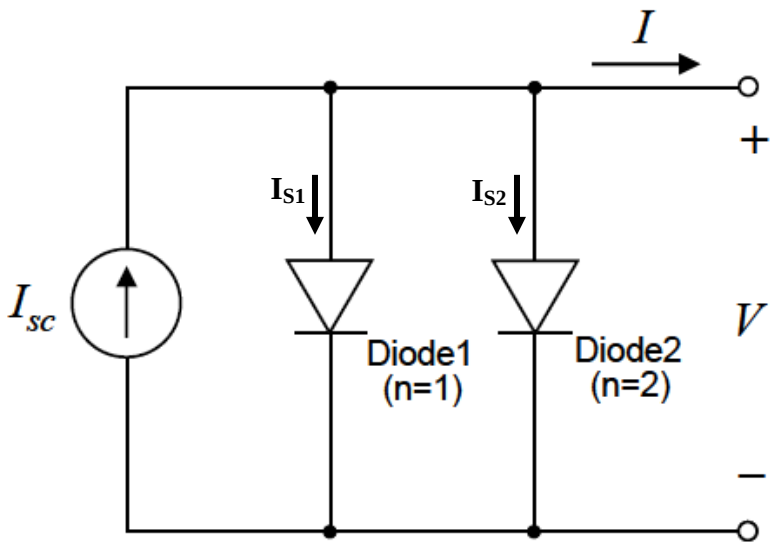

Figure 1.12: The equivalent circuit model of a solar-cell [3].

VII Parasitic Resistance Effects

Equation (1.46) neglects the parasitic series and shunt resistances typically associated with real solar cells. If we consider the parasitic series resistance, R_S, and shunt resistance, R_{Sh}, in a real solar-cell, Eq (1.46) and Figure 1.12 will then be modified to Eq (1.52) and Figure 1.13, respectively [3],

$$I = I'_{SC} - I_{S1}\left(e^{q(V+IR_S)/KT} - 1\right) - I_{S2}\left(e^{q(V+IR_S)/2KT} - 1\right) - \frac{(V+IR_S)}{R_{Sh}} \qquad (1.52)$$

Similarly, we can rewrite Eq (1.52) by combining the two dark current terms into one,

$$I = I'_{SC} - I_S\left(e^{q(V+IR_S)/nKT} - 1\right) - \frac{(V+IR_S)}{R_{Sh}} \qquad (1.53)$$

where I'_{SC} is the short-circuit current when there are no parasitic resistances.

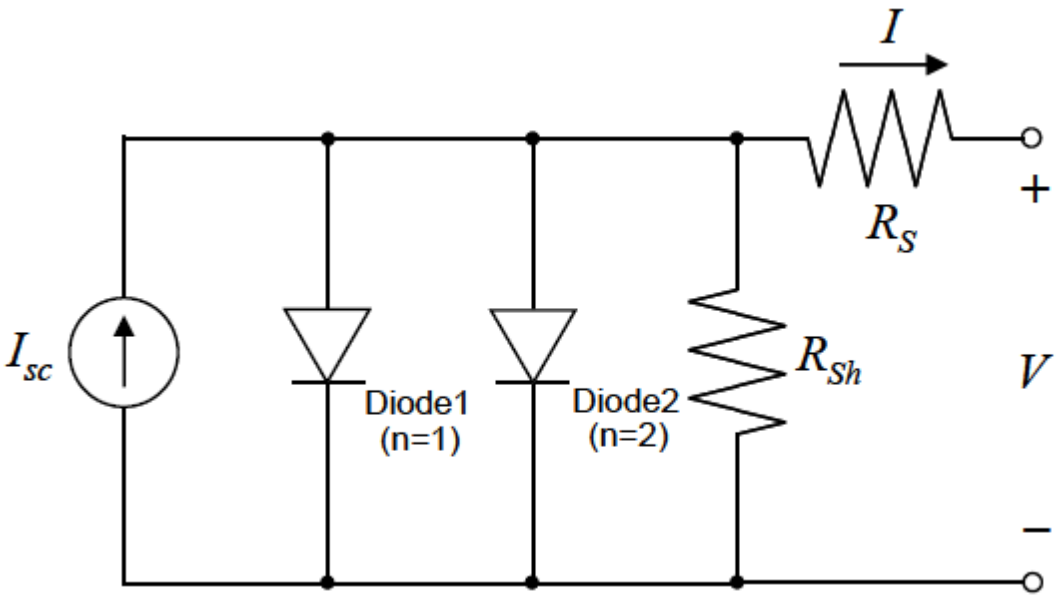

Figure 1.13: The equivalent circuit model of a solar-cell with parasitic resistances [3].

The effect of these parasitic resistances on the *I –V* characteristic is shown in Figures 1.14 and 1.15. As can be seen in the Figure 1.14, the series resistance, R_S, has no influence on the open-circuit voltage, but will reduces the short-circuit current if the R_S becomes too large. Oppositely, as can be seen in the Figure 1.15, the shunt resistance, R_{Sh}, has no influence on the short-circuit current, but will reduce the open-circuit voltage if the R_{Sh} becomes too small. The causes of series resistance including many components, such as contact electrode resistance (especially the front electrode), lateral resistance between front-contact electrodes, resistance of each component layer, and etc. On the other hand, the shunt resistance is caused by leakage-current pathways inside the device [3]. In practice the FF is influenced by a series resistance Rs, and a shunt resistance Rsh.

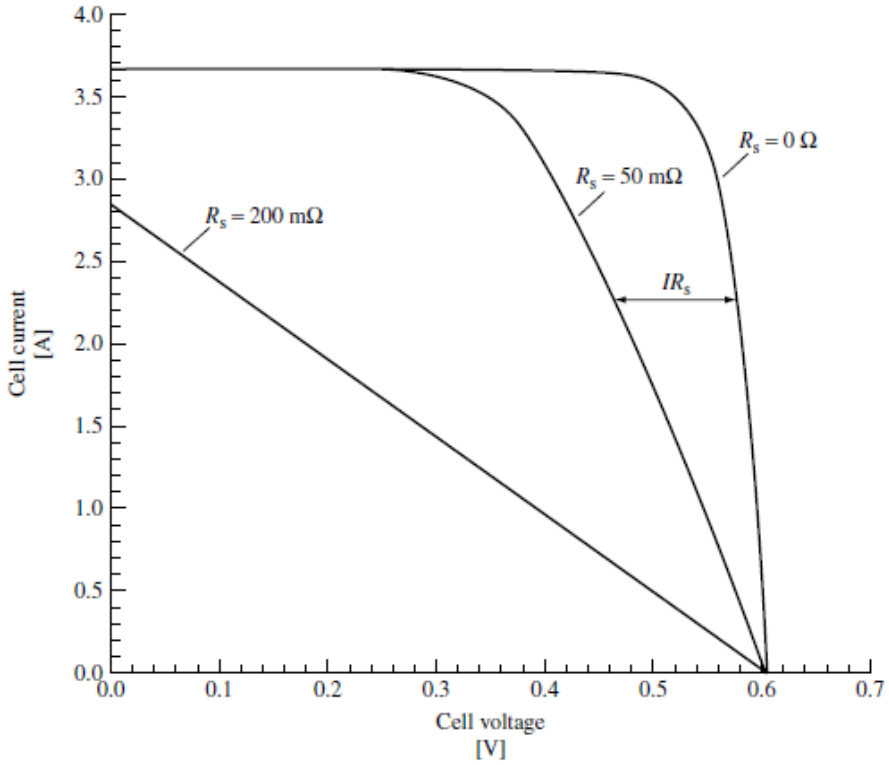

Figure 1.14: Effect of series resistance Rs on the current-voltage characteristic of a solar cell ($R_{Sh} \rightarrow \infty$)[3]

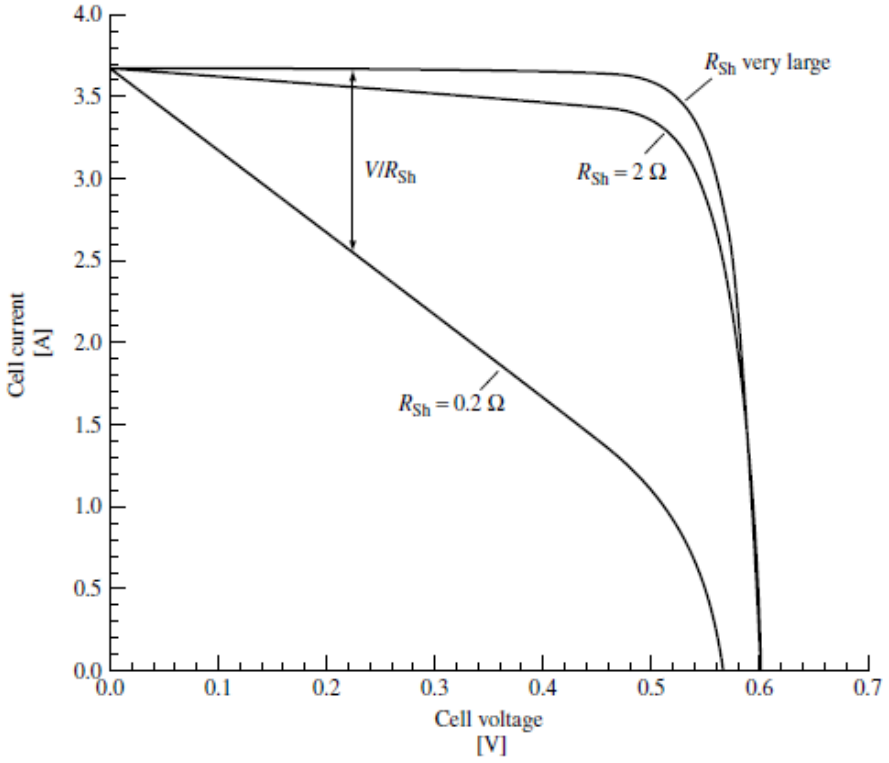

Figure 1.15: Effect of shunt resistance Rsh on the current-voltage characteristic of a solar cell ($R_S = 0$) [3]

VIII Losses in Solar Cell

Solar cells suffer from various losses which reduce their efficiency significantly. In this section, the primary loss mechanisms are briefly described and various techniques, which have been used to mitigate these losses, are presented.

VIII.1 Absorption losses

The efficiency of a solar cell is strongly dependent on the material bandgap (Eg), as discussed previously, photons with energy below the bandgap (E < Eg) will be lost. Moreover, solar cells have a limited thickness and the semiconductor materials they are made of have finite absorption coefficients so even some photons with energies above the bandgap will not be absorbed due to the absence of an infinite absorber. For a single-junction device under a fixed spectrum, there is an optimum bandgap where the efficiency reaches a maximum. For the standard AM1.5 spectrum according to the Shockley-Queisser limit, maximum efficiency of 33% at a bandgap of 1.4 eV is theoretically predicted [11]. Hence, non-absorption of sunlight exerts a significant impact on the solar cell efficiency but can be minimized by using direct bandgap semiconductor materials with high absorption coefficients and by using multi-junction.

VIII.2 Thermalization

Photons with energies much greater than the bandgap (E > Eg) are strongly absorbed by the device with the excess energy above the bandgap lost as heat [12], the solution, in this case using optimum bandgap.

VIII.3 Recombination

If the charge carriers recombine before reaching the solar cell contacts, the absorbed energy gets lost as a photon (radiative) or a phonon (non-radiative) or as kinetic energy to another free carrier (Auger). Recombination may occur in the bulk material or at the surface. Techniques such as surface passivation and the use of back-surface field BSF are often employed to reduce recombination and using high quality direct bandgap semiconductor materials limited by radiative recombination [13].

VIII.4 Reflection

Fresnel reflections due to the air/semiconductor interface lead to substantial losses in a solar cell. These losses which are refractive index dependent can be minimized by using optimal anti-reflective (AR) coatings. The AR coating material and thickness is chosen for maximum photocurrent generation at relevant incident angles. In addition, a back reflector is often used to increase absorption by reflecting the light into the cell for potential reabsorption [14].

VIII.5 Shading

The metallic grid on the front surface will reflect some of the impinging light. In addition, the antireflection coating on the surface will not be perfect for all wavelengths, generating also some undesired reflections in non-metalized areas. Contact patterns optimization is thus performed to minimize shading. Back-contacted solar cells and transparent electrodes are also used to reduce shading losses [14].

VIII.6 Series Resistance Losses

Ohmic or resistive losses occur due to the photocurrent owing through the device and the resistive metal contacts. These losses can be partly mitigated by optimized doping concentrations to improve carrier collection [14].

Conclusion

It has been the objective of this chapter to give a basic understanding of the physical principles that underlie the operation of solar cells. In this chapter, the basic equations governing solar cell operation have been presented. Toward that end, the fundamental physical characteristics of solar cell materials that permit the conversion of light into electricity have been presented. These characteristics include the ability of semiconductors to absorb photons by conferring that energy to carriers of electrical current and the ability of semiconductor materials to conduct electricity. The basic operating principles of the solar cell (a carefully designed *pn*-junction diode) were derived from the (simplified) equations describing the dynamics of holes and electrons in semiconductors. This led to the definition of the solar cell figures of merit, the open-circuit voltage (V_{OC}), the short-circuit current (I_{SC}), the fill factor (FF), and the cell efficiency (η). The two key factors determining solar cell efficiency are electron-hole pair generation and recombination -were identified and discussed. Also, several loss factors were addressed. It is clear that even though a material with near-optimal bandgap for photovoltaic energy conversion is available, the efficiency is limited when using a single junction. Multiple junctions are needed to increase conversion efficiency. In this way, the solar spectrum is divided into portions that are absorbed more efficiently in the different materials (junctions), without optical losses, which will be discussed in detail in chapter 2.

References

[1] https://www.momjunction.com/articles/sun-facts-for-kids_00455286/#gref
[2] https://www.astronomytrek.com/10-interesting-facts-about-our-sun/
[3] Antonio Luque and Steven Hegedus. Handbook of photovoltaic science and engineering. Published by John Wiley & Sons, Ltd, 2003.
[4] ATLAS User's Manual Device Simulation Software Copyright 2007, SILVACO International.
[5] Angèle Reinders, Pierre Verlinden, Wilfried van Sark, and Alexandre Freundlich.Photovoltaic Solar Energy: From Fundamentals to Applications, First Edition. Published by John Wiley & Sons, Ltd, 2017.
[6] Augustin McEvoy, Tom Markvart, and Luis Castaner. Practical handbook of photovoltaics : fundamentals and applications.– 2nd edition. Copyright © Published by Elsevier Ltd, 2012.
[7] https://www.electronics-tutorials.ws/diode/diode_2.html
[8] Carlos Algora and Ignacio Rey-Stolle. Handbook of Concentrator Photovoltaic Technology, First Edition. © 2016 John Wiley & Sons, Ltd. Published by John Wiley & Sons, Ltd, 2016.
[9] M. Yamaguchi, "III–V compound multi-junction solar cells: present and future", Solar Energy Materials and Solar Cells, Volume 75, Issues 1-2, Pages 261-269, ISSN 0927-0248, 10.1016 / S0927-0248(02)00168-X, 2003.
[10] http://www.alternative-energy-tutorials.com/energy-articles/solar-cell-i-v-characteristic.html
[11] W. Shockley and H. J. Queisser, \Detailed balance limit of e_ciency of p-n junction solar cells," Journal of applied physics, vol. 32, no. 3, pp. 510-519, 1961.
[12] P. Wrfel, Thermodynamic limitations to solar energy conversion, Physica E: Low-dimensional Systems and Nanostructures, vol. 14, no. 12, pp. 18-26, 2002.
[13] J. Nelson, The physics of solar cells. Imperial College Press, 2003.
[14] L. C. Hirst and N. J. Ekins-Daukes, Fundamental losses in solar cells,"Progress in Photovoltaics: Research and Applications, vol. 19, no. 3, pp. 286-293, 2011.

Chapter 2

High-efficiency Multi-junction Solar Cells

Chapter 2
High-efficiency Multi-junction Solar Cells

Introduction

In the first part, this chapter briefly reviews the history of solar cells. We also review recent progress with laboratory cells; the efficiency records solar cells are included. In addition, describe special features of III-V multi-junction (MJ) solar cells in comparison to conventional single-junction solar cells. In the second part, we describe the principle, design, and configurations, cell interconnection technologies of III–V multi-junction solar cells. In addition, we describes some of the different approaches and designs for III–V solar cells and make some predictions about the future of MJ cells in the last part in order to provide a foundation to facilitate the discussion of results in terms of the long-term goal of this work: multi-junction solar cells are able to achieve significantly higher efficiencies than single junctions due to better spectral utilization.

I Towards renewable energy

Modern life requires ever greater amount of energy usage. Energy is needed to power all sorts of electrical machinery that make our life so much easier as well as all kinds of electronics, be it for work or pleasure. Energy is needed everywhere, even in extremely remote places such as outer space. Thus, it is necessary to replace existing sources, which are mostly fossil fuels, with alternative ones which are friendlier to the environment. In addition, fossil fuels are not abundant in nature and their finite amount requires the development of renewable energy sources. Renewable energy such as solar energy, wind and water power, geothermal and biomass energy, may hold the key to solving the energy puzzle as they are abundant and do not produce any CO_2. One of the most important renewable energy sources is the electromagnetic energy from the sun. Devices which are able to convert the sun energy (electromagnetic waves) into electrical energy are generally called photovoltaic devices (PV), solar cells (SC) or photovoltaic cells (PVCs). The requirements of a PV device are high efficiency, low cost, environment resistance (durability) and easy fabrication method. Concerning photovoltaic devices, we can find different types, where the energy process conversion is different for each of them.

I.1 Advantages of Photovoltaic Technology

Photovoltaic cells are the most remarkable photo-conversion devices and the most emerging renewable energy resource. Below are the key advantages of solar panels [1].

- Solar energy is free energy. Fuel source is enormous, easily accessible and infinite.
- Clean technology (green energy); do not contribute to climate change or any kind of pollution. No emissions, combustion or nuclear waste disposal.
- Generated anywhere there is sunlight, tropical, rural, urban, distributed or grid-feeding mode.
- High reliability of solar cell modules (manufacturers guarantee over 25 years).
- Proximity to demand, no transmission cost, can be used for stand-alone and grid-connected applications.
- Non-toxic (except CdTe), made up of thin semiconductor wafers or films.

- Photovoltaic cells are totally silent and have no mechanically moving parts – they are a perfect solution for residential areas.
- Easily integrated into new or existing building structures (Rapid installation).
- Operating and maintenance costs for Photovoltaic panels are considered to be low, almost negligible, compared to costs of other renewable energy systems.

II Brief History and Progress in Solar Cell Technology

Photovoltaic effect, which means the conversion of light energy into electrical energy, was first reported by Edmund Becquerel in 1839. He observed that photocurrents were produced when light illuminated the platinum electrodes which were coated with silver chloride or silver bromide and immersed in electrolyte [2].

After the discovery, more than one hundred years, there is no significant breakthrough for the early solar-cells until the 1950s, with the improvement in processing technique of silicon solid-state electronics. In 1954, Chapin et al. from Bell Lab utilized a diffused silicon p-n junction to make a solar-cell with an efficiency of approximately 6 % [3]. It's a milestone for solar-cell develops history because it implied that the conception of using solar cell to generate electricity may be feasible. After several decades of development, modern solar cells have been made by several different material systems, including single crystalline silicon (sc-Si), polycrystalline silicon (poly-Si), hydrogenated amorphous silicon (α-Si:H), III-Vs, II-VIs (CdTe), I-III-VI_2s (CIGS: ($Cu(In,Ga)Se_2$)), organic, and dye-sensitized.

The theoretical limit of single-junction solar cells, known as the Shockley-Queisser limit, was explored by William Shockley and Hans-Joachim Queisser in 1961. The calculation determined that using a single p-n junction with bandgap material between 1.3 and 1.4 eV with air mass (AM) 1.5 spectrum light illumination, the maximum output power efficiency achieved could be about a third of the incident light power density converted to useful power output [4].

Multi-junction solar cells were experimented with and developed later in the 20th century to improve upon the Shockley-Queisser limit through the use of materials with high absorption over a greater fraction of the solar spectrum.

One of the major factors of energy loss in a solar cell is the gap between the photon energy and the bandgap energy of the photovoltaic material. No absorption would occur if the photon energy was smaller than the bandgap energy and merely the part equal to the bandgap energy out of the photon energy could be extracted as electric power leaving the other part wasted as heat if larger. Multi-stacking of photovoltaic materials of different bandgap energies is therefore commonly used for high efficiency III-V solar cells to reduce this energy loss and absorb the photon energy from the sunlight spectrum more widely and efficiently, taking advantage of the tunability of bandgap energies and lattice constants with the compositions of III-V semiconductor compounds, called multi-junction or tandem cells.

On the other hand, III-V compound materials, which have the advantages of direct-bandgap (high absorption coefficient), adjustable bandgap by varying the composition of component element (bandgap engineering), and high radiation resistance (for space application), also have the epitaxial technology and research basis supported by the optoelectronics industry [5].

But, the major drawback of III-V compound solar-cells is the very expensive manufacture cost and this is also the main reason why III-V solar-cells have not extensively used in terrestrial commercial market, although the III-V solar-cells have already been used as the power supply for satellites in space applications. Therefore, the concept of "concentration" is been adopted. The solar-cell under concentration can using a smaller cell size to generate equal output power and transfer the manufacture cost to the much more cheaper concentrator module components, such as the Fresnel lens, heat sink, and solar tracking system. Thus decreasing the cost and let the III-V solar-cells more competitive, improved power/weight ratios and better radiation resistances compared to silicon devices.

Multi-junction solar cells have been studied since 1960 [6]. The first multi-junction device was demonstrated in early 1980s, and it converted 16% of the solar energy into electricity [7].
One of the most common and highest efficiency two 2J solar cells consists of a combination of $In_{0.48}Ga_{0.52}P$ and GaAs with the same lattice constant of 5.64 A and the bandgap energy of 1.86 eV and 1.42 eV, respectively [8, 9]. This InGaP/GaAs solar cell has the highest efficiency of 30.3% under AM1.5G solar spectrum with 1-sun intensity (100 mW/cm^{-2}) among monolithic 2J solar cells [9, 10]. Current world record efficiency for dual-junction cells is 34.1% achieved with an InGaP/GaAs device and the highest recorded efficiency is 46% [11] by a four-junction wafer-bonded solar cell [12].

For 3J cells, most commonly so far, a Ge bottom cell is added to the InGaP/GaAs 2J cell to form an InGaP/GaAs/Ge structure for Ge's lattice constant of 5.66 A nearly equal to that of InGaP/GaAs. This 3J structure is grown on a Ge substrate and an advantage that Ge is a cheaper and mechanically stronger material than GaAs relative to cells grown on GaAs substrates. The current formally-reported highest efficiency solar cell is actually an InGaP/GaAs/Ge 3J cell with the efficiency of 40.7% at 240 suns under AM1.5D [13, 14].

The current record holder for solar cell efficiency is held by the Fraunhofer ISE/ Soitec concentrator-type photovoltaic multi-junction solar cell at 46% efficiency. The cell, independently verified by AIST in Japan, is a wafer-bonded GaInP/GaAs//GaInAsP/GaInAs four-junction (4-J) cell under a 508-fold concentration of AM 1.5d spectrum sunlight with a fill factor of 85.1% and efficiency of 46% [15]. For non-concentrator photovoltaics, the current record is the Boeing-Spectrolab five-junction (5-J) direct bonded cell at 38.8% efficiency at one sun under the AM 1.5G spectrum at 25°C [16]. The maximum theoretical limit efficiency of multi-junction solar cells is 86.8% [17].

The energy conversion efficiencies of III-V solar cells have been steadily increasing year-to-year, multi-junction solar cells have been a hot topic of research and development for large-scale energy generation for terrestrial applications as outlined in Figure 2.1. The progress made by various solar technologies (MJSC, Si, ThinFilm, Organic, etc.) in the last 43 years from the year 1975 to 2018 has been summarized in a single graph plotted by the Department of Energy's National Renewable Energy Laboratory (NREL).

Figure 2.1 illustrates the best laboratory efficiencies obtained for various materials and technologies. Current research has achieved a maximum of 46% efficiency for a concentrated four-junction cell.

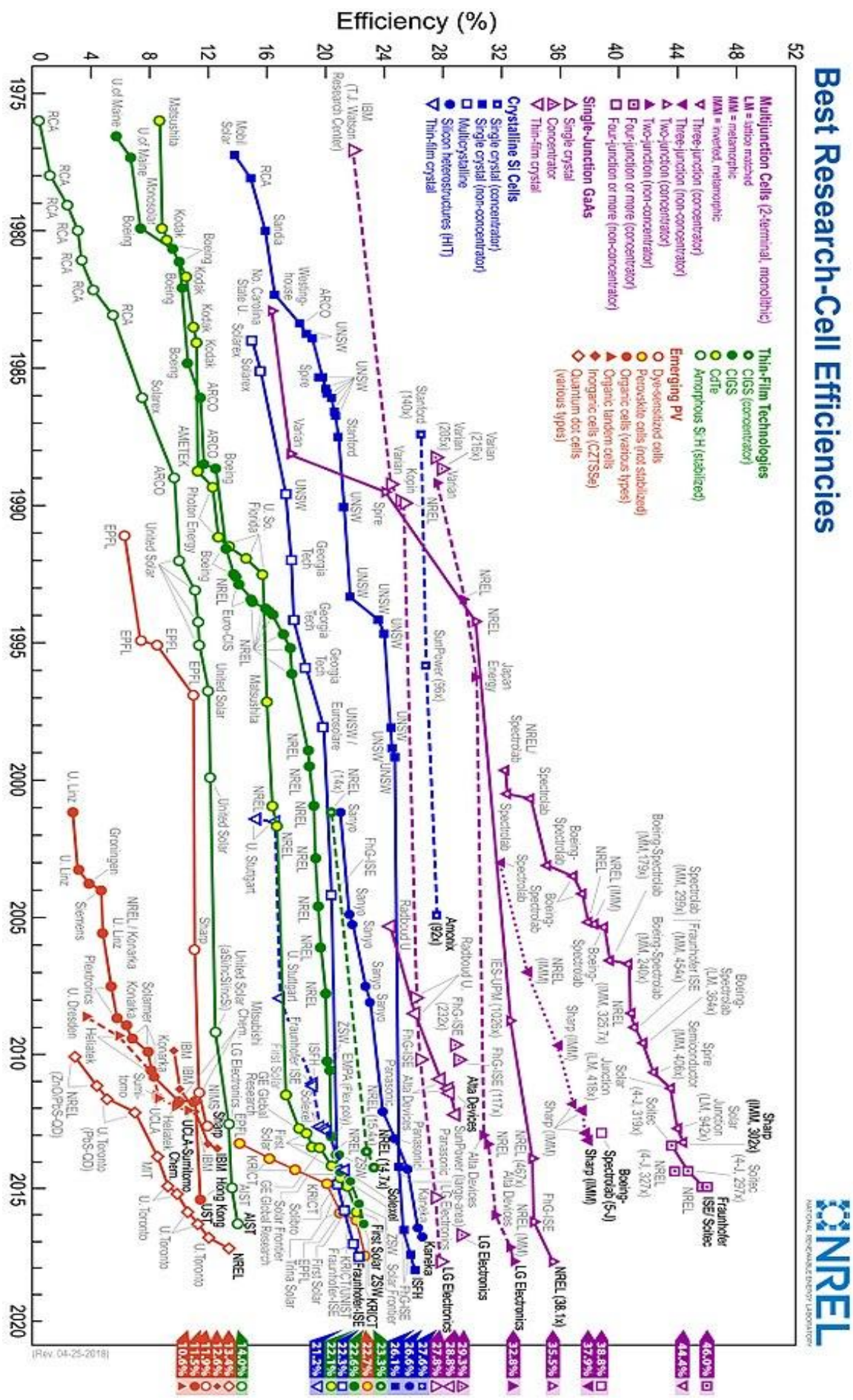

Figure 2.1: Chronological record energy-conversion efficiencies of solar cells. over time [18] .

There are four categories of solar cells indicated by different colors in the plot: Multi-junction III-V (GaAs, InGaP/GaAs/Ge, etc.) Solar Cell, Crystalline Si Cells, Thin-Film Technologies, Emerging PV. Table 2.1 summarizes general categories of solar cell technologies by the best efficiencies.

Table 2.1: General Categories of Solar Cell Technologies by the best efficiencies

Technology	Best efficiency
Emerging PV Nano-crystalline and Nano-structured Solar Cells (quantum dot solar cells) New Concepts (Multi-Exciton-Generation MEG) DSSC (Dye-Sensitized Solar Cell) Organic/Polymer Solar Cells	**22.7%** DSSC (Dye-Sensitized Solar Cell)
Thin Films Amorphous Si (a-Si) CdTe (Cadmium Telluride) CIGS (Copper-Indium Gallium Selenide)	**23.3%** CIGS (concentrator)
Silicon Monocrystalline or single crystalline silicon (mono-Si sc-Si); Poly- or multicrystalline silicon (poly-Si or mc-Si): Ribbon silicon	**27.6%** single crystalline (concentrator)
III-V Solar Cell Single-junction GaAs Multi-junction (InGaP/GaAs/Ge) Concentrating Photovoltaics, CPV)	**46%** four-junction (concentrator)

It is clear that the III-V multi-junction solar cells have the highest promise of increasing the efficiency as evidenced by the efficiency.

III High-Efficiency III-V Solar cells

Solar cells made of III-V semiconductors reach the highest efficiencies of any photovoltaic technology so far. The materials used in such solar cells are composed of compounds of elements in groups III and V of the periodic table. III-V multi-junction solar cells differ from conventional single-junction solar cells in several aspects. This section introduces these features.

III.1 III-V Single Junction Solar Cells

III-V Compounds such as gallium arsenide (GaAs), indium phosphide (InP) and gallium antimonide (GaSb) have direct energy bandgaps, high optical absorption coefficients and good values of minority carrier lifetimes and mobilities (in highly pure, single crystal material) making them excellent materials for making high efficiency solar cells.

In 1956, Jenny et al. from RCA laboratory used a diffused single crystalline GaAs p-n junction to fabricate a solar-cell with an efficiency of 6.5 % [19], which was at the same order as the Si cell reported at the same period [20].

The most efficient single-junction GaAs solar-cell with an efficiency of 29.3 % under 49.9 suns [21].

A single junction device is able to convert solar radiation with energy above the bandgap value of the absorber material. Single-junction solar cells have two major loss mechanisms: thermalization and transmission. Photons of energy less than the semiconductor bandgap are transmitted through the material without being absorbed (transmission), while photons of energy in excess of the bandgap do not generate electron-hole pairs but convert that excess energy to heat which limits the efficiency of the cell.

Multi-junction solar cells (MJSCs) consist of a stack of n-p semiconductor diodes of different materials, each chosen to absorb a different part of the solar spectrum. As light passes through the stack, the short wavelengths are absorbed in the top junction who has a large Eg, and longer wavelengths are absorbed in each of the subsequent junctions. This arrangement minimizes the impact of transmission and thermalization losses by providing materials that are capable of absorbing the vast majority of photons within the solar spectrum, and by ensuring that each photon is absorbed in a junction with Eg similar to the photon energy.

III.2 III-V Multi-junction Solar Cells

III.2.1 Basic Principles of Multi-Junction Solar Cells

An Multi-junction (MJ) solar cell with two, three, or more junctions is a set of the same number of p–n junctions made from different materials, stacked on the top of each other, including metallic contacts on the top and bottom of the solar cell [22, 23]. The idea is to subdivide the incident solar spectrum into several parts to be absorbed for the different sub-solar cells; each one has an optimized efficiency for a certain range of wavelengths in the spectrum of the incident sunlight. The goal is to find the best and most advantageous band-gap combination for each sub-solar cell to convert the total incident solar light with the maximum possible efficiency.

In order to optimize conversion efficiency of a photovoltaic cell, the solar cell should absorb as much of the spectrum as possible, and so bandgaps should cover a wide range. Besides, bandgaps of adjacent layers should differ by an as small amount as possible, because the amount of excess energy from light converted to heat is equal to the difference between the photon energy and the bandgap of the absorbing material [24].

Multi-junction solar cells consist of some single-junction solar cells stacked upon each other, so that each layer going from the top to the bottom has a smaller bandgap than the previous, and so it absorbs and converts the photons that have energies greater than the bandgap of that layer and less than the bandgap of the higher layer [25]. Alloys of groups III and V of the periodic table are good candidates for fabricating such multi-junction cells: their bandgaps span a wide spectral range, and most of the band gaps have direct electronic structure, implying a high absorption coefficient, and their complex structures can be grown with extremely high crystalline and optoelectronic quality by high-volume growth techniques [26].

As shown in Figure 2.2, the single-junction solar cell can only absorb a certain portion of solar spectrum. In the case of silicon, the maximum theoretical efficiency is only 28% (Figure 2.2 a) [27], while for a multi-junction cell (Figure 2.2 b), each junction with different energy band gap can absorb different portion of the solar spectrum, thus the maximum theoretical efficiency can be 86.8% [27] much higher than the best case of single junction.

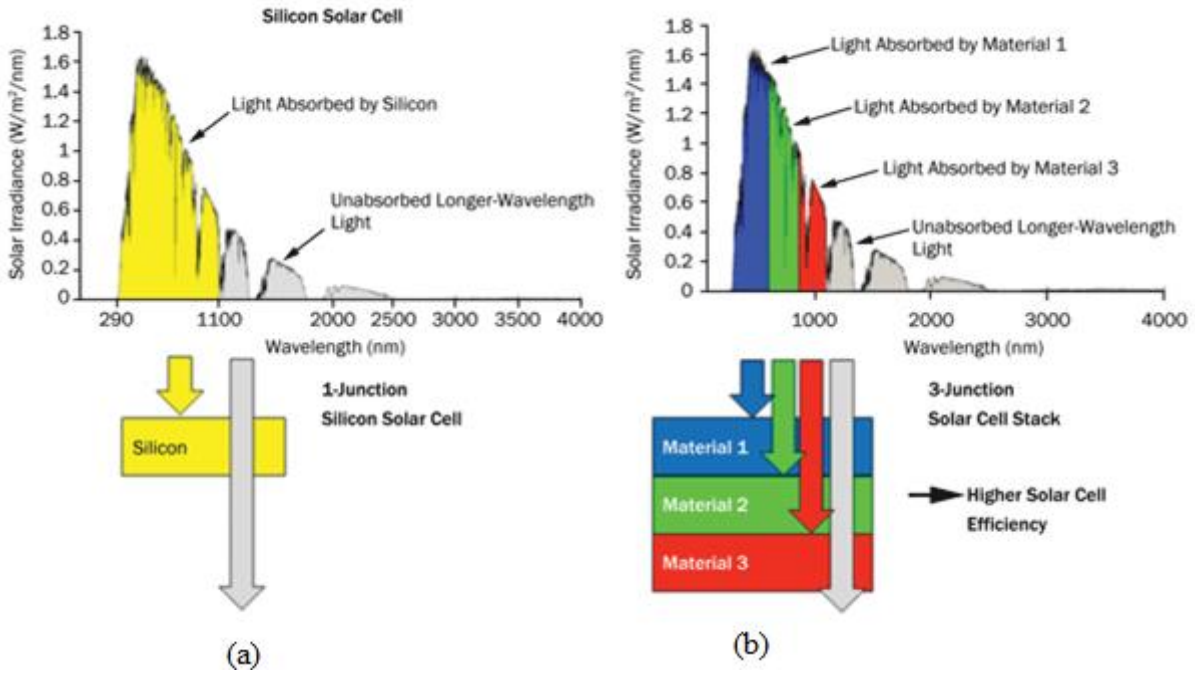

Figure 2.2: Light absorption for (a) Single-junction solar; (b) Multi-junction solar cell [28]

A typical structure of a triple junction solar cell is illustrated in Figure 2.2. In this case, each sub-cells is based on several materials with different band-gaps. The p–n solar cell with the highest band-gap is located on the top of the MJ solar cell stack to absorb the highest-energy photons, and the other sub-cells are placed in decreasing order of the band-gap with the aim to capture photons with less energy (longer wavelengths). The plot shows the air mass (AM) 1.5 direct (AM1.5D, ASTM G-173-03) reference spectrum with the dashed vertical lines indicating the band-gaps as an example for the top Gallium Indium Phosphide (GaInP; Eg1=1.9 eV), the middle Gallium Arsenide (GaAs; Eg2=1.42 eV) sub-cells and the bottom sub-cells in this example is Germanium (Ge; Eg3=0.67 eV). The sub-cells must be stacked in a sequence by following the rule of: Eg1> Eg2> Eg3, to ensure the efficient distribution and absorption of sub-bandgap photons in the lower sub-cells [29]. Therefore, the bandgaps must decrease from top cell to bottom cell in order to prevent the upward sub-cells absorbs the portion of light which is designated for the downward sub-cells.

Figure 2.3 shows the conventional GaInP/GaAs/Ge triple junction solar cell and is the main device to be studied in this thesis. Two highly-doped tunnel junctions with large bandgap are used in order to interconnect the three sub-cells but remain transparent to the incident sunlight at the same time. Here we use three steps to explain the principles when the sunlight incidents on the triple-junction solar-cell:

Step1: The photons with energy $h\nu > Eg1$ will be absorbed by the GaInP top cell, and photons with energy $h\nu < Eg1$ will transmit to the GaAs middle cell.

Step2: The photons with $Eg2 < h\nu < Eg1$ will be absorbed by the GaAs middle cell, and photons with energy $h\nu < Eg2$ will transmit to the Ge bottom cell.

Step3: Finally, the remaining photons with $Eg3 < h\nu < Eg2$ will be absorbed by the Ge bottom cell.

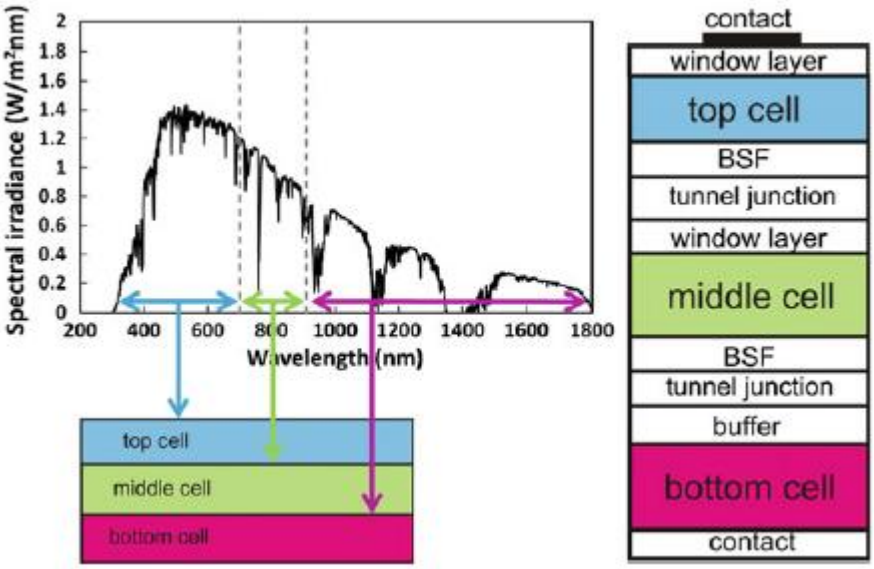

Figure 2.3: Portions of the solar spectrum absorbed in a multi-junction solar cell (left) and a schematic of a typical monolithic multi-junction solar-cell solar cell (right) [30]

Window layers should be included on the top sub-cells to decrease the surface recombination velocity, and a back surface field (BSF) layer should also be used to minimize scattering and loss of charge carriers at the tunnel junction. It is necessary that both layers should be as transparent as possible so the photons can be absorbed in the active regions of the device [31]. This is shown in Figure 2.3 (right side).

The key to the success of modern III-V solar cells is based on the development of advanced growth technologies, mainly molecular beam epitaxy, metal organic chemical vapor deposition, metal organic vapor phase epitaxy and other similar techniques. It is necessary to have high-accuracy epitaxial growth to obtain a highly efficient MJ solar cell. This means that there is little difference between the lattice constants of adjacent layers. In recent years, III–V multi-junction solar cells have usually been grown by metal-organic vapor phase epitaxy (MOVPE) reactors, resulting in the favorable economics of growth as well as high crystal quality. Large-area commercial MOVPE reactors are available from different companies [32, 33].

The bandgap values selected for the Multi-junction Solar Cells (MJSC) depend on the number of junctions used. Several concepts for MJSC have been investigated and they include optically splitting the spectrum into bands that correspond to the bandgaps of discrete cells, mechanically stacking discrete cells on top of one another and growing, monolithically, the cells in a stack where they are physically, electrically and optically connected. For both the mechanically and monolithically stacked cells the incident light must pass through the stack from highest bandgap sub-cell to the lowest, they are sometimes called cascade cells. However, work has continued on mechanically stacked devices which also yield high efficiencies. Mechanically stacked devices offer greater flexibility in terms of the sub-cells and electrical connections that can be used. Two essential requirements for monolithic devices are a suitable materials system that enables the growth of efficient sub cells on top of one another and that the current produced by each should be matched since they are connected in series.

III.2.2 Monolithically Versus Mechanically Stacked Multi-Junction Solar Cells

Two technological approaches have been investigated over the years (see Figure 2.4). In the mechanically stacked approach, the sub-junctions are fabricated separately on their individual substrates and then combined into one single mechanically stacked multi-junction device. As a result, each junction has its own contacts and can be connected separately. The main advantages of this approach are that the individual cells do not need to be lattice-matched and that each solar cell can be contacted individually. However, mechanically stacked cells have a lot of additional volumes and weight due to the stacking mechanisms used, the complexity of fabrication and assembly, as well as the higher material costs due to the multiple substrates usually lead to higher overall costs, this is a serious disadvantage for space applications. In addition, a significant amount of energy is lost due to reflection as a light goes from one cell to the other. In an attempt to eliminate these problems, another possibility for making tandem cells is the so-called monolithically stacked approach. In the monolithic approach, the monolithically stacked Multi-Junction (MMJ) solar cells have different solar cell materials grown directly on only one substrate and connected in series by tunnel diodes. This approach allows several materials to be stacked, resulting in a final device with only one positive contact and one negative contact as in a conventional single-junction solar cell. The current in such a device is always limited by the lowest current generated by one of the p-n junctions. The band-gap energies of the materials and the overall device structure, therefore, have to be chosen carefully. Although currently being state-of-the-art, there are some inherent restrictions for the monolithic design, such as the requirements of current matching and lattice matching; on the other hand, monolithic cells require well controlled epitaxial growth. However, mechanically stacked multi-junction **(**MSMJ) does not suffer from these limitations, and offer a very generic way of realizing multi-junction solar cells [34].

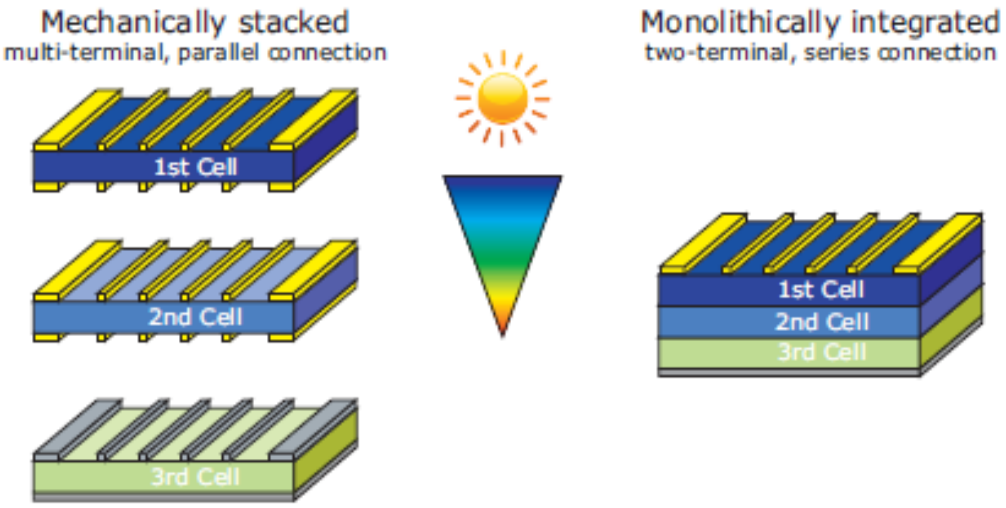

Figure 2.4: Two approaches for realizing multi-junction solar cells. Mechanically stacked vs. Monolithically stacked multi-junction solar cells [34].

III.2.2.1 Monolithic Multi-junction Solar Cells

Integrating all the components for a multi-junction solar cell into one monolithic structure places some constraints upon the multi-junction solar cell design. In general, the highest quality semiconductor junctions are achieved using lattice-matched semiconductor material. However, since the sub-cells are connected together in series internally, the current passing in the solar cell will be limited by the junction producing the lowest current. It is therefore important to engineer sub-cells producing similar current at maximum power and this can be difficult to achieve using only lattice-matched materials, so a number of monolithic lattice-mismatched (or metamorphic) multi-junction solar cells have been attempted where the lattice parameter is graded from one semiconductor junction to another.

The typical band structure for a double-junction solar cell is shown in Figure 2.5, showing the physical stacking of semiconductor layers and the band structure. Many of the components from the single-junction solar cell are present, notably the presence of a window layer and back surface field (BSF). The interconnection of the junctions is critically important in a monolithic cell and is achieved using a tunnel junction. The problem with simply connecting cells together lies in the fact that new junctions would be created between cells. Those junctions would be reversed–biased and their depletion–region electrostatic field would oppose the flow of carriers towards the contacts. Stacking such n-on-p junctions would lead to p-on-n diodes in between the sub-cells, which would block current flow. This would prevent the cell from producing any current. Instead, specially prepared tunnel junctions can be used to solve this problem. A reverse–biased tunnel junction will conduct current the desirable way, due to the tunneling phenomenon. The tunnel layers are always more heavily–doped than the cell layers.

Typically, tunnel junctions are formed by growing a heavily doped n++, layer adjacent to a heavily doped p++ layer, thereby bringing the conduction band of the n++ semiconductor to almost overlap energetically with the valence band of the p++ semiconductor. For this reason, intermediate junctions formed between the tunneling junctions and the cells will conduct current from the p to the p++ regions and from the n++ to the n regions. Each of the photovoltaic n-p junctions are interconnected with p++/n++ tunnel diodes which are intended to provide an ohmic conductive path from the p-type base of one junction into the n-type emitter of the next junction [35]. This will allow current flow instead of hindering it. In practice, tunnel junctions can be difficult to achieve. Firstly the junction must be transparent, meaning relatively high-bandgap semiconductors must be used, increasing the doping density required to achieve the same peak tunnel current [36]. Secondly, actually achieving very abrupt p++/n++ layers and preventing dopant diffusion during the remainder of the epitaxial growth is also challenging. One important means for preventing dopant diffusion has been the use high-bandgap materials (typically AlGaAs or AlInGaP) that act as diffusion barriers around the tunnel junction [37] as well as serving as useful window/BSF layers; for clarity, these barriers are not shown in Figure 2.5.

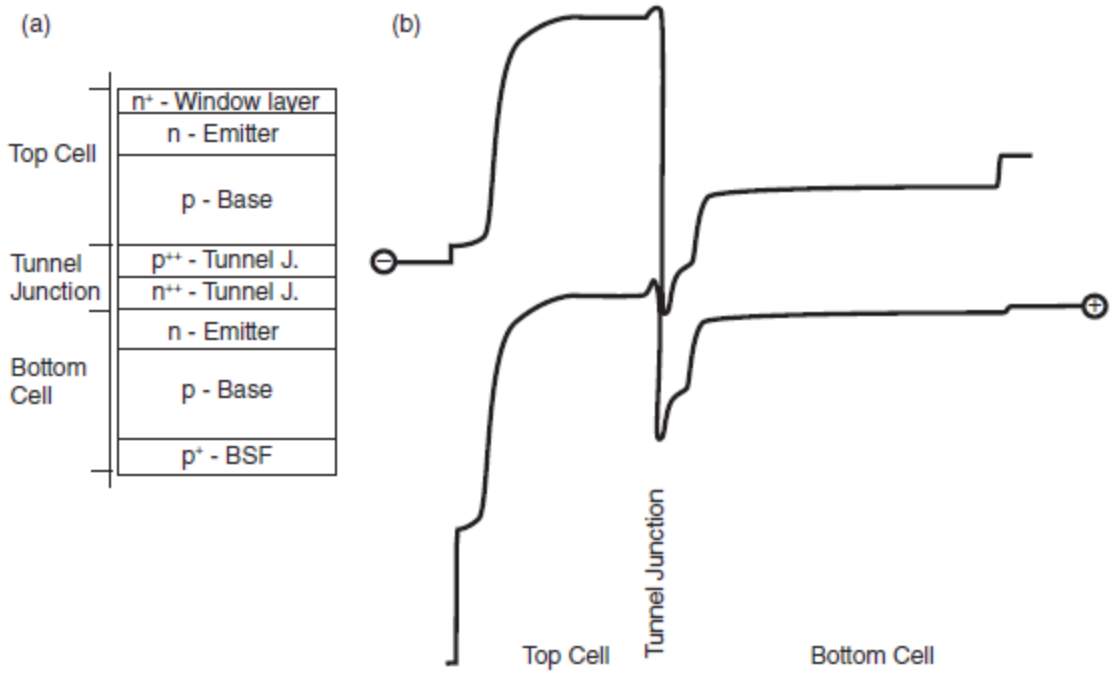

Figure 2.5: A monolithic double-junction solar cell with a tunnel junction interconnect: (a) schematic layer diagram and (b) band diagram showing top cell, tunnel junction, lower cell and rear BSF [38].

III.2.2.1.1 Analysis of Monolithic GaInP/GaAs Double-Junction Solar Cell

The idea of fabricating the double-junction tandem solar cell structures, as mentioned in last section, is theoretically simple and straightforward. However the development of practical devices towards research and commercial application has encountered numerous difficulties in terms of material quality and the fabrication methods. Before the early 80's, many researchers have started to fabricate the double-junction tandem structures based on the maturely developed Silicon (Si) cell technology. Various kinds of III-V semiconductor compound alloys, including GaAs, AlGaAs, GaInAs and GaAsP have been employed to grow on the top of the Si bottom cell by mechanical stacking technique. The theoretical efficiency predicted for such kinds of material sub-cells combinations are as high as ~40 %, however, the actual tested efficiency turned out to be much lower than theory, due primarily to the material defects generated by the material itself or the lattice mismatch between the top and bottom sub-cells [39]. For instance, the lattice-matched AlGaAs/GaAs double-junction tandem structure, with a bandgap combination of 1.9 and 1.42 eV, has been calculated for a theoretical efficiency of 36 % under the standard atmospheric solar simulation (AM1.5G spectrum). Nevertheless, the intrinsic oxygen-induced defects existed in the AlGaAs sub-cells has largely limited the further optimization of such a structure [40]. Eventually, in 1984 the novel material combination, namely the GaInP/GaAs double-junction tandem structure, has been fabricated with a theoretical efficiency of 34 % and become the first widely tested multi-junction solar cell device [39]. Soon after its first realization, the performance of the GaInP/GaAs double-junction tandem solar cell increases rapidly in the following decade, thanks to the extensive research efforts on improving the electronic and optical properties of the top GaInP/GaAs sub-cells and the structural engineering of both sub-cells in achieving the current-matching condition [41].

The schematic diagram showing the configuration of different layered structure of a typical double-junction tandem solar cell is depicted in Figure 2.6.

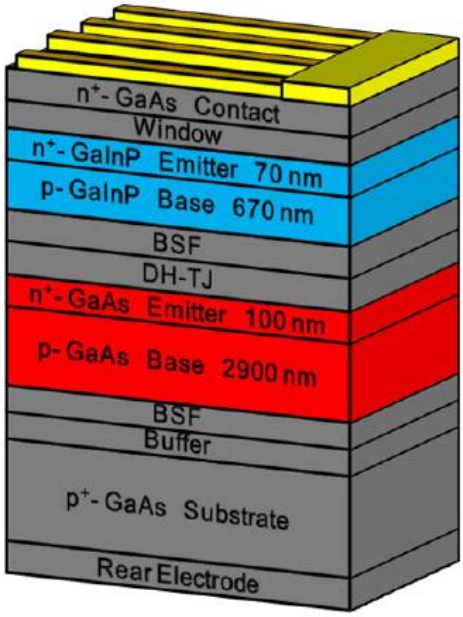

Figure 2.6: Schematic diagram of the GaInP/GaAs double-junction tandem solar cell structure [42].

The major function and material property of each layer will be briefly discussed as follows:

The most crucial elements of the entire double-junction solar cell structure are the top and the bottom sub-cells which serve as the main absorbing and converting layers of the solar illumination. In the typical III-V semiconductor double-junction configuration, the two sub-cells are usually designed with the conventional *p*-*n* junction, with the *p*-type doped base region and the *n*-type doped emitter region quantum-mechanically connected together by the space-charge region [43]. The materials of the two sub-cells need to be carefully chosen, as mentioned in the beginning of this chapter, such that the bandgap energy of each sub-cells is tuned and resonant to a specific range of the solar spectrum.

The other important layers features observed from the double-junction tandem configuration in Figure 2.6 are the window layer grown a top the emitter regions of the top sub-cells and the BSF layers grown under the base regions of two sub-cells. The purpose of fabricating the emitter window layer is obvious: to reduce the surface recombination of the minority holes by passivating the surface states related to the emitter region [39]. These surface states could be efficient recombination centers of minority carrier, and the impacts can be quantified by a parameter namely the surface-recombination velocity, *S* [44]. A high surface-recombination velocity could decrease the photoresponse of the top GaInP sub-cells, especially in the blue portion of the solar spectrum [39]. For the top GaInP sub-cells used in the high-efficiency GaInP/GaAs double-junction configuration, a good material candidate for fabricating the top emitter window layer would be the AlInP alloy, due to its satisfaction on the criteria of an effective window layer such as the closely-matched lattice constant with GaInP and the large enough valence band offset with respect to the emitter region [39]. On the other hand, the function of the BSF layers grown under the base regions of both top and bottom sub-cells is very similar to that of the top sub-cells emitter window layer: to

passivate the interface recombination between the base and the tunnel junction (for top sub-cells) / the buffer layer (for bottom sub-cells) [45]. The loss of minority carriers, in this case, electrons, at these interfaces can also be characterized by the surface-recombination velocity *S*, and the high value of *S* at these surfaces could influence both the photoresponse and the open-circuit voltage of the sub-cells [39]. Typical material choices for fabricating a good BSF layer with the criteria similar to those in the emitter window layer include high bandgap disordered GaInP, AlGaInP and AlInP alloys for both the top GaInP and bottom GaAs sub-cells [39, 45]. It is worth to mention that in the growth consideration of both the window layer and BSF layer, the doping types should be the same with its adjacent region, i.e., *n*-type for window layer and *p*-type for BSF layer, and the doping density should be as high as possible, typically $\geq 10^{18}$ cm^{-3}. This is because a high concentration of majority-type doping at the window and BSF layer could generate an *p*-*n* junction-like interface between the emitter and front contact, and between the base and tunnel junction / buffer layer, in which the electric field induced by the high-low doping difference could introduce a barrier to impede the diffusion of minority carriers to the surface [46].

The tunnel junction (TJ) structure is another imperative component in the double-junction and other multi-junction tandem solar cell structures since it serves the fundamental purpose of connecting the sub-cells into a monolithic tandem configuration. The criteria for a well-designed TJ structure include the low electrical resistance, i.e., a high tunneling current between the interconnected sub-cells, and a good transparency for low energy photons which are designated for the lower sub-cells. The typical TJ is simply a *p*++-on-*n*++ junction, in which the *p*++ and *n*++ denote the heavily doped concentration, normally within the order of 10^{19} cm^{-3} [47].

III.2.2.1.2 Analysis of Monolithic GaInP/GaAs/Ge Triple-Junction Solar Cells

The state-of-the-art III–V solar cell in space and concentrator applications and the most widely multi-junction cell manufactured on the market today. The monolithic triple junction InGaP/GaAs/Ge is the lattice-matched triple-junction solar cell. It is a direct descendant of the original GaInP/GaAs dual junction solar cell grown on a Ge bottom cell [48]. A three-junction cell made up of the InGaP top cell with direct band-gap of about 1.9 eV, a GaAs middle cell with a band-gap energy of 1.42 eV and a Ge bottom cell with band-gap of 0.67eV is lattice-matched. The maximum theoretical efficiency for this system is 38% at AM 1.5 [49]. It could be said that the addition of the Ge sub-cells was the natural development after the accumulated research done in GaAs solar cells grown on Ge substrates. Indeed, Germanium is a reasonable candidate to be used as the third junction, due to its low bandgap (0.67 eV) and its lattice constant very close to that of GaAs. In Figure 2.7 a typical GaInP/GaAs/Ge triple junction cell is illustrated.

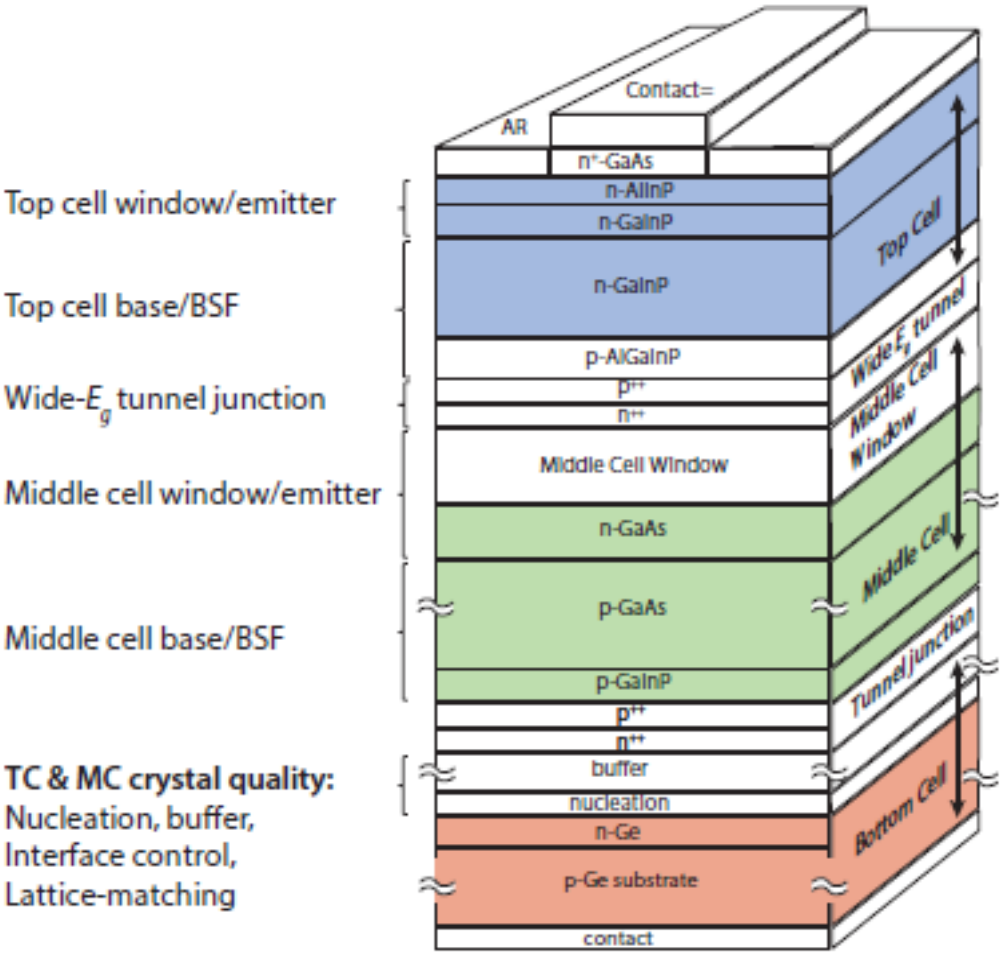

Figure 2.7**:** Illustrating a typical III-V triple junction solar cell [50].

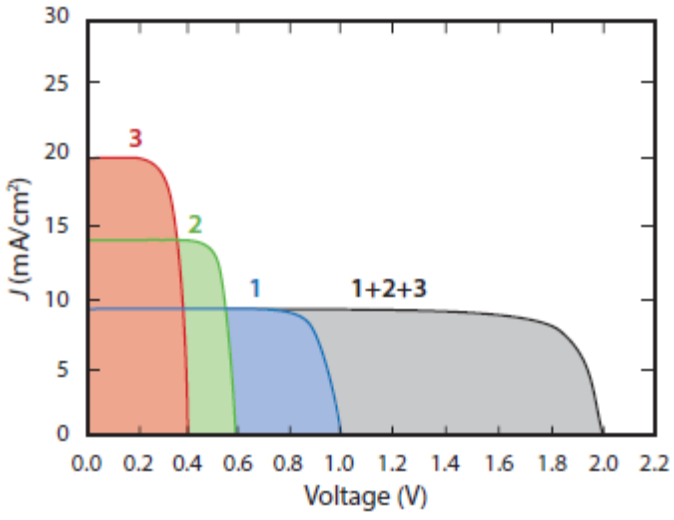

Figure 2.8**:** The J-V curves of the three junctions used in the III-V triple junction cell and J-V curves of the III-V triple junction cell (1+2+3) [50].

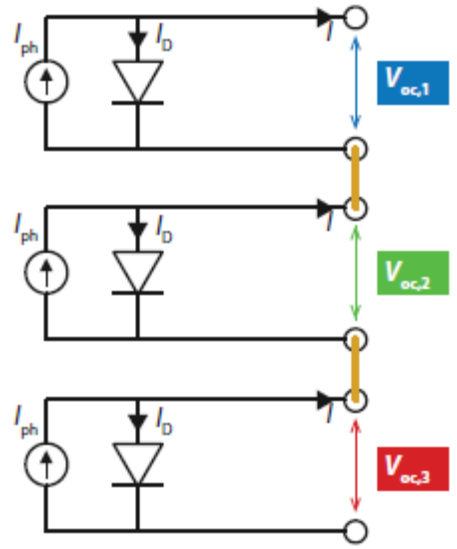

Figure 2.9**:** The equivalent circuit of the three junctions connected in series [50].

Let now take a closer look on how a multi-junction solar cell works. Light will enter the device from the top. As the spectral part with the most energetic photons like blue light has the smallest penetration depth in materials, the junction with the highest band gap always acts as the top cell. On the other hand, as the near infrared light outside the visible spectrum has the longest penetration depth, the bottom cell is the cell with the lowest band gap [50].

Figure 2.8 shows the J-V curve of the three single p-n junctions. We observe p-n junction 1 (GaInP) has the highest open circuit voltage and the lowest short circuit current density, which means that this p-n junction has the highest band gap (1.9 eV). In contrast, p-n junction 3 (Ge) has a low open circuit voltage and a high current density; consequently it has the lowest band gap (0.67 eV). p-n junction 2 (GaAs) has a band gap in between (1.42 eV). Hence, if we are designing a triple-junction cell out of these three junctions, junction 1 will act as the top cell, junction 2 will act as the middle cell and junction 3 will act as the bottom cell.

For understanding how the J-V curve of the triple junction looks like, we take a look at the equivalent circuit. Every p-n junction in the multi-junction cell can be represented by the circuit of a single-junction cell, as discussed in chapter 1. As the three junctions are stacked onto each other, they are connected to each other in series, as illustrated in Figure 2.9. In a series connection, the voltages of the individual cell add up in the triple junction cell. Further, the current density in a series connection is equal over the entire solar cell; hence the current density is determined by the p-n junction generating the lowest current. The resulting J-V curve is also illustrated in Figure 2.8. We see that the voltages add up and the current is determined by the cell delivering the lowest current [50].

Multi-junction solar cells (MJSC) split the solar spectrum into different bands that are then converted into electricity by optimized sub-cells. Such partitioning is shown in Figure 2.10 for three classic solar cell designs used at some point in CPV systems GaAs single junction; GaInP/GaAs dual-junction; and GaInP/GaAs/Ge triple-junction solar cells.

Figure 2.10 illustrates the two aspects in which MJSCs outperform single junction solar cell devices. First, despite the fact that a single junction GaAs solar cell (Figure 2.10 left) and a dual-junction GaInP/GaAs solar cell (Figure 2.10 center) use the same fraction of the AM1.5d solar spectrum, an increase in efficiency is observed in the latter by a gain in Voc attributable to the high bandgap top cell. In other words, the fraction of the spectrum absorbed by the GaInP top cell in the dual-junction design is transformed into electricity with lower thermalization losses compared to the GaAs single junction solar cell. Second, in the transition from a dual GaInP/GaAs (Figure 2.10 center) to a triple GaInP/GaAs/Ge (Figure 2.10 right) solar cell it is the new spectral band accessible by the Ge bottom cell that is responsible for the efficiency increase. The Ge sub-cells increases the *Voc* without affecting the current of the multi-junction cell. By itself, Ge would have high thermalization losses and a relatively low efficiency. In summary, the use of several bandgaps offers the possibility of reduced thermalization losses and/or access to wider portions of the solar spectrum [51].

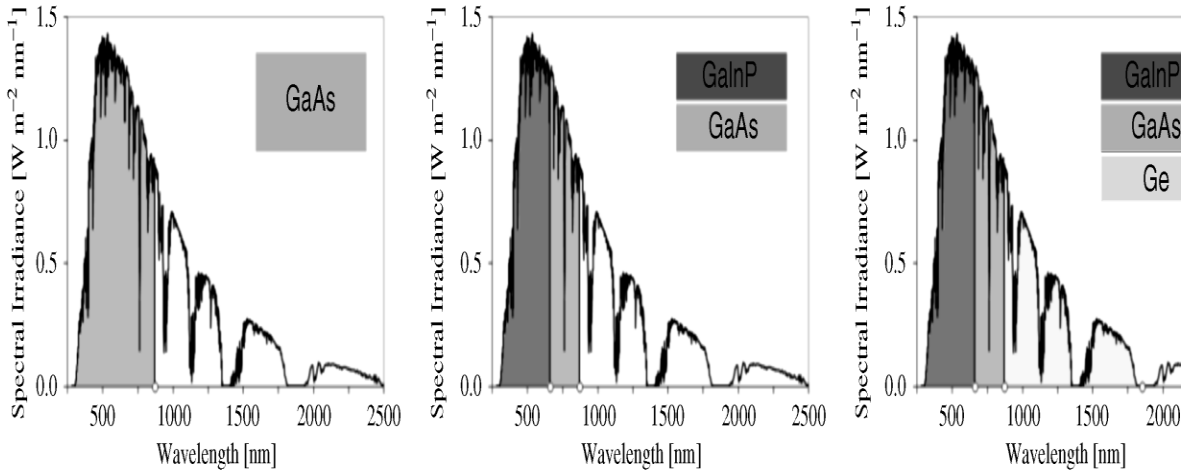

Figure 2.10: Examples of how spectrum is used by different solar cells: (left) Single junction GaAs solar cell; (center) Dual-junction GaInP/GaAs solar cell; (right) Triple junction GaInP/GaAs/Ge solar cell [51]

The single crystal Ge wafer serves as the starting substrate for the growth of the GaAs and GaInP upper sub-cells. The most common growth method is metal organic chemical vapor deposition (MOCVD) and certainly the most relevant for mass production, but molecular beam epitaxy is also used [52]. The junction in the Ge wafer is usually formed during the initial stages of the deposition process. The main advantage of Ge is that it is closely lattice matched to the GaAs and GaInP sub-cells (see Figure 2.11). This lattice matching helps to ensure the growth of relatively perfect GaAs and GaInP sub-cells . The band gap of Ge, however, is too low to yield the optimum 3-junction efficiency with GaAs and GaInP. Nevertheless, it does boost the Voc of the device [53].

III.2.3 Multi-junction Solar Cells Concept

Bandgap and lattice matching are central to multi-junction solar cell designs. But to maximize the efficiency of multi-junction devices, other characteristics are also desirable. Foremost of these for a monolithic, series-connected, two-terminal multi-junction device is that each of the sub-cells should have matched currents. That is, they should absorb photons at the same overall rate, thus producing the same current.

III.2.3.1 Bandgaps versus Lattice Constants

A semiconductor material has many types of properties, but the most relevant considerations in the design of an efficient MJ solar cell are the energy gap and the lattice constant. The energy gap is equivalent to the energy that is necessary to free a bond electron in the crystal, thereby creating a hole in the valence band and an electron in the conduction band. In this case, it corresponds to the minimum energy of the photon to be absorbed for the semiconductor material. The lattice constant is the physical dimension of the unit cell in the crystal lattice of the semiconductor. The ideal situation should be that the different materials of multilayer semiconductor devices have the same lattice constant, or at least as close as possible, to avoid dislocations and decrease the number of defects and thermal, mechanical, and electrical stresses that can act as recombination centers [54].

Realizing III–V multi-junction solar cells with an optimal band-gap combination can be a challenging task. To understand the problems it is important to note that each (III–V) semiconductor is characterized by a band gap as well as a characteristic lattice constant. The band-gap combination of the most common GaInP–GaAs–Ge triple-junction solar cell is indicated as an example. As all materials in this structure nearly have the same lattice constant (see Figure 2.11), the approach is called lattice matched. In contrast to this devices with material combinations that are not lattice matched to each other are called lattice mismatched or metamorphic.

Figure 2.11 shows the energy gap versus lattice constant for several elements and alloy materials which are important for III–V solar cells. Lines between different materials represent semiconductors that can be created by combining different amounts of the two materials. Ge, GaAs and InGaP have roughly the same lattice constant with different bandgaps, which facilitates achieving good material quality, and compositions of these materials are currently used to create high-efficiency triple-junction cells.

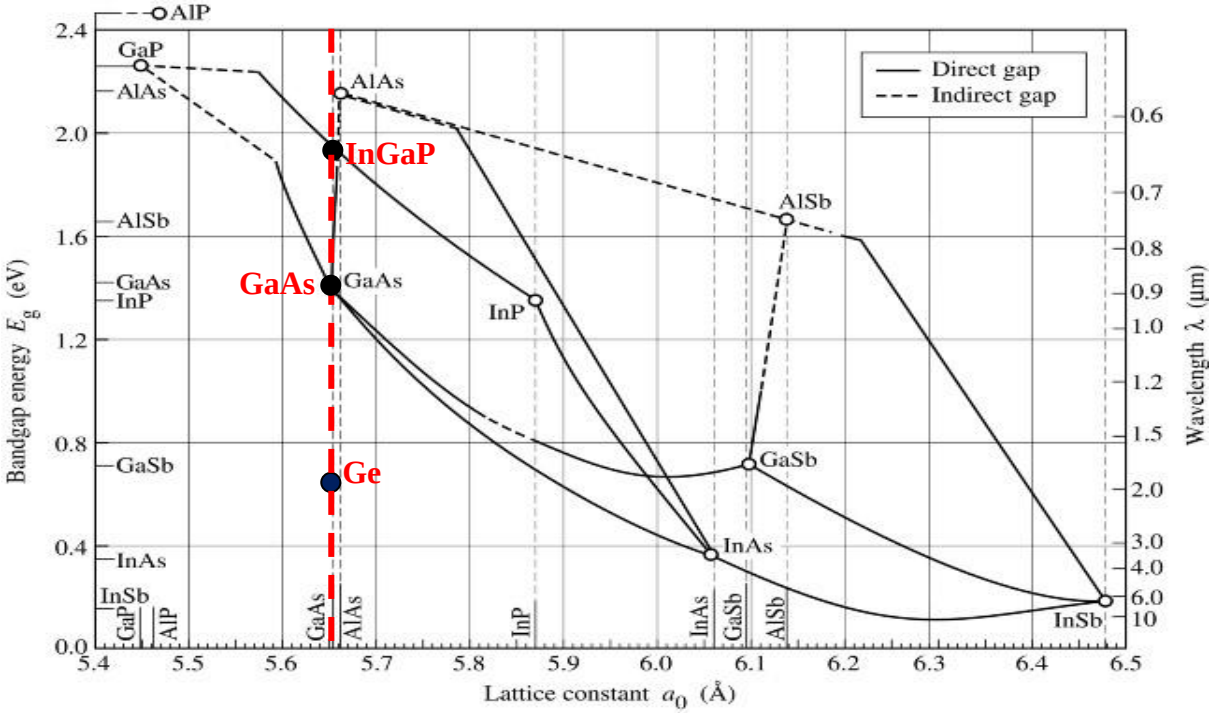

Figure 2.11: Bandgap energy and lattice constant of various III—V semiconductors at room temperature (adopted from Tien, 1988) [55].

III.2.3.2 Current Matching

The serial architecture of monolithically-grown multi-junction solar cells makes matching of currents a desirable characteristic [56]. The ideal situation is when all of the sub-cells generate the same light-generated current. However, the total output current of the multi-junction solar cell is limited to the smallest of the currents produced by any of the individual junctions because the sub-cells are connected in series. The total device voltage is the sum of the voltage of each sub-cell. If this is the case, the currents through each of the sub-cells are constrained to have the same value. Absorption of the photons is determined by the energy gap of the semiconductor material alloy and its absorption coefficient. The latter parameter indicates how far into material photons of a specific energy can penetrate before they are absorbed by the material [57].

The current produced by a semiconductor junction depends on a number of factors, but most notably, the number of incident photons exceeding the semiconductor's bandgap, and the absorption constant of the material. A layer must be made thinner if the photons that exceed the bandgap are in abundance. At the same time, a layer with a low absorption constant must be made thicker, since on average a photon must pass through more of the material before being absorbed, after materials are selected with desired bandgaps and lattice constants, the thickness of each layer must be determined based on the material's absorption constant and the number of incident photons with a given energy, so that each layer will generate the same photocurrent [56].

III.2.3.3 Keys to High Efficiency Multi-Junction Solar Cells

The most important keys to highly efficient MJ solar cells are the abilities to match the current of all junctions at the optimal working condition and match the lattice constant of all epitaxial layers to the substrate to achieve high crystalline quality. These two requirements place strict limits on the possible choice of epitaxial materials and substrates used for the devices.

The current matching condition puts a constraint on the choice of the sub-cells bandgaps. From Figure 2.8, it can be seen that each of the three sub-cells can produce a certain current that is directly related to the number of photons absorbed. These sub-cells have to work under the same current since they are connected in series. This current usually limited by the lowest current produced by the sub-cells if they were to work independently. In order to achieve the highest possible energy conversion efficiency, all the sub-cells have to produce the same current at their optimum working conditions. Therefore, the current matched bandgaps have to partition the solar spectrum into almost equal parts in terms of photon numbers. And the current matched bandgaps change as the solar spectrum (air mass condition) varies. It should be noted that the current matched bandgaps also change with solar concentration. This is because the optimum working current for each sub-cells does not increase exactly linearly with solar concentration due to various competing recombination mechanisms. Usually, many different sets of current matched bandgaps exist and a set of optimum bandgaps can be found to give the highest conversion efficiency.

After the optimum bandgaps of an N-junction solar cell are determined, the desirable materials with the right bandgap need to be identified. These materials are usually grown on single crystal substrates by various epitaxial techniques. In order to get high quality epitaxial materials, the material lattice constant should be the same or close to the substrate lattice constant, which is therefore called the "lattice-matching condition". This condition puts a very strict restriction on the possible materials that can be used for MJ solar cells monolithically grown for a particular substrate. There are several common semiconductor substrates such as Si, Ge, GaAs, InP, InAs and GaSb, each with a different lattice constant [58]. Figure 2.11 shows the energy bandgaps of various alloys as a function of lattice constant. As can be seen, for each of the substrates, there exists a few binary or ternary materials with the same lattice constant. This means if a substrate is chosen, only a few different materials with certain bandgaps can be found to be lattice-matched to the substrate. But usually these bandgaps can hardly meet the current matching condition described previously. And it will be even more difficult to reach the optimum bandgaps selected from all the possible current matched designs. Therefore, it is usually very challenging to meet both the current matching and lattice matching conditions simultaneously in a real MJ solar cell design. And a practical design is usually a compromise between these two conditions.

Moreover, tunnel junctions are necessary to connect adjacent sub-cells. The key to make a good tunnel junction is the high doping of both n- and p-type regions, which is not trivial at times. Furthermore, good window layer not only has to meet lattice matching condition but also requires large bandgap. And good anti-reflection coating is also important, which has to work for a much broader spectrum range than the coating for single junction solar cells [59].

III.2.4 State-Of-The-Art Multi-Junction Solar Cells

The III-V compound multi-junction solar-cells are developing in a very quick velocity, the world record efficiency is continuously updated in recent years. This section will briefly introduce the state-of-the-art triple-junction III-V compound solar-cells right now by three main categories. The three types of triple junction solar cells are current-matched, metamorphic, and inverted metamorphic. The traditional is the current-matched, where materials are chosen based on matching the lattice constants to reduce crystal defect during production. For the metamorphic and inverted metamorphic, there is a buffer layer that gradually changes the lattice constant. This transition layer is found between the bottom and middle sub-cell, while the top and middle is still lattice matched. This allows for tunability, reducing the thermalization losses. This also changes the bottom sub-cells to a lower bandgap to reduce the transmission losses.

III.2.4.1 Lattice-matched (LM) Configuration

One of the main problems of the MJ solar cell is related to the various lattice constants of the semiconductor alloy material of each layer and the need to grow an MJ solar cell when several materials with different lattice constants are necessary to obtain the highest overall device efficiency. If the materials of the separate p–n junctions have the same lattice constant, which facilitates achieving good material quality, and then it is easier to grow the MJ solar cell.

In this approach, the cells are called lattice-matched (LM) cells. Here a single substrate is used to grow all the materials for the different sub-cells. The main disadvantage of this strategy is that the materials with different band-gaps selected for the sub-cells should have the same, or a very close, lattice constant. This constraint decreases maximum efficiency because it is not possible to select the best materials for each sub-cells in terms of band-gap, to maximize material quality the choice of bandgaps is limited to lattice matched materials. As a consequence, bandgap combinations are relatively far from the target of optimum values. This is the case of the mainstream triple-junction GaInP/GaAs/Ge design. Advantages of this design include reduced cost and demonstrated long term reliability resulting from its simplicity and lack of defects [60], but the drawback of this lattice matched design is that current matching condition is not achieved. The Ge bottom cell can produce large current mismatch of the current between the Ge bottom cell and the top two cells. Therefore, various approaches try to overcome the strong current mismatch by increasing the absorption in the upper two cells or by integrating an additional junction between the GaAs and the Ge sub-cells.

III.2.4.2 Metamorphic (MM) Configuration

One approach to increase the number of possible semiconductor materials that can be selected is to use materials with different lattice constants but with thin layers to decrease the stress in the structure. These solar cells are called metamorphic-mismatched (MM) cells. This option increases the list of possible materials that can be used, but it still limits the flexibility to select the

best materials for the sub-cells. This problem is critical when four or more different materials with several lattice constants are necessary to create an MJ solar cell. Here a single substrate is also used to grow all the materials for the different sub-cells. However, in this case a certain lattice mismatch is allowed in the quest to approach the optimum bandgaps. Advantages of this design include potentially higher efficiencies than lattice matched and moderate costs. [61].

One way to address the large current mismatch between the Ge bottom cell and the two upper junctions is to lower the band gap energies of the two top sub-cells. This can be accomplished by adding indium to both sub-cells. The addition of indium (In) to both sub-cells increases their respective lattice constants relative to that of Ge and the monolithic combination of these lattice-mismatched materials is commonly called a metamorphic structure.

In theory, the efficiency of this device should increase monotonically with indium (In) concentration up to the point where the top two sub-cells are current matched to the Ge bottom cell. In practice, however, this has not happened. The lattice mismatch between the Ge sub-cells and the GaInP and GaInAs sub-cells causes dislocations to form during the growth process. These dislocations degrade the minority carrier lifetime in the GaInAs and GaInP sub-cells and reduce the efficiency of the multi-junction device [62].

III.2.4.3 Inverted Metamorphic (IMM) Configuration

There is another device structure called inverted-metamorphic (IMM). The basic idea of the inverted metamorphic concept (IMM) is to avoid some of the lattice mismatch problems by growing the multi-junction solar cell upside down (or inverted). In this case, the epitaxial structure is grown inverted order to the conventional growth direction on a suitable substrate starting with the top sub-cells. Later, the original growth substrate is removed, and the front metallic contact is deposited on the top layer [63].

As sketched in Figure 2.12, the growth sequence starts with the growth of the top or high band gap cell followed by the cell with the next lower band gap. By growing the top cell first, followed by the middle cell, the electronic quality of the top and middle sub-cells , being lattice matched to the substrate, is preserved and relatively unaffected by the subsequent growth of the bottom cell. Usually the growth of the bottom sub-cells is preceded by the growth of a transparent buffer layer to transition the lattice constant from the GaAs substrate to that of the bottom sub-cells. With this, lattice defects created in the buffer layer can only degrade the bottom cell.

The first two sub-cells can hence be grown lattice matched to the GaAs or Ge substrate. A metamorphic buffer gradually increases the lattice constant for the sub-cells that is grown last. Afterward, the substrate of the top cell is removed using liftoff techniques. Finally, the epitaxial structure is processed to solar cells.

A drawback for the IMM approach compared to Ge-based structures is the higher complexity of cell processing connected with substrate removal, which may lead to higher production costs and low yield. Yet these disadvantages might be counterbalanced by lower material costs if the substrate can be reused. Another benefit of the IMM structure in particular for space application is their possible lower weight and the chance to realize flexible devices.

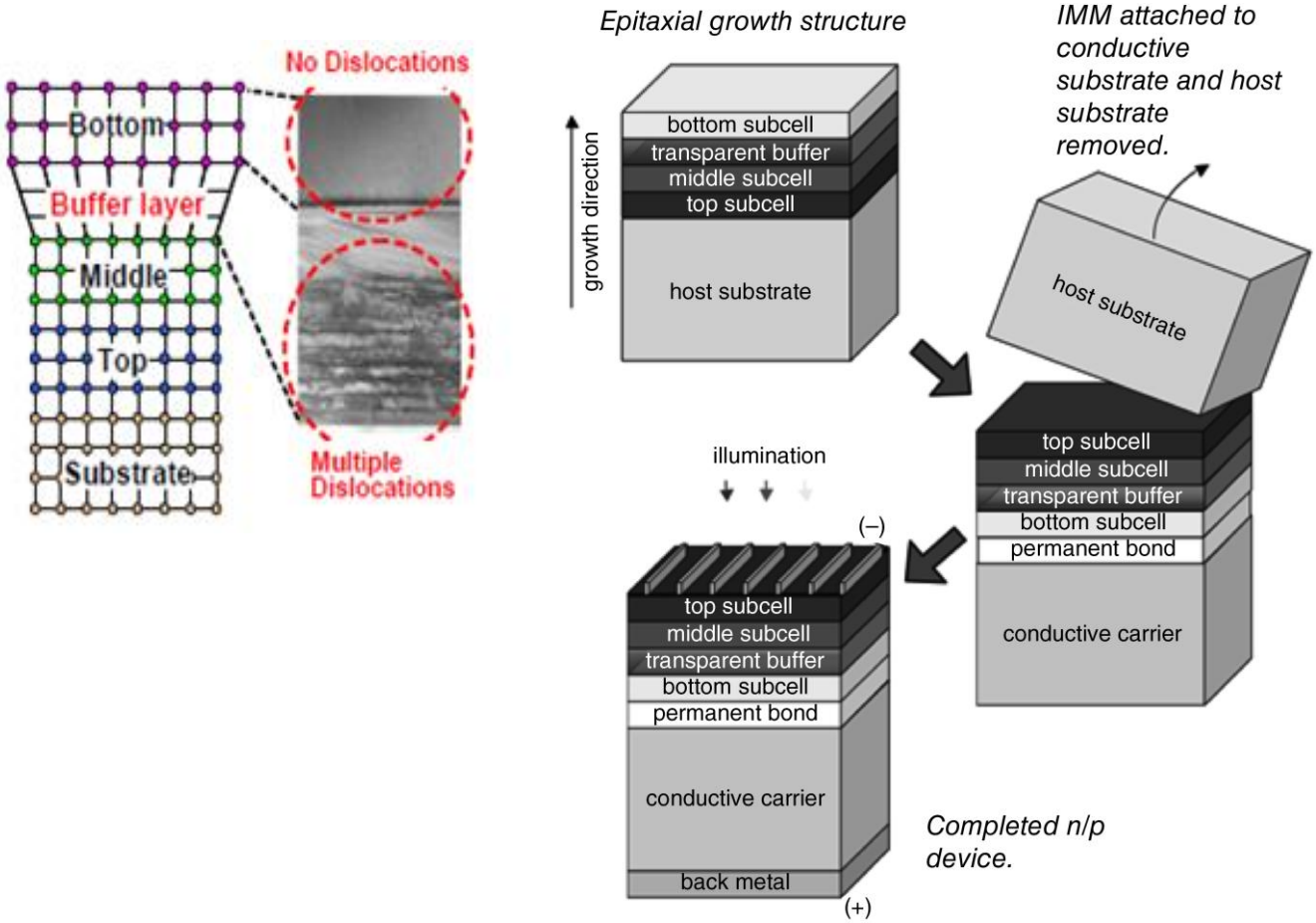

Figure 2.12: Scheme of the production process of IMM solar cells [51]

III.2.4.3.1 Inverted Metamorphic (IMM) InGaP/GaAs/InGaAs

III.2.4.3.1.1 Optimization of the Band Gap

In the present structure using a Ge bottom cell as Lattice-matched InGaP/InGaAs/Ge, combination of the band gap is not optimal. Too much current generated in the bottom cell is wasted due to the series connection as shown in Figure 2.8. There are two main approaches to attaining current balance and improving efficiency as shown in Figure 2.13. One way is reducing the band gap of both the top and middle cells. Combining the InGaP top (1.7 eV), InGaAs middle (1.2 eV), and Ge bottom (0.65 eV) is thought to be optimal. This lattice mismatch configuration is called a metamorphic (MM) structure. In the MM structure, short-circuit current is expected to be improved compared to that of the present structure. The other way is increasing the band gap energy of the bottom cell for achieving a current matched triple junction. One way to do this is to replace the Ge with a 1-eV $Ga_{0.7}In_{0.3}As$ bottom cell [64]. Adding a 1-eV solar cell can boost the device efficiency but only if the electronic quality of it and the other two junctions remain high. An optimal combination of band gaps is obtained by changing the bottom cell from Ge to InGaAs (1.0-0.97 eV) with a lattice mismatch of about 2% larger than that of GaAs and is the biggest impediment to achieving high efficiency. This is called an inverted metamorphic (IMM) structure. In the IMM structure, the Voc is expected to be improved over that of the present structure. On the other hand, in the new structure using an InGaAs bottom cell with a band gap of 0.97 eV, generated currents in the top, middle, and bottom cells are well balanced. By changing the bottom cell from Ge (0.67 eV) to InGaAs (0.97 eV), the Voc is improved without reducing short-circuit current, as shown in Figure 2.15 [65].

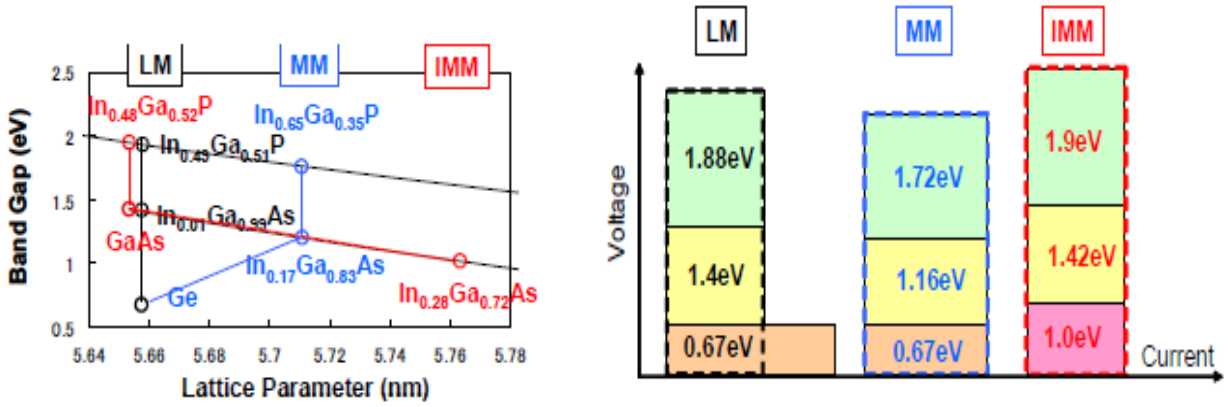

Figure 2.13: Combination of band-gaps and lattice parameters for three types of triple junction cell. Voltage and current for sub-cells are also shown [65].

III.2.4.3.1.2 Cell Fabrication Process for the IMM Structure

The fabrication process of a cell with the IMM structure is shown in Figure 2.14. Solar cell layers are grown using the MOCVD method on a GaAs substrate. InGaP top and GaAs middle cell layers that are lattice matched to the substrate are grown first and then a lattice mismatched InGaAs bottom cell is grown by inverting the order. As a result, good crystal quality is attained in at least the top and middle cells. The structure and growth condition of a buffer layer between the middle and bottom cells is optimized to avoid introducing any threading dislocations in the bottom cell. After the growth of the cell layers, they are separated from the substrate, flipped over, and mounted to a handling substrate. In this present process, the GaAs substrate used for epitaxial growth is removed using an etching process. In the MOCVD growth process, the method for growing the buffer layer has the greatest import on attaining high performance for the lattice-mismatched InGaAs bottom cell. After the growth of a step-graded buffer layer in which the lattice parameter of InGaAs is increased and a relatively thick over-shutting layer is grown, an InGaAs bottom cell layer with 2% lattice mismatching is grown. To attain a high Voc, threading dislocations should be confined in the buffer layer. Generation of misfit dislocations in the bottom cell is not avoidable, but threading dislocations are not acceptable [65].

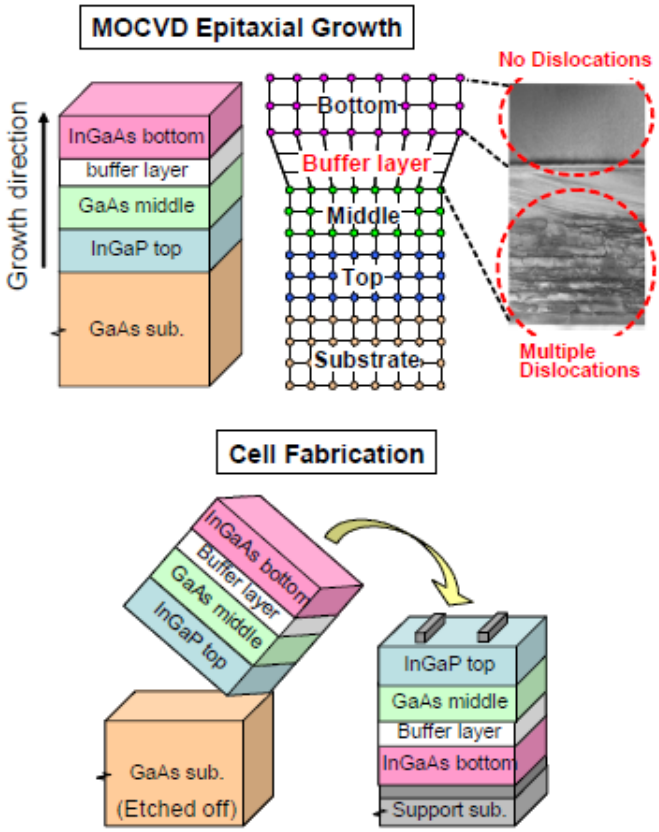

Figure 2.14: Cell fabrication by Inverted layers transfer process [65].

III.2.4.3.1.3 Characteristics of an IMM Triple-Junction Cell

Figure 2.15 shows comparison of (a) IV curve and (b) spectral response for the present triple-junction cell with a Ge bottom cell and the new triple-junction cell using a 0.97-eV InGaAs bottom cell. For the new structure, the absorption edge of the bottom cell is shifted to a shorter wavelength region and a current balance among three sub-cells is obtained. No change in Isc and an increase in Voc are confirmed.

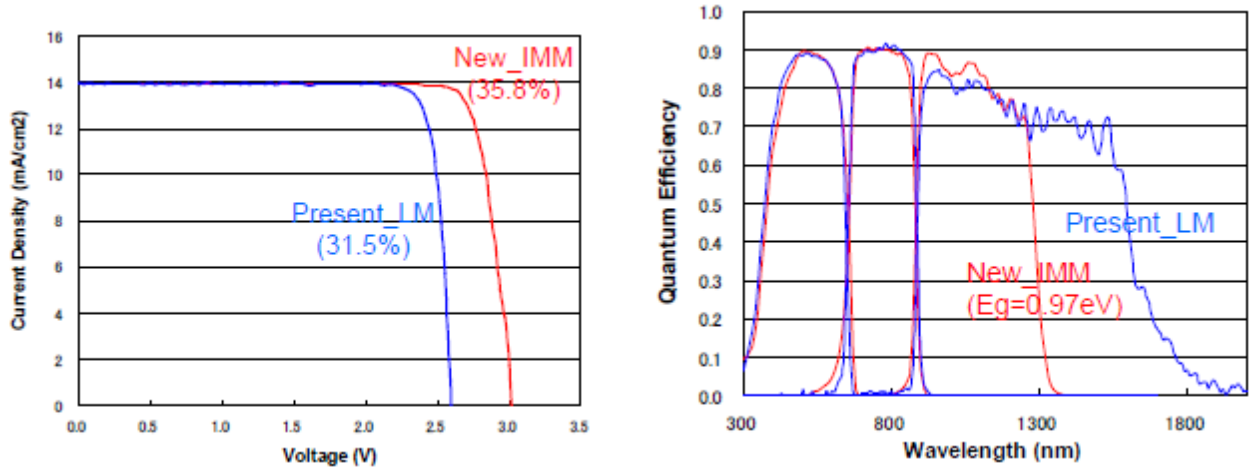

(a) IV curve (b) spectral response

Figure 2.15: Comparison of IV curve and spectral response for new triple junction cell with inverted metamorphic (IMM) structure and the present cell with lattice-matched (LM) structure [65]

III.2.4.4 Description of Different Cell Approaches

Multi-junction solar cells implement high-efficiency photovoltaic devices by incorporating materials with different bandgaps trying to get, as close as possible, to the optimum combinations. In the race to reach a higher number of junctions with the appropriate bandgaps, many materials, device configurations and manufacturing approaches have been explored. To further increase the efficiency of III-V multi-junction solar cells, various approaches are currently being investigated by research groups around the world will be discussed in this section.

III.2.4.4.1 Design Optimization of the Existing Layers

The efficiency of the present-day triple-junction solar cell can be improved by design optimization of each sub-cell. In the past, triple-junction cell efficiency has been improved by using disordered GaInP instead of ordered as top cell material: disordered GaInP has the higher bandgap than ordered (1.9 eV). An alternative to GaInP - top layer, $Al_{0.37}Ga_{0.63}As$ or AlGaInP with the bandgap of 1.98 eV can be used, which has the similar lattice constant and bandgap energy. In the past, the drawback of this approach was a high sensitivity of these materials to oxygen and water contamination, but recent results are promising [66, 67]. The efficiency can be increased by replacing the GaAs layer with a 1.25eV-bandgap material: this second layer could collect a larger current while reducing the number of photons transmitted to the Ge layer [68, 69].

III.2.4.4.2 Increasing the Number of Junctions

Another possible design improvement is to progress to devices with more than three junctions. Four-junction solar cells have been suggested using a material with a bandgap of 1.0 eV [70]. For this purpose, GaInNAs is considered as the most studied and it can be grown lattice - matched to Ge. Five- and six-junction cell designs partition the solar spectrum into narrower wavelength ranges than triple-junction cells that allow all the sub-cells to be better current matched to the low-current- producing sub-cells [71, 72].

III.2.4.4.3 III-Vs on Silicon

Multi-junction solar cells based on a silicon bottom junction are very attractive due to the relatively low cost of silicon substrates. Since the early 90s research efforts have been ongoing to grow III–V solar cells on silicon substrates (1.1 eV) [73]. The interest in this field has increased in recent years in order to replace the expensive Ge substrate of today's lattice-matched triple-junction solar cells with lower-cost Si. Moreover, the higher band gap of Si compared with Ge leads to an increase of the theoretical energy-harvesting efficiency by 3% [74]. The main challenges here are to overcome the 4.1% difference in lattice constant between Si and GaAs and to handle the difference in thermal expansion coefficient. As it is extremely challenging to achieve good material quality for direct GaAs growth on Si, different buffer layers are investigated to increase the lattice constant gently [75, 76]. Figure 2.16 shows the III-Vs on Silicon approach.

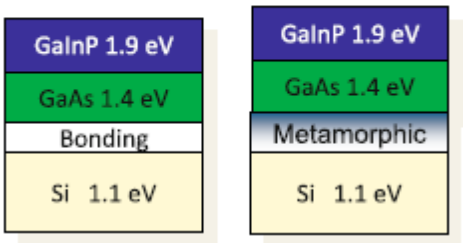

Figure 2.16: Schematic illustration of the III-V solar cell on Si concept

III.2.4.4.4 Quantum Dot and Quantum Well Multi-Junction Solar Cells

In recent years it has been proposed and experimentally verified that the use of nanostructures, such as quantum wells, quantum dots, quantum wires, offer the potential for high photovoltaic efficiency by tailoring the properties of existing materials, and for reducing of cost using self-assembling of nanostructures [77, 78]. Solar cells composed of quantum wells (QW) or quantum dots (QD) have attracted much attention over the last two decades. Much of the attention has been directed towards achieving higher efficiencies for single junction cells such as the intermediate band solar cell [79, 80]. But another use is to alter or engineer the effective band gap of a solar cell absorber by inserting quantum wells or dots [81, 82]. For example, it is possible to lower the effective band gap or absorption threshold of a silicon solar cell by introducing Ge quantum dots or that of GaAs by introducing InAs dots [83]. This approach has been applied extensively to modify the middle GaAs sub-cells of a multi-junction cell [84]. By introducing InAs or GaInAs quantum dots or quantum wells one can lower the effective band edge and increase the middle cell photocurrent. Theoretical calculations showed that an overall gain in energy harvesting efficiency between 3% and 9% relative to the lattice-matched triple-junction solar cell is possible [85].

III.2.4.4.5 Concentrator Photovoltaic

Multi-junction solar cells are very expensive and firstly they were used only in space applications. Concentration of sunlight made these cells economically viable for the use on Earth. The key elements of a photovoltaic concentrator are low-cost concentrating optics (a system of lenses or reflectors) to focus sunlight on a small area of solar cells, mounting, single or dual-axis tracking to improve performance of the system, and high-efficiency solar cells. If the concentration factor is very high, then the cost of the solar cell is only a small part of system cost and therefore the cost of the cell is justified. Concentrator operation well suited for multi-junction photovoltaic cells also because increasing the concentration ratio improves the performance of the photovoltaic cells even more [86, 87].

Figure 2.17 compares theoretical and realized energy efficiencies for single junction and multi-junction solar cells, under 1-sun and concentrated sunlight as a function of the number of junction. Multi-junction solar cells have the potential for achieving ultra-high conversion efficiencies of over 50%, and are promising for both space and terrestrial applications due to their wide photoresponse [88].

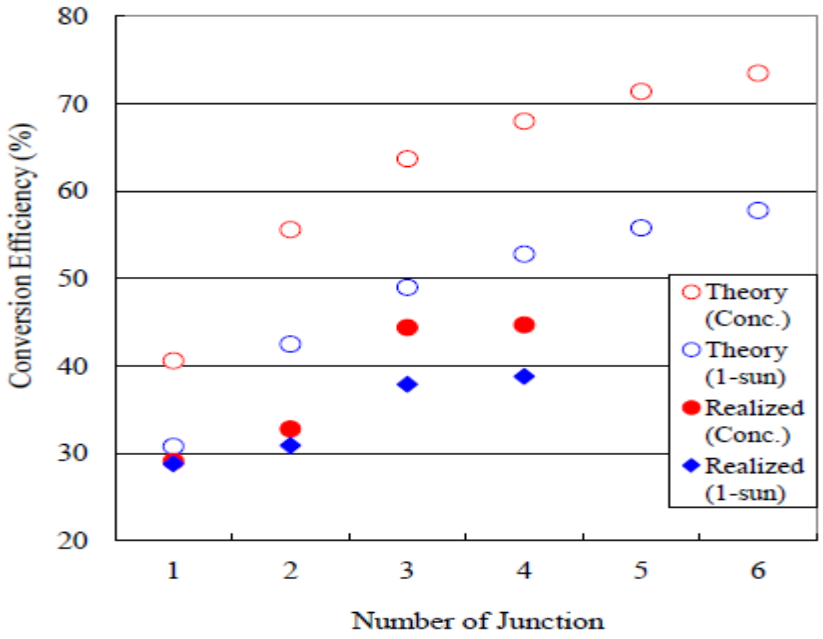

Figure 2.17: Theoretical conversion efficiencies of single-junction and multi-junction solar cells in comparison with experimentally realized efficiencies for 1 Sun intensity and under concentration [88].

Table 2.2 shows theoretical conversion efficiencies of MJ solar cells at 1-sun and under concentration in ideal case. As shown in Table 4, 3-5 compound Multi-Junction (MJ) and concentrator solar cells have great potential of more than 50% [89].

Table 2.2: Theoretical efficiencies of multi-junction solar cells in ideal case

Number of junction	Conversion efficiency under 1-sun	Conversion efficiency under concentrator
1	30.8%	40.8%
2	42.9%	55.7%
3	49.3%	63.8%
4	68.2%	86.8%

III.2.5 Key Issues for Super High-Efficiency MJ Solar Cells

Multi-junction cells with different bandgaps are stacked in tandem so that the cells cover a wide wavelength region from 300 nmto 1800 nm. Cell materials are selected by choosing bandgap energies close to the optimal bandgap energy combination found from theoretical efficiency calculations, and by considering lattice matching to substrates and reducing impurity problems. Table 2.3 shows key issues for realizing super-high efficiency MJ solar cells. The key issues for realizing super- high-efficiency MJ solar cells are 1. Sub-cell material selection, 2. Tunnel junction for sub cell interconnection, 3. Lattice-matching, 4. Carrier confinement, 5. photon confinement, 6. Anti-reflection in wide wavelength region and so forth. For concentrator applications by using MJ cells, the cell contact grid structure should be designed in order to reduce the energy loss due to series resistance, and tunnel junction with high tunnel peak current density is necessary. Because cell interconnection of sub-cells is one of the most important key issues for realizing high-efficiency MJ solar cells [88].

Table 2.3: Key issues for realizing super-high-efficiency multi-junction solar cells [88]

Key issue	Past	Present	Future
Top cell materials	AlGaAs	InGaP	AlInGaP
The 3rd cell materials	None	Ge	InGaAsN etc.
Bottom cell materials	GaAs	Ge	Si, Ge, InGaAs
Substrate	GaAs	Ge	Si, Ge, GaAs, metal
Tunnel junction	DH-structure GaAs tunnel junction (TJ)	DH-structure InGaP TJ.	DH-structure InGaP or GaAs TJ
Lattice matching	GaAs middle cell	InGaAs middle cell	(In)GaAs middle cell
Carrier confinement	InGaP-BSF	AlInP-BSF	Wide-gap-BSF Quantum dots (QDs)
Photon confinement	None	None	Back reflector Bragg reflector, QDs, etc.
Others	None	Inverted epitaxial growth (epitaxial growth from top cell to bottom cell layers on substrate)	Inverted epitaxial growth, epitaxial lift off (Peeled thin film off technique)

Conclusion

While single-junction solar cells may be capable of attaining AM1.5 efficiencies of up to 29%, III-V multi-junction solar cells appear capable of realistic efficiencies of up to 50% and are promising for space and terrestrial applications because of their high conversion efficiency and better radiation-resistance. This chapter has shown how III-V multi-junction solar cells are able to achieve high efficiency. The great choice of III-V semiconductor materials with different alloys allows various design options. The rise of multi-junction solar technology required years of research to open up access to the lattice constant-bandgap map, to improve the quality of the important materials, and manufacturing complexity will finally determine the most successful approaches for achieving optimum performance. Promising research avenues are in nanotechnology, wafer bonding, and lattice mismatch growth, while others remain to be explored in the future. A great deal of attention has been given to theoretical efficiency calculations of novel types of solar cells, and now work on materials and processing methods is needed to fulfill these promises. A great deal of work in the materials area remains before solar cell performance can begin to approach theoretical limits.

III-V Multi-junction solar cells are the most efficient of all. The search for higher-efficiency solar cells continues. Future increases in performance are likely, III-V multi-junction solar cells have already reached efficiencies above 40% and a further increase toward 50% can be expected. These cells are needed to reduce the size and mass for satellite power systems and to provide cost-competitive terrestrial power in concentrator systems. Triple-junction solar cells based on III-V semiconductors as the InGaP/GaAs/Ge cell will be widely used because this system has already been developed. Simulations of III-V Single-junction and monolithically and mechanically stacked multi-junction solar cells are central to this thesis and will be discussed in detail in chapter 3 and chapter 4 respectively.

References

[1] https://www.solarvis.energy/advantages-and-disadvantages-of-solar-photovoltaic/
[2] M. D. Archer, "The Past and Present," in Clean Electricity from Photovoltaics, edited by M. D. Archer and R. Hill, Ch.1, pp. 1-31, Imperial College Press, 2001.
[3] D. M. Chapin, C. S. Fuller and G. O. Pearson, "A New Silicon p-n Junction Photocell for Converting Solar Radiation into Electrical Power," Journal of Applied Physics, vol. 25, pp. 676-677, 1954.
[4] W. Shockley and H. J. Queisser, "Detailed balance limit of efficiency of p-n junction solar cells," *Journal of Applied Physics*, vol. 32, pp. 510–519, 1961.
[5] Green MA, et al. Solar cell efficiency tables (version 51). Prog Photovolt Res Appl; 26:3–12, 2018.
[6] Antonio Luque and Steven Hegedus. Handbook of photovoltaic science and engineering, 2003.
[7] M. Wolf, Limitations and possibilities for improvement of photovoltaic solar energy converters, Proc. Inst. Radio Engineers, vol. 48, 1960.
[8] J. M. Olson et al, *Appl. Phys. Lett.* **56**, 623, 1990.
[9] T. Takamoto et al, *Appl. Phys. Lett.* **70**, 381, 1997.
[10] M. A. Green et al, *Prog. Photovolt. Res. Appl.* **13**, 387, 2005.
[11] M. A. Green, K. Emery, Y. Hishikawa, W. Warta, and E. D. Dunlop, "Solar Cell Efficiency Tables (Version 45)," Progress In Photovoltaics: Research And Applications, vol. 23, pp. 1–9, 2015.
[12] Fraunhofer ISE, "New world record for solar cell efficiency at 46% French-German cooperation confirms competitive advantage of European Photovoltaic inductry." http://www.ise.fraunhofer.de/en/pressand- media/press-releases/press-releases-2014/new-world-record-forsolar- cell-efficiency-at-46-percent, December 2014.
[13] R. R. King et al, *Proc. 4th International Conference on Solar Concentrator*, El Escorial, 2007.
[14] R. R. King et al, *Appl. Phys. Lett.* **90**, 183516, 2007.
[15] F. Dimroth, et al, "Four-junction waferbonded concentrator solar cells," *IEEE Journal of Photovoltaics*, vol. 6, no. 1, pp. 343–349, Jan 2016.
[16] P. T. Chiu, et al, "35.8% space and 38.8% terrestrial 5J direct bonded cells," in 40th IEEE Photovoltaic Specialist Conference, Denver, CO, pp. 0011–0013, Jun 2014.
[17] F. Dimroth. 3-6 junction photovoltaic cells for space and terrestrial applications, Photovoltaic Specialists Conference, 2005.
[18] https://en.wikipedia.org/wiki/Solar_cell#/media/File:PVeff(rev180425).jpg.
[19] D. A. Jenny, J. J. Loferski, and P. Rappaport, "Photovoltaic Effect in GaAs p-n Junctions and Solar Energy Conversion," Physical Review, vol. 101, pp. 1208-1209, 1956.
[20] D. M. Chapin, C. S. Fuller and G. O. Pearson, "A New Silicon p-n Junction Photocell for Converting Solar Radiation into Electrical Power," Journal of Applied Physics, vol. 25, pp. 676-677, 1954.
[21] Green MA, et al. Solar cell efficiency tables (version 51). Prog Photovolt Res Appl. ;26:3–12, 2018.
[22] Yamaguchi M, Takamoto T, Araki K, Ekins-Daukes N, Multi-junction III-V solar cells: current status and future potential. Sol Energy 79(1):78–85, 2005.

[23] King R, et al, Solar cell generations over 40% efficiency. Prog Photovolt Res Appl 20(6):801–815, 2012.

[24] K. Zweibel, Basic photovoltaic principles and methods, New York: Van Nostrand Reinhold, 1984.

[25] B. Burnett, The basic physics and design of III-V multi-junction solar cells, 2002.

[26] M. Yamaguchi, Present status of R&D super-high-efficiency III-V compound solar cells in Japan, Proc. 17th Photovoltaic European Conference, 2001.

[27] N.V.Yastrebova, "High-efficiency multi-junction solar cells : current status and future potential", 2007.

[28] D. Derkacs, R. Jones-Albertus, F. Suarez, and O. Fidaner, "Lattice-matched multi-junction solar cells employing a 1 ev GaInNAsSb bottom cell", Journal of Photonics for Energy, vol. 2, no. 1, pp. 021805{1, 2012.

[29] D.J. Friedman, J.M. Olson, S.R. Kurtz, High-efficiency III-V Multi-junction Solar Cells, John Wiley and Sons, 2011.

[30] Eduardo F, et al, "Multi-junction Concentrator Solar Cells: Analysis and Fundamentals". Chapter 2 in "High Concentrator Photovoltaics: Fundamentals, Engineering and Power Plants", Springer International Publishing Switzerland 2015.

[31] Cotal H, et al, III-V multi-junction solar cells for concentrating photovoltaics. Energy Environ Sci 2(2):174–192, 2009.

[32] Tobin S, et al, Assessment of MOCVD and MBE growth GaAs for high-efficiency solar cell applications. IEEE Trans Electron Devices 37(2):469–477, 1990.

[33] Jackrel D, et al, Dilute nitride GaInNAs and GaInNAsSb solar cells by molecular beam epitaxy. J Appl Phys 101(11):114916, 2007.

[34] Antonio L. Luque and Viacheslav M. Andreev, editors. Concentrator Photovoltaics. Springer Series in optical sciences. Springer, 2007.

[35] Wolfgang Guter and Andreas W. Bett. IV-Characterization of devices consisting of solar cells and tunnel diodes. In *IEEE 4th World Conference on Photovoltaic Energy Conversion*, pages 749–752. IEEE, 2006.

[36] Jeffrey F.Wheeldon, et al. Performance comparison of AlGaAs, GaAs and InGaP tunnel junctions for concentrated multi-junction solar cells. *Progress in Photovoltaics*, pages 442–452, Nov 2010.

[37] H. Sugiura, C. Amano, A. Yamamoto, and M. Yamaguchi. Double heterostructure GaAs tunnel junction for a AlGaAs/GaAs tandem solar-cell. *Japanese Journal Of Applied Physics Part 1-Regular Papers Brief Communications & Review Papers*, **27**(2):269–272, 1988.

[38] Gavin Conibeer, Arthur Willoughby. Solar Cell Materials: Developing Technologies, First Edition. © 2014 John Wiley & Sons, Ltd. Published 2014 by John Wiley & Sons, Ltd.

[39] D.J. Friedman, J.M. Olson, S.R. Kurtz, High-efficiency III-V Multi-junction Solar Cells, John Wiley and Sons, 2011.

[40] J.M. Olson, S.R. Kurtz, A.E. Kibbler, P. Faine, A 27.3% efficient Ga0.5In0.5P/GaAs tandem solar cell, Appl. Phys. Lett., 56 623-625, 1990.

[41] S.R. Kurtz, P. Faine, J.M. Olson, Modeling of two-junction, series-connected tandem solar cells using top-cell thickness as an adjustable parameter, J. Appl. Phys., 68 (1990) 1890-1895.

[42] Z. Deng, R.X. Wang, et al, Super transverse diffusion of minority carriers in GaxIn1−xP/GaAs double-junction tandem solar cells, Sol. Energy., 110 214-220, 2014.

[43] B.G. Streetman, S.K. Banerjee, Solid state electronic devices, Pearson Prentice Hall, 2009.

[44] T. Takamoto, E. Ikeda, H. Kurita, M. Ohmori, Over 30% efficient InGaP/GaAs tandem solar cells, Appl. Phys. Lett., 70 381-383, 1997.

[45] T. Takamoto, et al, Two-Terminal Monolithic In0.5Ga0.5P/GaAs Tandem Solar Cells with a High Conversion Efficiency of Over 30%, Jpn. J. Appl. Phys., 36 (1997) 6215-6220.

[46] J.G. Fossum, Physical operation of back-surface-field silicon solar cells, Electron Devices, IEEE Transactions on, 24 322-325, 1977.

[47] Z. Deng, R.X. Wang, J.Q. Ning, C.C. Zheng, S.J. Xu, Z. Xing, S.L. Lu, J.R. Dong, B.S. Zhang, H. Yang, Super transverse diffusion of minority carriers in GaxIn1−xP/GaAs double-junction tandem solar cells, Sol. Energy., 110 214-220, 2014.

[48] Kurtz, S.R., Faine, P. and Olson, J.M. , Modeling of two-junction, series-connected tandem solar cells using top-cell thickness as an adjustable parameter,'*Journal of Applied Physics*, 68, 1890, 1990.

[49] Mary D Archer and Martin A Green. Clean Eectricity From Photovoltaics, Second edition. © . Published by Imperial College Press, 2015.

[50] Solar Energy Fundamentals, Technology, and Systems. Edited by Klaus Jäger Olindo Isabella, Arno H.M. Smets, René A.C.M.M. van Swaaij, Miro Zeman. Copyright Delft University of Technology, 2014.

[51] Carlos Algora and Ignacio Rey-Stolle. Handbook of Concentrator Photovoltaic Technology, First Edition. © John Wiley & Sons, Ltd. Published 2016 by John Wiley & Sons, Ltd, 2016.

[52] Kurtz, S.R., Olson, J.M., Kibbler, A.E. and Asher, S. Model for incorporation of zinc in MOCVD growth of Ga0.5In0.5P. Proceedings of the 4th International Conference on Indium Phosphide and Related Materials, Newport RI, USA 21–24 April, pp. 109–112, 1992.

[53] Friedman D.J. and Olson, J.M. Analysis of Ge junctions for GaInP/GaAs/Ge three-junction solar cells. ProgressinPhotovoltaics, 9, 179–189, 2001.

[54] Washburn J, Kvam EP, Liliental-Weber Z. Defect formation in epitaxial crystal growth. J Electron Mater 20(2):155–161, (1991)

[55] E. Fred Schubert, *Light-emitting diodes*. Cambridge: Cambridge University Press, 2006.

[56] G. P. Smestad, Optoelectronics of solar cells, Bellingham, WA: SPIE Press, 2002.

[57] Simon MS, Kwok KN (2006) Physics of semiconductor devices. Wiley, New York

[58] S.-N. Wu, D. Ding, S. R. Johnson, S.-Q. Yu, and Y.-H. Zhang, "Four-junction Solar Cells Using Lattice-matched II-VI and III-V Semiconductors," *Prog. Photovolt: Res. Appl.*, vol.18, pp.328-333, 2010.

[59] S. Wang, D. Ding, et al, "MBE Growth of II-VI Materials on GaSb Substrates for Photovoltaics Applications," *J. Cryst. Growth*, vol. 311, pp. 2116-2119, 2009.

[60] García I, Rey-Stolle I, Galiana B, Algora C. A 32.6 % efficient lattice-matched dual-junction solar cell working at 1000 suns. Appl Phys Lett 94(5):0535509, 2009.

[61] Araki K, Yamaguchi M, Kondo M, Uozumi H. Which is the best number of junctions for solar cells under ever-changing terrestrial spectrum? In: 3rd World conference on photovoltaic energy conversion, pp 307–312, 2003.

[62] Fetzer, C.M., King, R.R., Colter, P.C. etal. High-efficiency metamorphic GaInP/GaInAs/Ge solar cells grown by MOVPE. Journal of Crystal Growth, 261, 341–348, 2004.

[63] King R, et all. Advances in high-efficiency III-V multi-junction solar cells. Adv Opto Electron, 2007.

[64] Schultz, J.C., Klausmeierbrown, M.E., Ristow, M.L. etal. Development of High-Quantum-Efficiency, Lattice-Mismatched, 1.0-eV GaInAs Solar Cells. JournalofElectroncMaterrials, 22,

755–761, 1993.

[65] T. Takamoto, T. et al., World's highest efficiency triple-junction solar cells fabricated by inverted layers transfer process. Proceedings of the 35th IEEE Photovoltaics Specialists Conference, Honolulu, Hawai, pp. 412_417, 2010.

[66] T. Takamoto et al., Multi-junction solar cell technologies - high efficiency, radiation resistance, and concentrator applications, Proc. 3rd Photovoltaic Energy Conversion Conference, 2003.

[67] C. M. Fetzer et al., 1.6/1.1 eV metamorphic GaInP/GaInAs solar cells grown by MOVPE on Ge, J. Crystal Growth, 276, 2002.

[68] R. R. King, Bandgap engineering in high-efficiency multi-junction concentrator cells, Proc. International Conference on Solar Concentrators for the Generation of Electricity or Hydrogen, 2005.

[69] C. B. Honsberg, Paths to ultra-high efficiency (>50% efficient) photovoltaic devices, 20th European Photovoltaic Solar Energy Conference, 2005.

[70] Antonio Luque and Steven Hegedus, Handbook of photovoltaic science and engineering. Published by John Wiley & Sons, Ltd, 2003.

[71] R. R. King, Bandgap engineering in high-efficiency multi-junction concentrator cells, Proc. International Conference on Solar Concentrators for the Generation of Electricity or Hydrogen, 2005.

[72] F. Dimroth, 3-6 junction photovoltaic cells for space and terrestrial applications, Photovoltaic Specialists Conference, 2005.

[73] James, L.W. Effects of concentrator chromatic aberration on multi-junction cells. 1st World Conference on Photovoltaic Energy Conversion –24th IEEE Photovoltaic Specialists Conference, pp. 1799–1802, 1994.

[74] Sentaurus. Synopsys, Mountain View, CA, USA. Available: http://www.synopsys.com/

[75] S.F. Fang, K. Adomi, S. Iyer, H. Morkoc¸, H. Zabel, C. Choi, et al., Gallium arsenide and other compound semiconductors on Silicon, J. Appl. Phys. 68 R31–58, 1990.

[76] R.K. Ahrenkiel, et al. Minority carrier lifetime of GaAs on silicon, J. Electrochem. Soc. 137 996–1000, 1990.

[77] Myong S. Y., Recent progress in inorganic solar cells using quantum structures, Recent patents on nanotechnology, p. 67-73, February 2007.

[78] R. R. King et al., Metamorphic III-V materials, sublattice disorder and multi-junction solar cell approaches with over 37% efficiency, Proc. 19th European Photovoltaic Solar Energy Conf, 2004.

[79] Antolin, E., Martí, A., Farmer, C.D. *etal*. Reducing carrier escape in the InAs/GaAs quantum dot intermediate band solar cell. *Journal of Applied Physics*, 108, 064513–7, 2010.

[80] Sogabe, T., Shoji, Y., Ohba, M. *et al*. Intermediate-band dynamics of quantum dots solar cell in concentrator photovoltaic modules. *ScientificReports*, 4, 47921-1–47921-7, 2014.

[81] Kitatani, T, *et al*. Photocurrent and photoluminescence in InGaAs/GaAs multiple quantum well solar cells. *Japanese Journal of Applied Physics, Pt1, Japanese Journal of Applied Physics*, 35, 4371–4372, 1996.

[82] Browne, B, *et al*. Triple-junction quantum-well solar cells in commercial production, in 9th International Conference on Concentrator Photovoltaic Systems (CPV-9), Miyazaki Jampan 15–17 April, AIP Conference Proceedings, pp. 3–5, 2013.

[83] Tomic´, S., Sogabe, T. and Okada, Y. In-plane coupling effect on absorption coefficients of

InAs/GaAs quantum dots arrays for intermediate band solar cell, Progress in Photovoltaics: Research and Applications, 23(5), 546–558, 2014.

[84] Walker, A.W., et al. The effects of absorption and recombination on quantum dot multi-junction solar cell efficiency. IEEE Journal of Photovoltaics, 3, 1118, 2013.

[85] Sentaurus. Synopsys, Mountain View, CA, USA. Available: http://www.synopsys.com/

[86] A. W. Bett et al. Development of III-V-based concentrator solar cells and their application in PV modules," Proc. 29th IEEE Photovoltaic Specialists Conference, 2002.

[87] R. McConnell et al., DOE high performance concentrator PV project, International Conference on Solar Concentrators for the Generation of Electricity or Hydrogen, 2005.

[88] Yamaguchi M. Fundamentals and R&D status of III-V compound solar cells and materials. Phys. Status Solidi C, 1–11, 2015.

[89] Laurentiu Fara and Masafumi Yamaguchi. Advanced solar cell materials, technology, modeling, and simulation, First Edition. © Copyright © by IGI Global, 2013.

Chapter 3

Simulating Single Junction Solar Cells Using Silvaco TCAD

Chapter 3
Simulating Single Junction Solar Cells Using Silvaco TCAD

Introduction

In general, modeling has an important role to play in the design, development and understanding of semiconductor devices. It enables the exploration and optimization of a wide range of variables, without fabricating devices in practice. As a result, modeling can substantially reduce the time and cost required for developing a specific device, finding the important trends of design variables on device performance, and eventually a suitable design prior to the fabrication stage. In this chapter, the commercial software package Silvaco is used to design and optimize the various single junction solar cell structures. Silvaco is one of the TCAD (technology computer-aided design) tools, which use 2D/3D finite element analysis to model various semiconductor devices. Although simulations using Silvaco usually takes longer to complete, these simulations use real material parameters. Therefore, the efficiency predictions from Silvaco are closer to experimental ones compared with detailed balance model. Furthermore, the modeling accuracy often depends on the choice of physical models and associated material parameters.

This chapter discusses the simulation setup and results for different single junction solar cell types and models as defined in the previous chapters. Armed with a foundation in fundamental semiconductor properties from chapter 1, the features and characteristics of semiconductor *p-n* junctions are investigated by using the SILVACO Atlas software. From this point, the important characteristics short circuit current density (Jsc), open circuit voltage (Voc), maximum power (Pmax), Fill factor (FF), efficiency η and also the frequency response, photogeneration rate of single junction solar cells will be discussed. The effects of window and back surface field BSF layers on the important characteristics, which determine the performance of a solar cell, will be discussed. A comparison of solar cell performance is also given for various materials such as gallium indium phosphide (InGaP), gallium arsenide (GaAs) and germanium (Ge). In order to validation of the models, a comparison between simulated and reported performances in the literature is also included. Optimization of single junction solar cell is the basis for multi-junction solar cell optimization and therefore is introduced first, which will be discussed in detail in chapter 4.

I General Simulation Methodology

Building a solar cell and testing it to determine if it performs as desired is too expensive and time-consuming, especially considering that this process may have to be repeated numerous times until a solar cell is built that produces the desired results. Silicon Valley Company (Silvaco) has created ATLAS, a technology computer-aided design (TCAD) software program that effectively simulates the behavior of semiconductor devices. Silvaco's ATLAS program is the software used in this thesis to simulate the performance of solar cells. Silvaco ATLAS is a physically based device simulator that enables to simulate the electrical, optical, and thermal behavior of semiconductor devices physics in two or three dimensions. The idea of using physically based simulation is to gain data difficult or impossible to measure.

Silvaco ATLAS uses finite element analysis. In other words, the device in question is approximated onto a two or three-dimensional grid with a number of grid points called nodes. The transport of carriers through a structure can be modeled by applying to the node a set of differential equations derived from Maxwell's equations. These equations include Poisson's equation, the continuity equations and the transport equations. Poisson's equation combines the variations in electrostatic potential and the local charge densities. The electron and holes densities change as a result of generation, recombination, and transport processes that are taken into account by using the transport and continuity equations.

The equations are solved by an iterative method. The software chooses initials values and the next step state is calculated using the equations. If the values converge, the simulation stops when the change between the two steps is less than a defined value. If the initial values are too far from the convergence, the simulation may diverge. In the purpose of preventing divergence or making the convergence faster, it is possible to use intermediate steps. In this case, the illumination is simulated at intermediate values from zero to one sun.

Basic simulation steps are:

- Creation of the grid, i.e. the definition of the structure and regions and the node points.
- Determination of material parameters (doping, thicknesses, etc.) and models used.
- The solution in thermo-dynamical equilibrium.
- Calculation of I-V, P-V, spectral response curves …etc under illumination.

II Incident spectrum

The light source used in our simulations was the AM1.5G spectrum to illuminating solar cells in this thesis, which is used for terrestrial applications, as shown in Figure 3.1. The total power in this spectrum is approximately 0.1000 W/cm^2.

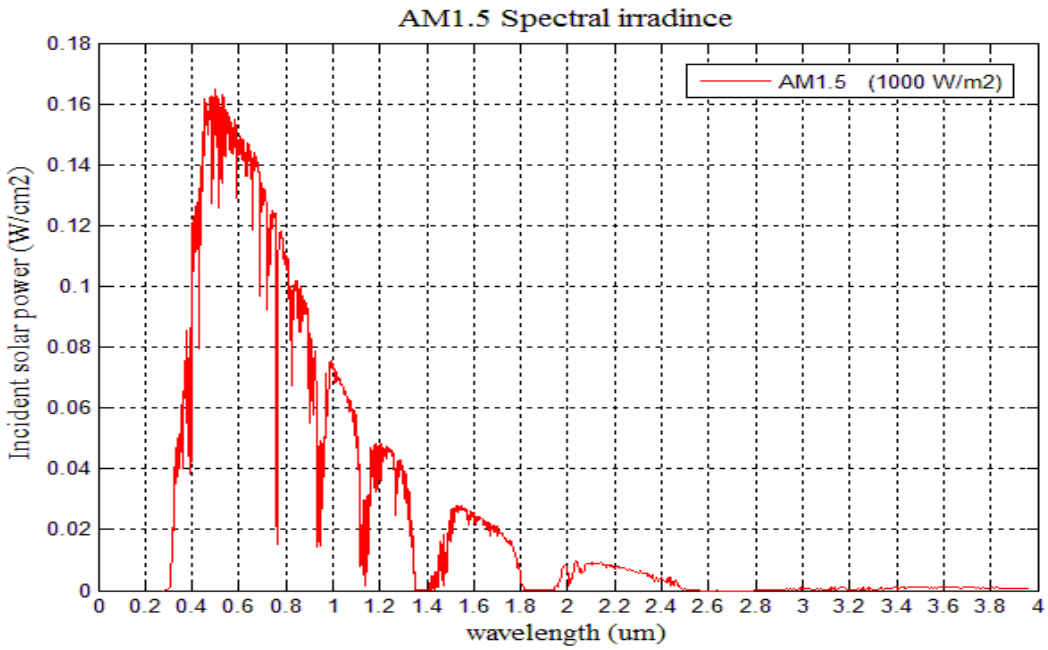

Figure 3.1: AM1.5G Solar Spectrum

III Unoptimized Single-Junction Solar Cell Modeling

The optimization of a single-junction solar cell model starts with the building of a p–n junction which is the simplest possible device. This involves a thorough verification process.

III.1 Unoptimized InGaP Solar Cell

The first solar cell that was modeled individually and simulated using Silvaco ATLAS was simple unoptimized Indium Gallium Phosphide InGaP single-junction solar cell. The cell's structure is shown in Table 3.1:

Table 3.1: Structure of the simple unoptimized InGaP solar cell

Layer	Type	Material	Doping	Thickness
Emitter	n	InGaP	$5x10^{17}$ /cm^3	0.18 µm
Base	p	InGaP	$1x10^{17}$ /cm^3	0.60 µm

The Indium Gallium Phosphide InGaP solar cell consists of two layers apart from the anode and cathode, the active region comprises of the emitter and base regions of n and p doped InGaP. The emitter is doped at $5x10^{17}$ donors /cm^3 and the base at $1x10^{17}$ acceptors /cm^3. The nominal layer thicknesses are 0.18 µm and 0.6 µm for the emitter and base, respectively.

The InGaP material has higher bandgap (Eg = 1.9eV). Therefore, its V_{OC} is expected to be larger. This also agrees with Figure 3.2. According to the same figure, Jsc is expected to be lower. The J-V and P-V curves for the simple unoptimized InGaP solar cell are shown in Figure 3.2:

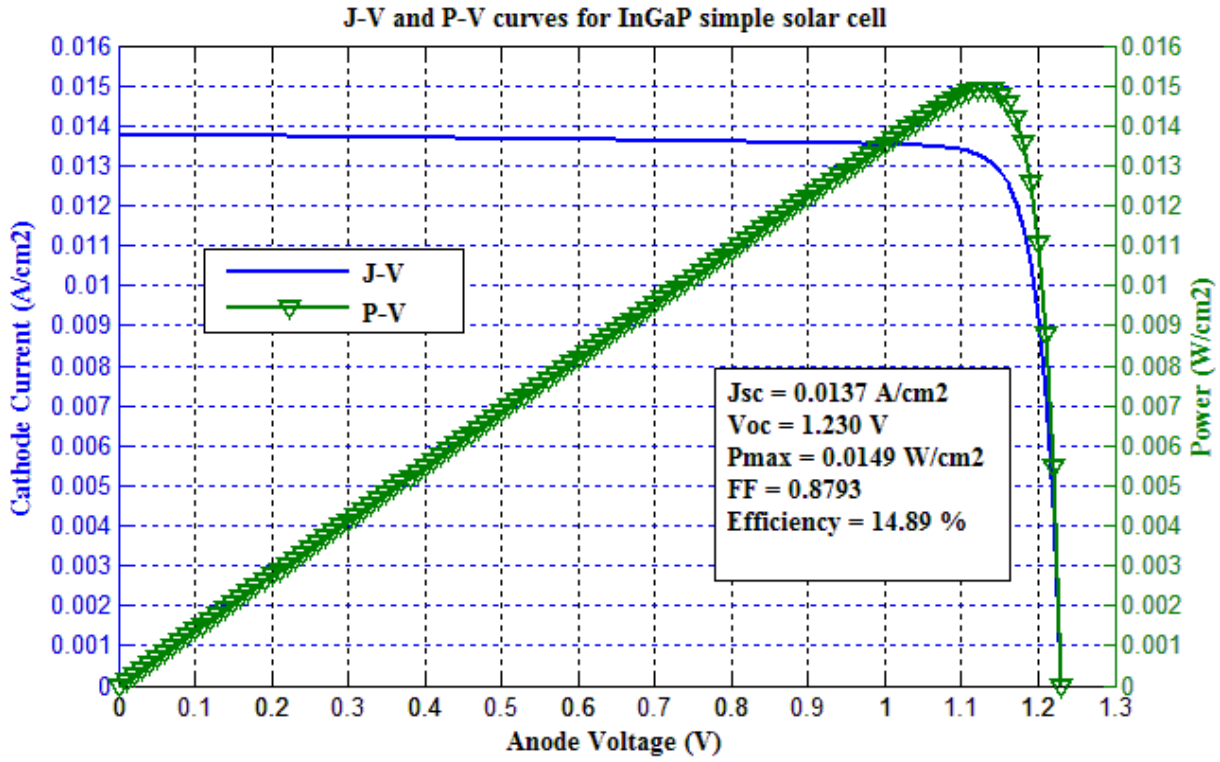

Figure 3.2: J-V and P-V curves for InGaP simple unoptimized solar cell

The five most important characteristics of the simple unoptimized InGaP solar cell are organized in Table 3.2:

Table 3.2: Simple unoptimized InGaP solar cell characteristics

	Jsc (A/cm^2)	Voc (V)	Pmax (W/cm^2)	FF	η %
Unoptimized InGaP solar cell	0.0137	1.230	0.0149	0.8793	14.89

The spectral response of a simple unoptimized InGaP solar cell should approach zero at a wavelength of approximately 0.652 μm:

$$\lambda(\mu m) = \frac{1{,}24}{\text{Eg}\,(eV)} = \frac{1{,}24}{1{,}9} = 0{,}652\ \mu m$$

As expected, this graph does approach zero at 0.675 μm. It is also important to note that the spectral response is closely correlated to the spectrum. As will see in Figure 3.3, simple InGaP solar cell collects the shorter wavelength light from 0.3 to 0.675 μm.

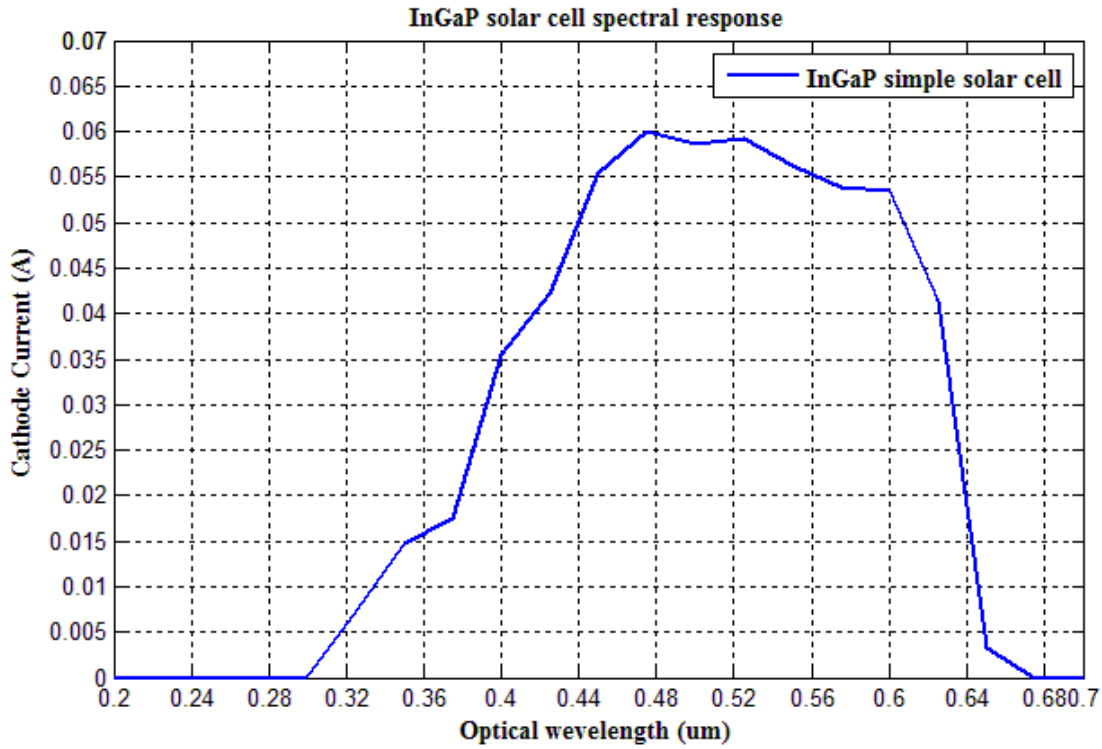

Figure 3.3: Spectral response of simple unoptimized InGaP solar cell

The frequency response (Figure 3.3) can be used in researching ways to improve performance. The goal is to expand the frequency range in which the solar cell is active and thus produces current.

If the spectral response does not go to zero, the model will allow the solar cell to respond to these higher wavelengths and give incorrect results. So this simple InGaP solar cell model demonstrates that Silvaco ATLAS software is capable of providing a very accurate model of a solar cell.

III.2 Unoptimized GaAs Solar Cell

The next solar cell that was modeled individually and simulated using Silvaco ATLAS was the simple unoptimized Gallium Arsenide GaAs single-junction solar cell. The cell's structure is shown in Table 3.3:

Table 3.3: Structure of simple unoptimized GaAs solar cell

Layer	Type	Material	Doping	Thickness
Emitter	n	GaAs	$2x10^{18}$ /cm^3	0.01 μm
Base	p	GaAs	$1x10^{17}$ /cm^3	004 μm

The Gallium Arsenide GaAs solar cell consists of two layers apart from the anode and cathode, the active region comprises of the emitter and base regions of n and p doped GaAs. The emitter is doped at $2x10^{18}$ donors /cm^3 and the base at $1x10^{17}$ acceptors /cm^3. The nominal layer thicknesses are 0.01 μm and 4 μm for the emitter and base, respectively.

The GaAs material, when lattice–matched to InGaP, has low bandgap than InGaP (Eg = 1.42eV). Therefore, its V_{OC} is also expected to be lower. This also agrees with Figure 3.4. According to the same figure, GaAs solar cell is expected produces relatively high current. The J-V and P-V curves for the simple unoptimized GaAs solar cell are shown in Figure 3.4:

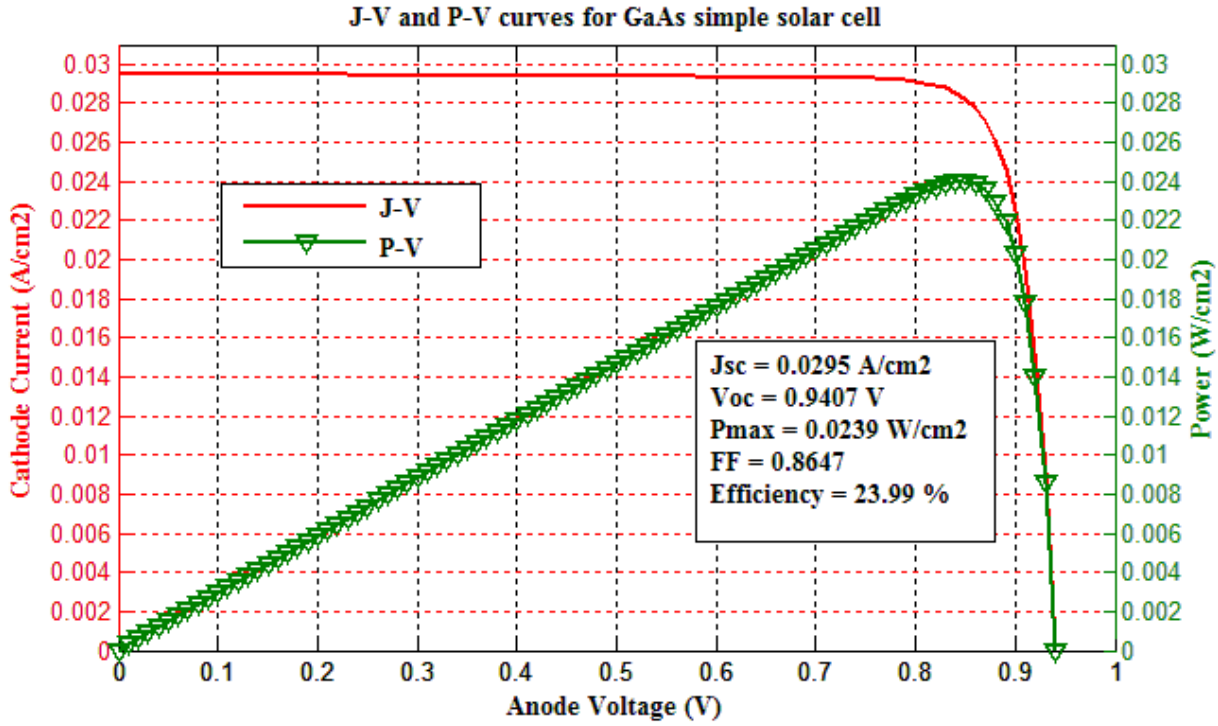

Figure 3.4: J-V and P-V curves for GaAs simple unoptimized solar cell

The five most important characteristics of the simple unoptimized GaAs solar cell are organized in Table 3.4:

Table 3.4: Simple unoptimized GaAs solar cell characteristics

	Jsc (A/cm^2)	Voc (V)	Pmax (W/cm^2)	FF	η %
Unoptimized GaAs solar cell	0.0295	0.9407	0.0239	0.8647	23.99

The spectral response of a simple unoptimized GaAs solar cell should approach zero at a wavelength of approximately 0.873 μm:

$$\lambda(\mu m) = \frac{1{,}24}{\text{Eg}\ (eV)} = \frac{1{,}24}{1{,}42} = 0{,}873\ \mu m$$

As expected, this graph does approach zero at 0.95 μm. It is also important to note that the spectral response is closely correlated to the spectrum. As will see in Figure 3.5, simple GaAs solar cell collects the small and mid-range wavelengths from 0.3 to 0.95 μm.

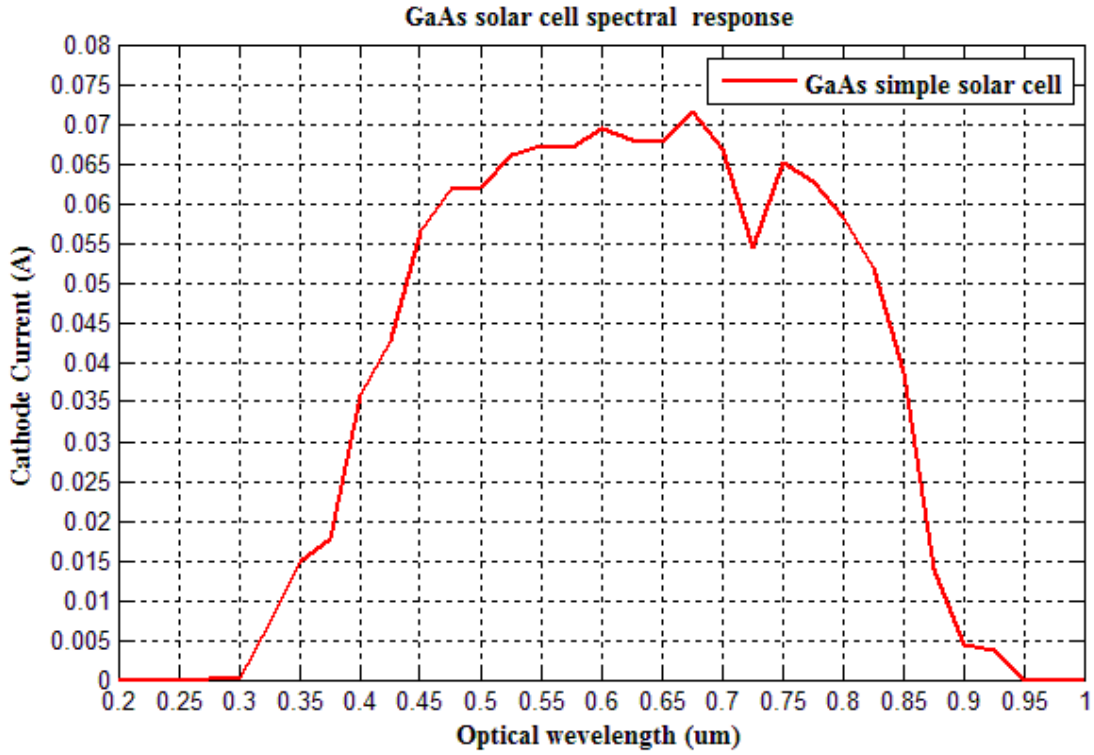

Figure 3.5: Spectral response of simple unoptimized GaAs solar cell

If the spectral response does not go to zero, the model will allow the cell to respond to these higher wavelengths and give incorrect results. This simple GaAs solar cell model demonstrates that Silvaco ATLAS software is capable of providing a very accurate model of a solar cell.

III.3 Unoptimized Ge Solar Cell

The last solar cell that was modeled individually and simulated using Silvaco ATLAS was the simple unoptimized Ge single-junction solar cell. The cell's structure is shown in Table 3.5:

Table 3.5: Structure of simple unoptimized Ge solar cell

Layer	Type	Material	Doping	Thickness
Emitter	n	Ge	$2x10^{18}$ /cm^3	0.10 µm
Substrate	p	Ge	$1x10^{17}$ /cm^3	300 µm

The Germanium Ge solar cell consists of two layers apart from the anode and cathode, the active region comprises of the emitter and base regions of n and p doped Ge. The emitter is doped at $2x10^{18}$ donors /cm^3 and the base at $1x10^{17}$ acceptors /cm^3. The nominal layer thicknesses are 0.1 µm and 300 µm for the emitter and base, respectively. For purposes of mechanical strength, the cell should also be built on a much thicker (0.3mm) substrate.

The Ge material, has low bandgap than GaAs (Eg = 0.67 eV). Therefore, its V_{OC} is also expected to be lower. This also agrees with Figure 3.6. According to the same figure, Ge solar cell is expected produces the higher current. The J-V and P-V curves for the simple Ge solar cell are shown in Figure 3.6:

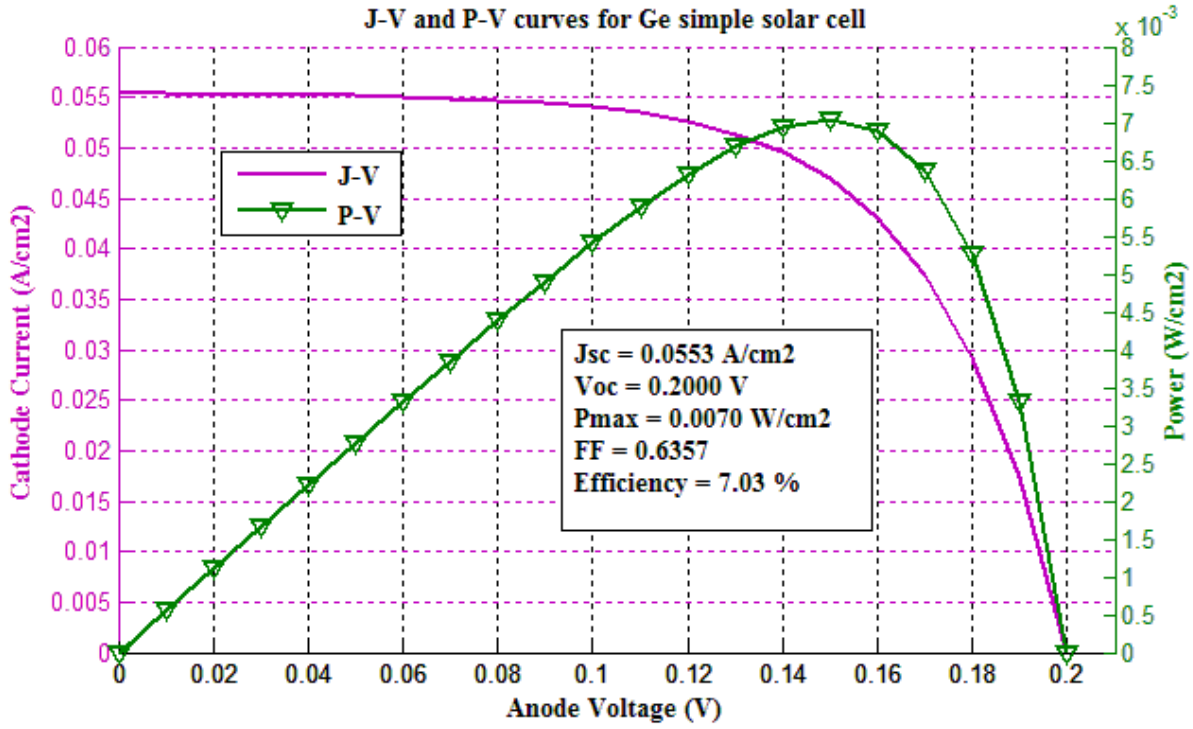

Figure 3.6: J-V and P-V of simple unoptimized Ge solar cell

The five most important characteristics of the simple unoptimized Ge solar cell are organized in Table 3.6:

Table 3.6: Simple unoptimized Ge solar cell characteristics

	Jsc (A/cm^2)	Voc (V)	Pmax (W/cm^2)	FF	η %
Unoptimized Ge solar cell	0.0553	0.2000	0.0070	0.6352	7.03

The spectral response of a simple unoptimized Ge solar cell should approach zero at a wavelength of approximately 1,878 μm:

$$\lambda(\mu m) = \frac{1,24}{\text{Eg}\ (eV)} = \frac{1,24}{0,66} = 1,878\ \mu m$$

As expected, this graph does approach zero at 1.875 μm. It is also important to note that the spectral response is closely correlated to the spectrum. As will see in Figure 3.7, Ge collects the small, mid-range and large wavelengths light from 0.3 to 1.82 μm.

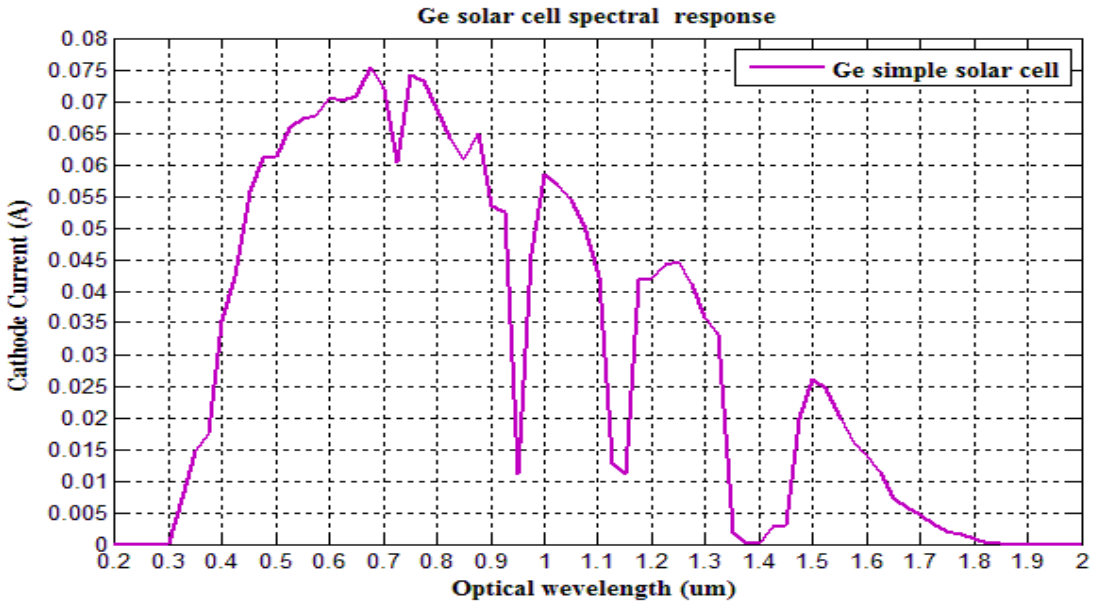

Figure 3.7: Spectral response of simple unoptimized Ge solar cell

If the spectral response does not go to zero, the model will allow the cell to respond to these higher wavelengths and give incorrect results. This Ge cell model demonstrates that Silvaco ATLAS software is capable of providing a very accurate model of a solar cell.

III.4 Comparison of Unoptimized InGaP, GaAs and Ge Solar Cells

III.4.1 J-V Characteristics Curves

The comparison of the J-V characteristics of the materials of each sub-cell of a multi-junction solar cell helps to explain why this type of solar cell is often more efficient than any single-junction solar cell. A comparison of the output of simple unoptimized Ge, GaAs and InGaP solar cells is shown in Figure 3.8:

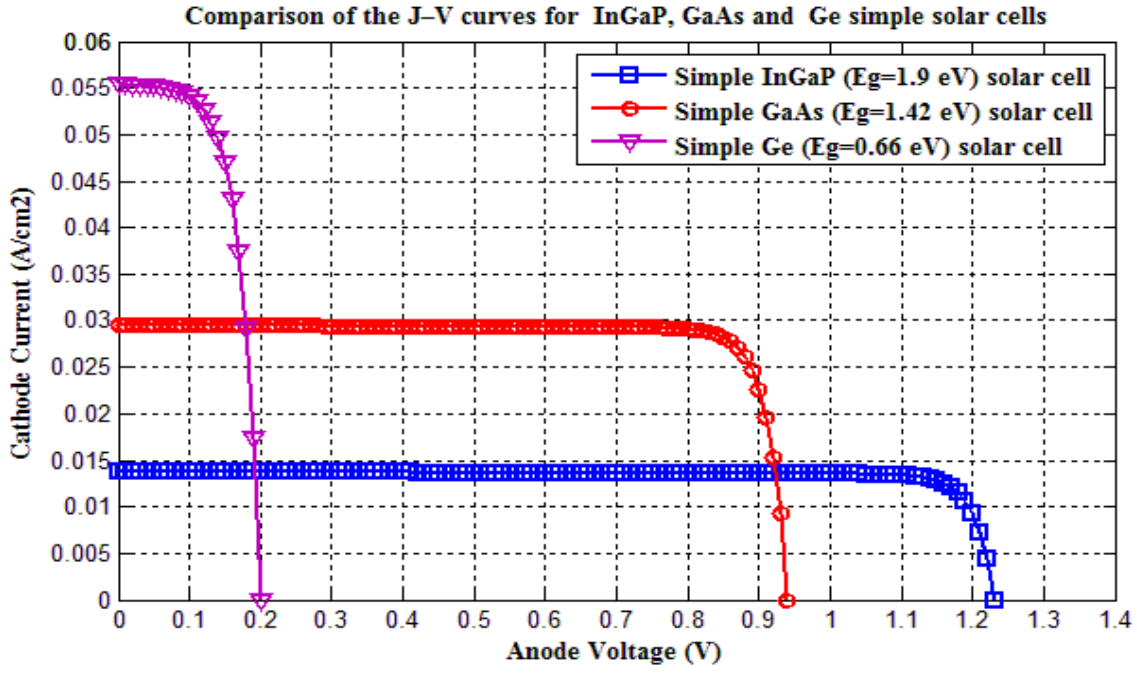

Figure 3.8: J–V curves for simple Ge, GaAs and InGaP solar cells

The indium gallium phosphide (InGaP) solar cell creates the least current but the highest voltage. The gallium arsenide (GaAs) solar cell produces the second most current and voltage. Finally, the germanium (Ge) solar cell creates the most current and the least voltage.
The comparison of the five most important characteristics of the simple Ge, GaAs and InGaP solar cells are organized in Table 3.7:

Table 3.7: Comparison of the characteristics for simple unoptimized Ge, GaAs and InGaP solar cells

	Jsc (A/cm^2)	Voc (V)	Pmax (W/cm^2)	FF	η %
InGaP (Eg=1,9 eV)	0.0137	1.230	0.0149	0.8793	14.89
GaAs (Eg=1,42 eV)	0.0295	0.9407	0.0239	0.8647	23.99
Ge (Eg=0,67 eV)	0.0553	0.2000	0.0070	0.6352	7.03

As Table 3.7 show, V_{OC} directly proportional to the band gap of the solar cell, on the contrary Jsc is inversely proportional to the band gap of the solar cell.

III.4.2 P-V Characteristics Curves

The P-V graphs show that the current-voltage product is positive, and the solar cell generates power when the voltage is between 0 and Voc. The GaAs solar cell produces the most maximum power Pmax (0.0239 W/cm^2) but the second most voltage. The InGaP solar cell creates the second most maximum power Pmax (0.0149 W/cm^2) but the highest voltage. Finally, the Ge solar cell creates the least maximum power Pmax (0.0070 W/cm^2) and the least voltage as shown in Figure 3.9.

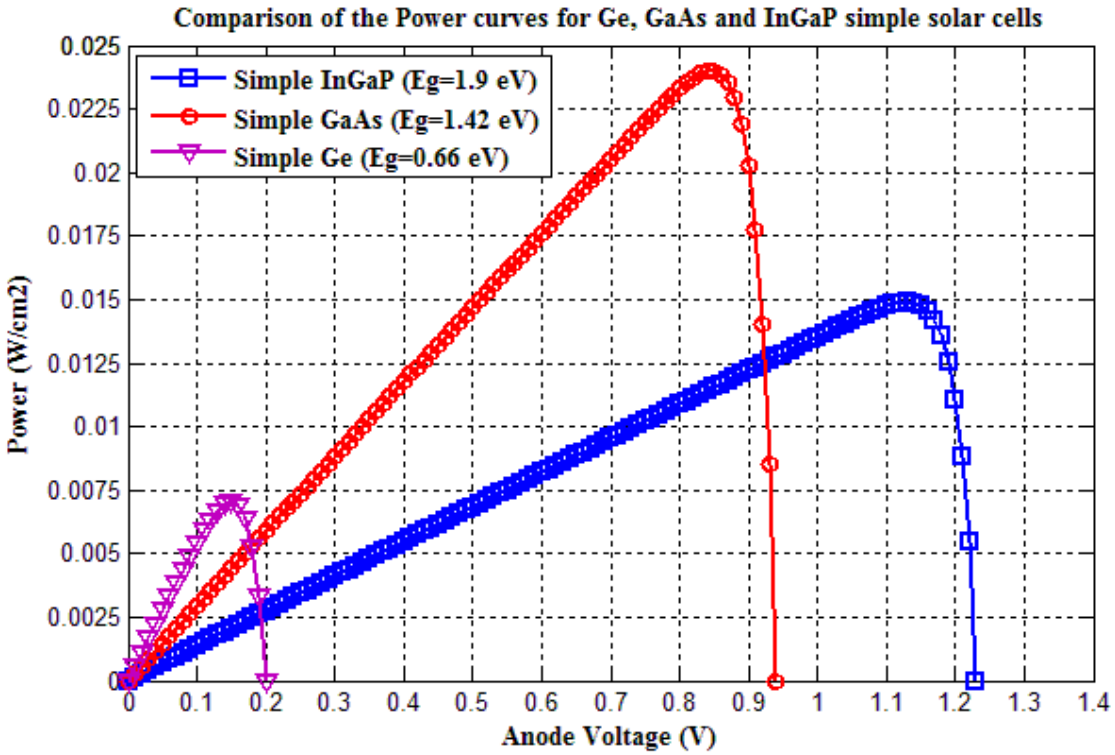

Figure 3.9: P-V curves for simple unoptimized InGaP, GaAs and Ge solar cells

III.4.3 Spectral Responses

Another factor in determining a combination of materials is the spectrum of light that each material will absorb. As seen in Figure 3.10, InGaP collects the shorter wavelength light from 0.3 to 0.675 μm and passes the rest through, GaAs collects the small and mid-range wavelengths from 0.3 to 0.95 μm and passes the large wavelengths from 0.3 to 1.82 μm onto Ge.

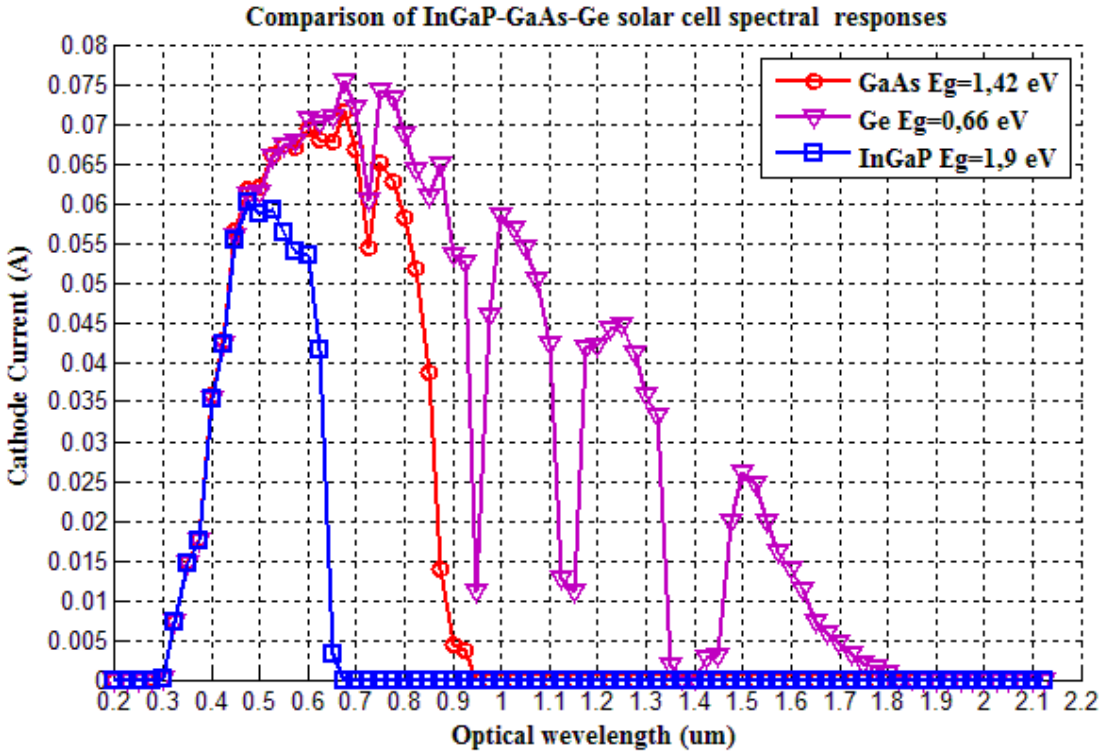

Figure 3.10: Spectrum responses for simple unoptimized InGaP, GaAs and Ge on AM1.5 spectrum

IV Optimization of Single Junction Solar Cell Structure

From the discussions in the foregoing section, the poor performance of the simple single junction solar cells indicated is due to the fact that the device structure is unoptimized. Optimization of single junction solar cell is the basis for multi-junction solar cell optimization and therefore is introduced first. As mentioned previously in chapter 1, as photogeneration takes place, minority carriers diffuse towards the junction of the cell. However, some of them tend to diffuse the opposite way, towards the front and the back surface of the cell, introducing more losses. To avoid that, in a single junction solar cell, a lightly doped layer is usually sandwiched between two highly doped layers, namely window and BSF layer can help provide a large potential barrier, so that reflect minority carriers (electrons and holes) towards the junction to eliminate the unwanted surface recombination, and usually improve the quantum efficiency. In the optimization process, the values of each layer thickness and doping level need to be determined. The InGaP, GaAs and Ge single-junction solar cells are made up of the layers: window, Back Surface Field (BSF), base, emitter, and the contact layer. Table 3.8 illustrates the construction of the solar cell under consideration for this chapter.

Table 3.8: Optimization of Single Junction Solar Cell Structure.

Window n+
Emitter n
Base p
BSF p+

IV.1 Optimization of InGaP Solar Cell

The device structure shown in Table 3.9 represents a complete InGaP solar cell optimized with respect to the device considered in the foregoing section with dimensions and concentrations. So now the Indium Gallium Phosphide InGaP solar cell consists of five layers apart from the anode and cathode, the active region comprises of the emitter and base regions of n and p doped InGaP retain the nominal thicknesses and dopings from the foregoing discussion of the unoptimized device.

The solar cell device is optimized by the inclusion of two layers; one is AlGaAs (Eg=2.14 eV) layer acting as a back surface field (BSF) and the second is AlGaAs (Eg=2.14 eV) layer acting as the top window. The BSF and window layers are both 0.01 μm thick with high doping levels $5x10^{19}$ /cm^3 donor concentration (n+) in the window layer and $5x10^{18}$ /cm^3 acceptor concentration (p+) in the BSF layer.

The BSF and window layers, being of larger bandgap and appropriately doped than the active region (InGaP), provide for large electric fields at the two ends of the active portion of the device. These electric fields reflect and accelerate minority carriers towards the junction thus reducing surface recombination effects and increasing solar efficiency. This is clearly seen in the simulated band diagram in Figure 3.11. Together with its AlGaAs window and BSF layers the complete optimized InGaP solar cell becomes like in Table 3.9:

Table 3.9: Structure of completely optimized an InGaP solar cell

Layer	**Type**	**Material**	**Doping**	**Thickness**
Window	n+	AlGaAs	$5x10^{19}$ /cm^3	0.01 μm
Emitter	n	InGaP	$5x10^{17}$ /cm^3	0.18 μm
Base	p	InGaP	$1x10^{17}$ /cm^3	0.60 μm
BSF	p+	AlGaAs	$5x10^{18}$ /cm^3	0.01 μm

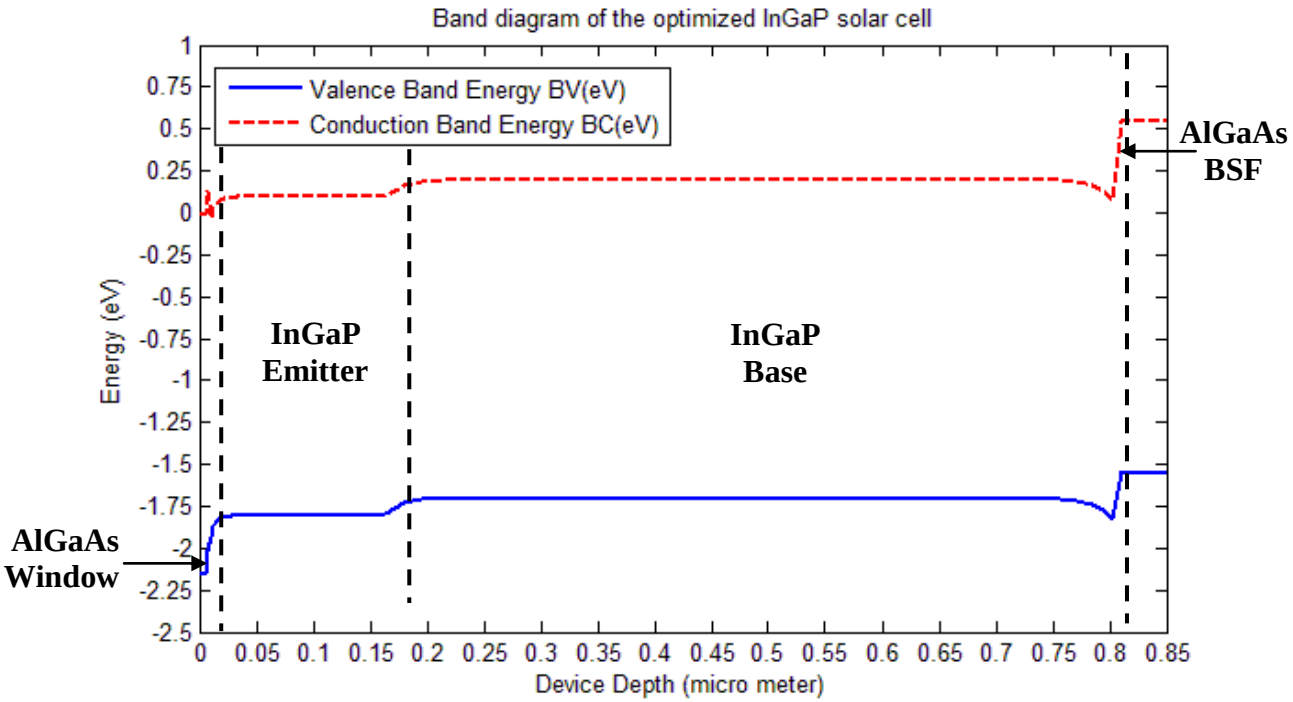

Figure 3.11: Simulated band diagram of the optimized InGaP solar cell under illumination

As seen in The Figure 3.11, window and BSF layers introduce large potential barriers for minority carriers at either end of the device; this causes photogenerated minority carriers to preferentially traverse towards the junction, as mentioned previously in chapter 1.

The J-V and P-V curves for the complete optimized InGaP solar cell are shown in Figure 3.12:

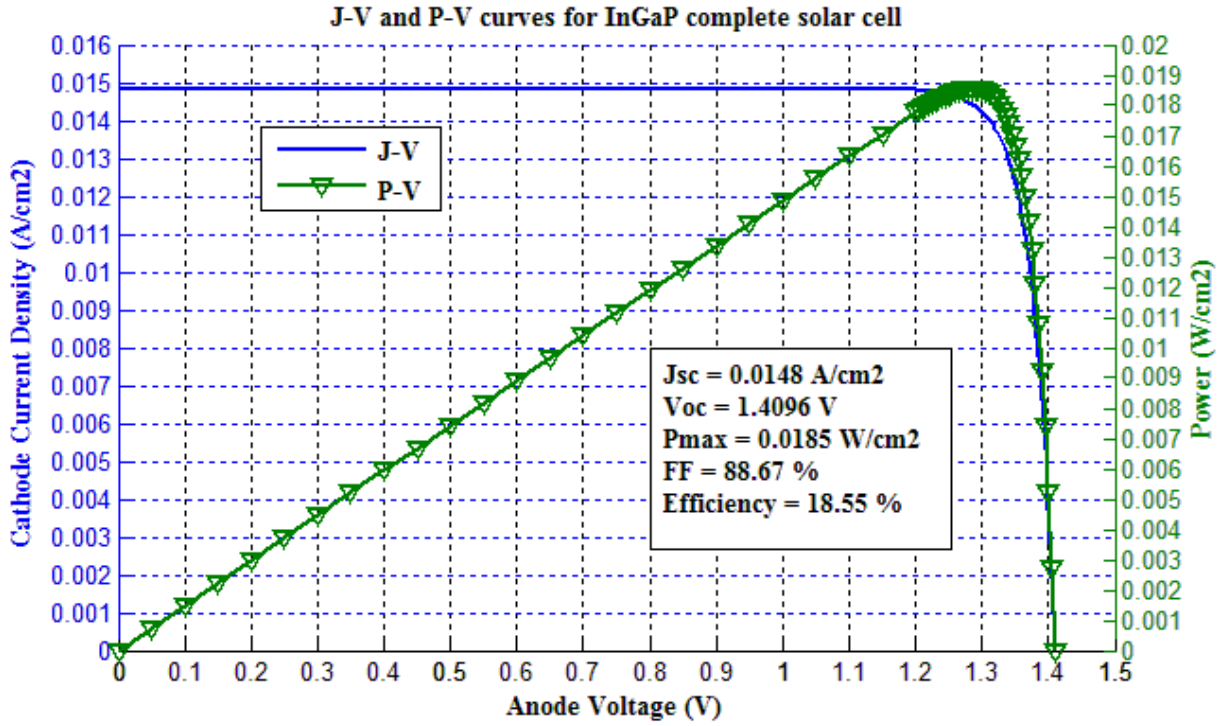

Figure 3.12: J-V and P-V characteristics of a complete optimized InGaP solar cell

Simulated results for the open-circuit voltage Voc, short-circuit current density Jsc, maximum power Pmax, fill factor FF, and device efficiency η of the complete optimized InGaP solar cell are summarized in Table 3.10:

Table 3.10: Complete optimized InGaP solar cell characteristics

	Jsc (A/cm^2)	Voc (V)	Pmax (W/cm^2)	FF	η %
Optimized InGaP solar cell	0.0148	1.4096	0.0185	0.8867	18.55

From Table 3.9, the Structure device design can be considered to be optimized. Comparing this to the device unoptimized design in Table 3.1, it is evident that the AlGaAs window and BSF layers play a large role in improving the performance of a single-junction solar cell.

Part of the allure of using a device simulator is to look at physical properties not easily investigated under experimental conditions. As an example of this, Figure 3.13 shows a surface plot of the photogeneration rate throughout the device of complete InGaP solar cell under AM1.5 illumination. The device layers shown in the surface plot from top to bottom are the window, emitter, Base, and BSF layer. The plot indicates that the majority of photogeneration does, in fact, occur within the first micron of depth in the active region (InGaP emitter and base).

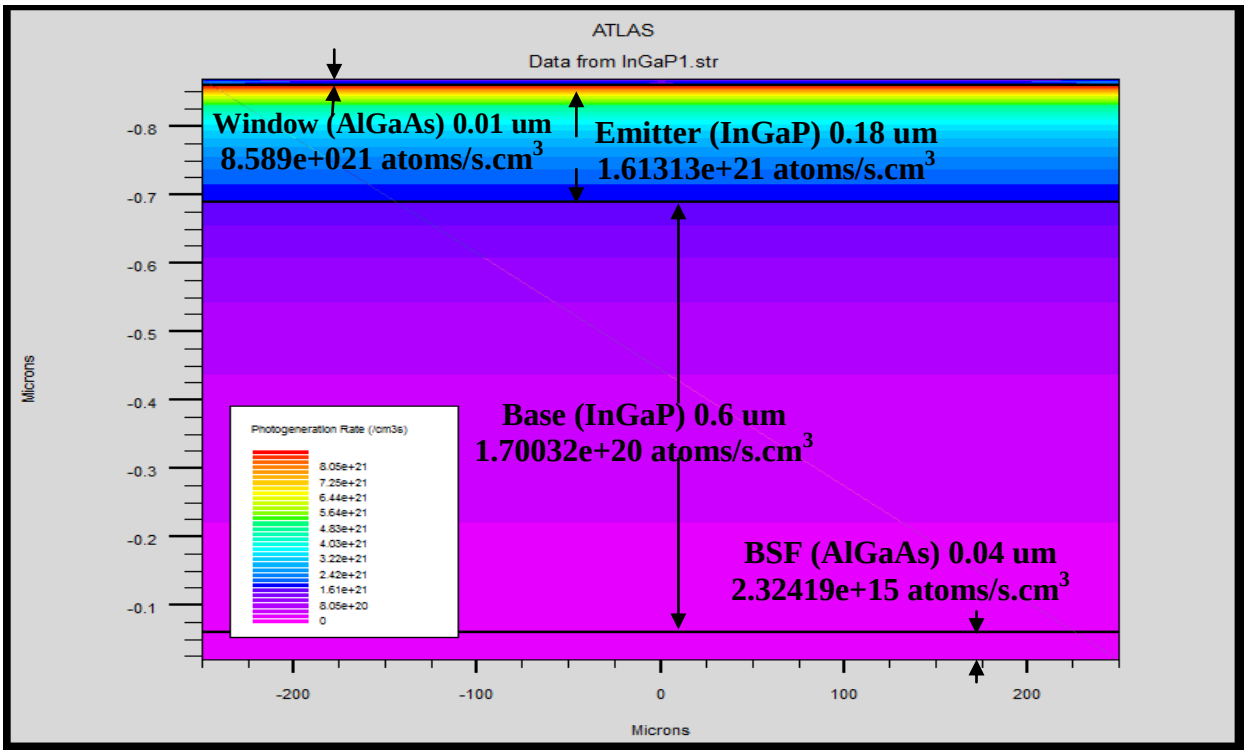

Figure 3.13: Carrier photogeneration rate of optimized InGaP solar cell plotted as a surface plot throughout the device structure

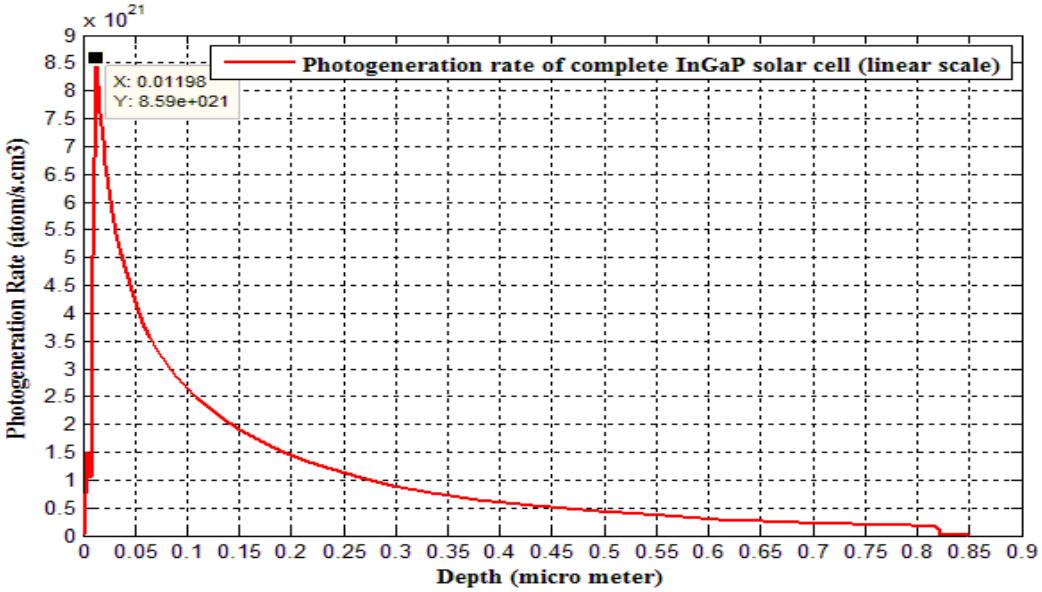

Figure 3.14: Carrier photogeneration rate of complete optimized InGaP solar cell plotted as a function of device depth on a linear scale

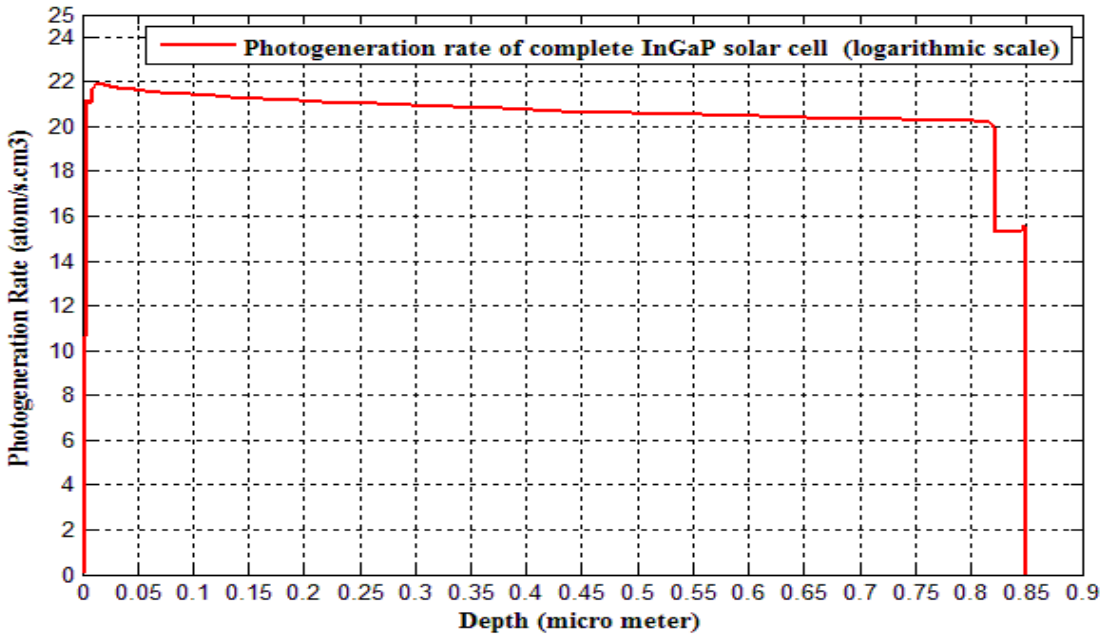

Figure 3.15: Carrier photogeneration rate of complete optimized InGaP solar cell plotted as a function of device depth on a logarithmic scale

To better see the photogeneration throughout the device, Figure 3.14 plots this data as a function of depth on a linear scale. The plot indicates that the majority of photogeneration ($8.589x10^{21}$ atoms/s.cm^3) does, in fact, occur within the first micron of depth (0.01198 μm) in emitter (InGaP) layer, and Figure 3.15 plots this data as a function of depth on a logarithmic scale. The plot indicates that discontinuities in this plot occur at Base-BSF interfaces at 0.82 μm of depth. Additionally, the substantial decrease in photogeneration from $1.70032x10^{20}$ (atom/s.cm^3) in the base (InGaP) layer at 0.81 μm to $2.09352x10^{15}$ (atom/s.cm^3) at 0.82 μm of depth in the BSF

(AlGaAs) layer indicates that the vast majority of photons of the shorter wavelength light from 0.3 to 0.675 μm have already been absorbed by that point. So the photogeneration throughout the complete optimized InGaP solar cell is displayed in occurs only in the active region (InGaP emitter and base) with 0.80 um thick and no photogeneration occurs in window layer at the first 0.01 μm of depth, BSF layer at 0.82 μm of depth as shown in Figure 3.13**,** Figure 3.14 and Figure 3.15**.**

IV.2 Comparison of the Unoptimized and Optimized InGaP solar cells

A comparison of the J-V and P-V curves of the simple unoptimized and complete optimized InGaP solar cells are shown in Figure 3.16,

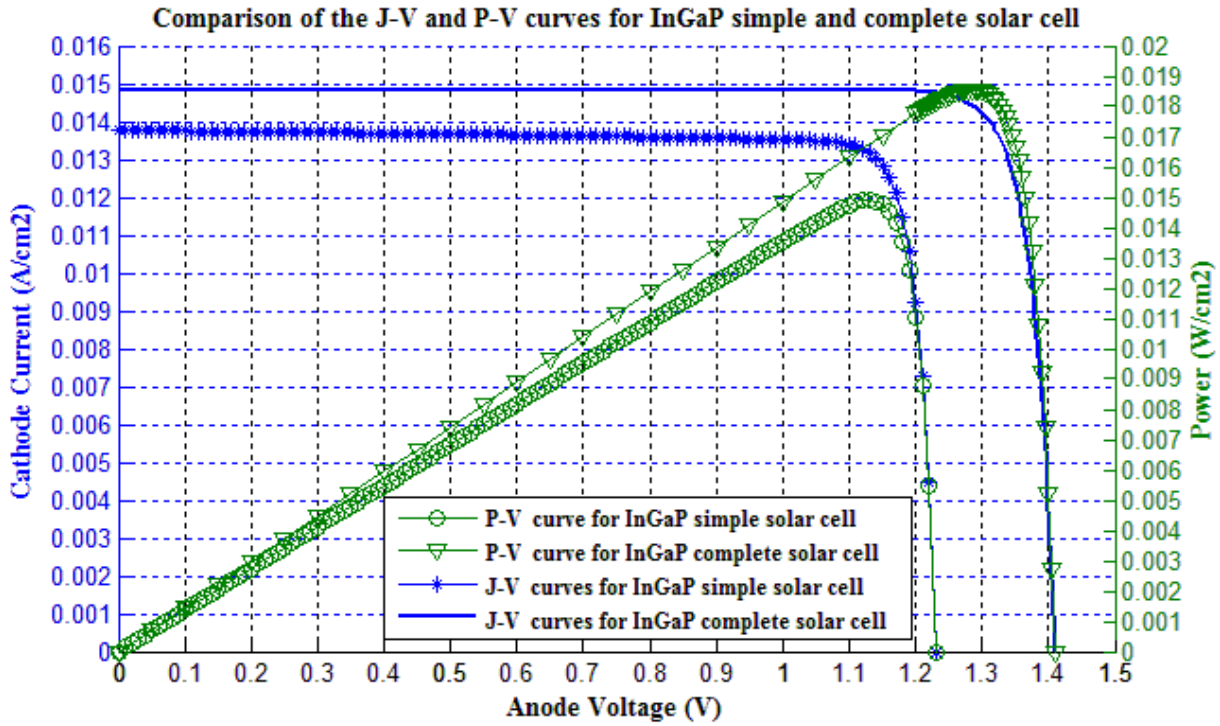

Figure 3.16: J-V and P-V curves for InGaP solar cell before and after optimization under AM1.5G

The Comparison of the five most important characteristics of the InGaP solar cell before and after optimization is organized in Table 3.11:

Table 3.11**:** Parameters for InGaP solar cell before and after optimization under AM1.5G

	Jsc (A/cm^2)	Voc (V)	Pmax (W/cm^2)	FF	η %
Unoptimized InGaP solar cell	0.0137	1.230	0.0149	0.8793	14.89
Optimized InGaP solar cell	0.0148	1.4096	0.0185	0.8867	18.55

The optimized InGaP solar cell now has an increase of Jsc from 0.0137 to 0.0148 A/cm^2 and V_{OC} from 1.230 to 1.409 V. Therefore increase of η from 14.89 to 18.55 %. From Figure 3.16 and Table 3.11 the device design can be considered to be optimized.

IV.3 Optimization of GaAs solar cell

A similar solar cell can be built using GaAs. With its own InGaP BSF is lattice-matched to GaAs and AlGaAs window layers are important improvements. The Gallium Arsenide GaAs solar cell consists of four layers apart from the anode and cathode, the active region comprise of the emitter and base regions of n and p doped retain the nominal thicknesses and dopings from the foregoing discussion of the unoptimized device.

The solar cell device is optimized by the inclusion of two layers; one is InGaP (Eg=1.9 eV) layer acting as a back surface field (BSF) and the second is AlGaAs (Eg=2.14 eV) layer acting as the top window. The InGaP BSF layer and AlGaAs window layer are both 0.01 µm thick with high doping levels $1x10^{19}$ /cm^3 donor concentration (n+) in the window layer and $7x10^{18}$ /cm^3 acceptor concentration (p+) in the BSF layer. The complete Optimized solar cell looks like in Table 3.12:

Table 3.12: Structure of completely optimized a GaAs solar cell

Layer	Type	Material	Doping	Thickness
Window	n+	AlGaAs	$1x10^{19}$ /cm^3	0.01 µm
Emitter	n	GaAs	$2x10^{18}$ /cm^3	0.01 µm
Base	p	GaAs	$1x10^{17}$ /cm^3	004 µm
BSF	p+	InGaP	$7x10^{18}$ /cm^3	0.01 µm

The J-V and P-V curves for the complete optimized GaAs solar cell are shown in Figure 3.17:

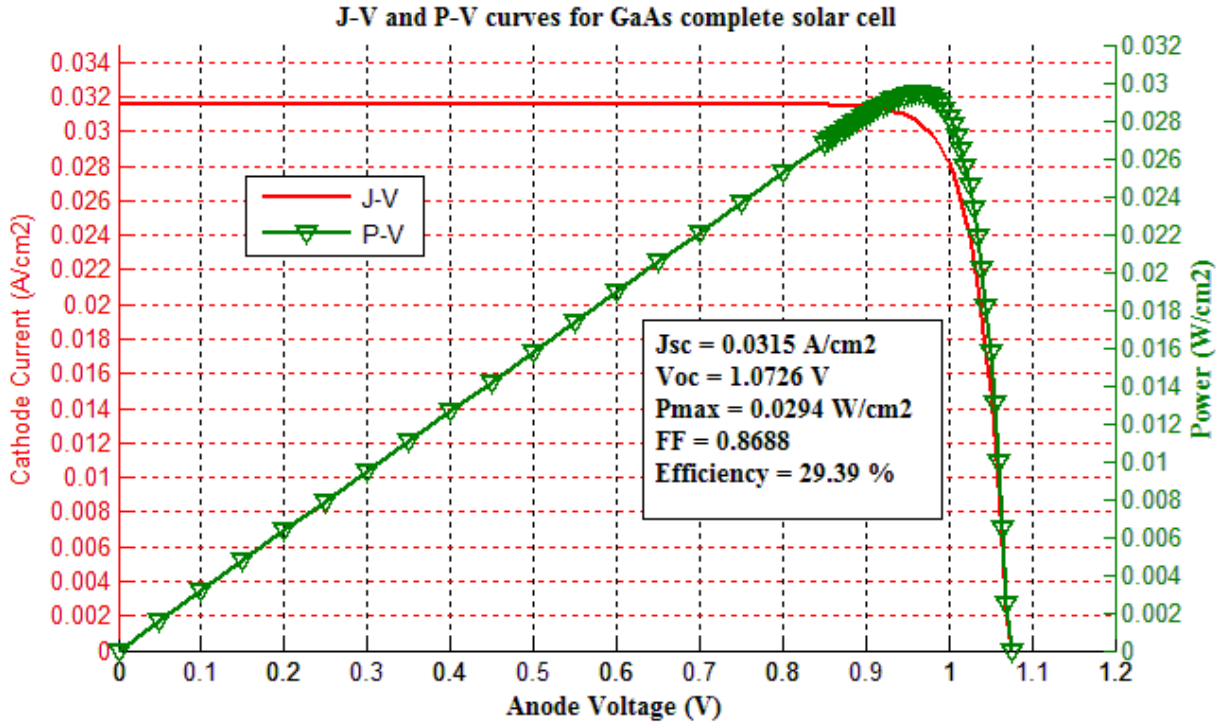

Figure 3.17: J-V and P-V characteristics of a complete optimized GaAs solar cell.

Simulated results for the open-circuit voltage Voc, short-circuit current density Jsc, maximum power Pmax, fill factor FF, and device efficiency η of the complete optimized GaAs solar cell are summarized in Table 3.13:

Table 3.13: Complete optimized GaAs solar cell characteristics

	Jsc (A/cm^2)	Voc (V)	Pmax (W/cm^2)	FF	η %
Optimized GaAs solar cell	0.0315	1.0726	0.0294	0.8688	29.39

IV.4 Comparison of the Unoptimized and Optimized GaAs solar cells

A comparison of the J-V and P-V curves of the simple unoptimized and complete optimized GaAs solar cells are shown in Figure 3.18

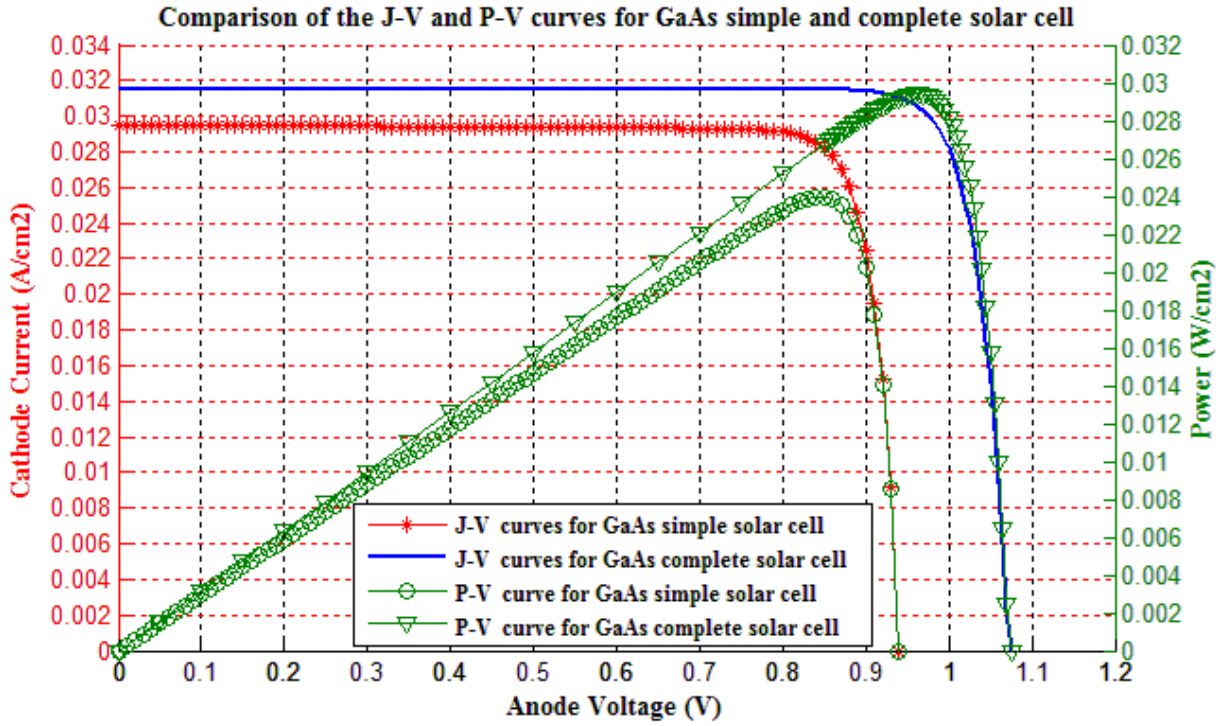

Figure 3.18: J-V and P-V curves for GaAs solar cell before and after optimization under AM1.5G

The comparison of the five most important characteristics of the GaAs solar cell before and after optimization is organized in Table 3.14:

Table 3.14: Parameters for GaAs solar cell before and after optimization under AM1.5G

	Jsc (A/cm^2)	Voc (V)	Pmax (W/cm^2)	FF	η %
Unoptimized GaAs solar cell	0.0295	0.9407	0.0239	0.8647	23.99
Optimized GaAs solar cell	0.0315	1.0726	0.0294	0.8688	29.39

The optimized GaAs solar cell now has increase of Jsc from 0.0295 to 0.0315 A/cm^2 and V_{OC} from 0.9407 to 1.0726 V. Therefore increase of η from 23.99 to 29.39 %.

IV.5 Optimization of Ge solar cell

The complete optimized Germanium Ge solar cell consists of three layers apart from the anode and cathode, The active region comprises of the emitter and base regions of n and p doped Ge retain the nominal thicknesses and dopings from the foregoing discussion of the unoptimized

device. The solar cell device is optimized by the inclusion of GaAs (Eg=1.42 eV) layer acting as the top window with 0.05 µm thick and high doping levels $7x10^{18}$ /cm^3 donor concentration (n+). The complete Ge solar cell with its own GaAs window layer becomes like in Table 3.15:

Table 3.15: Structure of complete optimized a Ge solar cell

Layer	Type	Material	Doping	Thickness
Window	n+	GaAs	$7x10^{18}$ /cm^3	0.05 µm
Emitter	n	Ge	$2x10^{18}$ /cm^3	0.10 µm
Substrate	p	Ge	$1x10^{17}$ /cm^3	300 µm

The J-V and P-V curves for the complete optimized Ge solar cell are shown in Figure 3.19:

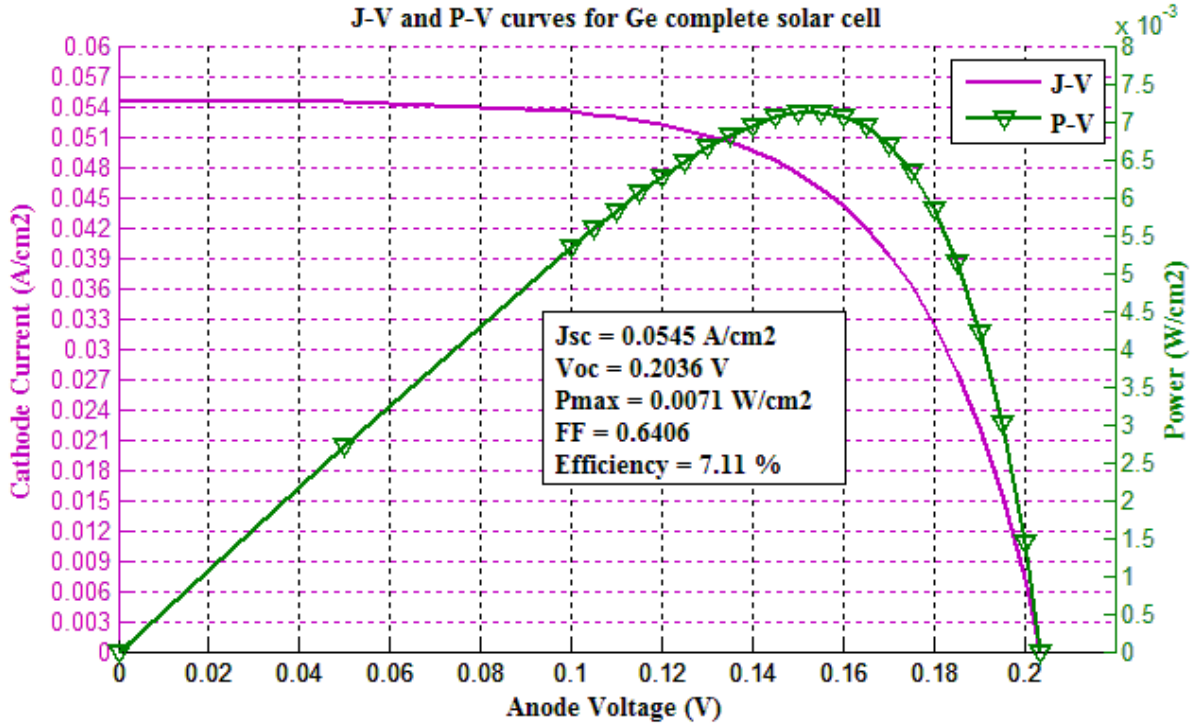

Figure 3.19: J-V and P-V characteristics of a complete optimized Ge solar cell

Simulated results for the open-circuit voltage Voc, short-circuit current Jsc, maximum power Pmax, fill factor FF, and device efficiency η of the complete Ge solar cell are summarized in Table 3.16:

Table 3.16: Complete optimized Ge solar cell characteristics

	Jsc (A/cm^2)	Voc (V)	Pmax (W/cm^2)	FF	η %
Optimized Ge solar cell	0.0545	0.2036	0.0071	0.6406	7.11

IV.6 Comparison of the Unoptimized and Optimized Ge solar cells

A comparison of the J-V and P-V curves of the simple unoptimized and complete optimized Ge solar cells are shown in Figure 3.20:

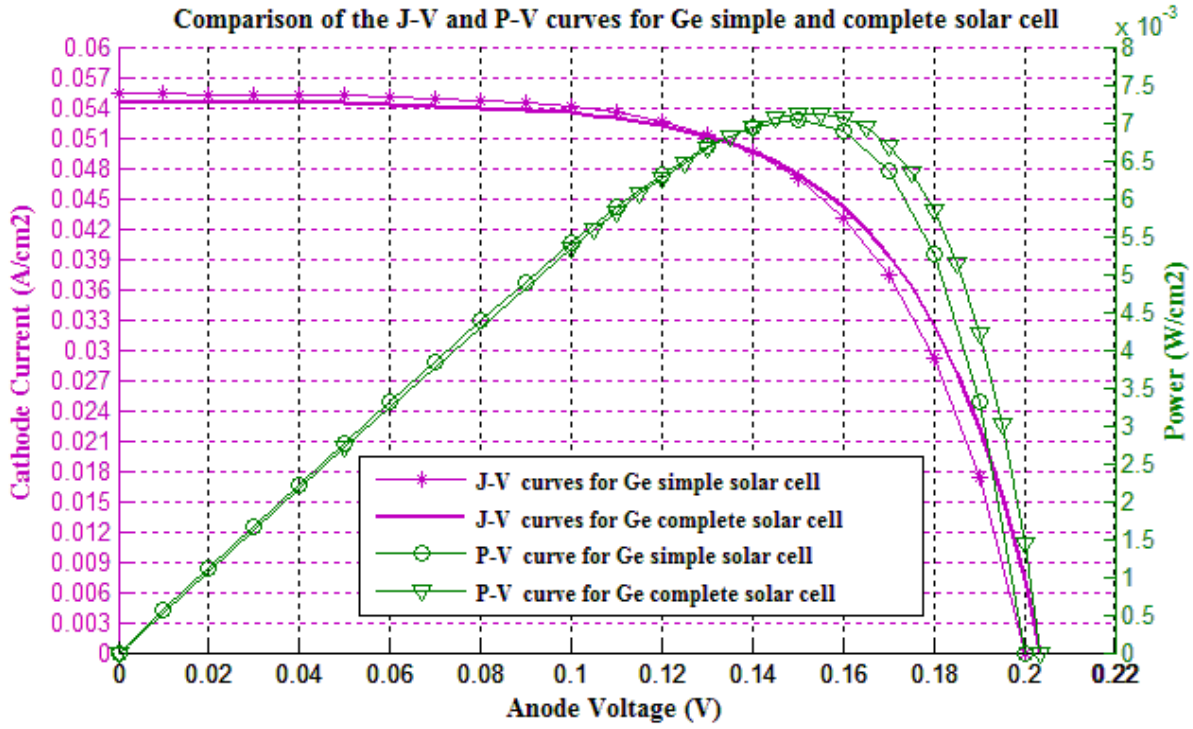

Figure 3.20: J-V and P-V curves for Ge solar cell before and after optimization under AM1.5G

The comparison of the five most important characteristics of the Ge solar cell before and after optimization is organized in Table 3.17:

Table 3.17: Parameters for Ge solar cell before and after optimization under AM1.5G

	Jsc (A/cm^2)	Voc (V)	Pmax (W/cm^2)	FF	η %
Unoptimized Ge solar cell	0.0553	0.2000	0.0070	0.6352	7.03
Optimized Ge solar cell	0.0545	0.2036	0.0071	0.6406	7.11

The optimized Ge solar cell now has an increase of V_{OC} from 0.2000 to 0.2036 V. Therefore increase of η from 7.03 to 7.11 %, but it slightly drops of Jsc from 0.0553 to 0.0545 A/cm^2. The main limiting factor in the Ge solar cell efficiency is the relatively low fill factor (0.64), this can be attributed to the influence of the series resistance of the leads when obtaining the J-V characteristics.

IV.7 Comparison of Optimized Single Junction InGaP, GaAs and Ge Solar Cells

Table 3.18 shows the five most important characteristics of the three optimized single p-n junctions.

Table 3.18: Comparison of the characteristics for Optimized Ge, GaAs and InGaP solar cells

p-n junction	Material	Jsc (A/cm^2)	Voc (V)	Pmax (W/cm^2)	FF	η %
1	InGaP (Eg=1,9 eV)	0.0148	1.4096	0.0185	0.8867	18.55
2	GaAs (Eg=1,42 eV)	0.0315	1.0726	0.0294	0.8688	29.39
3	Ge (Eg=0,67 eV)	0.0545	0.2036	0.0071	0.6406	7.11

We observe p-n junction 1 (InGaP) has the highest open circuit voltage and the lowest short circuit current density, which means that this p-n junction has the highest band gap (1.9 eV). In contrast, p-n junction 3 (Ge) has a low open circuit voltage and a high current density; consequently it has the lowest band gap (0.67 eV). p-n junction 2 (GaAs) has a band gap in between (1.42 eV). Hence, if we are designing a triple-junction cell out of these three junctions, junction 1 will act as the top cell, junction 2 will act as the middle cell and junction 3 will act as the bottom cell, as will see in chapter 4.

V Validation of Results with Simulation and Experimental Data

In order to validate our models, we simulated an InGaP, GaAs, and Ge single-junction solar cell and the results are compared to published simulation and experimental data. The results compared favorably with corresponding simulation and experimental data for similar InGaP, GaAs, and Ge single-junction solar cell structure layers (window, emitter, base, BSF) using the same some parameters as optical parameters AM1.5G. Some differences are due to the variations in the material, thickness, and doped profile. Table 3.19, Table 3.20 and Table 3.21 shows the various comparisons of our optimized design with other previous findings and found the results of our simulation model gives a good result with high efficient performance than other proposed in various works of literature. Comparison with the experimental performance of single-junction solar cells confirms the accuracy of the analysis using Silvaco ATLAS software simulator. Enhancing InGaP, GaAs, and Ge single-junction PV characteristics, with the simulated findings described here, will lead to enhancement in multi-junction solar cells.

Table 3.19 shows summarize the PV characteristics for our simulated single-junction InGaP solar cell, in comparison with simulation and experimental data based on InGaP [1, 2, 3]. We observed that the performance and results produced from this simulation model are comparable to experimental data of similar manufactured solar cells as in reference [1, 2], the results are also comparable to simulation data as in reference [3] using a commercial software Silvaco ATLAS simulator. The present InGaP solar cell exhibits higher conversion efficiency and fill factor values than the experimental and simulated InGaP solar cells.

Table 3.19: Comparison of InGaP Single-junction solar cell performance parameters, for simulation versus measurements

	Reference	Year	Illumination	Jsc (A/cm^2)	Voc (V)	FF	η (%)
Experimental Data	[1]	1997	AM1.5G	0.015	1.39	0.87	18.5
	[2]	2015	AM1.5G	0.0146	1.44	0.87	18.54
simulation Data	[3]	2014	AM1.5G	0.013	1.26	0.86	15.15
	[Our work]	2018	AM1.5G	0.0148	1.40	0.88	18.55

Interestingly, our simulated single-junction InGaP solar cell performance (Jsc, Voc) matches perfectly with experimental data reported in [1, 2]. This model refers to the very good agreement between simulated and experimental data. The InGaP single-junction solar cell has the best photovoltaic conversion efficiency of 18.55% with the Voc of 1.40V, a Jsc value of 0.0148 A/cm^2, and a FF of 88%. This proves the validity of the numerical model and the used input data, thus setting a starting point for a deeper understanding and further structure optimization of multi-junction solar cells based on InGaP.

Table 3.20 shows summarize the PV characteristics for our simulated single-junction GaAs solar cell, in comparison with simulation and experimental data based on GaAs [4, 5, 6]. We observed that the performance and results produced from this simulation model are comparable to experimental data of similar manufactured solar cells as in reference [4, 5], the results are also comparable to simulation data as in reference [6] using AFORS-HET software simulator. The present GaAs solar cell exhibits higher conversion efficiency and short circuit current density values than the experimental and simulated GaAs solar cells.

Table 3.20: Comparison of GaAs Single-junction solar cell performance parameters, for simulation versus measurements

	Reference	Year	Illumination	Jsc (A/cm^2)	Voc (V)	FF	η (%)
Experimental Data	[4]	2017	AM1.5G	0.0289	1,092	0.85	26.83
	[5]	2011	AM1.5G	0.0296	1.107	0.84	27.6
simulation Data	[6]	2016	AM1.5G	0.03	1.108	0.86	28.7
	[Our work]	2018	AM1.5G	0.0315	1.0726	0.86	29.39

Interestingly, our simulated single-junction GaAs solar cell performance (Jsc, FF) matches perfectly with simulation data reported in [6] and matches relatively for (Jsc) with experimental data reported in [5], while a noticeable difference is observed in FF. This difference was assigned to resistive losses. As a result, this model refers to the very good agreement between AFORS-HET and Silvaco ATLAS software simulator. The GaAs single-junction solar cell has the best photovoltaic conversion efficiency of 29.39% with the Voc of 1.0726 V, a Jsc value of 0.0315 A/cm^2, and a FF of 86%. This proves the validity of the numerical model and the used input data, thus setting a starting point for a deeper understanding and further structure optimization of multi-junction solar cells based on GaAs.

Table 3.21 shows summarize the PV characteristics for our simulated single-junction Ge solar cell, in comparison with simulation and experimental data based on Ge [7, 8, 9]. We observed that the performance and results produced from this simulation model are comparable to experimental data of similar manufactured solar cells as in reference [7, 8], the results are also comparable to simulation data as in reference [9] using D-AMPS-1D software simulator. The present Ge solar cell exhibits higher conversion efficiency and short circuit current density values than the experimental and simulated Ge solar cells.

Table 3.21: Comparison of Ge Single-junction solar cell performance parameters, for simulation versus measurements

	Reference	Year	Illumination	Jsc (A/cm^2)	Voc (V)	FF	η (%)
Experimental Data	[7]	2003	AM1.5G	0.0458	0.245	0.59	6.7
	[8]	2009	AM1.5G	0.0432	0.264	0.69	7.9
simulation Data	[9]	2012	AM1.5G	0.0257	0.220	0.65	5.6
	[Our work]	2018	AM1.5G	0.0545	0.2036	0.64	7.11

Interestingly, our simulated single-junction Ge solar cell performance (Voc) matches relatively with experimental data reported in [7], while a noticeable difference is observed in FF and

Jsc. This difference was assigned to resistive losses and doped profile, and matches relatively for (η) with experimental data reported in [8]. As a result, this model refers to the very good agreement between simulated and experimental data. The Ge single-junction solar cell has the best photovoltaic conversion efficiency of 7.11% with the Voc of 0.2036 V, a Jsc value of 0.0545 A/ cm^2, and a FF of 64%. This proves the validity of the numerical model and the used input data, thus setting a starting point for a deeper understanding and further structure optimization of multi-junction solar cells based on Ge.

Conclusion

In this chapter, a comprehensive 2D numerical model of a single-junction InGaP, GaAs, and Ge solar cells are presented. First, numerical models of unoptimized InGaP, GaAs and Ge solar cells are built and optimized with the window and back surface field BSF layers. For each solar cell, design shows the expected positive correlation between Eg and Voc and Jsc. Surface recombination reduces the quantum efficiency and therefore reduces the solar cell working current. Passivation layers can reduce the surface recombination and so do the window and BSF layer. From the results and discussions in this chapter, it is evident that the addition of windows and BSF layers to the simple unoptimized solar cell structure is one of the most important improving the performance of a solar cell. As a result, good simulation results are obtained for all three single-junction solar cells. An efficiency of η= 18.55% for InGaP, η= 29.39 % for GaAs, and η= 7.11% for Ge single junction solar cells under 1 sun AM1.5G are predicted by this model. These results furnish a better understanding of the physical behaviors of the window and BSF layers in future highly efficient solar cell devices. The results also establish a starting point for future simulation of multi-junction solar cells.

This numerical model offers a cost effective and time efficient way to optimize a single-junction solar cell, and it complements the experiments by exploring the design space in-between experiments. Therefore the ability to model such devices would prove useful in the analysis of both present and future solar cell designs. Furthermore, this numerical simulation can not only give detailed device designs but also provide many physical quantities and some of them are hard to probe from experiments. These physical quantities include band diagram, generation rate profile, spectral response, etc. These physical quantities can be used to understand the device limits and help to further optimize the device performance.

Single-junction semiconductors can generate higher current due to photon absorption over the broader spectral region but will not produce high open circuit voltage because of the limitations of dark current of the low bandgap material, this limits them within the Shockley efficiency limit of 30%. Multi-junction solar cells formed with several sub-cell layers effectively split the solar radiation spectrum and overcome the limitation of single-junction cells producing higher voltage and current-matched to the bottom sub-cell, promoting to higher efficiency. So far, the discussion of single junction solar cells has been focused on the well known III-V semiconductor InGaP, GaAs and Ge. These solar cells are primarily intended to be the first step towards the achievement of highly-efficient multi-junction solar cells, in order to develop high-efficiency lattice matched InGaP/GaAs dual-junction and InGaP/GaAs/Ge triple-junction solar cells. Simulation of mechanically and monolithically stacked multi-junction solar cells will be discussed in detail in chapter 4.

References

[1] Ming-Ju Yang, et al. Photoluminescence analysis of InGaP top cells for high-efficiency multi-junction solar cells. Solar Energy Materials and Solar Cells, 45(4):331 – 339, 1997.

[2] Essig-S, et al. Progress towards a 30% efficient GaInP/Si tandem solar cell. Energy Procedia 77, 464_469, 2015.

[3] Jung Woo Leem and Jae Su Yu. Theoretical modeling and optimization of III–V GaInP/GaAs/ Ge monolithic triple-junction solar cells. Journal of the Korean Physical Society, Vol. 64, No. 10, pp. 1561-1565, May 2014.

[4] Ming Stephanie Essig , et al. Raising the one-sun conversion efficiency of III–V/Si solar cells to 32.8% for two junctions and 35.9% for three junctions. Nature Energy, 17144, 2017.

[5] Kayes, B. M. et al. 27.6% conversion efficiency, a new record for single-junction solar cells under 1 sun illumination. Proc. 37th IEEE Photovolt. Spec. Conf. IEEE, 2011.

[6] Kim, S., Hwang, S.-T., Yoon,W. & Lee, H.-M. High performance GaAs solar cell using heterojunction emitter and its further improvement by ELO technique. Proc. 32nd Euro. Photovolt. Sol. Energy Conf. EU-PVSEC, 2016.

[7] N.E. Posthuma, G. Flamand and J. Poortmans. Development Of Stand-Alone Germanium Solar Cells For Application In Space Using Spin-On Diffusants. 3rd World Conferewe on Phorovollaic Energy Conversion Ma.), 11-18, Osoku. Japan, 2003.

[8] G. Flamand, et al. Development Of Mechanically Stacked Multi-Junction Solar Cells Applying Thin, One-Side Contacted Iii-V Cells. 24th European Photovoltaic Solar Energy Conference, 21-25, Hamburg, Germany, September 2009.

[9] Marcela Barrera a,b,n, et al. Numerical simulation of Ge solar cells using D-AMPS-1D code. Physica B 407 3282–3284, 2012.

Chapter 4

Simulating Multi-Junction Solar Cells Using Silvaco TCAD

Chapter 4
Simulating Multi-Junction Solar Cells Using Silvaco TCAD

Introduction

Manufacturing a solar cell and testing it to determine if it performs as desired are too expensive and time-consuming, considering that these processes may have to be repeated numerous times until a solar cell is built to produce the desired results. To gain a real understanding and realization of all the phenomena occurring inside the solar cell devices, firstly, the development of a reliable simulation model is very essential; simulations have often been performed using a Silvaco ATLAS device simulator**.**

In order to optimize conversion efficiency of a photovoltaic cell, the solar cell should absorb as much of the spectrum as possible, and so bandgaps should cover a wide range. Multi-junction solar cells are able to achieve significantly higher efficiencies than single junctions due to better spectral utilization. The idea is to subdivide the incident solar spectrum into several parts to be absorbed for the different sub-solar cells; each one has an optimized efficiency for a certain range of wavelengths in the spectrum of the incident sunlight. The goal is to find the best and most advantageous band-gap combination for each sub-solar cell to convert the total incident solar light with the maximum possible efficiency.

Chapter 4 has been dedicated to the methodology introduced in chapter 1, chapter 2 and the results of chapter 3 to provide a complete simulation of a multi-junction solar cell. After successfully modeling the single-junction InGaP, GaAs and Ge solar cells in chapter 3, to its inclusion in the dual-junction and triple-junction solar cells structure, the primary goal of this chapter is to describe the multi-junction optimization of solar cell and simulation results of a lattice matched mechanically and monolithically InGaP/GaAs dual-junction and InGaP/GaAs/Ge triple-junction stacked solar cell. We design and optimize mechanically and monolithically III-V solar cells by using a commercial software Silvaco ATLAS simulator to obtain the important device characteristics short circuit density (Jsc), open circuit voltage (Voc), maximum power (Pmax), Fill factor (FF), efficiency η. For the optimized cell structure, the frequency response and the photogeneration rate distributions are also investigated. As validation of the models, a comparison between simulated and reported performances in the literature is also included.

I Optimization of Solar Cell

The light from the sun is made up of a range of wavelengths and corresponding photon energies. The efficiency of single junction cells is partially limited by the inability to fully utilize the multiple photon energies in the incident wave. Since electrons in the cell's material need specific energy to overcome the band gap, an incident photon must have that same specific energy to free the electron from its binding. Photons with energies greater than the band gap, the fraction of energy greater than the band gap are lost as heat. Photons with energies less than the band-gap pass through the material without generating electric power.

Once single-junction devices have been optimized for materials composition and quality and best device structure and processing, there are essentially two ways that solar cell efficiency can be substantially increased. One approach is to use concentrator solar cells. The next approach was to develop multi-junction solar cells that can utilize the total solar spectrum with different wavelengths. Solar cells are stacked with respect to the energy gap of the semiconductor. Multi-junction cells are also called tandem cells.

As mentioned previously in chapter 2, one understands the idea for creating multi-junction, solar cells when considering the solar spectrum, different materials accept different wavelengths of sunlight, which correspond to different levels of input power from the sun. When p-n junctions of different materials with varying band gaps are stacked on top of each other, the light passing through the top layers is absorbed in the underlying layers. This increases the efficiency of the overall cell.

An important advantage of multi-junction cells is that each layer can be assigned to a specific range of the solar spectrum using elements with different band gap energies, it can be seen that the front layer absorbs high-energy photons, the next layer, photons with slightly less energy, and so on. The sub-cells are connected in series; therefore, the sub-cell with the lowest current defines the overall current for the cell, but the voltage of the cell is the sum of the voltages produced by each sub-cell. A solar cell consisting of multiple layers that accept more of the available light increases the useful power provided to the solar cell and produces a greater output power.

According to the discussion in chapter 3, our materials used to form multi-junction solar cells are InGaP, GaAs, and Ge. These materials are lattice matched with a lattice constant of 5.65 Å (at 300 K) making it possible to stack them on top of one another to create a multi-junction solar cell, to avoid dislocations and decrease the number of defects and thermal, mechanical, and electrical stresses that can act as recombination centers. There are two types of multi-junction cells: a mechanically stacked tandem cell and a monolithic tandem cell. A mechanically stacked tandem consists of individually grown cells that are stacked and connected by transparent glue. A monolithic tandem cell consists of multiple cells in which all cells are grown on top of each other in one growth-run connected by tunnel junctions.

II Simulation of Multi-Junction Solar Cells

According to the discussion in the chapter 3, once the three InGaP, GaAs and Ge single solar cells had each been built, modeled, and verified Silvaco ATLAS as an accurate means to model solar cells, we will proceed to develop a InGaP/GaAs dual-junction and InGaP/GaAs/Ge triple-junction solar cells based on the single-junction designed previously, an InGaP (E_g = 1.9eV) is placed on top in order to absorb the high energy photons and allow the lower-energy photons to pass through. GaAs (E_g = 1.42eV) is the middle cell and absorbs middle energy range photons and allows the rest to pass through. Ge (E_g = 0.67eV) is used for the bottom cell so that it can absorb the remaining photons.

II.1 InGaP/GaAs Dual-junction Solar Cell

There are two types of InGaP/GaAs dual-junction solar cell: a mechanically stacked tandem cell and a monolithic tandem cell.

II.1.1 Mechanically Stacked Multi-Junction Cell Solar Design

The current matching requirement and tunnel junctions can be omitted by using a mechanical stacking approach, where a number of individual cells can be independently optimized and subsequently mechanically placed on top of one another, each using part of the incident spectrum. Since Mechanically Stacked Solar Cells (MSSC) are electrically separated, where each III-V sub-cell is still grown on separate substrates and have multiple terminals instead of two and processed individually, as discussed in Chapter 2. This stacked cell fabrication route provides the greatest possibilities for efficiency gains and cost-savings as the dual challenges of III-V substrate cost and light absorption in substrates are tackled.

II.1.1.1 Mechanically Stacked InGaP/GaAs Dual-Junction Solar Cell

In a first attempt to create an InGaP/GaAs dual-junction monolithic tandem cell, the mechanically stacked structure Table 4.1 was used for simplicity. This design places the optimized InGaP solar cell atop the optimized GaAs solar cell retain the nominal thicknesses and dopings from the foregoing discussion of the optimized device studied in chapter 3. For purposes of mechanical strength, the GaAs solar cell should also be built on a much thicker (≅0.3mm) substrate; GaAs is a good material to use. The two cells are not in contact. Instead, they are separated by a thin layer of vacuum. The vacuum is a very good insulator; it does not absorb or alter light as it goes through it.

Table 4.1: Mechanically stacked InGaP/GaAs dual solar cell

Sub-Cell	Layer	Type	Material	Doping	Thickness
InGaP Top sub-cell Eg = 1.9 eV	Window	n+	AlGaAs	$5x10^{19}$ /cm^3	0.01 µm
	Emitter	n	InGaP	$5x10^{17}$ /cm^3	0.18 µm
	Base	p	InGaP	$1x10^{17}$ /cm^3	0.60 µm
	BSF	p+	AlGaAs	$5x10^{18}$ /cm^3	0.01 µm
Vacuum	**Vacuum**				
GaAs Bottom sub-cell Eg = 1.42 eV	Window	n+	AlGaAs	$1x10^{19}$ /cm^3	0.01 µm
	Emitter	n	GaAs	$2x10^{18}$ /cm^3	0.01 µm
	Base	p	GaAs	$1x10^{17}$ /cm^3	004 µm
	BSF	p+	InGaP	$7x10^{18}$ /cm^3	0.01 µm
GaAs Substrate	Substrate	p+	GaAs	$1x10^{18}$ /cm^3	300 µm

In the case of the first design mentioned in Table 4.1, the sunlight strikes the InGaP sub-cell layer having the highest bandgap first. This layer will absorb photons of energy 1.9eV and higher and will transmit the less energetic photons to the next sub-cell (GaAs) in the stack. GaAs sub-cell will capture photons having energy less than 1.9eV but equals to or higher than 1.42eV. This arrangement makes use of the fact that junctions behave like low-pass photon energy filters transmitting only sub-bandgap light and acting like optical elements splitting spectrum to appropriate junctions for multi-junction photoconversion. The dual-junction solar cell will trade a lower current density for higher voltage and will divide the spectrum more efficiently.

The electrical characteristics of the InGaP top sub-cell are the same, so V_{OC} = 1.4096 V and Jsc = 0.0148 mA/cm^2. The Jsc GaAs bottom sub-cell characteristics are changed and now it has a drop Jsc = 0.0166 mA/cm^2 and slightly changes of V_{OC} = 1.0539 V. In this comparison, the GaAs bottom sub-cell has the highest Jsc but lowest Voc, and the InGaP top sub-cell has the lowest Jsc but highest Voc. The J-V curve for the GaAs bottom sub-cell is shown in Figure 4.1:

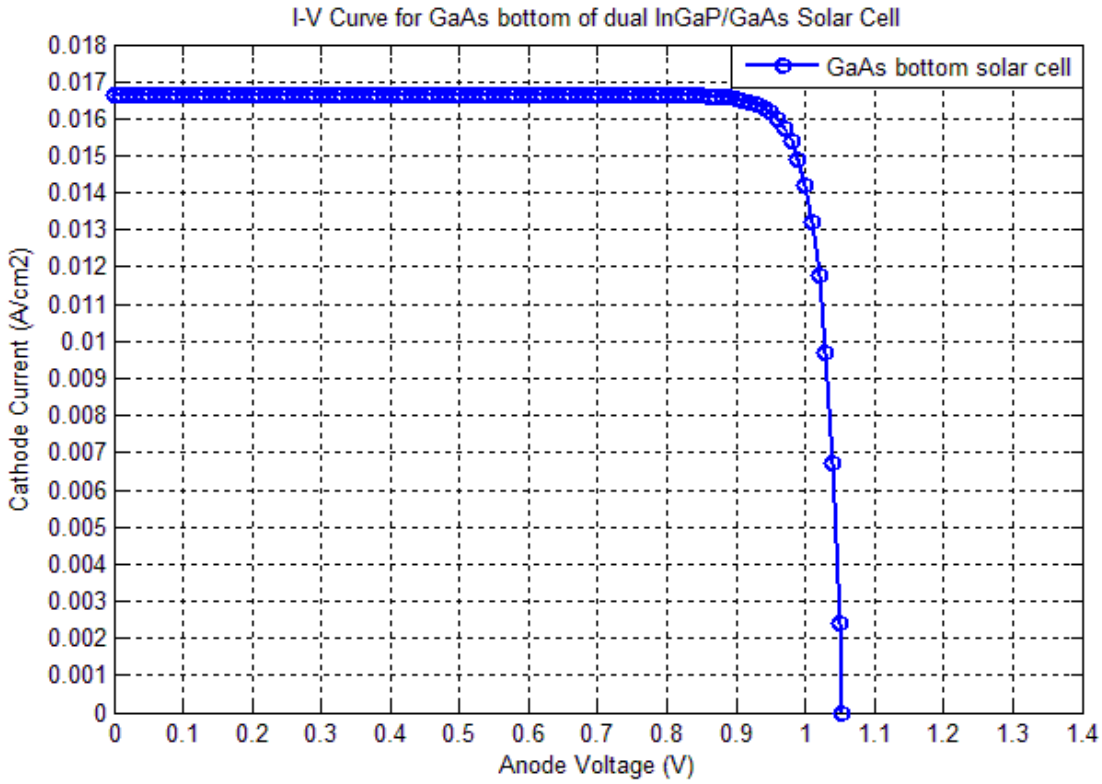

Figure 4.1: J-V Curve for GaAs bottom sub-cell of InGaP/GaAs dual-junction solar cell

The five most important characteristics of the GaAs bottom sub-cell of InGaP/GaAs dual–junction solar cell are organized in Table 4.2:

Table 4.2: GaAs Bottom sub-cell characteristics of InGaP/GaAs dual-junction solar cell

	Jsc (A/cm^2)	Voc (V)	Pmax (W/cm^2)	FF	η %
GaAs Bottom sub-cell	0.0166	1.0539	0.0153	0.8750	15.35

After successfully modeling the dual-junction solar cell, as expected, both cells produce the same voltage as before. The InGaP top sub-cell is totally unaffected. On the contrary, the GaAs bottom sub-cell produces less short circuit current density (Jsc = 0.0166 mA/cm^2) due to the fact that higher energy photons have been absorbed by all the layers over it, this can be seen in the new frequency response Figure 4.3. In this case, the GaAs bottom sub-cell is not current-matched to the current produced by the InGap top sub-cell (Jsc = 0.0148 mA/cm^2).

II.1.1.2 Comparison of the GaAs Individual and Bottom Sub-Cell of InGaP/GaAs Dual – Junction Solar Cell

The performances of the individual complete GaAs cell compared to that of the GaAs bottom sub-cell. A comparison of the J–V curves of the individual optimized GaAs solar cell and GaAs bottom sub-cell of InGaP/GaAs dual-junction solar cells is shown in Figure 4.2:

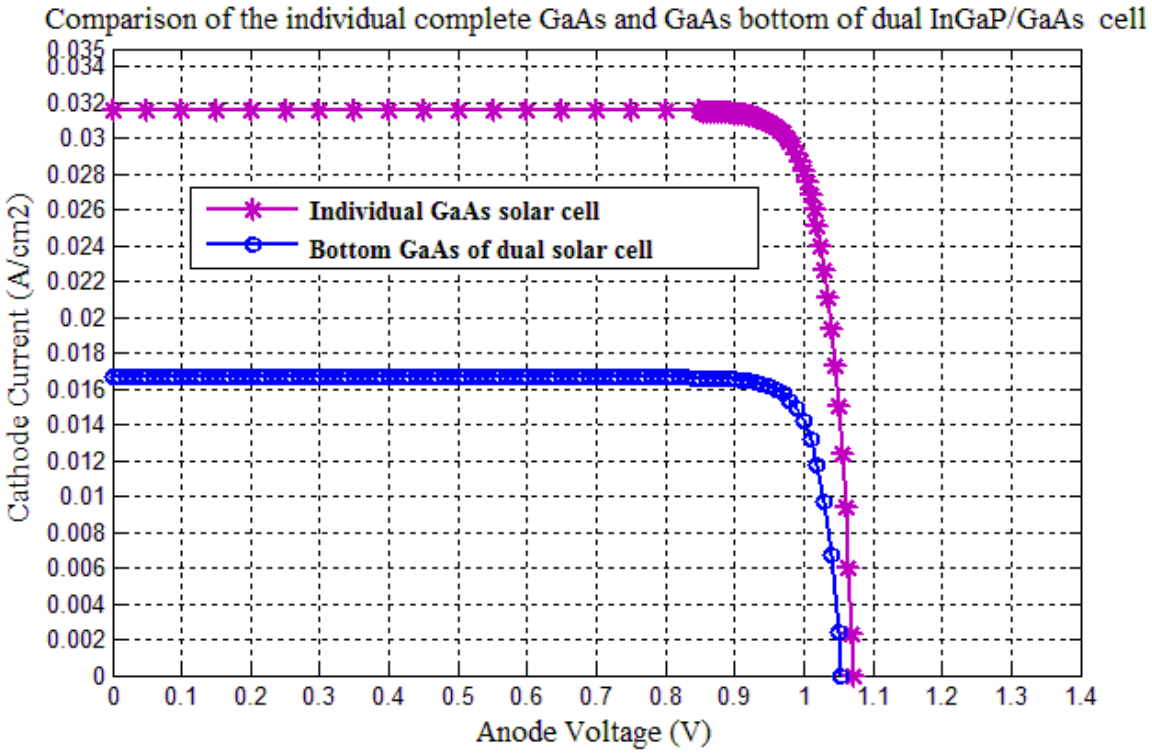

Figure 4.2: J–V curves for individual GaAs solar cell and GaAs bottom sub-cell of InGaP/GaAs dual-junction solar cell

The comparison of the five most important characteristics of the individual GaAs solar cell and GaAs bottom sub-cell of InGaP/GaAs dual-junction solar cell are organized in Table 4.3:

Table 4.3: Comparison of the characteristics for individual GaAs solar cell and bottom GaAs sub-cell of dual InGaP/GaAs solar cell

	Jsc (A/cm^2)	Voc (V)	Pmax (W/cm^2)	FF	η %
Individual GaAs solar cell	0.0315	1.0726	0.0294	0.8688	29.39
Bottom GaAs sub-cell	0.0166	1.0539	0.0153	0.8750	15.35

As expected, bottom GaAs sub-cell of dual InGaP/GaAs solar cell now has decreased of Jsc from 0.0315 to 0.0166 A/cm^2 and slightly changes of V_{OC} from 1.0726 to 1.0539 V. Therefore decrease of η from 29.39 to 15.35 %.

For comparison of spectral responses for the stacked sub-cells and individual complete cell, as we will see in Figure 4.3 and as expected, the InGaP top sub-cell is totally unaffected it has the same spectral response it collects the same shorter wavelength light from 0.3 to 0.675 μm and passes the rest through. On the contrary, the GaAs bottom sub-cell his spectral response changed it collects just the mid-range wavelengths from 0.48 to 0.95 μm, due to the fact that higher energy photons have been absorbed by the InGaP top sub-cell over it, so the range wavelengths from 0.3 to 0.48 μm absorbed by the InGaP top sub-cell.

As we will see in Figure 4.3, it is clear that the tandem cell is better suited to perform photoconversion throughout a wider range of wavelengths. This is by virtue of each sub-cell being situated such that they are able to more effectively convert a certain section of the solar spectrum.

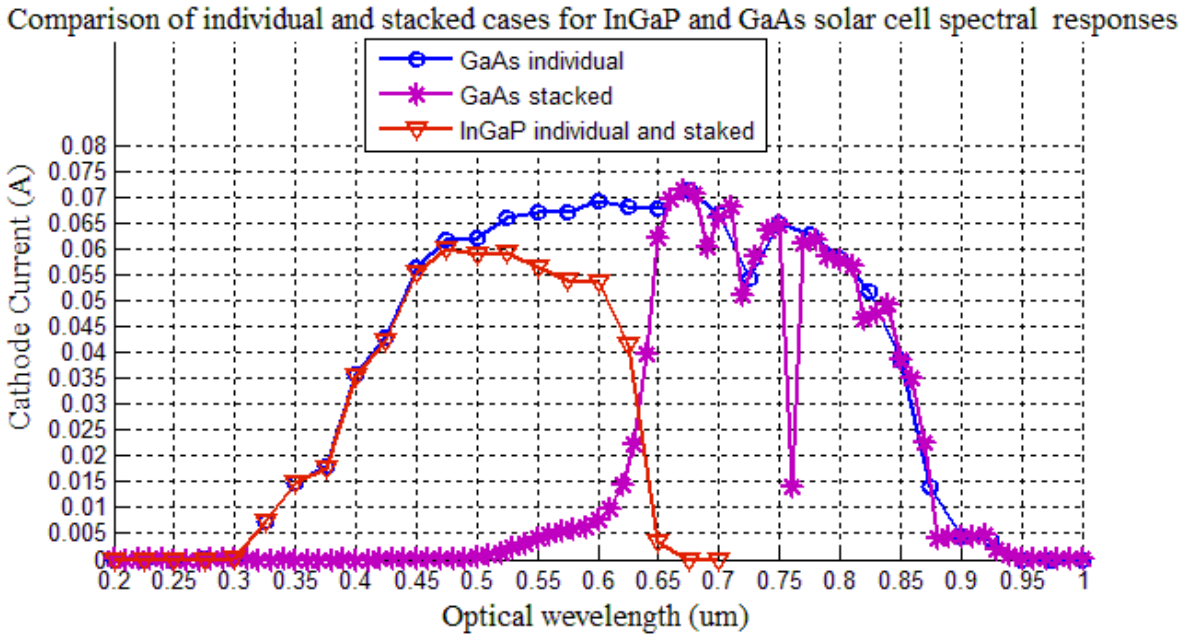

Figure 4.3: Spectral responses curves for individual and stacked cases for InGaP and GaAs solar cell

Another important graph shows the photo-generation rate plotted as a surface plot throughout the device structure, as we will see in Figure 4.4, Figure 4.5 and Figure 4.6. Note how the InGaP top and the GaAs bottom sub-cells are active and produce current in different wavelengths, according to their spectral response. Figure 4.4 shows a surface plot of the photogeneration rate throughout the optimized InGaP/GaAs dual-junction solar cell under AM1.5 illumination. The device layers are shown in the surface plot from the InGaP top sub-cell to GaAs bottom sub-cell. The legend within the figure defines the solar cell's photo-generation rates (e−/h+ pairs) per (s.cm^3). The Figure 4.4 indicates that the majority of photogeneration (8.589x10^{21} atoms/s.cm^3) does, in fact, occur within the first fraction of micron of depth in emitter InGaP layer where the majority of the light is absorbed and gradually decreases from emitter to base and from InGaP top sub-cell to GaAs bottom sub-cell.

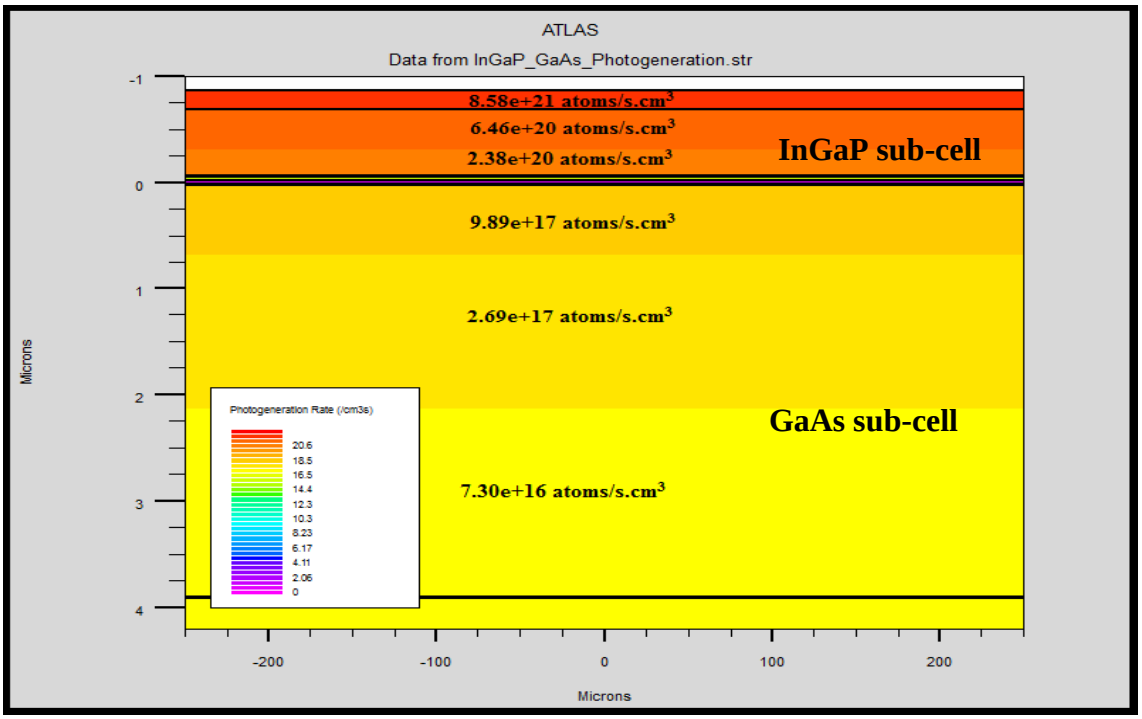

Figure 4.4: View of the carrier photogeneration rate, in the InGaP/GaAs dual-junction solar cell under AM1.5 illumination

Similarly, for a shorter wavelength range from 0.3 to 0.47 μm light source, as shown in Figure 4.5, the photogeneration occurs primarily in the InGaP top sub-cell; no photogeneration occurs in the GaAs bottom sub-cell, this corresponds with spectral responses curves for individual and stacked cases for InGaP and GaAs solar cell in the Figure 4.3.

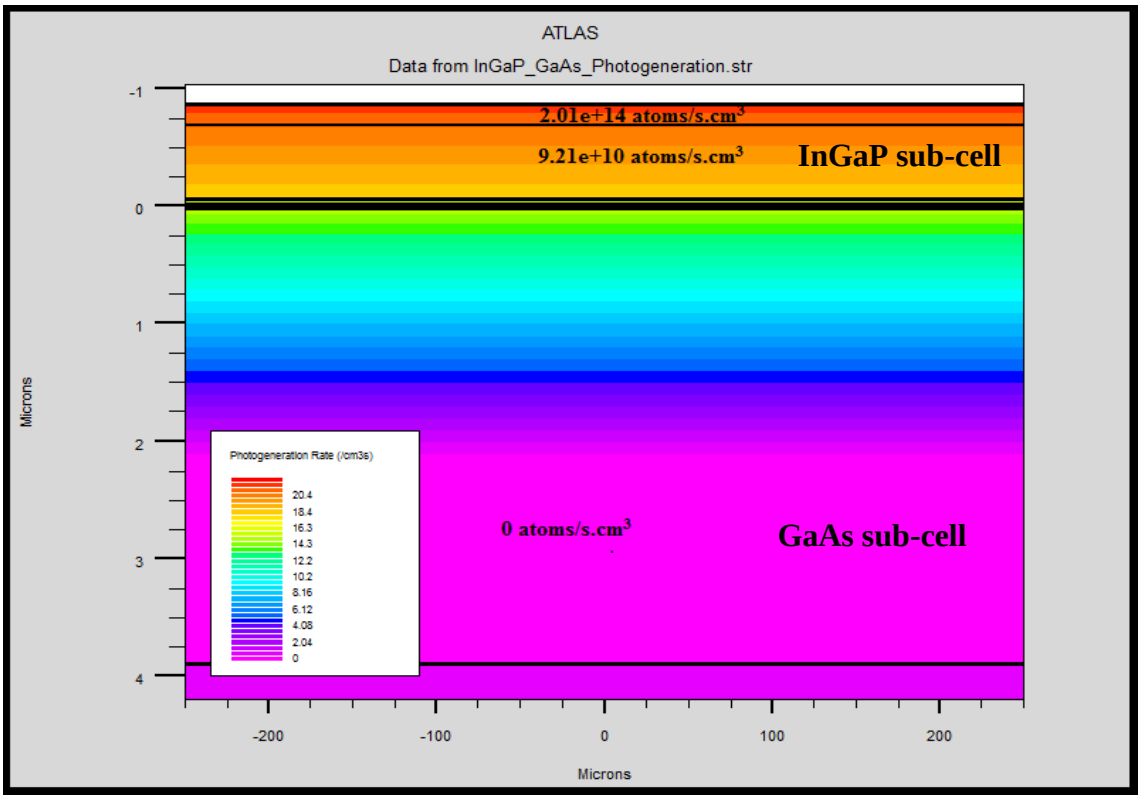

Figure 4.5: Photogeneration rate distributions throughout the device for a range shorter wavelength light from 0.3 to 0.47 μm illumination

On the contrary, as expected for mid-range wavelengths from 0.48 to 0.95 μm light source, as shown in Figure 4.6, InGaP top sub-cell is transparent to the incident light thus allowing the GaAs bottom sub-cell to be the primary current source, the photogeneration occurs in the GaAs bottom sub-cell; no photogeneration occurs in the InGaP top sub-cell, this corresponds with spectral responses curves for individual and stacked cases for InGaP and GaAs solar cell in the Figure 4.3.

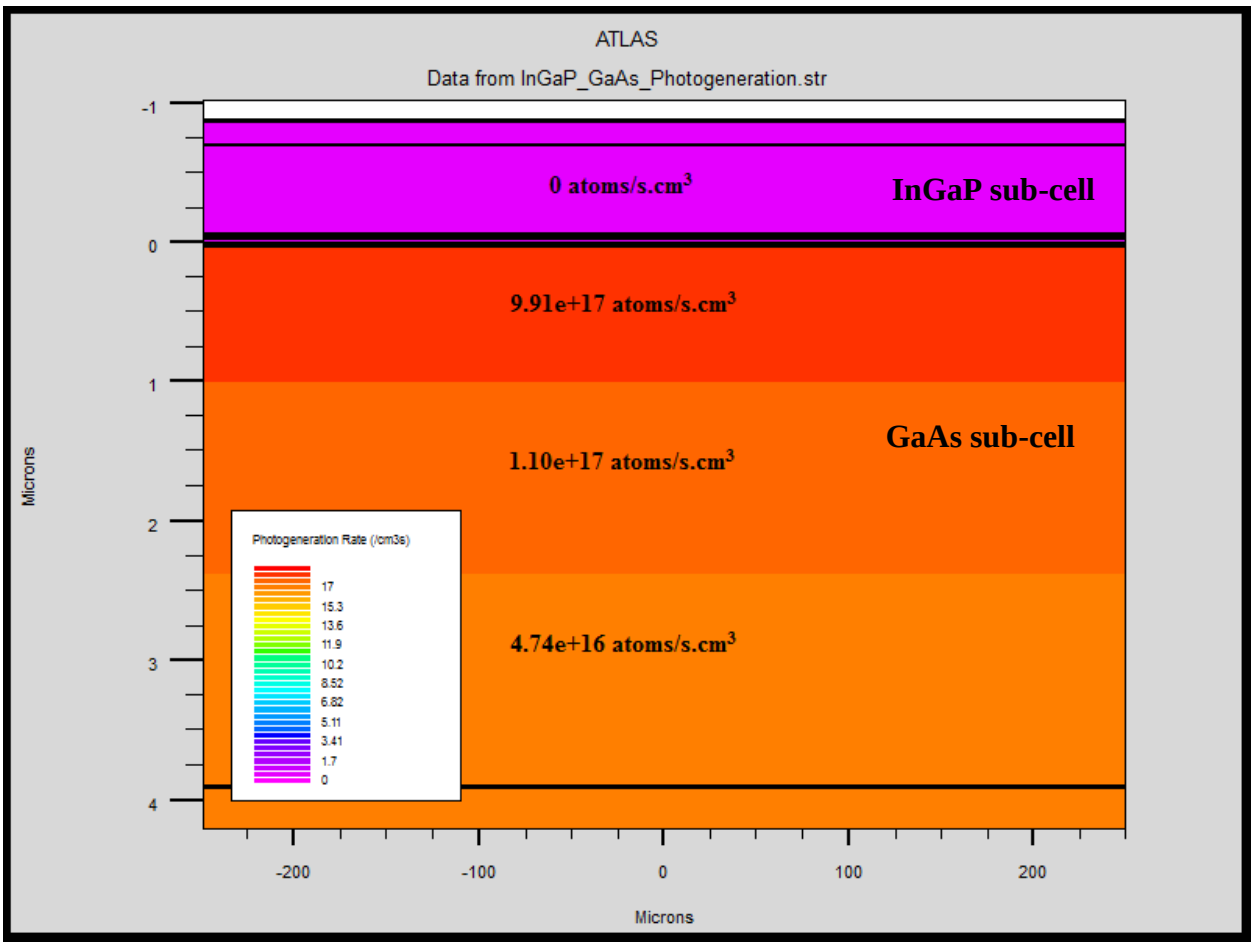

Figure 4.6: Photogeneration rate distributions throughout the device for mid-range wavelengths light from 0.48 to 0.95 μm illumination

II.1.2 Monolithically Stacked Multi-Junction Solar Cell Design

Simulation of monolithically stacked multi-junction solar cells is more complex than mechanically stacked cells, since accurate models of tunnel junctions are needed; a model consisting of a monolithically stacked InGaP/GaAs dual-junction solar cell connected by InGaP tunnel diode is developed. This model has been used together with the InGaP/GaAs mechanical stack model to evaluate the cell performance under AM1.5 illumination.

II.1.2.1 Monolithically Stacked InGaP/GaAs Dual-Junction Solar Cell

The device considered in this section is the InGaP/GaAs monolithically dual-junction solar cell, the dual-junction device, or more generally a multi-junction device, increases solar efficiency by enabling additional and more efficient absorption throughout the solar spectrum. The InGaP top sub-cell more efficiently collects short-wavelength light while remaining transparent to the light more efficiently collected by the GaAs bottom sub-cell, as mentioned in the previous section. This is the placement of the InGaP over the GaAs solar cell to build our dual-junction solar cell. The problem with simply connecting cells together lies to the fact that new junctions would be created between cells. Those junctions would be reversed–biased and their depletion–region electrostatic field would oppose the flow of carriers towards the contacts. This would prevent the cell from producing any current. Instead, specially prepared tunnel junctions can be used to solve this problem. For the two sub-cells made of p-n junctions that are n-type on p-type material, in between the InGaP and GaAs sub-cells is n-on-p InGaP tunnel junction with high doping levels $8x10^{18}$ donors $/cm^3$ and $8x10^{19}$ acceptor $/cm^3$, the tunnel junctions are p^{++}-type on n^{++}-type material. The greater doping concentration of the tunnel junctions allows for the free flow of carriers from the p^+ to the p^{++} regions and from the n^{++} to n^+ regions. The tunnel-junction interconnects between sub-cell layers is to provide a low resistance connection (ohmic conduction) between the p^+-type back surface field (BSF) layer of the InGaP top sub-cell and the n^+-type window layer of the GaAs bottom sub-cell. This layer allows for electrons in the top sub-cell to recombine with holes in the bottom sub-cell by means of internal field emission thus driving the current. The InGaP/GaAs dual-junction monolithic tandem solar cell becomes like in Table 4.4:

Table 4.4: Structure of InGaP/GaAs dual-junction monolithic tandem solar cell

Sub-Cell	Layer	Type	Material	Doping	Thickness
InGaP Top sub-cell Eg = 1.9 eV	Window	n+	AlGaAs	$5x10^{19}$ $/cm^3$	0.01 µm
	Emitter	n	InGaP	$5x10^{17}$ $/cm^3$	0.18 µm
	Base	p	InGaP	$1x10^{17}$ $/cm^3$	0.60 µm
	BSF	p+	AlGaAs	$5x10^{18}$ $/cm^3$	0.01 µm
InGaP Tunnel junction	Emitter	p++	InGaP	$8x10^{18}$ $/cm^3$	0.015 µm
	Base	n++	InGaP	$8x10^{19}$ $/cm^3$	0.015 µm
GaAs Bottom sub-cell Eg = 1.42 eV	Window	n+	AlGaAs	$1x10^{19}$ $/cm^3$	0.01 µm
	Emitter	n	GaAs	$2x10^{18}$ $/cm^3$	0.01 µm
	Base	p	GaAs	$1x10^{17}$ $/cm^3$	004 µm
	BSF	p+	InGaP	$7x10^{18}$ $/cm^3$	0.01 µm
Substrate	Substrate	p+	GaAs	$1x10^{19}$ $/cm^3$	300 µm

After successfully modeling InGaP/GaAs dual-junction monolithic tandem solar cell, the electrical characteristics are Jsc = 0.0149 A/cm^2, Voc = 2.4642V and η = 33.28%. The J-V curve for complete optimized InGaP/GaAs dual-junction monolithic solar cell is shown in Figure 4.7.

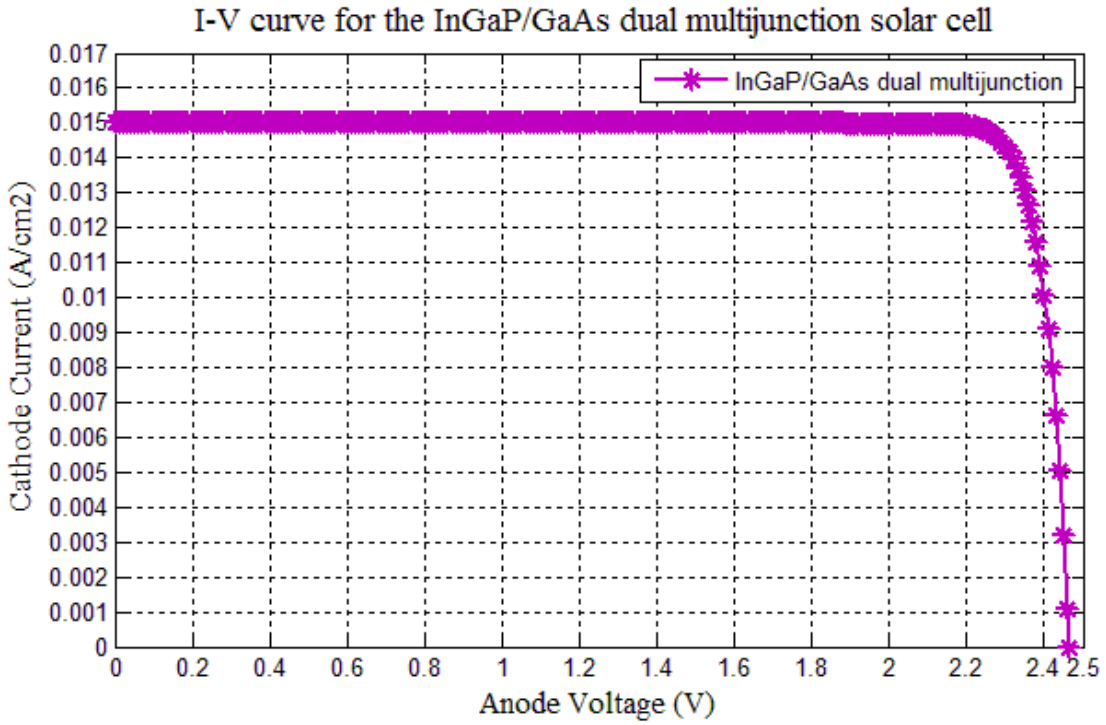

Figure 4.7: J-V curve for InGaP/GaAs dual-junction monolithic tandem solar cell

The five most important characteristics of the complete optimized InGaP/GaAs dual-junction monolithic Solar cell are organized in Table 4.5:

Table 4.5: InGaP/GaAs dual-junction monolithic solar cell characteristics

	Jsc (A/cm^2)	Voc (V)	Pmax (W/cm^2)	FF	η %
InGaP/GaAs dual-junction solar cell	0.0149	2.4642	0.0332	0.9010	33.28

II.1.2.2 Comparison of the Top, Bottom Sub-Cells and Dual InGaP/GaAs Solar Cells

After imported the sets of data into MATLAB software in order to combine them into one set of data that represented the overall J-V curve of the dual-junction solar cell, Figure 4.8 and Table 4.6 shows a comparison of J-V curves for InGaP top, GaAs bottom and InGaP/GaAs dual –junction solar cells, as expected, the total current will be determined by the layer with the lower output current, it is top InGaP cell (Jsc= 0.0148 A/cm^2), the simulated complete InGaP/GaAs dual-junction solar cell produced Jsc = 0.0149 A/cm^2, while the voltage from each is added together to give the overall voltage $V_{tandem} = V_{top} + V_{bottom}$ so V_{tandem}=1.4096+1.0539 = 2.4635 V, the simulated complete InGaP/GaAs dual-junction solar cell produced V_{OC} = 2.4642 V. These results lead to We successful modeling of the InGaP/GaAs dual-junction monolithic tandem solar cell. These valid results illustrate how well Silvaco ATLAS is at modeling multi-junction solar cells. The next case to be examined is the three-junction solar cell ensured that the efficiency would increase.

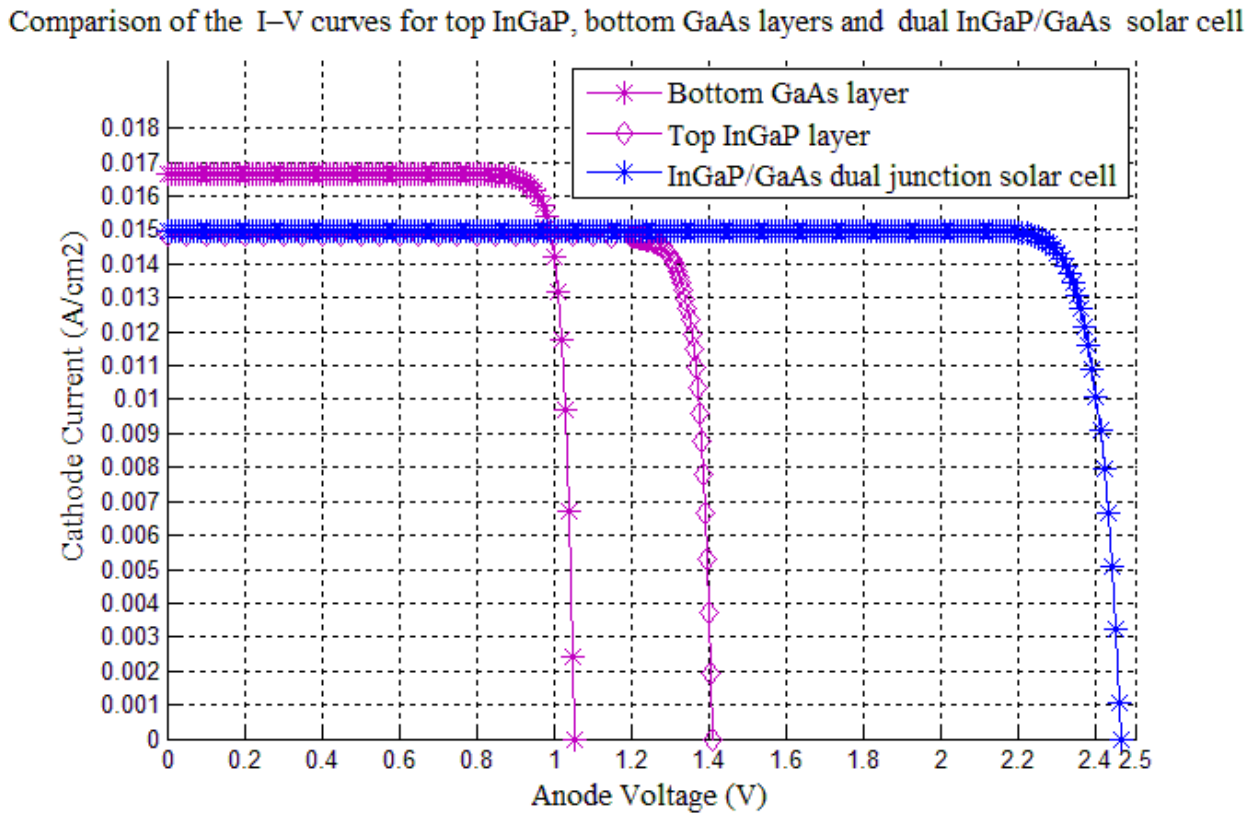

Figure 4.8: J–V curves for InGaP top, GaAs bottom and InGaP/GaAs dual–junction solar cells

The comparison of the five most important characteristics of the InGaP top, GaAs bottom sub-cells and InGaP/GaAs dual–junction solar cells are organized in Table 4.6:

Table 4.6: Comparison of the characteristics for the InGaP top, GaAs bottom sub-cells and InGaP/GaAs dual-junction solar cell

	Jsc (A/cm^2)	Voc (V)	Pmax (W/cm^2)	FF	η %
InGaP Top sub-cell	0.0148	1.4096	0.0185	0.8867	18.55
GaAs Bottom sub-cell	0.0166	1.0539	0.0153	0.8750	15.35
InGaP/GaAs Dual-junction solar cell	0.0149	2.4642	0.0332	0.9010	33.28

II.1.3 Current-Matching in InGaP/GaAs Dual-Junction Solar Cell

The sub-cells in our initial InGaP/GaAs dual-Junction solar cell design were not current-matched as shown in Figure 4.10. As been mentioned above that the calculated Jsc's of GaInP and GaAs sub-cells are 0.0148 A/cm^2 and 0.0166 A/cm^2, respectively. This result clearly indicates that the Jsc of the GaInP/GaAs dual-junction solar cell is limited by the GaInP top sub-cell that has the lowest current output. Therefore, appropriate design changes in our InGaP/GaAs dual-junction solar cell structure were required to realize the current-matching condition between the sub-cells.

In a multi-junction cell, one of the most important design criteria is to achieve the current-matching between the sub-cells. In this section, we design the InGaP/GaAs dual-junction solar cell by optimizing short-circuit current matching between InGaP top and GaAs bottom sub-cells.

The multi-junction solar cells are typically current-matched by optimizing the doping and the thicknesses of various layers in each sub-cell. As the base thickness of top InGaP cell become thicker, the Jsc is increased for the top cell and the Jsc is decreased for the middle cell. Thus, we optimized the base thicknesses in the GaAs and the InGaP sub-cells to achieve the current-matching condition, for numerical simulation, the base thickness of top InGaP cell is optimized from 0.6 to 0.65 um with a $1x10^{18}$ cm^{-3} base doping concentration and the base thickness of bottom GaAs cell is optimized from 4 to 1.65 um under AM1.5G illumination.

Figure 4.9 shows the optimized current density-voltage (J-V) curves characteristics of the InGaP/GaAs dual-junction solar cell and InGaP top sub-cell, GaAs bottom sub-cell under AM1.5G illumination. It is to certify that the top and bottom sub-cells are current matching. Current-matching enables to extract the best performance from the InGaP/GaAs dual-junction cell, as a result, a short-circuit current density (Jsc) of 0.0149 A/cm^2, an open-circuit voltage (Voc) of 2.5374 V and a conversion efficiency (η) of 33.69 % are obtained, leading to an optimum current matching condition between top and middle sub-cells. The tandem cell short circuit current density represents the maximum value generated by the InGaP top sub-cell and practically matched by the GaAs bottom sub-cell photocurrent.

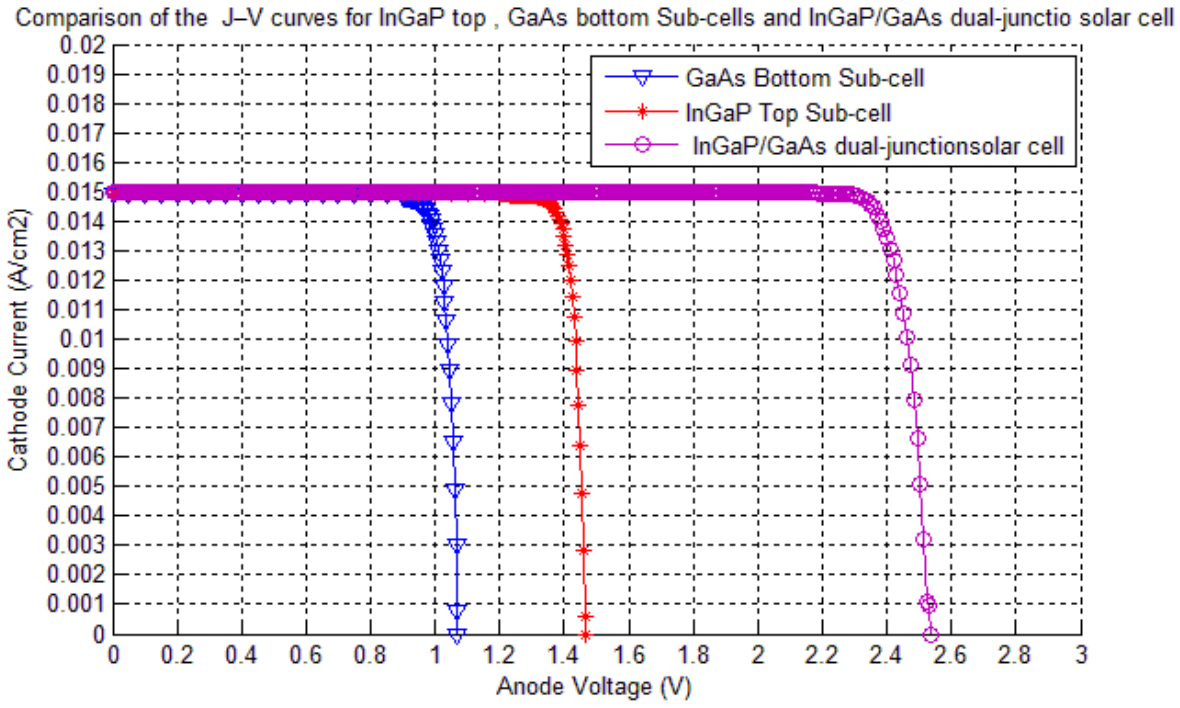

Figure 4.9: J–V curves for InGaP top, GaAs bottom sub-cells and InGaP/GaAs dual-junction solar cell

The cell parameters extracted before and after achieving the current-matching condition between the two sub-cells and tandem solar cell were summarized in Table 4.7.

Table 4.7: Parameters for InGaP top, GaAs bottom sub-cells and tandem solar cell before and after optimization under AM1.5G.

	Jsc (A/cm^2)	Voc (V)	Pmax (W/cm^2)	FF	η %
	Before current matching				
InGaP Top sub-cell (Eg=1.9 eV)	0.0148	1.4096	0.0185	0.8867	18.55
GaAs Bottom sub-cell (Eg=1.42 eV)	0.0166	1.0539	0.0153	0.8750	15.35
InGaP/GaAs Dual-junction solar cell	0.0149	2.4642	0.0332	0.9010	33.28
	After current matching				
InGaP Top sub-cell (Eg=1.9 eV)	0.01490	1.4660	0.0197	0.9059	19.78
GaAs Bottom sub-cell (Eg=1.42 eV)	0.01493	1.0714	0.0139	0.8701	13.91
InGaP/GaAs Dual-junction solar cell	0.0149	2.5374	0.0336	0.8887	33.69

It can be seen that, as the InGaP base becomes thicker from 0.6 to 0.65 with highly doped from $1x10^{17}$ cm^{-3} to $1x10^{18}$ cm^{-3} base doping concentration in the InGaP top sub-cell the Jsc current density produced becomes larger due to an increase in the absorption depth for the photons to be absorbed in the p-InGaP base, as a result, now has increase of photo-generate current density Jsc from 0.0148 to 0.01490 A/cm^2 and now the optimized current-matching InGaP/GaAs dual-junction solar cell has an increase of V_{OC} from 2.4642 to 2.5374 V. Therefore increase of efficiency η from 18.55 to 19.78 %, thus, allowed fewer photons to pass through to the bottom GaAs sub-cell, resulting in a reduction of photo-generate current density Jsc in the GaAs sub-cell at the cost of increase in Jsc from the InGaP sub-cell, as a result, now has a decrease of Jsc from 0.0166 to 0.01493 A/cm^2. Therefore decrease of efficiency η from 15.35 to 13.91 %.

II.2 InGaP/GaAs/Ge Triple-Junction Solar Cell

After the demonstration of mechanically and monolithically stacked GaAs/Ge dual-junction solar cell, the InGaP/GaAs/Ge triple-junction solar cells were realized as well, following similar processing steps. Once InGaP/GaAs dual-junction solar cell had been built, modeled, and verified Silvaco ATLAS as an accurate means to model solar cells, the final step was to build the overall triple junction solar cell based on the dual-junction design. The transition from the InGaP/GaAs dual-junction solar cell to the InGaP/GaAs/Ge triple-junction solar cell implies the development of a third junction, namely the Ge bottom sub-cell. Ge is a material with very low bandgap (Eg = 0.67eV). This means that it can produce energy even with very low–energy photons. As InGaP and GaAs upper sub-cells absorb most of the high–energy photons, Ge is ideal for a bottom sub-cell in a triple-junction configuration

II.2.1 InGaP/GaAs/Ge Triple-Junction Solar Cell Mechanical Stack

In a first attempt to create an InGaP/GaAs/Ge triple-junction monolithic tandem solar cell, the mechanically stacked structure Table 4.8 was used for simplicity. The means by which this was accomplished was starting with a sub-cell of InGaP on top, a sub-cell of GaAs in the middle, and a bottom sub-cell consisting of Ge. The vacuum was placed in between these layers to simulate the tunnel junctions of the solar cell.

Table 4.8: Mechanically stacked InGaP/GaAs/Ge triple-junction solar cell

Sub-Cell	Layer	Type	Material	Doping	Thickness
InGaP Top sub-cell Eg = 1.9 eV	Window	n+	AlGaAs	$5x10^{19}$ /cm^3	0.01 µm
	Emitter	n	InGaP	$5x10^{17}$ /cm^3	0.18 µm
	Base	p	InGaP	$1x10^{17}$ /cm^3	0.60 µm
	BSF	p+	AlGaAs	$5x10^{18}$ /cm^3	0.01 µm
Vacum	**Vacum**				
GaAs Middle sub-cell Eg = 1.42 eV	Window	n+	AlGaAs	$1x10^{19}$ /cm^3	0.01 µm
	Emitter	n	GaAs	$2x10^{18}$ /cm^3	0.01 µm
	Base	p	GaAs	$1x10^{17}$ /cm^3	004 µm
	BSF	p+	InGaP	$7x10^{18}$ /cm^3	0.01 µm
Vacum	**Vacum**				
Ge Bottom sub-cell Eg = 0.67 eV	Window	n+	GaAs	$7x10^{18}$ /cm^3	0.05 µm
	Emitter	n	Ge	$2x10^{18}$ /cm^3	0.10 µm
	Substrate	p	Ge	$1x10^{17}$ /cm^3	300 µm

In case of the first design mentioned in Table 4.8 the sunlight strikes the InGaP sub-cell layer having the highest bandgap first. This layer will absorb photons of energy 1.9eV and higher and will transmit the less energetic photons to the next sub-cell layer (GaAs) in the stack. GaAs sub-cell layer will capture photons having energy less than 1.9eV but equals to or higher than 1.42eV. The Ge subcell layer will absorb photons of energy equals to and higher than 0.67 eV but less than 1.42eV. This arrangement makes use of the fact that junctions behave like low-pass photon energy filters transmitting only sub-bandgap light and acting like optical elements splitting spectrum to appropriate junctions for multi-junction photo conversion. The triple-junction solar cell will trade a lower current density for higher voltage and will divide the spectrum more efficiently. The J-V curve for the GaAs middle and Ge bottom sub-cell of InGaP/GaAs/Ge triple multi-junction solar cell are shown in Figure 4.10 and Figure 4.11 respectively:

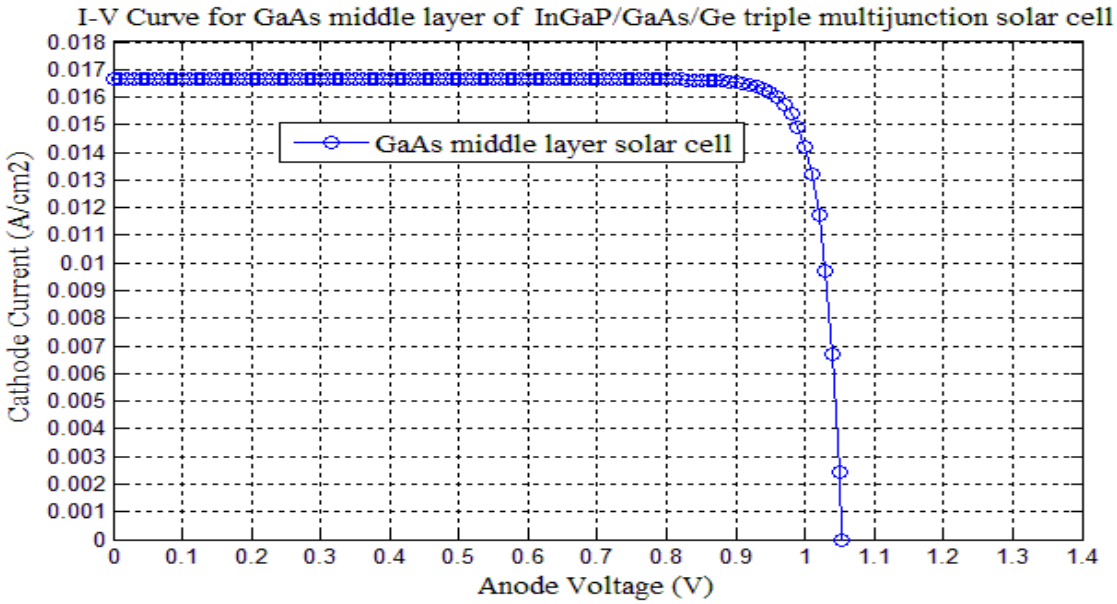

Figure 4.10: J-V Curve for GaAs middle sub-cell of InGaP/GaAs/Ge triple multijunction solar cell

The five most important characteristics of the GaAs middle sub-cell of InGaP/GaAs/Ge triple junction solar cell are organized in Table 4.9:

Table 4.9: GaAs middle sub-cell characteristics

	Jsc (A/cm^2)	Voc (V)	Pmax (W/cm^2)	FF	η %
GaAs middle sub-cell	0.0166	1.0539	0.0153	0.8750	15.35

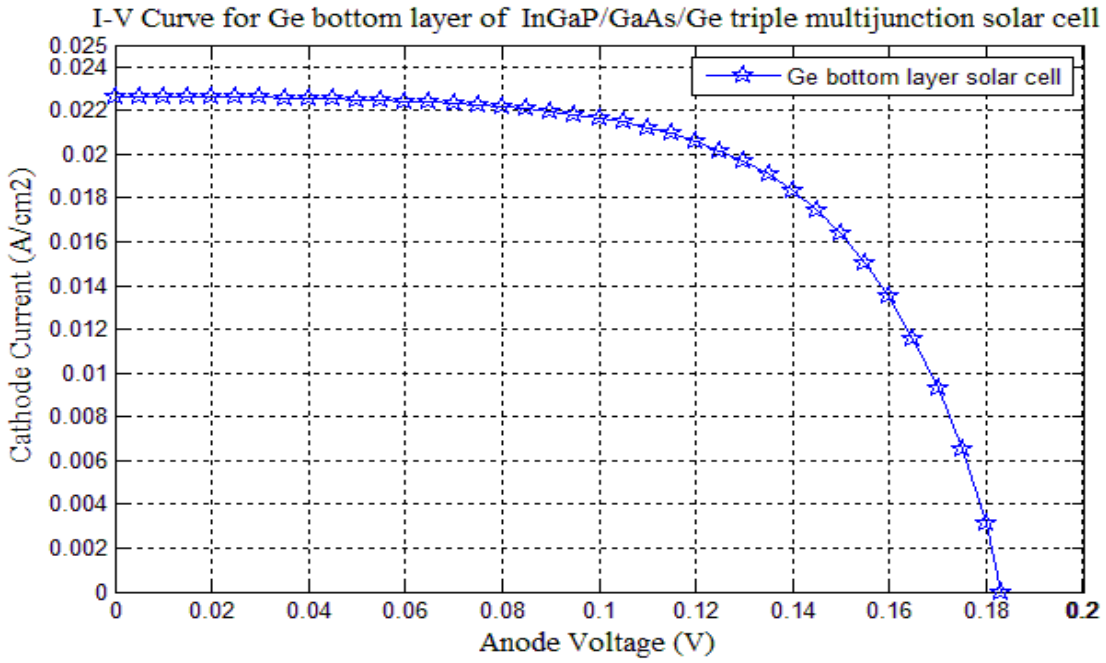

Figure 4.11: J-V Curve for Ge bottom sub-cell of InGaP/GaAs/Ge triple multi-junction solar cell

The five most important characteristics of the Ge bottom sub-cell of InGaP/GaAs/Ge triple junction solar cell are organized in Table 4.10:

Table 4.10: Ge bottom sub-cell characteristics

	Jsc (A/cm^2)	Voc (V)	Pmax (W/cm^2)	FF	η %
Ge bottom sub-cell	0.0226	0.1838	0.0025	0.6178	2.57

The electrical characteristics of the InGaP top sub-cell are the same, so V_{OC} = 1.4096 V and Jsc = 0.0148 mA/cm^2. The Jsc GaAs middle sub-cell and Ge bottom sub-cell characteristics are degraded and now it has a drop Jsc = 0.0166 mA/cm^2 and slightly change of V_{OC} = 1.0539 V for GaAs middle sub-cell as the same case in the GaAs bottom sub-cell for InGaP/GaAs dual-junction solar cell, Jsc = 0.0226 mA/cm^2 and slightly change of V_{OC} = 0.1838 V for Ge bottom sub-cell.

After successfully modeling the InGaP/GaAs/Ge triple-junction solar cell, as expected, each cell produces the same voltage as before. The InGaP top sub- cell is totally unaffected. On the contrary, the GaAs middle and Ge bottom sub-cells produce less current, due to the fact that higher energy photons have been absorbed by all the sub-cells over it. This can be seen in the new frequency response Figure 4.14 and Figure 4.15.

II.2.1.1 Comparison of Individual Cells and Sub-Cells of the InGaP/GaAs/Ge Triple-Junction Solar Cell

In order to extract an overall J-V curve, three sets of anodes and cathodes were placed on the top, middle, and bottom layers of the cell, which then obtained three J-V curves. Before combining the data to achieve one overall curve, the three curves were compared to their respective individual cell to ensure that the middle and bottom sub-cells J-V characteristics had degraded due to the top sub-cell absorbing some of the incident light.

After successfully modeling the triple-junction solar cell, as expected, both cells produce the same voltage as before. The output of top sub-cell and the individual complete InGaP solar cell is the same we saw in Figure 3.12 (chapter 3). These two curves are identical because they have the same parameters and the same incident light shone on them. A comparison of the outputs of the middle sub-cell to the individual GaAs solar cell and the bottom sub-cell to the individual Ge solar cell are found in Figure 4.12, Table 4.11 and Figure 4.13, Table 4.12 respectively. In these two comparisons, it can be clearly seen that the effect of placing a layer above it significantly reduces the characteristics of that cell, due to the fact that higher energy photons have been absorbed by all the layers over it, this can be seen in the new frequency response Figure 4.14 and Figure 4.15; however, having this extra power absorption available is what makes the multi-junction solar cell more efficient than a single solar cell.

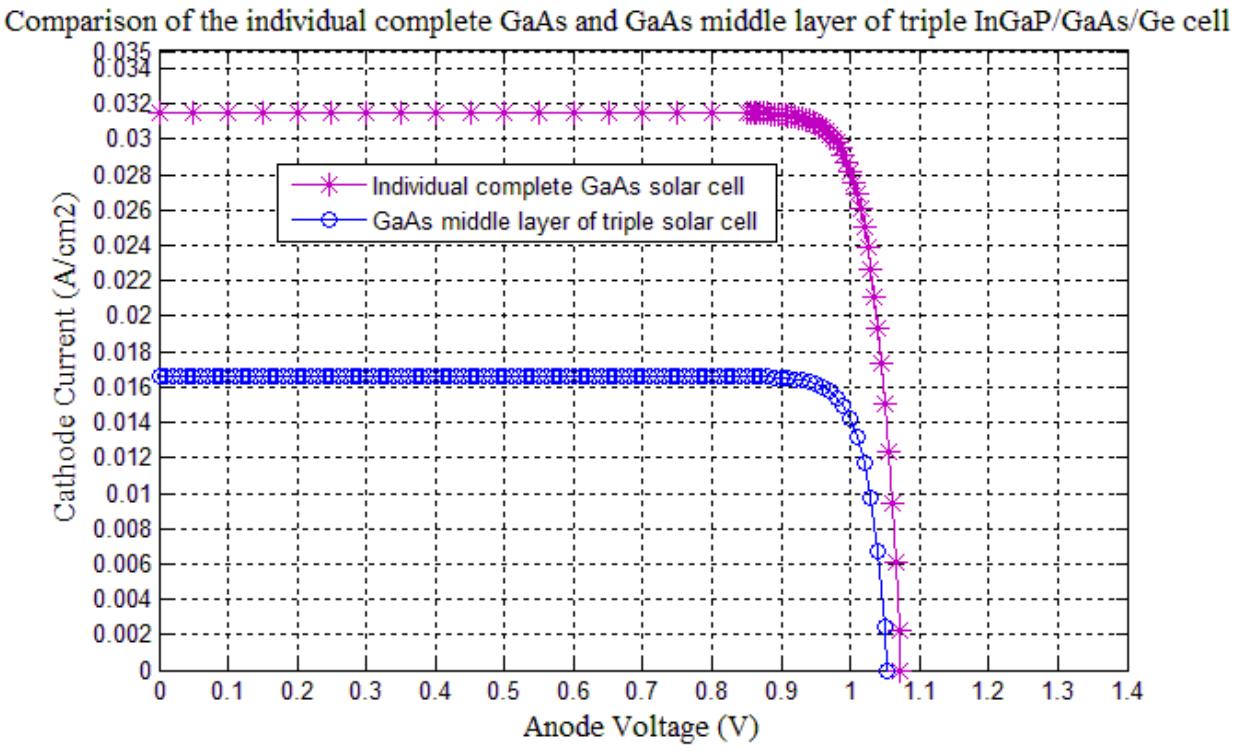

Figure 4.12: J-V curves of an Individual GaAs cell and the middle sub-cell of the triple junction InGaP/GaAs/Ge solar cell

The comparison of the five most important characteristics of the individual GaAs solar cell and middle sub-cell of the InGaP/GaAs/Ge triple-junction solar cell are organized in Table 4.11:

Table 4.11: Comparison of the characteristics for Individual GaAs solar cell and middle sub-cell of the InGaP/GaAs/Ge triple junction solar cell

	Jsc (A/cm^2)	Voc (V)	Pmax (W/cm^2)	FF	η %
Individual GaAs solar cell	0.0315	1.0726	0.0294	0.8688	29.39
GaAs middle sub-cell	0.0166	1.0539	0.0153	0.8750	15.35

As expected, GaAs middle sub-cell of the triple-junction InGaP/GaAs/Ge solar cell now has a drop of Jsc from 0.0315 to 0.0166 A/cm^2 and slightly changes of V_{OC} from 1.0726 to 1.0539 V. Therefore decrease of η from 29.39 to 15.35 %.

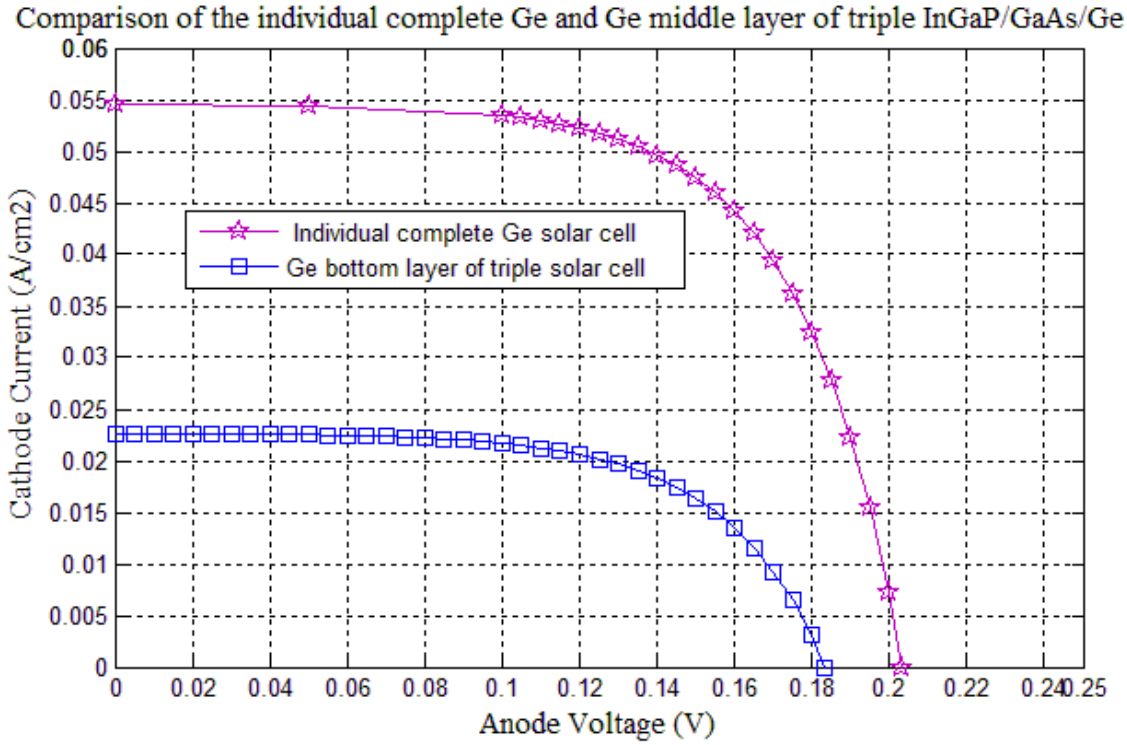

Figure 4.13: J-V curves of an Individual Ge solar cell and the bottom sub-cell of the InGaP/GaAs/Ge triple junction solar cell

The comparison of the five most important characteristics of the individual Ge solar cell and the bottom sub-cell of the InGaP/GaAs/Ge triple junction solar cell are organized in Table 4.12:

Table 4.12: Comparison of the characteristics for Individual Ge solar cell and the bottom sub-cell of the InGaP/GaAs/Ge triple junction solar cell

	Jsc (A/cm^2)	Voc (V)	Pmax (W/cm^2)	FF	η %
Individual Ge solar cell	0.0545	0.2036	0.0071	0.6406	7.11
Ge bottom sub-cell	0.0226	0.1838	0.0025	0.6178	2.57

As expected, Ge bottom sub-cell of the triple junction InGaP/GaAs/Ge solar cell now has a drop of Jsc from 0.0545 to 0.0226 A/cm^2 and slightly changes of V_{OC} from 0.2036 to 0.1838 V. Therefore drop of η from 7.11 to 2.57 %.

For comparison of spectral responses for the stacked sub-cells and individual solar cell, as we saw in Figure 4.3 and as expected the InGaP top sub-cell is totally unaffected it has the same spectral response it collects the same shorter wavelength light from 0.3 to 0.675 µm and passes the rest through. On the contrary, the GaAs middle sub-cell his spectral response changed it collects just the mid-range wavelengths from 0.48 to 0.95 µm, due to the fact that higher energy photons have been absorbed by the top InGaP sub-cell over it, so the range wavelengths from 0.3 to 0.48 µm absorbed by the InGaP top sub-cell as shown in Figure 4.14 and Figure 4.16.

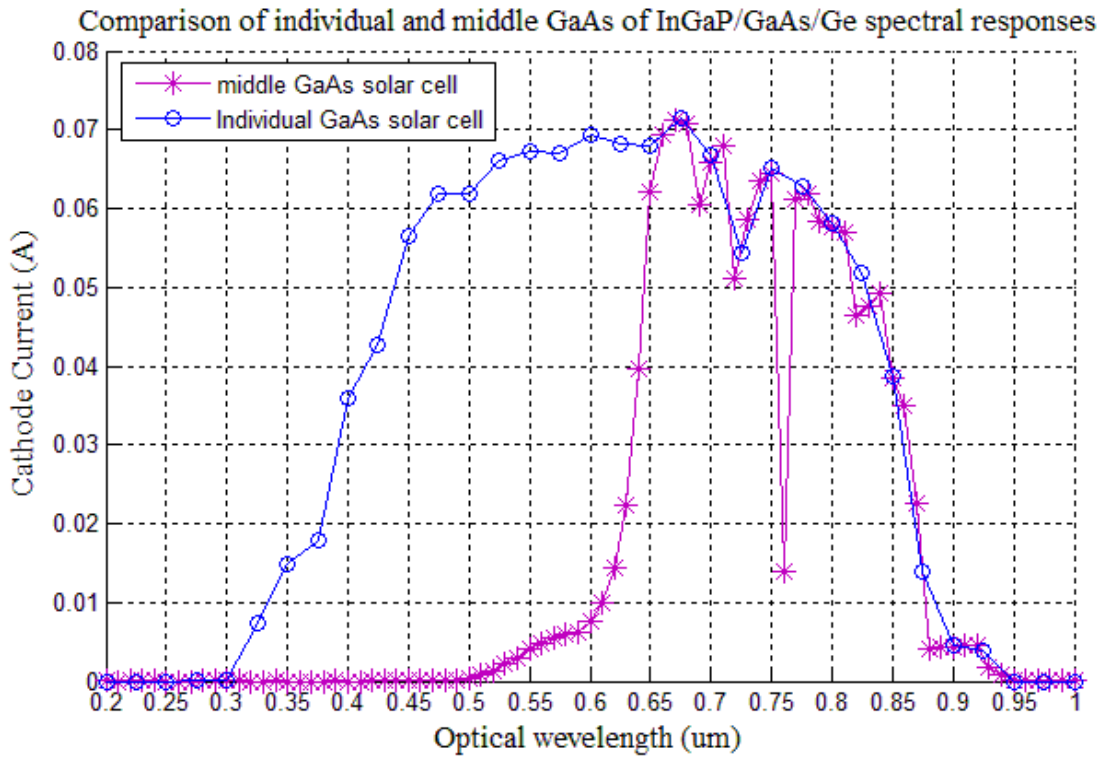

Figure 4.14: Spectral responses comparison of individual and GaAs middle sub-cell of InGaP/GaAs/Ge triple-junction solar cell

The Ge bottom sub-cell his spectral response changed it collects the small, mid-range and large wavelengths light from 0.84 to 1.82 µm as shown in Figure 4.15, due to the fact that higher energy photons have been absorbed by the InGaP top and the GaAs middle sub-cells over it, so the range wavelengths from 0.3 to 0.84 µm absorbed by the InGaP top and the GaAs middle sub-cells as shown in Figure 4.16.

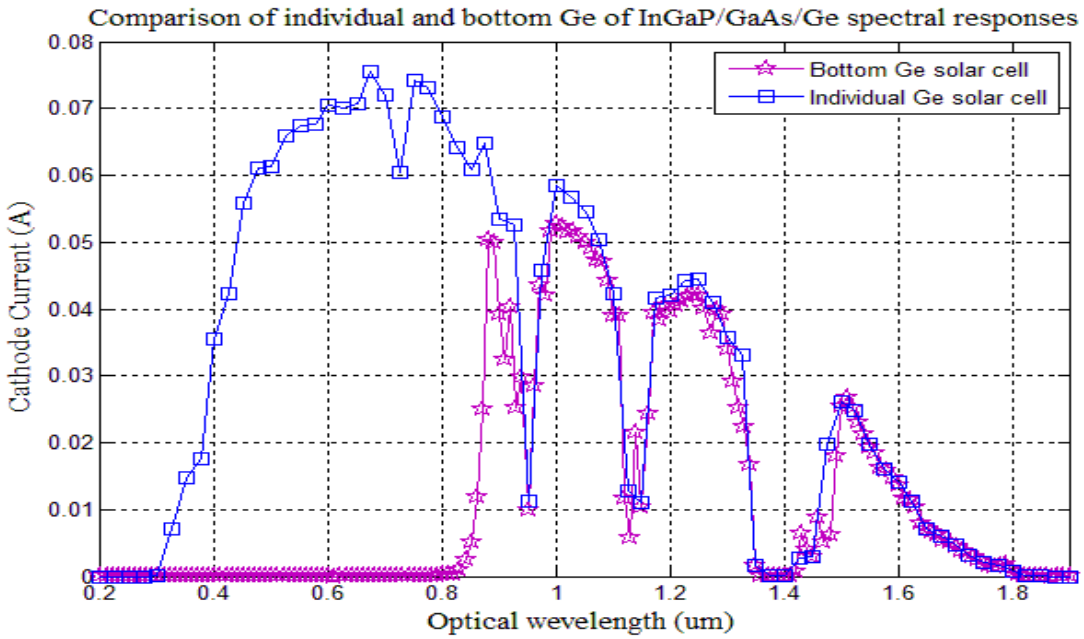

Figure 4.15: Spectral responses comparison of individual and Ge bottom solar cell of InGaP/GaAs/Ge triple-junction solar cell

In comparing the spectral response of the InGaP, GaAs, Ge sub-cells Figure 4.16 show it is clear that the multi-junction solar cell is better suited to perform photo-conversion throughout a wider range of wavelengths. This is by virtue of each sub-cell being situated such that they are able to more effectively convert a certain section of the solar spectrum.

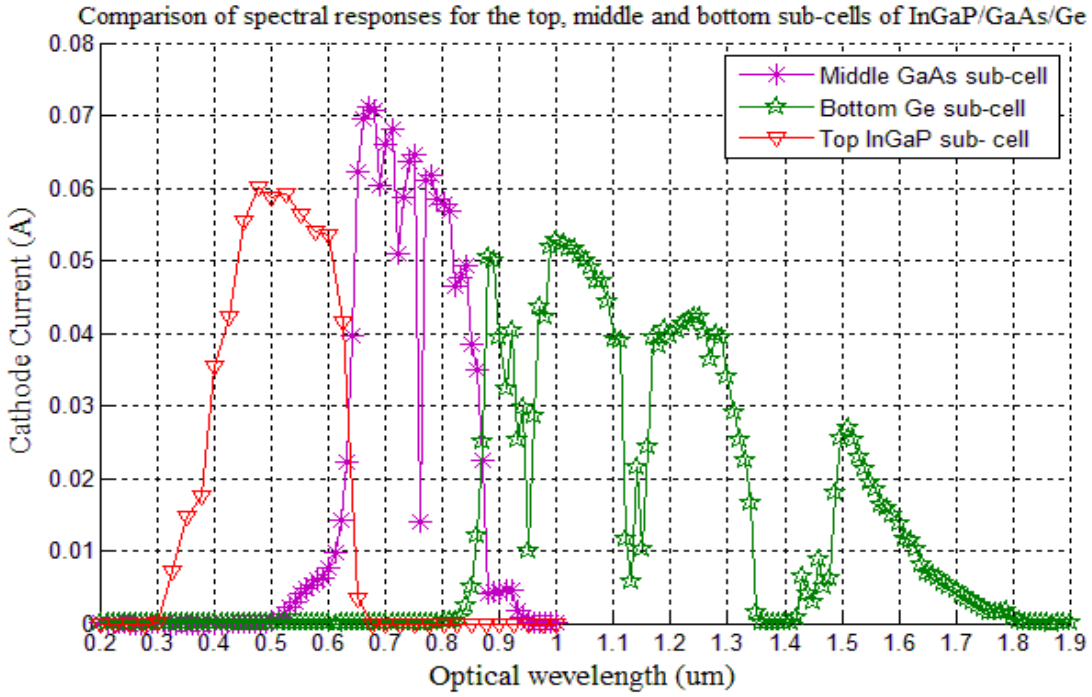

Figure 4.16: Spectral response of the InGaP/GaAs/Ge triple-junction solar cell showing the contributions of each sub-cell.

Like before, the frequency responses of both the individual and sub-cells have been produced and can be seen in Figure 4.17.

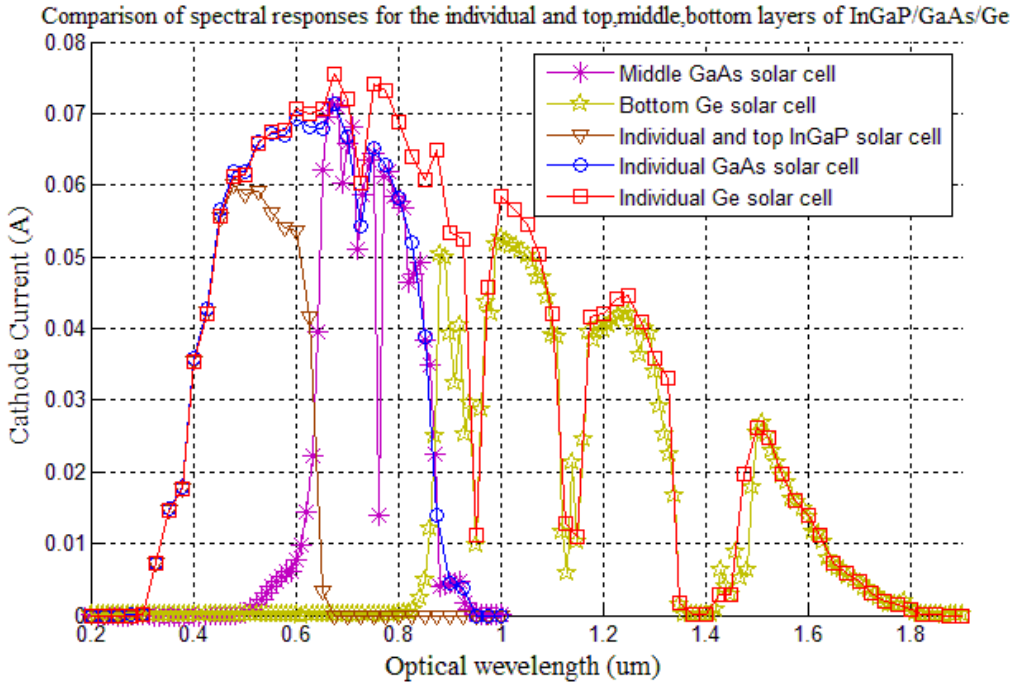

Figure 4.17: Spectral responses for the individual and top, middle, bottom sub-cells of InGaP/GaAs/Ge triple-junction solar cell

Another interesting graph shows the photogeneration rate versus the wavelength of the light. Note how the InGaP top, GaAs middle and Ge bottom sub-cells are active and produce current in different wavelengths, according to their frequency response as shown in Figure 4.18

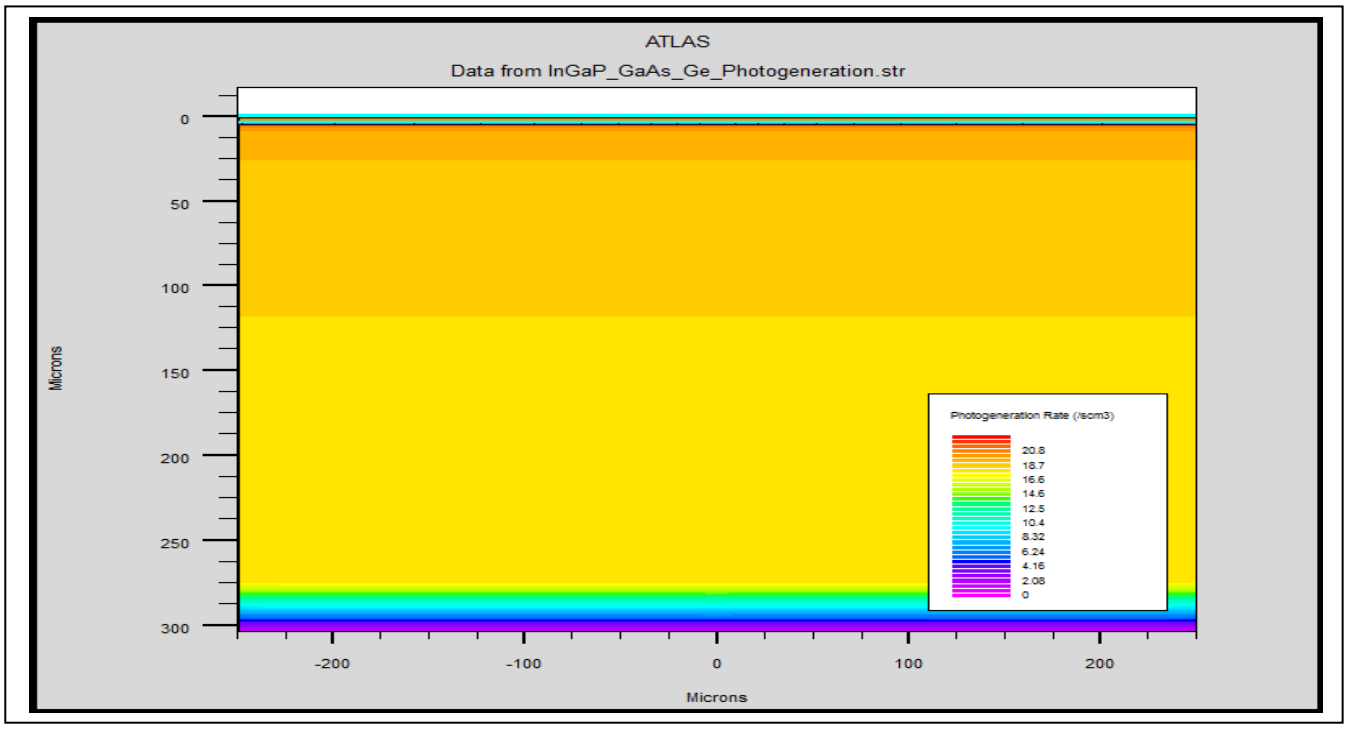

Figure 4.18: Photogeneration rate distributions throughout the InGaP/GaAs/Ge mechanically triple-junction solar cell under AM1.5 spectrum illumination

According to Figure 4.16, for a shorter wavelength light from 0.3 to 0.675 µm illumination the photogeneration throughout the InGaP top sub-cell is displayed in occurs only in the InGaP top sub-cell as shown in Figure 4.19 this indicates that, at these wavelengths, the vast majority of photogeneration occurs due to the InGaP top sub-cell and no photogeneration occurs in GaAs middle and Ge bottom sub-cells as shown in Figure 4.20.

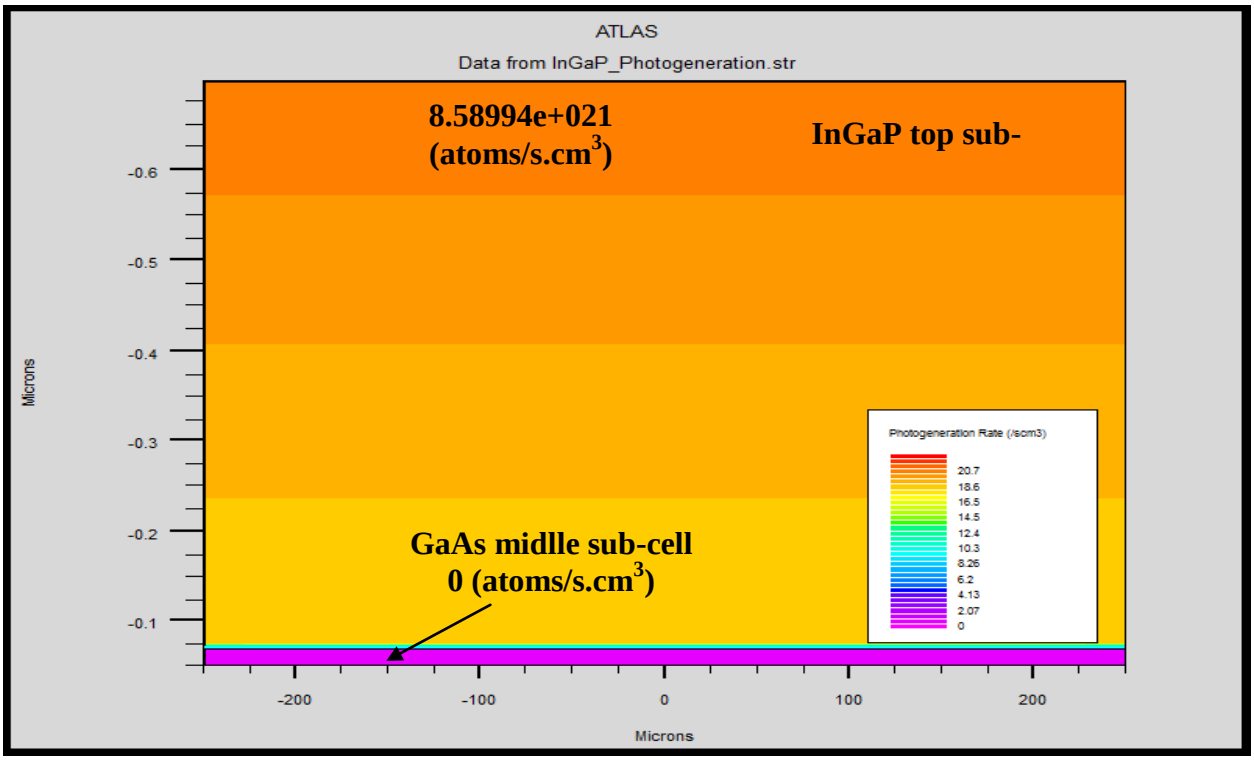

Figure 4.19: Photogeneration rate distributions throughout the InGaP top sub-cell (expanded view) of InGaP/GaAs/Ge triple-junction mechanically stacked solar cell for a shorter wavelength light from 0.3 to 0.675 µm illumination

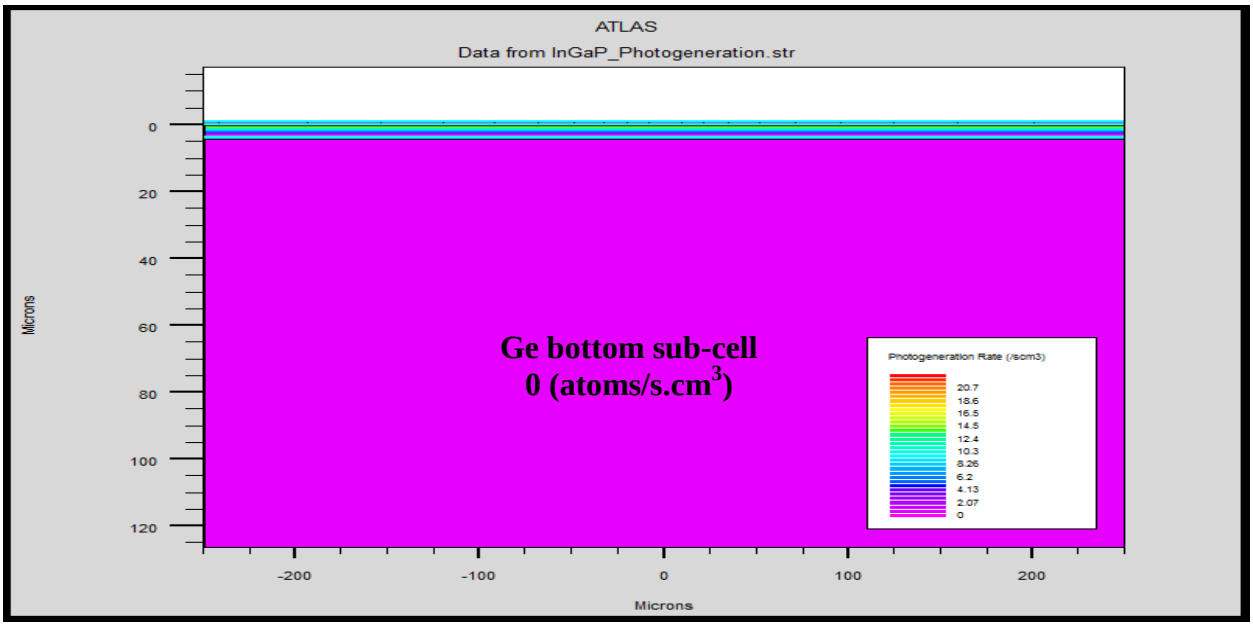

Figure 4.20: Photogeneration rate distributions throughout the InGaP/GaAs/Ge triple-junction mechanically stacked solar cell for a shorter wavelength light from 0.3 to 0.675 µm illumination

On the contrary, according to the Figure 4.16, for a mid-range wavelengths from 0.48 to 0.95 µm illumination, the photogeneration throughout the GaAs middle sub-cell is displayed in occurs only in the GaAs middle sub-cell as shown in Figure 4.21 this indicates that, at these wavelengths, the vast majority of photogeneration occurs due to the GaAs middle sub-cell and no photogeneration occurs in InGaP top and Ge bottom sub-cells as shown in Figure 4.22.

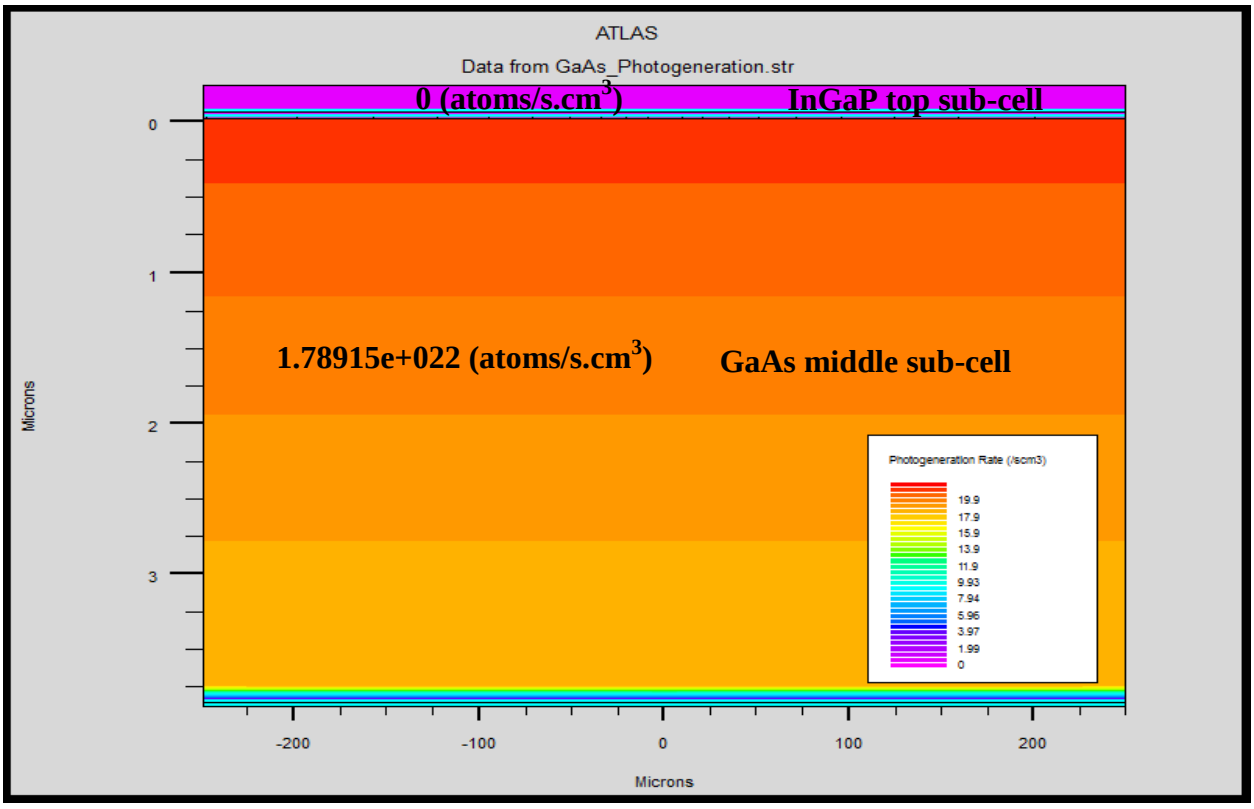

Figure 4.21: Photogeneration rate distributions throughout the GaAs middle sub-cell (expanded view) of InGaP/GaAs/Ge triple-junction mechanically stacked solar cell for a mid-range wavelengths from 0.48 to 0.95 µm illumination

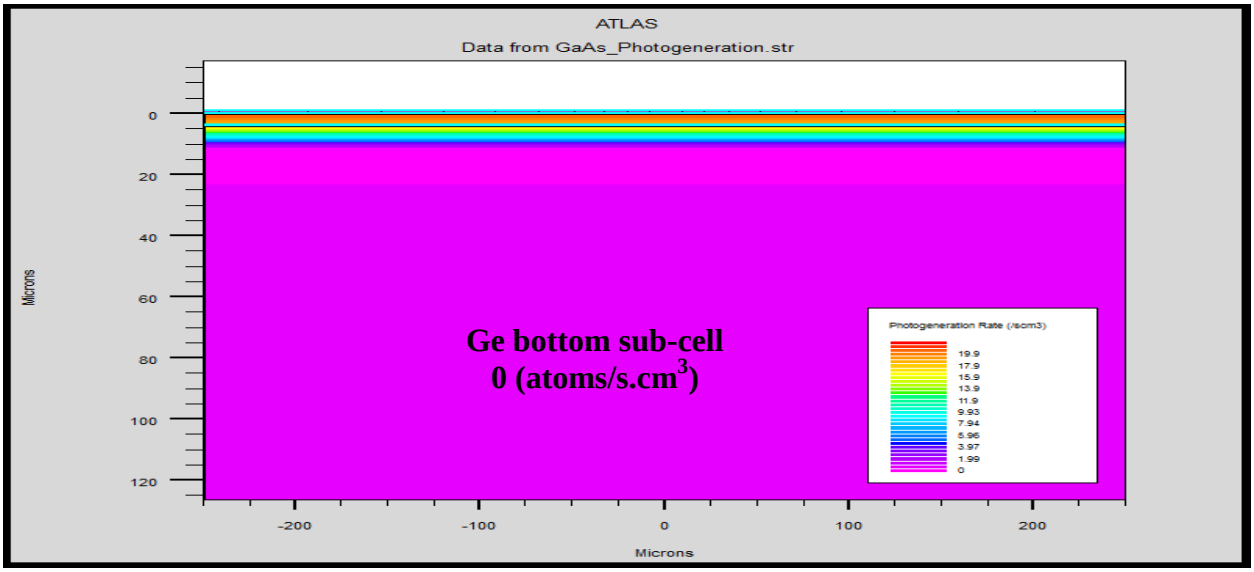

Figure 4.22: Photogeneration rate distributions throughout the InGaP/GaAs/Ge triple-junction mechanically stacked solar cell for a mid-range wavelengths from 0.48 to 0.95 µm illumination

On the other hand, according to the Figure 4.16, for a large wavelengths light from 0.84 to 1.82 μm illumination, the photogeneration throughout the Ge bottom sub-cell is displayed in occurs only in the Ge bottom sub-cell as shown in Figure 4.23 this indicates that, at these wavelengths, the vast majority of photogeneration occurs due to the Ge bottom sub-cell and no photogeneration occurs in InGaP top, GaAs middle sub-cells as shown in Figure 4.24.

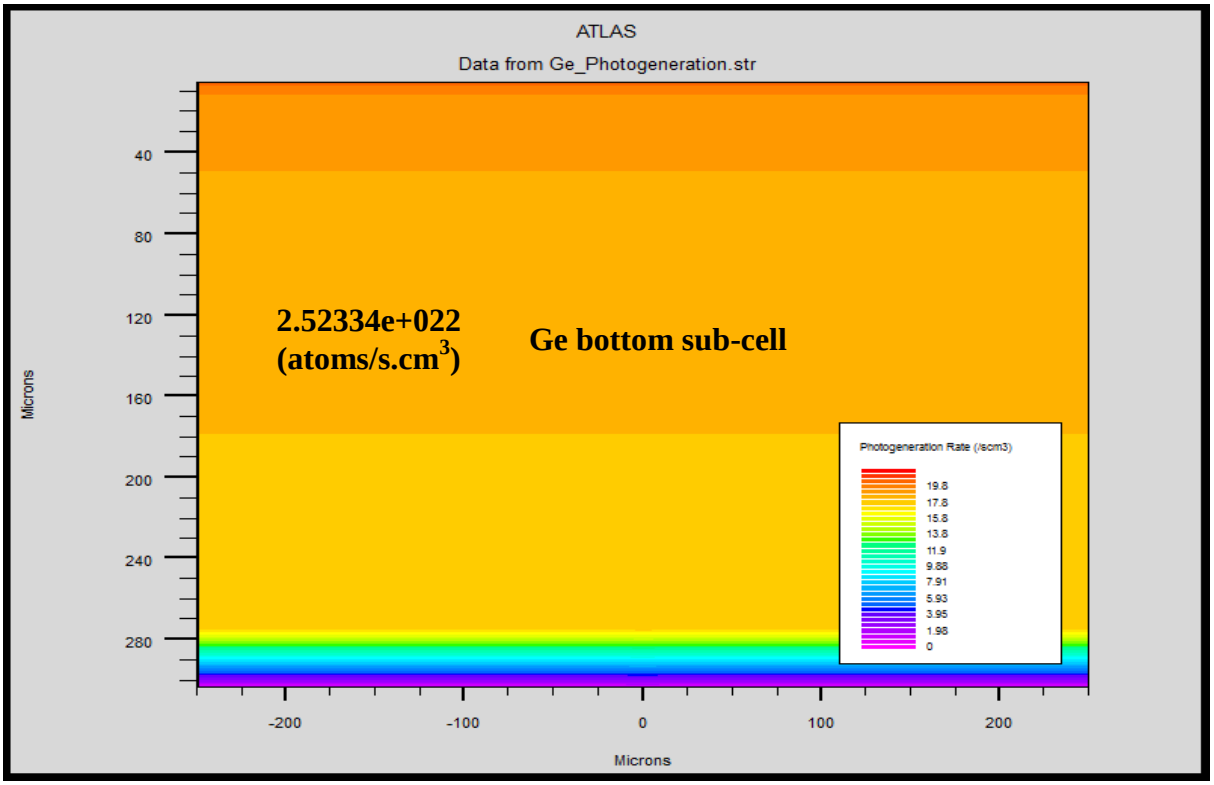

Figure 4.23: Photogeneration rate distributions throughout the Ge bottom sub-cell (expanded view) of InGaP/GaAs/Ge triple-junction mechanically stacked solar cell for large wavelengths from 0.84 to 1.82 μm illumination

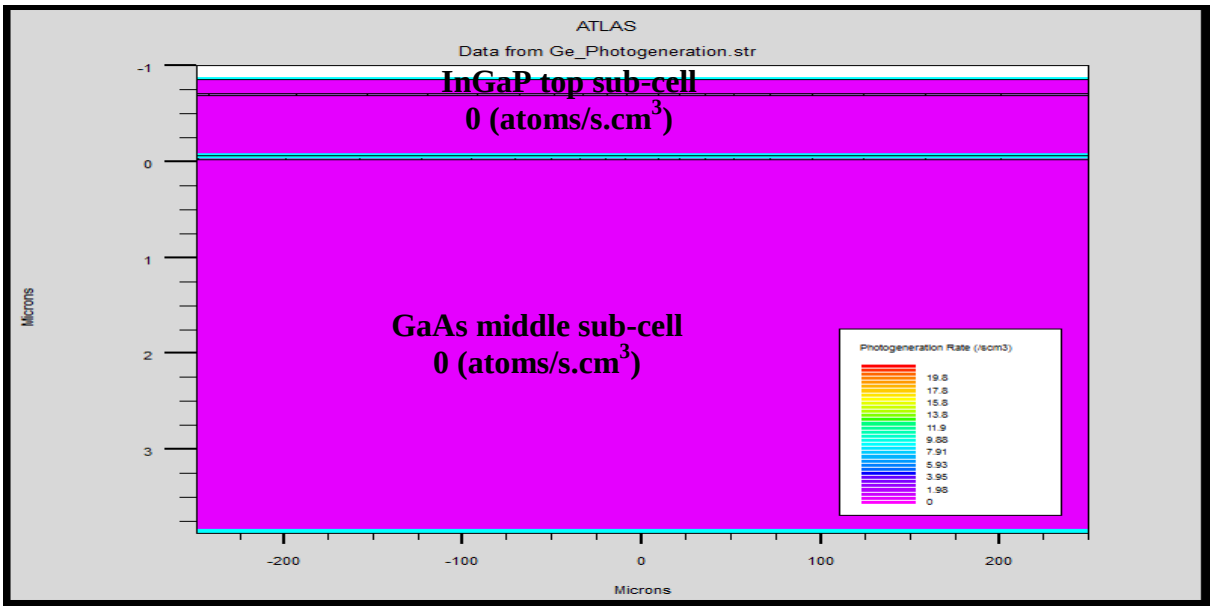

Figure 4.24: Photogeneration rate distributions throughout the InGaP/GaAs/Ge triple-junction mechanically stacked solar cell for a large wavelengths from 0.84 to 1.82 μm illumination

As a result, in the photogeneration rate distributions in Figure 4.19, in the shorter wavelength range from 0.3 to 0.675 μm, the photogeneration occurs only in the InGaP top sub-cell region. As the incident wavelength becomes longer, the major contribution of the photogeneration is shifted from the InGaP top sub-cell region to the Ge bottom cell area via the GaAs middle sub-cell. In the mid-range wavelength from 0.48 to 0.95 μm, photogeneration occurs only in the GaAs middle sub-cell region because the InGaP sub-cell is transparent to the incident light as shown in Figure 4.21. In the large wavelength range from 0.84 to 1.82 μm, photogeneration occurs only in the Ge bottom sub-cell region because the InGaP and the GaAs sub-cells are transparent to the incident light as shown in the Figure 4.23. Also, no photogeneration was observed at a wavelength over 1.82 μm, which confirms the spectral responses result in Figure 4.16.

II.2.2 Monolithically Stacked InGaP/GaAs/Ge Triple-Junction Solar Cell

After successfully modeling InGaP/GaAs/Ge triple-junction mechanical stacked solar cell, the next step is to connect the three cells using the tunnel junctions. As shown in Table 4.13, the monolithic triple-junction solar cell is composed of three sub-cells: namely, InGaP (top), GaAs (middle), and Ge (bottom) junctions stacked in series. Two highly-doped tunnel junctions (i.e., p++-InGaP/n++-InGaP and p++-GaAs/n++-GaAs) are placed between each pair of three sub-cells. The complete InGaP/GaAs/Ge triple-junction solar cell becomes like in Table 4.13:

Table 4.13: Structure of InGaP/GaAs/Ge triple-junction monolithic solar cell

Sub-Cell	Layer	Type	Material	Doping	Thickness
InGaP Top sub-cell Eg = 1.9 eV	Window	n+	AlGaAs	$5x10^{19}$ /cm^3	0.01 μm
	Emitter	n	InGaP	$5x10^{17}$ /cm^3	0.18 μm
	Base	p	InGaP	$1x10^{17}$ /cm^3	0.60 μm
	BSF	p+	AlGaAs	$5x10^{18}$ /cm^3	0.01 μm
InGaP Tunnel junction	Emitter	p++	InGaP	$8x10^{18}$ /cm^3	0.015 μm
	Base	n++	InGaP	$8x10^{19}$ /cm^3	0.015 μm
GaAs Middle sub-cell Eg = 1.42 eV	Window	n+	AlGaAs	$1x10^{19}$ /cm^3	0.01 μm
	Emitter	n	GaAs	$2x10^{18}$ /cm^3	0.01 μm
	Base	p	GaAs	$1x10^{17}$ /cm^3	004 μm
	BSF	p+	InGaP	$7x10^{18}$ /cm^3	0.01 μm
GaAs Tunnel junction	Emitter	p++	GaAs	$8x10^{18}$ /cm^3	0.015 μm
	Base	n++	GaAs	$8x10^{19}$ /cm^3	0.015 μm
Ge Bottom sub-cell Eg = 0.67 eV	Window	n+	GaAs	$7x10^{18}$ /cm^3	0.05 μm
	Emitter	n	Ge	$2x10^{18}$ /cm^3	0.10 μm
	Substrate	p	Ge	$1x10^{17}$ /cm^3	300 μm

After successfully modeling InGaP/GaAs/Ge triple-junction monolithic tandem solar cell, the electrical characteristics are Jsc = 0.0149 A/cm^2, V_{OC} = 2.6478 V and η = 35.54 %.
The J-V curve for InGaP/GaAs/Ge triple-junction monolithic solar cell is shown in Figure 4.25:

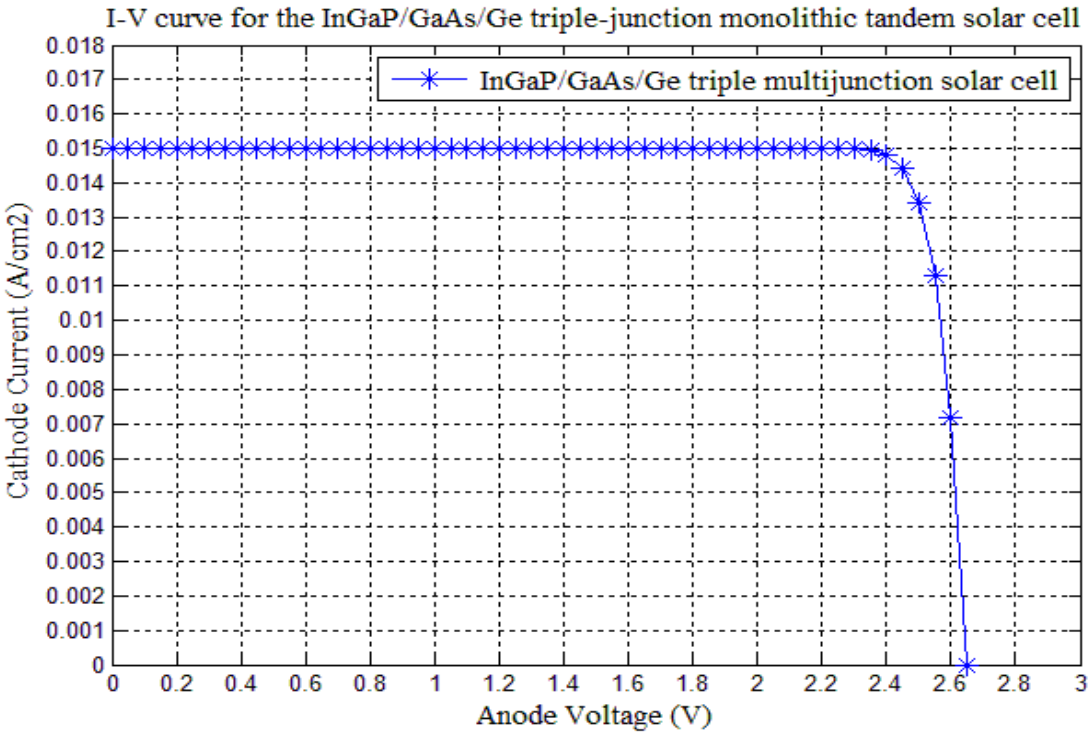

Figure 4.25: J-V curve for InGaP/GaAs/Ge triple-junction monolithic tandem solar cell

The five most important characteristics of the InGaP/GaAs/Ge triple-junction monolithic tandem solar cell are organized in Table 4.14:

Table 4.14: Characteristics of InGaP/GaAs/Ge triple-junction monolithic solar cell

	Jsc (A/cm^2)	Voc (V)	Pmax (W/cm^2)	FF	η %
InGaP/GaAs/Ge triple-junction cell	0.0149	2.6478 V	0.0355	0.9013	35.54 %

II.2.2.1 Comparison of the Sub-Cells, InGaP/GaAs Dual-Junction and InGaP/GaAs/Ge Triple-Junction Solar Cells

After imported the sets of data into MATLAB in order to combine them into one set of data that represented the overall J-V curve of the triple junction solar cell, Figure 4.26 shows a comparison of J-V curves and Table 4.15 shows a comparison the five most important characteristics for the InGaP top, GaAs middle, Ge bottom sub-cells and InGaP/GaAs dual junction, InGaP/GaAs/Ge triple-junction solar cells. In the case of the series-connected monolithic multi-junction solar cell, each sub-cell acts as a current source; thus, the maximum current density is limited to the smallest current source, as expected, the total current will be determined by the sub-cell with the lower output current, it is top InGaP sub-cell Jsc= 0.0148 A/cm^2 which is obviously very close to the InGaP/GaAs dual-junction and InGaP/GaAs/Ge triple-junction monolithic solar cell output current density Jsc = 0.0149 A/cm^2. The Voc value of the monolithic cell structure is nearly equal to the sum of Voc values of each sub-cell, so for InGaP/GaAs dual-junction solar cell $V_{Tandem} = V_{top\_InGaP} + V_{bottom\_GaAs}$ so V_{Tandem}=1.4096+1.0539 = 2.4635 V which is very close to the InGaP/GaAs dual-junction solar cell

output voltage V_{OC} = 2.4642V, while for InGaP/GaAs/Ge triple-junction solar cell $V_{Tandem} = V_{Top\_InGaP} + V_{Middle\_GaAs} + V_{Bottom\_Ge}$ so V_{Tandem}=1.4096+ 1.0539 + 0.1838 = 2.6473 V which is very close to the InGaP/GaAs/Ge triple-junction monolithic tandem solar cell output voltage V_{OC} = 2.6478 V.

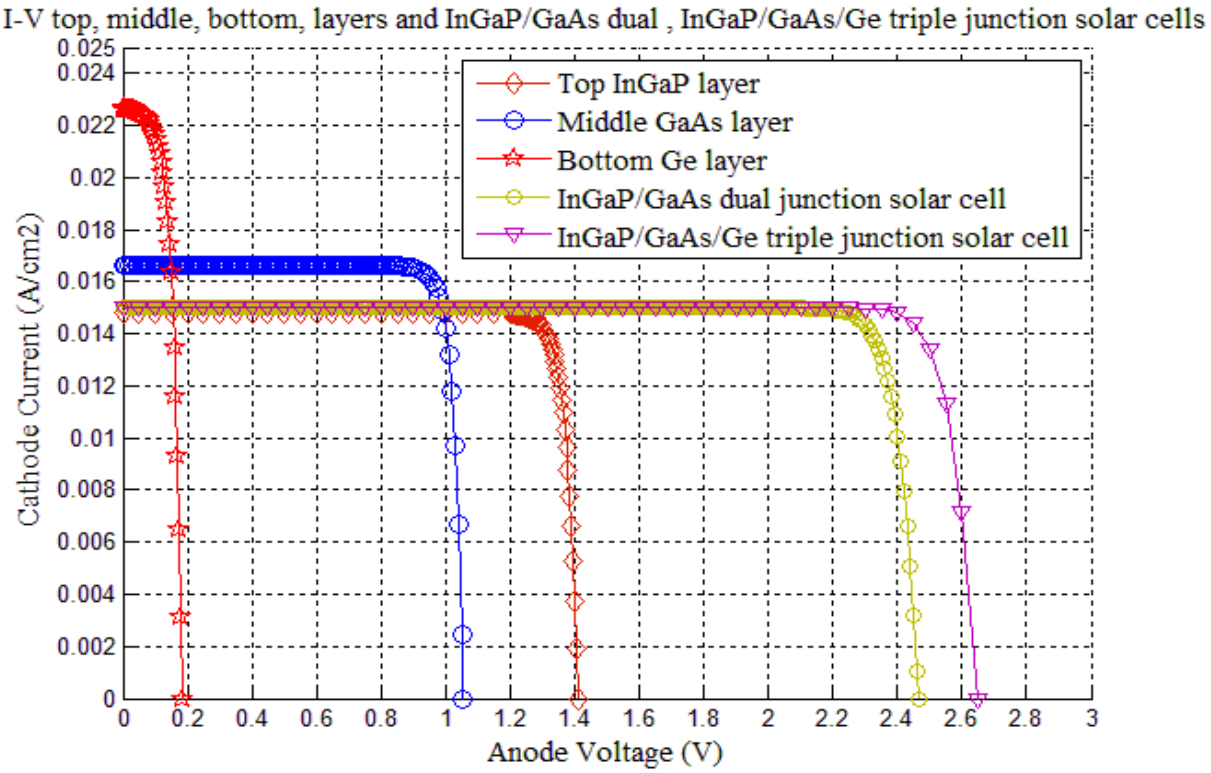

Figure 4.26: J–V curves for top, middle, bottom sub-cells and InGaP/GaAs dual junction, InGaP/GaAs/Ge triple junction solar cells

The comparison of the five most important characteristics of the top InGaP, middle GaAs, bottom Ge sub-cells and InGaP/GaAs dual-junction, InGaP/GaAs/Ge triple-junction solar cells are organized in Table 4.15.

Table 4.15: Comparison of the characteristics of top, middle, bottom sub-cells and InGaP/GaAs dual junction, InGaP/GaAs/Ge triple junction solar cells

	Jsc (A/cm^2)	Voc (V)	Pmax (W/cm^2)	FF	η %
InGaP Top sub-cell (Eg=1.9 eV)	0.0148	1.4096	0.0185	0.8867	18.55
GaAs Middle sub-cell (Eg=1.42 eV)	0.0166	1.0539	0.0153	0.8750	15.35
Ge Bottom sub-cell (Eg=0.67 eV)	0.0226	0.1838	0.0025	0.6178	2.57
InGaP/GaAs Dual-junction solar cell	0.0149	2.4642	0.0332	0.9010	33.28
InGaP/GaAs/Ge Triple-junction solar cell	0.0149	2.6478	0.0355	0.9013	35.54

The increase in efficiency for InGaP/GaAs dual-junction from 33.28 to 35.54% for InGaP/GaAs/Ge triple-junction solar cell. The modest increase in efficiency can be attributed to the increase in Voc from 2.46 V to 2.64 V ensured that the efficiency would increase. The active Ge sub-cell in triple-junction GaInP/GaAs/Ge solar cell increases the voltage of the solar cell, since it is in series with the top two sub-cells. The Voc of Ge sub-cell is quite small (only 0.1838 V) and does not seem to be very important. However, increases of 2.26 % in efficiency by adding the Ge bottom sub-cell. Even after the GaInP and GaAs sub-cells have absorbed the photons in the solar spectrum with energy greater than the 1.9 eV and 1.424 eV bandgap of InGaP and GaAs sub-cells respectively, the Ge sub-cell has the maximum photo-generation rate value ($2.52334x10^{22}$ atoms/s.cm^3) than the GaInP ($8.58994x10^{21}$ atoms/s.cm^3) and GaAs ($1.78915x10^{22}$ atoms/s.cm^3) sub-cells ,as a result, Ge bottom sub-cell can produce very high current density around 0.0226 A/cm^2 in the 0.67 eV-bandgap. Since the Ge cell has far more photogenerated current density than the GaInP and GaAs cells, the Ge cell does not limit the multi-junction cell current. Unfortunately, this advantage will largely remain unused, as this current will be choked by the above InGaP and GaAs sub-cells in the stack. We successful modeling of the InGaP/GaAs dual-junction and InGaP/GaAs/Ge triple-junction solar cell illustrates how well Silvaco ATLAS is at modeling multi-junction solar cells.

III. Validation of Results with Simulation and Experimental Data

In order to validate our models, validation of the Silvaco ATLAS solar cell model can only be done by comparison of the model to other simulator software and to real experimental results. Therefore, we simulated an InGaP/GaAs and InGaP/GaAs/Ge multi-junction solar cell and the results are compared to published simulation and experimental data. The results compared favorably with corresponding simulation and experimental data for different and similar sub-cells structure of multi-junction solar cell using the same some parameters as optical parameters AM1.5G. Some differences are due to the variations in the material, thickness, and doped profile. Table 4.16 and Table 4.17 shows the various comparisons of our optimized design with other previous findings and found the results of our simulation model gives a good result with high efficient performance than other proposed in various works of literature. Comparison with the experimental performance of multi-junction solar cells confirms the accuracy of the analysis using Silvaco ATLAS software simulator. Enhancing InGaP, GaAs, and Ge sub-cells PV characteristics, with the simulated findings described in chapter 3, lead to enhancement in multi-junction solar cells here.

Table 4.16 shows summarize the PV characteristics for our simulated InGaP/GaAs dual-junction solar cell, in comparison with simulation and experimental data [1, 2, 3]. We observed that the performance (Jsc, Voc) and results produced from this simulation model are comparable to experimental data of similar manufactured solar cells as in reference [1, 2], the results are also comparable to simulation data as in reference [3] using a commercial software Silvaco ATLAS simulator. The present InGaP/GaAs dual-junction solar cell exhibits higher open circuit voltage, fill factor and conversion efficiency values than the experimental and simulated dual-junction solar cells. The important output results of the presented InGaP/GaAs dual -junction solar cell are compared with the previous works in Table 4.16.

Table 4.16: Comparison of InGaP/GaAs dual-junction solar cell performance parameters, for simulation versus measurements

	Solar cells	[reference] Description	Year	Jsc (A/cm^2)	Voc (V)	FF	η (%)
Experimental Data	InGaP/GaAs	[1]	2013	0.0141	2.512	0.87	31.1
	InGaP/GaAs	[2]	2017	0.0136	2,52	0.875	30.01
	InGaP/Si	[2]	2017	not reported	not reported	not reported	32.45
	GaAs/Si	[2]	2017	not reported	not reported	not reported	32.8
simulation Data	InGaP/GaAs	[3] Silvaco ATLAS	2012	0.0161	2.3969	0.87	32.39
	InGaP/GaAs	[Our work]	2018	0.0149	2.5374	0.88	33.69

Interestingly, our simulated InGaP/GaAs dual-junction solar cell performance (Jsc, Voc) matches perfectly with experimental data reported in researchs[1, 2]. This model refers to the very good agreement between simulated and experimental data. The InGaP/GaAs dual-junction solar cell has the best photovoltaic conversion efficiency of 33.69% with the Voc of 2.5374 V, a Jsc value of 0.0149 A/cm^2, and a FF of 88%. This proves the validity of the numerical model and the used input data, thus setting a starting point for a deeper understanding and further structure optimization of InGaP/GaAs/Ge triple-junction solar cell.

Table 4.17 shows summarize the PV characteristics for our simulated InGaP/GaAs/Ge triple-junction solar cell, in comparison with simulation and experimental data [4, 5, 6, 7]. We observed that the performance and results produced from this simulation model are comparable to experimental data of similar manufactured solar cells as in reference [4], the results are also comparable to simulation data as in reference [7] using Crosslight APSYS software simulator. The present InGaP/GaAs/Ge triple-junction solar cell exhibits higher fill factor and conversion efficiency values than the experimental and simulated triple-junction solar cells. The important output results of the presented InGaP/GaAs/Ge triple-junction solar cell are compared with the previous works in Table 4.17.

Table 4.17: Comparison of InGaP/GaAs/Ge triple-junction solar cell performance parameters, for simulation versus measurements

	Solar cells	Description [reference]	Year	Jsc (A/cm^2)	Voc (V)	FF	η (%)
Experimental Data	InGaP/GaAs/Ge	[4]	2009	0.0147	2.69	0.86	34.1
	InGaP/GaInAs/Ge	[5]	2015	0.0131	2.66	0.85	34.5
	InGaP/GaAs/Si	[6]	2019	0.1337	2.71	0.75	32.6
	InGaP/GaAs/InGaAs	[6]	2019	0.1366	2.52	0.78	30.9
simulation Data	InGaP/GaAs/Ge	[7] Crosslight APSYS	2007	0.0165	2.56	0.85	26.7
	InGaP/GaAs/Ge	[Our work]	2018	0.0149	2.6478	0.90	35.54

Interestingly, our simulated InGaP/GaAs/Ge triple-junction solar cell performance (Jsc, Voc) matches perfectly with experimental data reported in research [4], while a noticeable difference is observed in FF. This difference was assigned to resistive losses. As a result, this model refers to the very good agreement between Crosslight APSYS and Silvaco ATLAS software simulator. The InGaP/GaAs/Ge triple-junction solar cell has the best photovoltaic conversion efficiency of 35.54% with the Voc of 2.6478 V, a Jsc value of 0.0149 A/ cm^2, and a FF of 0.90.

Conclusion

Current state-of-the-art high efficiency photovoltaics are Multi-Junction Solar Cells (MJSC) composed of III-V semiconductors. In this chapter, an InGaP/GaAs dual-junction and InGaP/GaAs/Ge triple-junction solar cell have been modeled and simulated using TCAD SILVACO Atlas software. The whole process was done in stages and detailed explanations were provided. First, numerical models of GaAs, InGaP and Ge individual sub-cells are built. As a result, mechanically and monolithically stacked for InGaP/GaAs dual-junction cells and InGaP/GaAs/Ge triple-junction cells are demonstrated as well. Efficiencies of 33.28 % for InGaP/GaAs dual-junction solar cells, while 35.54 % for InGaP/GaAs/Ge triple-junction solar cells under one-sun terrestrial AM1.5G spectrum illumination (0.100W/cm^2, AM1.5G, 28^{o}C) are realized. Monolithic and mechanically stacked multi-junction solar cells have been developed with encouraging efficiencies, it is clear that the conversion efficiency of InGaP/GaAs/Ge is better than that of GaInP/GaAs solar cell and also better than that of single solar cells. The InGaP/GaAs and InGaP/GaAs/Ge efficiency is expected to be even higher, since a larger range of photon energies can be absorbed. The InGaP top sub-cell has a wider bandgap (1.9 eV) to absorb the short wavelength portion of the solar spectrum whilst passing through the mid-range wavelengths that will be absorbed more effectively by the GaAs middle sub-cell (i.e., having a bandgap of 1.42eV) and while passing through the longer wavelengths that will be absorbed more effectively by the Ge bottom sub-cell (i.e., having a bandgap of 0.67eV). In order to optimize InGaP/GaAs dual-junction, its most glaring shortcoming is that there is a current mismatch between the top InGaP and bottom GaAs sub-cells. Thus, we optimized the doping and the base thicknesses in the InGaP, GaAs sub-cells to achieve the current-matching condition. Then, we validated these results with simulation and experimental various literature results. This numerical model offers a cost effective and time efficient way to optimize the mechanical and monolithic stacked solar cell. With incorporating experimental parameters into the simulation model of III-V compound-based multi-junction solar cells, these theoretical analyses can provide a better understanding of the physical behaviors in photovoltaic devices. According to the discussion in this chapter, Silvaco ATLAS was an accurate means to model solar cells. This proves the validity of the numerical model and the used input data, thus setting with these results are potentially useful in future enhancements of multi-junction III–V semiconducting materials.

References

[1] Myles A. Steiner, et al. Effects of Internal Luminescence and Internal Optics on Voc and Jsc of III–V Solar Cells. IEEE Journal of Photovoltaics, Vol. 3, No. 4, October 2013.

[2] Essig S, et al. Raising the one-sun conversion efficiency of III–V/Si solar cells to 32.8% for two junctions and 35.9% for three junctions. Nature Energy;2(9):17144. https://doi.org/ 10.1038/nenergy.144, 2017.

[3] Khomdram Jolson Singh and Subir Kumar Sarkar. Highly efficient ARC less InGaP/GaAs DJ solar cell numerical modeling using optimized InAlGaP BSF layers. Opt Quant Electron 43:1 21 DOI 10.1007/s11082-011-9499-y, 2012.

[4] Andreas W. Bett, et al. Highest Efficiency Multi-Junction Solar Cell For Terrestrial And Space Applications. 24th European Photovoltaic Solar Energy Conference, 21-25, Hamburg, Germany. , September 2009.

[5] Green MA, et al. Improvements in sunlight to electricity conversion efficiency: above 40% for Director sunlight and over 30% for global. Paper 1AP.1.2, European Photovoltaic Solar Energy Conference 2015, Hamburg, September 2015.

[6] Yu-Cheng Kao, et al. Performance comparison of III–V//Si and III–V//InGaAs multijunction solar cells fabricated by the combination of mechanical stacking and wire bonding. 9:4308, 2019.

[7] Z. Q. Li, et al. Two-dimensional simulation of GaInP/GaAs/Ge triple junction solar cell. phys. stat. sol. (c) 4, No. 5, 1637– 1640, 2007.

Conclusion & Future Work

Conclusion & Future Work

Conclusion

In conclusion, this thesis introduces the important concepts in modeling multi-junction solar cells. The aim of this thesis is to develop a monolithically stacked an III-V InGaP/GaAs/Ge triple-junction solar cell, in a first attempt to create a monolithic tandem solar cell, the mechanically stacked structure used for simplicity, with each of the sub-junctions separately contacted. This approach provides a very generic way of realizing multi-junction solar cells. Several important parameters like frequency response, and photogeneration rate, open-circuit voltage (Voc), short-circuit current (Jsc), fill-factor (FF), maximum power point (MPP) and solar cell efficiency has been discussed. Since almost all research on advanced solar cells is currently conducted via expensive and complex experimentation, the proposed simulation method is expected to help reduce that cost, simplify the design process, and allow the designer to focus on the final result.

In this thesis, I have investigated three major topics, demonstration of individual InGaP, GaAs, and Ge sub-cells, demonstration of Lattice-matched Mechanically Stacked Multi-Junction (MSMJ) and monolithic InGaP/ GaAs dual-junction than InGaP/ GaAs/Ge triple-junction solar cells, in order to investigate the modeling of an InGaP/GaAs dual-junction and InGaP/GaAs/Ge triple-junction solar cell The discussion then progressed to the analysis of a *p-n* junction and the simulation of InGaP, GaAs and Ge single-junction solar cells using TCAD Silvaco ATLAS software in chapter 3. Chapter 4 then focused on modeling and simulating multi-junction solar cells. The whole process was done in stages and detailed explanations were provided.

In chapter 3, Very high-performance III-V single-junction solar cells have been demonstrated, with the best efficiencies of 18.55% for InGaP, 29.39% for GaAs and 7.11% for Ge respectively (under AM1.5). First, numerical models of Unoptimized InGaP, GaAs and Ge solar cells are built. The improved model is simulated again and new results are obtained with the inclusion of the window and back surface field BSF layers. These layers have been shown to provide a significant enhancement to the device. This has formed a paper was written and has already been accepted for publication “Efficiency improvement of single-junction InGaP solar cells by advanced photovoltaic device modeling”, Ahmed Benlekhdim, Ali Cheknane, Larbi Sfaxi, Hikmat S. Hilal, Optik, Volume 163, June 2018, Pages 8-15.

In chapter 4, after numerical models of GaAs, InGaP and Ge individual sub-cells are built, both and triple-junction solar cells are then placed in a mechanically and stacked configuration to investigate shadowing phenomena. As a result, mechanically and monolithically stacked for InGaP/GaAs dual-junction cells and InGaP/GaAs/Ge triple-junction cells are demonstrated as well. Monolithic and mechanically stacked multi-junction solar cells have been developed with encouraging efficiencies of 33.28 % for InGaP/GaAs dual-junction solar cells, while 35.54 % for InGaP/GaAs/Ge triple-junction solar cells under

one-sun terrestrial AM1.5G spectrum illumination (0.100W/cm2, AM1.5G, 28^{o}C) with minimal effort, it is clear that the conversion efficiency of InGaP/GaAs/Ge is better than that of GaInP/GaAs solar cell and also better than that of single solar cells.

In order to the validation of the results and for the purpose of evaluating the models, a comparison between simulated and reported performances in the literature is also included. As a result, this model refers to the very good agreement between simulated and experimental data and the simulation results closely approximate published results from experimentation. This comparison of experimental and simulated results will lead to more accurate and confident results for new cell designs and performance. The fact that the results also match is a good indication of the validity of this methodology. Therefore, the efficiency predictions from Silvaco ATLAS software are closer to experimental ones could be offered as a valid substitution for future high-efficiency solar cell design tool prior to the real fabrication process. The theoretical results of our simulation for single InGap, GaAs and Ge single-junction solar cell or for multi-junctions GaInP/GaAs double-junction and GaInP/GaAs/Ge triple-junction solar cells are high than experimental works, due primarily to the material defects generated by the material itself or the lattice mismatch between the top, middle and bottom sub-cell.

The model of InGaP, GaAs, Ge single-junction solar cells, InGaP/GaAs dual-junction and InGaP/GaAs/Ge triple-junction solar cells presented here proves that suitable models and material parameters are now available for comprehensive simulations of multi-junction solar cells within a semiconductor simulation environment. Modeling of the structures allows novel possibilities for studying the interaction of the sub-cells, thereby setting a starting point for a deeper understanding of these sophisticated devices as well as for structure optimization. Significant improvements in solar cell efficiencies nearing theoretical predictions are projected with improvements in cell material quality and processing. Although the triple junction cell is aimed at space applications for its high efficiency and radiation hardness, it could be a serious candidate for terrestrial applications when operated under concentrated illumination.

Although the modeling results presented in this thesis are encouraging for future design and optimization of III-V multi-junction solar cells and although this would potentially be cost-prohibitive depending on. Availability of a process line, physically constructing and utilizing the optimized cell design in the real world would lend validity to the simulation results and further solidify the optimization and modeling techniques in this research as valid methods for multi-junction solar cell design. It is hopeful that this work may serve as a guide to the next series of modeling and simulation efforts that will aid in the development of novel photovoltaic devices and that the analyses performed herein will aid in their experimental realization.

Future Work

However, due to the time limitations of this thesis, detailed results were not presented here. They may be researched in future work. Whole sections of the available design space were not simulated and may likely lead to a more optimized design than what was discovered during this research. Even given the remarkable performance of the lattice-matched GaInP/GaAs/Ge solar cell. As explained in the earlier chapter, multi-junction solar cells implement high-efficiency photovoltaic devices by incorporating materials with different bandgaps trying to get, as close as possible, to the optimum combinations. In the race to reach a higher number of junctions with the appropriate bandgaps, many materials, device configurations, and manufacturing approaches have been explored. Although the modeling results presented in this thesis are encouraging for future design and optimization of III-V solar cells; the simulation results will also provide necessary the feedback for further optimization of our model and the associated parameters to further improve the cell performance. In order to future design improvements, it is therefore necessary to explore new approaches with the potential to reach even higher efficiencies. Our future works will focus on the other approaches:

1. **Design optimization of the existing layers**

The band-gap combination of the InGaP/GaAs/Ge-based triple-junction solar cell leads to a not optimal split of the solar spectrum, causing a strong excess current in the Ge bottom cell. The drawback of this lattice matched design is that current matching condition is not achieved. Therefore, various approaches try to overcome the strong current mismatch by increasing the absorption in the upper two cells or by integrating an additional junction between the GaAs and the Ge sub-cell. Theoretically, an improvement in the efficiency of the GaInP/GaAs/Ge cell is predicted when the GaInP band gap is increased. In order to better match the current, the bandgaps of the top two cells need to be lowered to produce more current. Therefore, another combination of the top two cells $In_{0.56}Ga_{0.44}P$ and $In_{0.08}Ga_{0.92}As$ has been tried with energy bandgaps of 1.8 eV and 1.3 eV, respectively. These two materials have lower bandgap energies and can better match the current, these top and middle sub-cells could collect a larger current while reducing the number of photons transmitted to the Ge layer.

2. **Broadband antireflection coatings**

The multi-junction cell approach aims to efficiently collect and convert photons over a wide range of photon energies. Therefore the solar cell must absorb, rather than reflect, virtually all the incident light over this broad spectral region, necessitating the use of an effective, broadband antireflection (AR) coating. In order to minimize reflections and enhance absorption anti-reflection coatings (AR) are applied on the front surface of the solar cell.

3. **InGaP/GaAs/Si solar cell structure**

Traditional GaInP/GaAs/Ge triple-junction solar cells collect roughly twice as much current in the 0.67 eV Ge sub-cell as in the other two sub-cells, and this extra collected current is largely wasted. A more optimal design would have a bottom sub-cell with a bandgap of around 1.0 eV this would collect sufficient current to match the top two sub-cells

and would provide more voltage at the maximum power point than would a Ge sub-cell. Silicon has a bandgap of 1.12 eV, so it will be interesting to investigate silicon cell design for realizing a 3J InGaP/GaAs/Si solar cell structure on Si substrate. Because the Si bottom sub-cell's bandgap is higher than Ge, with the aim of providing a better current match than the 3-junction cell on germanium and possibly of higher efficiency while also using a lower-cost substrate.

4. Increasing the number of junctions

Another possible design improvement is to progress to devices with more junctions. Four-junction solar cells have been suggested using a material with a bandgap of 1.0 eV. For this purpose, GaInNAs is considered as the most studied and it can be grown lattice-matched to Ge. By inserting a 1 eV third junction into the GaInP/GaAs/Ge structure to form a 4-junction solar-cell with a bandgap combination of 1.9 eV/1.42 eV/1.0 eV/0.67 eV to form InGaP/GaAs/InGaAsN/Ge configuration is more optimal than the conventional triple-junction solar-cell theoretically.

5. Concentrator Photovoltaic

Multi-junction solar cells are very expensive and firstly they were used only in space applications. The concentrations of sunlight made these cells economically viable for the use on Earth and improve the performance of the solar cells to achieve a high-efficiency.

6. Nanostructures

The device energy conversion is limited by different parameters; one of these parameters is the material absorption range. So, it is critical to use materials that absorb as much of the sun light spectrum beyond the visible range. The insertion of quantum dots or quantum wells is one of the ways to enhance the absorption range of the material enabling new sub-band transitions in the material quantizing the energy levels. So other design approaches for efficiency improvement which have garnered the attention of the solar cell industry is the use of nanostructures, such as quantum wells or quantum dots to manipulate the effective band gap of an MJSC to extend that sub-cell’s absorption range. This allows device designers to increase the photocurrent in this sub-cell through are optimization of the top sub-cell, which allows for an overall increase in the full device photocurrent, and offer the potential for high photovoltaic efficiency by tailoring the properties of existing materials, and for reducing of cost.

7. Temperature and Radiation Effects

Solar cells for space missions are required to operate at high temperatures and in a harsh radiation environment. Therefore, it is necessary to study the behavior of multi-junction solar cells at high temperatures and with radiation damage.

8. Simulate with Different Air Mass Spectrums

The multi-junction cell in this thesis was optimized for the AM1.5G spectrum for terrestrial. Varying the air mass for space application will lead to a different relationship and importance correlation for the input factors than those found for the optimization in AM1.5G.

Appendix I

Silvaco ATLAS Modeling Software

Appendix I

Silvaco ATLAS Modeling Software

I Introduction to the Silvaco ATLAS Simulation Tool

TCAD is used in the computer-aided design and engineering semiconductor device design, fabrication process design, technology characterization for circuit design and in other areas. The TCAD software package used in this thesis work is created by Silvaco International and consists of *Athena*, *Atlas*, *Deckbuild* and *TonyPlot* programs [1].

Athena is a framework program that integrates several smaller programs into a more complete process simulation tool. It is a modular program that combines simulations into a more complete package allowing for the simulation of a wide range of semiconductor fabrication processes: *epitaxial growth, thermal oxidation, thermal diffusion and ion implantation, photolithography, etching, deposition dielectrics films, metallization and others*.

Atlas is a physically-based two and three dimensional (3D) device simulation tool. This allows for the simulation of a wide variety of modern semiconductor technologies. It predicts the electrical behavior of different semiconductor structures, and gives insight into the internal physical mechanisms associated with the device operation. *Atlas* is often used in conjunction with *Athena* using the physical structures and doping profiles generated by *Athena*.

DeckBuild: Simulation of a PV cell in ATLAS™ is made through a text input deck called DeckBuild, it is the graphical user interface (GUI) for Silvaco's TCAD programs that allows user to go transparently from *Athena* process simulation to *Atlas* device simulation, a run-time environment in which many different parameters of cell structure and composition must be defined. *DeckBuild* has numerous simulator specific and general debugger style tools, such as powerful extract statements, GUI based process file input, line by line runtime execution and intuitive input file syntactical error messages. The first line to be read by the program when running ATLAS™ using DeckBuild is the GO ATLAS command.

TonyPlot is the visualization tool. It provides comprehensive capabilities for viewing and analyzing simulator output. The data can be plotted as desired by the user either in one or two-dimensional graphs. The overlays feature helps in comparing the multiple simulation runs. *TonyPlot* includes animation features that permit viewing a sequence of plots in a manner showing solutions as a function of some parameter.

II General Simulation Methodology

The ATLAS simulation methodology is a form of finite element analysis. A mesh defines the device structure and the physical models are solved at each nodal point throughout that mesh.

II.1 Mesh Generation

The first step in building a device after the go atlas statement is to define the mesh. The mesh is a grid that covers the physical area in which the device will be constructed and simulated. The mesh is simply created by a series of vertical and horizontal lines with user defined spacing between them [2]. It bounds the physical area of the cell by creating a number of triangles in which the simulation will take place. Mesh specification also involves a tradeoff between accuracy and numerical efficiency. A fine defined mesh will lead to more accurate results, and on the other hand, a coarse mesh that minimizes the total number of grid points will lead to a larger numerical efficiency.

II.2 Regions

The next step was to define the material regions that correspond with the defined meshing for each layer. Each region is bound with precise location points defining a top position where the region starts and a lower position where the region ends.

II.3 Electrodes/Contacts

After defining the regions and materials, the next step is to create contacts on the device.

II.4 Doping

After creating the separate regions and assigning materials to those regions, the materials themselves can be doped. The DOPING statement is broken down into three sections. First, the distribution type can be either uniform, Gaussian, or complementary error function forms. Only the uniform distribution type was utilized in this thesis. Next, a concentration and type of doping must be specified. Finally, the region to be doped must be identified.

II.5 Material

Once the structure is completely assembled, the materials used to construct the device must themselves be defined. Each of the different materials used in the simulation and their individual properties such as Bandgap, Permittivity (Dielectric constant), Electron Affinity, Electron and Hole Mobility, Effective Density of States and Refractive Index are defined via the material statements with specific values [2].

II.6 Beam Statement

The beam statement selects the specified light spectrum of the source to which the solar cell is exposed. It specifies the position the light beam originates the starting and ending optical wavelengths for the beam. For the purposes of this thesis, the source is the sun, and the AM1.5 spectrum is used to simulate the energy received by a solar cell in a terrestrial application.

II.7 Physical Models

Physical models are specified using the MODELS statement. The physical models are grouped into five classes: mobility, recombination, carrier statistics, impact ionization, and tunneling [2]. The list of physical models available to the ATLAS software can be found in the ATLAS user's manual.

II.8 Solution Numerical Method

The method selected for solving the non-linear equations that make up the simulation can be user specified with the method call. ATLAS contains several numerical methods to calculate the solutions to semiconductor device problems. There are three main types of numerical methods. The first method is the GUMMEL type which is useful where the system of equations is weakly coupled but has only linear convergence. The next method is NEWTON, which is useful when the system of equations is strongly coupled and has quadratic convergence. This method causes ATLAS to spend extra time solving for quantities which are essentially constant or weakly coupled and also requires a more accurate initial guess to the problem to obtain convergence. For this thesis research, Newton's method was utilized. The final method is the BLOCK method which can provide faster simulation times in situations where the NEWTON method struggles. Numerical methods are given in the METHOD statements of the input file.

II.9 Solution Specification

This section of the input deck to ATLAS is where the simulation does its calculations to solve for the device specified. It is divided up into four parts: LOG, SOLVE, LOAD, and SAVE. The LOG statement creates save file for steady-state, transient, or DC data determined by a solve statement after the log statement.

II.10 Parameter Extraction and Plotting

The final section of the input deck is extracting the data and plotting it in a useful way. The two statements associated with this section are EXTRACT and TONYPLOT. The log files produced by ATLAS™ and the current-voltage cell characteristic can be plotted and observed in TONYPLOT. For this thesis research, Jsc, Voc, Pmax, fill factor, and efficiency are extracted along with the general IV characteristic curve.

References

[1] Vaidotas BARZDĖNAS and Romualdas NAVICKAS. Microtechnologies, © Vilnius Gediminas Technical University, 2012.

[2] ATLAS User's Manual, vols. 1-2, software version 5.6.0.R, Silvaco International, Santa Clara, CA, 2012.